Quantum Simulation of Nanoscale Transport in Direct Energy Conversion Materials: From Thermal-Field Emitters to Thermoelectrics

BY

TERENCE D. MUSHO

Dissertation

Submitted to the Faculty of the

Graduate School of Vanderbilt University

in partial fulfillment of the requirements

for the degree of

DOCTOR OF PHILOSOPHY

in

Interdisciplinary Materials Science

May, 2012

Nashville, Tennessee

APPROVED:
Professor D. Greg Walker
Professor Ron Schrimpf
Professor Alvin Strauss
Professor Norman Tolk
Professor Kalman Varga

Interdisciplinary Materials Science

Quantum Simulation of Nanoscale Transport in Direct Energy Conversion Materials: From Thermal-Field Emitters to Thermoelectrics

Terence D. Musho

Dissertation under the direction of Professor D. Greg Walker

In the ongoing struggle to resolve our current energy crisis, many agencies and researchers have spearheaded the application of direct energy conversion materials, such as thermoelectric and thermionic devices for waste heat recovery and power generation. However, the current state-of-the-art direct energy conversion materials are plagued by extremely low efficiencies that prevent a widespread solution. Recent effort to improve the efficiencies of these direct energy conversion materials has demonstrated a drastic increase through the inclusion of nanoscale features. With new advances in nanoscale materials comes the need for new models that can capture the underlying physics. Thus, this research has developed a necessary tool and a unique modeling approach (based on NEGF quantum simulations) that couples both the electrical and thermal response of nanoscale transport accounting for both the dissipative interactions of electron-phonon and phonon-phonon scattering. Through the aid of high performance computing techniques, the models developed in this research are able to explore the large design space of nano-structured thermoelectrics and thermionic materials. The models allow computational predictions to drive innovation for new, optimized, direct energy conversion materials.

A specific device innovation that has come from this research is the development of variably spaced superlattice (VSSL) devices, which are the next progression in band

engineering thermoelectric materials. Computational findings of VSSL materials predict a seven times increase in ZT at room temperature when compared to traditional superlattice devices. Other thermoelectric materials studied include nanocrystalline composites (NCC) which were predicted to outperform equivalent superlattice structures as a results of decreases electron filtering. In addition to thermoelectric materials, this research has developed a quantum modeling technique to investigate and optimize nano-tipped thermionic and thermal-field devices. Results have provided incite into the applicability of Richardson's theory in characterizing the emission from wide-band gap thermionic materials. Ultimately, the quantum models developed in this research are a necessary tool for understanding nanoscale transport and innovating new nanostructured materials.

To my mother and father,

Catharine and Matthew Musho

and

my lovely wife, Jennifer

ACKNOWLEDGMENTS

I would like to thank my wife supporting as I spent long hours in the lab working on this research. She kept me on track and helped me succeed in my graduate career. I would also like to thank my wife for proof-reading my manuscripts over the last couple of years.

I would like to thank Prof. Greg Walker for his mentoring and teachings. This work would have never been complete without his long discussion and input. I would also like to thank him for believing in my research and being my advocate in the research community.

I am in debt to the help and support from the staff at Vanderbilt's Advanced Computer Center for Research and Eduction (ACCRE). Their quick turn around on help tickets and reliable nodes made this work possible. Their trying time through the support of a new GPU nodes has made this work possible.

Finally, I would like to acknowledge my committee members for the insight into my research. I would like to thank Prof. Ron Schrimpf for his advise as a mentor and a researcher. I would like to thank Hank Paxton and Prof. Jim Davidson for their contribution of experimental data to enhance my thermionic research.

TABLE OF CONTENTS

LIST OF FIGURES

LIST OF TABLES

LIST OF SYMBOLS

l Length (nm)
A Area (cm^2)
T Temperature (K)
V Voltage (V)
I Current (A)
S Seebeck Voltage ($\mu V K^{-1}$)
σ Electrical Conductivity ($\Omega - m$)
PF Power Factor ($Wm^{-1}K^{-2}$)
ZT Thermoelectric Figure of Merit
k_e Electrical Thermal Conductivity ($Wm^{-1}K^{-1}$)
k_p Lattice Thermal Conductivity ($Wm^{-1}K^{-1}$)
N_d Doping Concentration (cm^{-3})
m_e Electron Mass (kg)
m^* Effective Mass
H Hamiltonian Energy (eV)
ϵ_f Fermi Energy (eV)
k_BT Boltzmann Temperature (K)
h Planck Constant (Js^{-1})
Ξ Transmission
q Charge of Electron (C)
I Identity Matrix
G Green's Function (eV)
Σ Self-Energy Term (eV)
E_o Vacuum Level (eV)
E_f Fermi Level (eV)
E Electric Field (Vcm^{-1})
ϕ Work Function (eV)
β Field Enhancement Factor
A_{eff} Effective Area of Emission (m^2)
K_1 Fowler-Nordheim Constant ($AeVV^{-2}$)
K_2 Fowler-Nordheim Constant ($eV^{-3/2}Vm^{-1}$)
ϵ Relative Permitivity
f_{FD} Fermi-Dirac Distribution
f_{BE} Bose-Einstein Distribution
FN Fowler-Nordheim
$NEGF$ Non-Equilibrium Green's Function

CHAPTER I

INTRODUCTION

For every dollar spent powering integrated circuit devices, nearly 60 cents is lost to thermal waste[1]. The automobile internal combustion engine is even less efficient, with 80 cents for every dollar being lost to waste heat due to combustion and mechanical inefficiencies[2]. In response to this issue, many agencies and researchers have been applying direct energy conversion devices such as thermoelectric power generators for waste heat recovery. However, the current state of thermoelectric technology is characterized by low efficiencies, limiting widespread application and preventing a practical solution to waste energy recovery. Over the past decade, recent advances in nanostructured materials have demonstrated a substantial increase in efficiency of these direct energy conversion materials and a possible avenue for solution-driven innovations. These new nanostructure materials are a step forward but require a more fundamental view point of the transport. To aid in understanding this transport and innovating more efficient materials this research has developed necessary tools to predict the electrical and thermal transport in nanoscale materials. The models developed incorporate dissipative effects providing a tool to design direct energy materials.

Forecasting the next ten years, direct energy conversion materials have the potential to significantly aid the current energy crisis. In the context of thermoelectrics, the technology is roughly one ZT away from being a major contributor to clean sustainable energy production (no secondary waste). However, in order to reach this goal, a greater understanding of the transport physics and further innovation of new, more complex materials is required. In contributing to this goal, this thesis research has developed two aspects. The first aspect is the innovation of new materials which rely on complex band engineered structures. The second aspect and most significant contribution is the development of new computational models (based on quantum theory) to aid in understand the nanoscale transport behavior of new nanostructured materials. Ultimately, the impact of this research in developing more efficient direct energy conversion materials is beyond the concept of innovating devices for large

[1]Based on approximate calculations of joule heating in a 45nm 760million transistor with a nominal turn on voltage of 500mV.

[2]Based on the calculation of a four-stroke Otto cycle assuming gasoline combustion and approximate losses due to mechanical friction

energy production or even the consumer market but rather has the potential to aid developing countries where the availability of cheap sustainable energy does not exist.

The objective of this research relies on two focused areas of direct energy conversion. The first area is nanostructured thermoelectrics where the research focused on developing a coupled quantum modeling approach that accounts for the interaction of electrical (electrons) and thermal (phonons) transport and is capable of predicting device level efficiencies. This was accomplished through the use of high-performance computing (HPC) resources and the incorporation of additional physics such as the dissipation due to electron-phonon interactions and phonon-phonon interactions. The second area of this research is development of a model which could predict the thermionic and field emission characteristics from a hot-body nano-tipped wide-band gap materials. More specifically, modeling the thermionic and field emission from a more fundamental view point and understanding how models developed for emission from metallic surfaces can be applied to the emission from wide-band gap materials. Both of these objectives rely on implementing a quantum mechanical modeling approach in which a non-equilibrium Green's function (NEGF) method is used to predict electrical and thermal transport performance based on inherit physical material parameters. One of the driving necessities for these models is to understand the influence of geometry on the transport and to optimize both the thermal and electronic structures for enhancement and potentially drastic increases in efficiency. This work required an interdisciplinary understanding of engineering, physics and computer science to develop model and new materials which incorporate major aspects of electrical and thermal research.

Motivation

Thermoelectric materials have been demonstrated since the 1950's when the first Systems Nuclear Auxiliary Power (SNAP-1) was developed for remote power generation. These initial devices require extremely high temperature source to maintain a reasonable efficiency and never could be justified for consumer application. Recent advances in new nanostructured materials have ushered in a new interest in thermoelectric power generation. Compounding these advances with the need for clean sustainable energy and you have great motivation to bring thermoelectric power generation to the consumer market. However, there is a need to first develop an understanding of the transport in these new materials in order to make informed decision on how to innovate more efficient nanostructured materials. Interestingly,

because these nanostructures are on the order of a 100 or less unit cells the physics of electrons and phonons transitions from a continuum regime to a quantum regime which is described by a statistical process. The statistics of these quantized particles is described through a quantum model and previous researchers using this approach have been limited to very small or simplified geometries. By including more physics in these quantum models, larger devices which resemble production level devices can be modeled and understood. Furthermore, the addition of more physics through coupling the electrical and thermal transport is a large motivator for this research because an understanding of both the electrical and thermal transport governs the efficiency of thermoelectrics. Additionally, understanding how nanostructured geometry affects the transport is a key aspect and provides a large design space which can be explored in pursuit of more efficient devices.

Thermoelectric devices have several advantages over traditional energy production and refrigeration methods which are appealing to the consumer market. The first appeal is that they have no secondary waste. This goes back to the essence of direct energy conversion where thermal energy, lattice vibrations, are converted directly to electrical energy. One can think of the electrons within the thermoelectric as being the working fluid in a vapor-compression cycle or a steam turbine. Another appealing aspect of thermoelectrics is the idea of waste heat recovery where thermoelectrics could be applied to the surface of any heat producing source and this heat could be directly converted to an electrical potential. Figure 1.1 is a visual illustration of the possible sources of waste heat. The first two, both the automobile and integrated circuit are seen as the most desired applications for waste heat recovery but waste heat produced by large fossil fuel power production (d) is extremely lucrative and often over shadowed. It is also worth noting that many of the advances in thermoelectrics for power production can be applied to cooling applications where the thermoelectric is used as a Peltier device to replace the household HVAC system or refrigeration system.

One way researchers are attempting to make thermoelectrics more appealing to the consumer market and help aid in our current energy crisis is by researching ways to make thermoelectric devices more efficient. With the recent advances in nanotechnology and the means to fabricate materials on the atomic scale, the ability to manipulate the electrical and thermal transport becomes a huge avenue for potentially altering the current thermoelectric devices and the trend of the industry. To put these nanotechnology modifications into perspective, one can think of adding features (different materials) to the thermoelectric materials which are about 3000 times

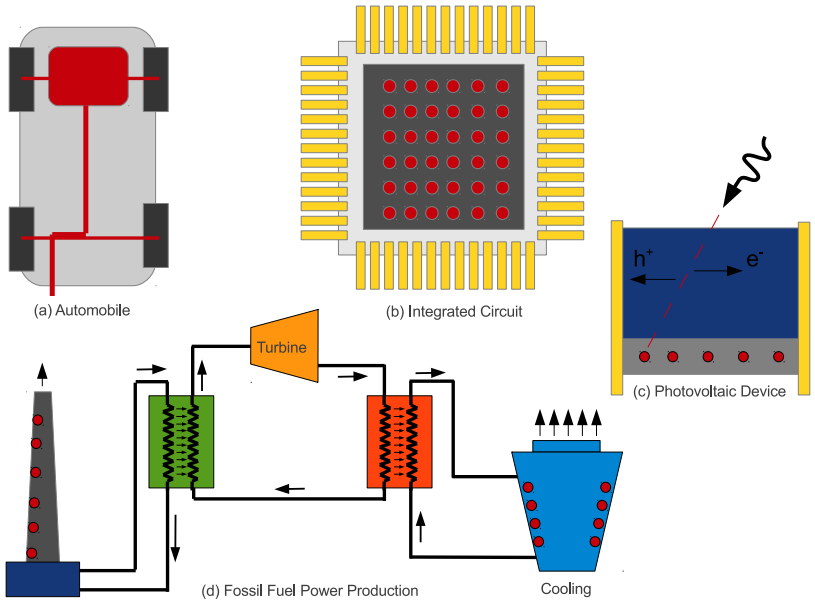

Figure 1.1 Illustration of possible waste heat recovery applications for direct energy conversion materials. (a) automobile, combustion and tribological losses, (b) integrated circuit, (c) photovoltaic cells, (d) fossil fuel energy production.

smaller than a human hair. When you start adding features this small the physics changes from a classical perspective to a quantum perspective.

When discussing the efficiency of a thermoelectric device, a common figure of merit that is often used to describe the overall efficiency of the device is known as the ZT value.

$$ZT = \frac{S^2 \sigma T}{k_e + k_p} \tag{1.1}$$

The figure of merit encompasses both the electrical and thermal performance of the devices. The main objective in designing a good thermoelectric is to have a large electrical contribution which includes a large Seebeck coefficient S and a large electrical conductivity σ. Additionally, the thermoelectric should have a low thermal conductivity which includes both the electrical and lattice contributions. Overall the ZT is maximized when the numerator is maximized and the denominator is minimized.

Often it is easy to gauge the efficiency of a devices when compared to a known efficiency such as a fossil fuel power production plant. The average return of a fossil

fuel burning plant is around 33% efficient. That is to say, about one third of the internal energy of coal is converted to potential energy in the power lines. This value can now be used to compare to a thermoelectric with a corresponding ZT as shown in Figure 1.2 for a given temperature ratio (T_C/T_H). With this efficiency in mind, Figure 1.2 demonstrates that a thermoelectric needs a ZT on the order of 2 to 3 to compete with a fossil fuel power production cycle. The ZT for current thermoelectrics lies between 1 to 2. Recent advances in thermoelectric devices have come from the implementation of nano-features within the thermoelectric materials. These nanofeatures interrupt the transport in a favorable way such that the ZT values increase. Because nano-features are geometric dependent, the design space of nanoscale thermoelectric materials become extremely large and previous modeling approaches do not provide the necessary underlying physics to capture the correct transport dynamics of these nanostructured materials. Thus, the main contribution of this research is to develop new models which capture the physics and employ high performance computational which can investigate a multi-scale device from atomistic sizes up to bulk sizes. This model will not only be able to predict thermoelectric performances from fundamental material properties but also innovate for new more efficient thermoelectric devices.

The second aspect of this research deals with thermionic direct energy conversion devices. Thermionics are very similar in context to thermoelectrics except they are not a solid device but rather a vacuum device where a vacuum region separates the hot and cold regions. Based on this description, thermionics have a district advantage over thermoelectrics because they eliminate the lattice contribution to the thermal conductivity. However, there are other aspects which offset the decreased lattice contributions. Those aspects include the amount of energy an electron must have to surpass the vacuum region or barrier energy. Similar to thermoelectrics, thermionic devices are limited to select applications due to their conversion efficiency. Many of the consumer applications outlined above for thermoelectrics are also applicable for thermionics. However, typically thermionics are reserved for extremely high temperature applications due to the current efficiency of the materials. If the efficiency of these thermionic devices are increased they have the potential to alleviate the current energy crisis. One of the more immediate applications of thermionics is for large energy production such as fossil fuel burning plants where a large amount of waste heat is produced.

The efficiency of thermionic devices can be framed in a similar manner to the thermoelectrics description that was posed in the previous few paragraphs. In the

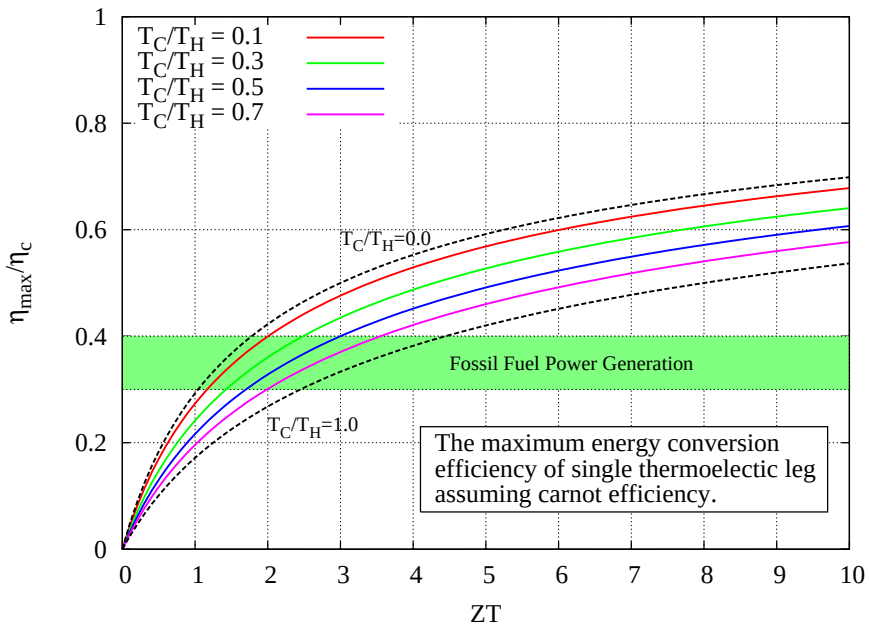

Figure 1.2 Plot of the normalized efficiency of thermoelectrics for different temperature differences versus ZT values. The maximum efficiency is divided by the Carnot efficiency. Plot based on theory by Ramalingam (2000)

thermionic case, the efficiency is framed in terms of a temperature not ZT. Figure 1.3 is a plot of the efficiency of an ideal cathode as a function of temperature. Similar to the thermoelectric plot, a banded region around 33% outlines the efficiency of a fossil fuel energy production cycle. The lines in Figure 1.3 are based on Richardson's theory of an ideal metallic cathode neglecting radiative losses. The figure suggests that the designer should select a material with the lowest work function to operate at a highest possible efficiency for a given temperature. It turns out if you search the periodic table, it is difficult to find a single elemental material that has a high melting temperature and low work function value. Traditionally, researchers have selected materials with extremely high melting temperatures, such as tungsten, with an associated work function of approximately 4.5eV and have increased the operating temperature to a value near the material's melting temperature to operate at a higher efficiency. However, this is not always possible given the application where a high temperature bath is not always present. Additionally, many melting temperatures of low work function salts are below 400K which are not applicative for near room temperature applications. Thus, thermionic emitters much like thermoelectrics, have been associated with low efficiencies which have limited their widespread application

in the consumer market. The current trend for new thermionic materials is to use wide-band gap semiconductors such as diamond which can be doped with elements such as nitrogen and hydrogen. The use of dopants in wide-band gap materials has the effect of lowering the work function value of the material. In order to understand the emission from these wide-band gap materials this research has developed a model based on fundamental material properties. The model devloped in this research is a necessary tool to understand the transport from a fundamental view point.

Similar to thermoelectrics, thermionic devices can be used as cooling devices by applying a moderate field to the thermionic device. Once a moderate field is applied to these devices they are in an emission region which is characterized by both thermal and field emission, hence the name thermal-field device. The addition of a field aids in removing electrons from the surface by influencing the band structure. Interestingly, instead of adding nano-features inside the material as is commonly done for thermoelectrics, in thermionics nano-features are added to the cathode surface to enhance emission. An applied field further enhances the emission by adjusting the geometry to further enhance the curvature of the local field lines around the nano-features. Similar to thermoelectrics, the transport is geometry dependent and rely on a quantum mechanical description which is not captured in a classical treatment of thermal-field emitters. By developing a model which can capture the emission from these thermal-field emitters the geometry can be optimized in order to optimize emission characteristics and predict the cooling potential.

Organization

The organization of this thesis work will begin by introducing thermoelectrics through a historical perspective along with the explanation of the current state-of-the-art in thermoelectric materials and modeling approaches. Following this discussion, the history of thermionic emission and field emission devices will be considered. The historical perspective of thermal-field emitters will introduce materials previously investigated and include explanation of previous models used to study these devices and their modeling limitations that ultimately motivate the modeling approach for this research.

The second chapter is a comprehensive explanation of the phonon modeling and electronic modeling theory with a development of the non-equilibrium Green's function quantum description used to model both the thermoelectric and thermionic devices. Specific explanation will emphasize the development of a coupled modeling

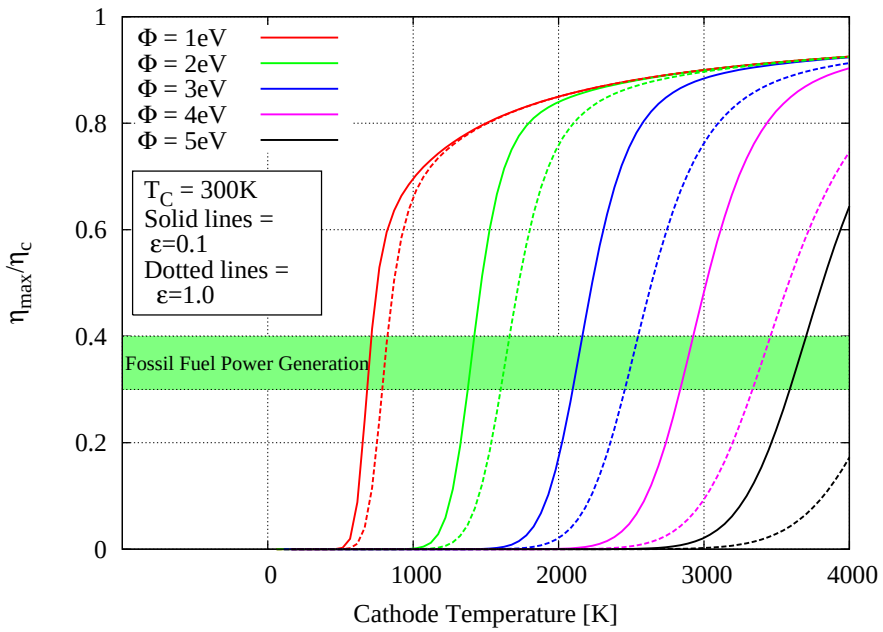

Figure 1.3 Plot of the optimal efficiency of thin film thermionic emitters at a given work function and cathode temperature. Assumed values of emissivity. Plot based on theory by Ingold (1961)

approach to facilitate the multiple phonon frequency scattering and dissipation from phonon-phonon interactions. Preceding the coupled thermoelectric model will be an elaboration of the thermal-field emission model which was adapted from the electronic portion of the thermoelectric model.

The third chapter will bring together the validation and verification of both the thermoelectric and thermionic models. The thermoelectric model will be validated first by looking at the phonon and electron model independently. The electron model will be validated based on the applied field dynamics and the model's ability to match thermoelectric values from the literature. The validation of the fully coupled model will also be compared to data in the literature. The thermal-field model will be validated against collaborated experimental data and verified with theory of metallic emitters.

The fourth chapter will demonstrate how the developed models from this research were used to optimize and innovated new nanostructured thermoelectric and thermionic devices. A specific device innovation that will be elaborated on is variably spaced superlattice (VSSL) thermoelectric materials. The other analyses include nanocrystalline composite materials and nano-tip thermal-field emitters.

The final chapter will conclude the findings and provide an outline of the contributions of this research. Additionally, discussion of future direction and future research will be provided. In conclusion, details on where the source code for all the models will be provided.

History of Thermoelectrics

The theoretical understanding of how thermoelectric generation and refrigeration operates has long been determined and was actually a collaboration of three independent theories defining an encompassing theory of thermoelectricity. In 1823, Thomas Johann Seebeck determined that when two dissimilar conductors formed a closed loop and one end of the junction was heated, a magnetic compass held near the junction would deflect in response to the applied temperature. Seebeck was under the impression that the phenomenon was magnetic when in actuality it was electromagnetic. None the less, in his 1823 paper (Seebeck, 1823), he researched several materials determining their, $\alpha^2\sigma$ parameter. The α later became known as the Seebeck coefficient with units of volts per degree temperature.

The next observation in contributing to the thermoelectric effect was by Jean Charles Athanase Peltier who observed changes in temperatures when a non-ambient temperature probe was applied in the vicinity of a heterojunction of two dissimilar metals while a current was applied. As Peltier increased the current he noted that the temperature would increase or decrease at the junctions. The Peltier effect was not equated to Seebeck's findings until Heinrich Lenz in 1835 determined that the direction of current governed whether thermal energy was absorbed or generated at the junction. In Lenz's experiments he used a bismuth-telluride junction to freeze water and then reversed the current to melt ice back into water. (Goldsmid, 1964)

In the 1850's William Thomson establish a relationship that accounted for both the effects of a current and temperature gradient applied to a homogeneous conductor. Termed the Thomson effect, this relation states that in a homogeneous conductor with a current passing through it and a temperature gradient applied across, thermal energy is either absorbed or generated along the conductor. He noted that the direction of the current governed whether the thermal energy was absorbed or generated in the conductor and the rate. He derived the Thomson coefficient which has units of V/K and is a measuring of cooling rate governed by the change in Seebeck coefficient over the change in temperature.

In the mid 1900's scientists begin to study thermoelectric materials from an

energy generation and/or refrigeration point of view. By now the understanding of thermoelectric effects were recognized but devices were never attempted. It was reasoned that a good thermoelectric device should have a large Seebeck coefficient with a low thermal conductivity. A dimensionless figure of merit was devised that encompasses these two competing effects in order to gauge the performance of the thermoelectric devices. The figure of merit is defined in Equation 1.1 where T is the average temperature of the device, S is the Seebeck coefficient, σ is the electrical conductivity, k_e is the electrical contribution to the thermal conductivity and k_p is the lattice contribution to thermal conductivity. Many researchers focused on metallic thermoelectrics due to their high electrical conductivity. Unfortunately, the electrical conductivity (σ) and electron thermal conductivity (k_e) are proportional because of the Wiedemann-Franz law which meant materials of ZT greater than 1 are difficult to find. This holds true for both the energy generation and refrigeration thermoelectric devices.

The implementation of semiconductors as thermoelectric materials began in the mid 1950's by Goldsmid and Douglas (1954) who demonstrated that a temperature of below zero degrees Celsius could be obtained using bismuth (Bi) telluride (Te) material junction. In using semiconductors, a decreased thermal conductivity could be achieved but at the expense of a electrical conductivity compared to that of a metal. The decreased thermal conductivity was a result of the decreased abundance of delocalized electrons which was responsible for the large contribution of thermal conductivity (k_e). The decreased electrical conductivity of semiconductor materials was only a slight hurdle until the transistor application took off in the late 1950's and early 1960's when doped semiconductor technology was discovered. Additionally, further enhancement of semiconductor materials were permitted by alloying the materials or creating a two-phase material. The alloyed semiconductor maintained considerable amount of electrical conductivity while decreasing the thermal conductivity considerably due to increased phonon scattering. At this point, both the Soviets and the Americans had a large research effort in thermoelectrics for military and space applications.

Figure 1.4 is a time-line perspective of the ZT values over the last few decades. ZT values prior to the 1996 are not included because the values plateaued at 1.5 since the implementation of bismuth-telluride alloys. The rise in the ZT in the 2000's is due to recent advances attributed to nanostructured thermoelectric materials being discovered. Nanostructured materials have given way to a new avenue for controlling both the thermal and electrical transport properties of material. It is from the

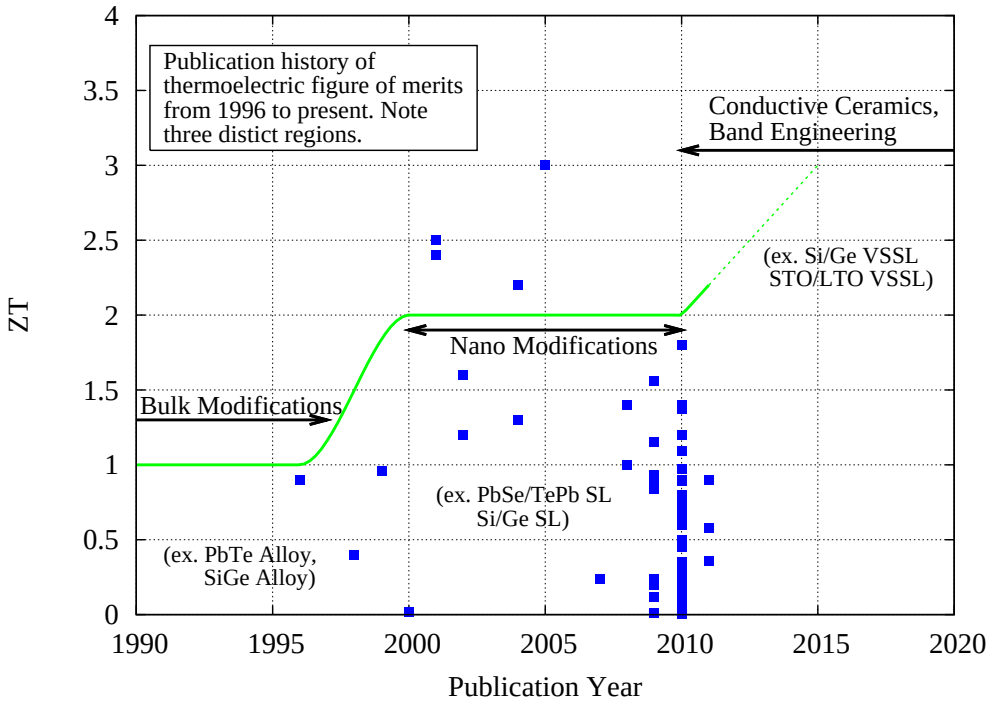

Figure 1.4 Timeline of thermoelectric figure of merit (ZT) over the last two decades. This plot also forecasts the trend of ZTs in the next decade through conductive oxide materials and band engineered materials. The highest point on the plot is based on predicted values by Harman et al. (2005) with a ZT=3 at 550K for Bi-doped n-type PbSeTe/PbTe quantum-dot superlattice (QDSL).

nanostructure point of view that the majority of the recent research and the proposed research in this study will focus. Researchers have had success using nanostructures to disrupt the thermal conductivity and to increase the electrical conductivity predicting ZTs upward of 2. Figure 1.4 demonstrates the projection of ZT values past 2010 where researchers will focus on more complex doped oxides and engineering the band structure of materials. The engineering of the band structure requires high fidelity computational tools such as the models developed in this research to optimize and engineer higher ZT materials. The next ten years may provide the necessary increase in ZT up to values of 2-3 to compete with vapor compression cycles.

Nanostructured Thermoelectrics

The majority of literature from the last decade focused on decreasing the thermal conductivity through nano-features. It has been reasoned by many, that

the thermal conductivity is much more rewarding to design around because it is more difficult to modify the electronic performance of wide-band gap semiconductors. However, this common wisdom has not limited the research targeted towards increasing the electrical transport. With the recent advances in deposition techniques the ability to build devices on the order of the de Broglie wavelength of electrons producing increased performance due to nanoscale transport effects (Hicks and Dresselhaus, 1993). This allows devices to be built in which the transport of electrons becomes ballistic in nature, giving rise to near quantum conductance performance. The following few paragraphs will focus on several nanostructures that have been investigated previously and will provide motivation for developing the required modeling techniques required to capture the physics of these nanostructured materials.

Metal Alloys/Nano-Granuals

Many researchers have investigated alloying well known bulk thermoelectric materials with hope of increased thermoelectric performance by decreasing the phonon mean-free path of the material. Many of these enhanced thermoelectric alloys show increases in efficiency because the thermal conductivity (k_p) decreases considerably where the electron mobility (μ) was already high and was less influenced by the addition of alloys. Much of the decrease in the thermal conductivity of these alloys can be explained from the addition of a different mass in the lattice promoting optical phonon frequencies and changing the group velocity of the material.

In 1997, Sales et al. (1997) looked at filled skutterudite structure in which good electrical conduction could be achieved while low thermal conductivities similar to glass were obtainable. Orihashi et al. (2000) had another approach where he showed that they can control the performance by the amount of tin that is introduced to the lead telluride structure (Orihashi et al., 2000). Orihashi et al. (2000) confirmed that if the material forms a complete solid solution then the lattice disordering becomes minimum and the thermal conductivity decreases. Similarly, (Chung et al., 2000) demonstrated in 2000 that single crystal $Cs_xBi_4Te_6$ could achieve a ZT of 0.8 where the amount of cesium incorporated could influence a more complex crystal structure increasing phonon scattering. The amount of cesium disrupted the lattice dynamics and decreases k_p and increased ZT. The notion of disrupting the lattice dynamics is apparent in current nano-structured thermoelectrics but the degree of scattering can be controlled by the layer thickness not the unit cell dimension as in these bulk materials.

In the thermoelectric community the "alloy limit" is the lowest thermal conductivity achievable for any concentration of a given alloy. A standard alloy limit often cited is the SiGe alloy limit has a thermal conductivity of $1\,\mathrm{Wm^{-1}K^{-1}}$ at 600K. This alloy limit is extremely hard to achieve with other alloys or better yet surpass. This limit arrives from the Wiedemann-Franz law in metallic solids that says that thermal and electrical conductivity are proportional to the Lorenz number. Many researchers (Vining et al., 1991) looked at alloying silicon and germanium, $\mathrm{Si}_x\mathrm{Ge}_{1-x}$, but could not surpass the alloy limit. Because the alloy limit could not be surpassed but only met only met with a $\mathrm{Si}_{0.2}\mathrm{Ge}_{0.8}$ alloy at 600K this is commonly taken as a standard reference material in the thermoelectric community. The inability to surpass this alloy limit gave rise to a new approach where the thermoelectric material began being constructed with nano-features using already well established thermoelectric materials.

Superlattices

As deposition processes became more available, such as molecular beam epitaxy (MBE) and Metal-Organic Chemical Vapour Deposition (MOCVD), researchers began investigating thin film mono-layer structures. A superlattice is defined as a planar structure with alternating layers of materials. One attribute that was leveraged because of the discrete nature of electron states within the thin layers was quantum confinement effects, in which, under low dimensionality the electron states are constrained and the density of states (DOS) diverges along the energy axis (Hicks and Dresselhaus, 1993). This concept can be visualized by treating electrons as a wave in which they can be represented by a string suspended between two boundaries. It is understood from classical dynamics that when the string is excited it will have a finite number of allowed modes which are a function of the distance between boundaries. As the boundary are moved further apart the number of allowed modes increase. The same principle holds for electrons acting as waves in a solid. It turns out these lowest modes are critical to the transport and are a function of the individual layer thickness. Because the low lying energy levels can be controlled by confining the waves in particular directions an additional aspect arises do to the degeneracies of the states. This advantage is referred to as a confinement effect in nanostructured materials. A common plot of the density of states under low dimensionality shows bulk density of state dispersion having a square root relation with increasing energy, a two dimension constrained device having a stair step, and one dimension will have a step function

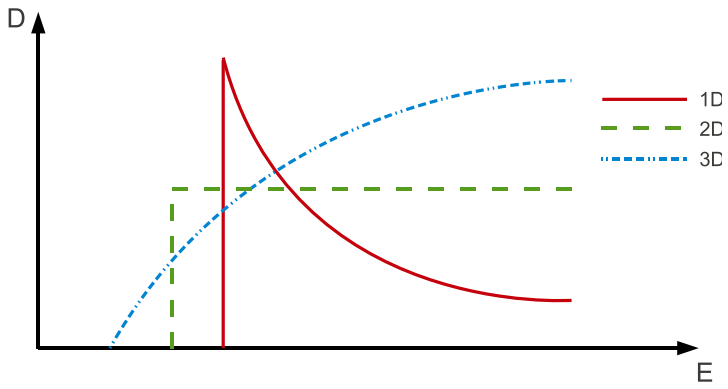

Figure 1.5 The confinement effect in nanostructured materials modifies the low lying energy states. This is evident in 1D and 2D confined structures when compared to bulk 3D structures. The 1D state is described by a one of square root of energy relation and the 2D is independent of energy.

with an inverse square root decay, see Figure 1.5. The abrupt step in the DOS times the Fermi function is what results in increased electrical transport. By controlling the degree of confinement the transport can be tuned. This is a critical aspect of VSSL materials which will be demonstrated later in this research.

An advantage that arrives from thin film structures is the decreased thermal conductivity (Lee et al., 1997) due to an acoustic mismatch arising from the alternating layers and the inter-facial thermal resistance. Each interface will contribute a specular or diffuse reflection to the incoming acoustical phonon. Because the thermal conductivity within the structure is governed by the contribution of acoustic phonons, under reduced number of states the thermal conductivity is decreased.

Another advantage of a thin film structure is the thermionic emission that can be achieved through barrier regions in the alternating layers. Because the conduction and valence band edge of either material do not lie exactly at the same energy level there exists a finite probability that tunneling or thermionic emission will contribute to the overall device transmission. Researchers (Mahan and Woods, 1998; Shakouri et al., 1998) have explained this phenomenon and designed Schottky like barriers in order to enhance the thermionic effect and to increase the thermoelectric efficiency.

In 2001, Venkatasubramanian et al. (2001) demonstrated a ZT of 2.4 could be achieved with p-type Bi_2Te_3/Sb_2Te_3 superlattice device. This was a significant finding that nanostructure can lead to increased figure of merits. However, other researchers have yet to reproduce these findings (Vineis et al., 2010) and the figure

of merit needs to be upwards of three to be marketable.

Bulusu and Walker (2008a, 2007b) demonstrated the use of non-equilibrium Green's functions (NEGF) to look at the thermoelectric performance of strained silicon-germanium superlattices. Their studies confirmed that quantum confinement of electronic states does contributed to an altered thermoelectric performance. It was also confirmed in Bulusu and Walker (2008a) studies that NEGF compares well to the available experimental values. One interesting finding that came out of the research was the studying of strain effects. Using deformation potentials (Van de Walle, 1989) Bulusu and Walker (2008a) was able to calculate the band offset for a given superlattice configuration. Under biaxial strain the results indicated that the silicon and germanium conduction band edges invert resulting in the conduction band edge of silicon being lower than the germanium conduction band edge. This inversion was only for band minima along the transport direction. This will become essential in constructing the band diagram in the study of variable spaced thermoelectrics where the conduction needs to be well defined in the presence of straining. The conduction of the straining must be well characterized in order for the strain mode to work correctly.

In an extension of Bulusu's work, Musho and Walker (2011b) have shown that the power factor plateaus after four layers. This gives confidence that the NEGF formalism can be used to investigate large structures that are comprised of hundreds of alternating layers. These finding are used to investigate superlattice type thermoelectric devices and give confidence in comparing to literature values with device lengths of hundreds of layers.

Nanocrystalline Composites

More recently, researchers have found methods of embedding nanocrystals inside of matrix materials forming a nanocrystalline composite (NCC) nanostructure. Again, these structures leverage the quantum effects at a small scale to increase the thermoelectric efficiency. Only a select number of researchers have studied the electronic effects of nanocrystals in thermoelectic devices. Wang et al. (2008) have experimentally studied free-standing PbSe nanocrystal thermoelectrics as a function of crystal size and has attributed an increase in electrical transport to confined states that are delta-like in shape and which are shifted closer or further from the conduction band edge depending on the size of the nanocrystals. Their qualitative explanation of shifted density of states is captured inherently in the quantum model presented in

this research.

Other researchers such as Zeng et al. (2007) experimentally studied the cross-plane electronic transport effects of nanostructures and found an increase in cross-plane Seebeck coefficient when inclusions were added. Zide et al. (2006) attributed the increase in Zeng's experiment to an electron filtering phenomenon and thermionic emission in the cross-plane direction. While their trends are commensurate with measurements, the magnitudes of the conductance in their Boltzmann-based type model is dependent on the scattering time, which is essentially a fitting parameter. These fitting parameters suggest large uncertainties for devices there have not experimentally tested. The modeling approach in the following research attempts to predict the transport from more fundamental quantities namely band offset and effective mass.

Using a NEGF method Musho and Walker (2011a) have demonstrated theoretically that the size of the nano-crystal can affect the thermoelectric electrical transport using a NEGF method. Full explanation of the results can be found in the results section (Section IV) of this thesis. There are two advantages to these structures: 1) increased density of states due to confinement and 2) planar transport effects. It was determined that moderate filtering was desired by constructing a device with small germanium nano-crystals that were spaced commensurate to the nano-crystal size. Because of the planar transport the nano-crystals acted as barriers resulting in the large Seebeck while still allowing transport around the barrier maintaining the mobility. Results showed that nanocrystalline composite devices could outperform equivalent characteristic length superlattice devices due to the moderate filtering (Musho and Walker, 2011a).

On the thermal side, several researchers (Glatz and Beloborodov, 2009; Hostler et al., 2008; Kim et al., 2006b) have increased the figure of merit through incorporation of defects, inclusions and nanoparticles in hopes of decreasing the phonon thermal conductivity (k_p). Experimental studies (Kim et al., 2006a) of NCC structures saw a noticeable decrease in the thermal conductivity compared to equivalent superlattice structures. Kim et al. (2006a) attributes the decrease in thermal conductivity to three factors, the most significant being the increase in phonon scattering as a results of the nanocrystals being on the order of the mean free path of phonons. Because the mean free path of phonons is larger than electrons it was argued that the nanocrystals don't influence the electrons maintaining the electrical conductivity.

Thermoelectric Modeling Approaches

Traditionally, the modeling of thermoelectrics was done based on continuum-type relations or models (Murphy-Armando and Fahy, 2008). More specifically, Boltzmann type modeling approaches were taken, which rely heavily on user-specified scattering parameters and particle-based theory. To be fully encompassing, the thermoelectric model must be able to predict both the thermal transport performance and the electrical transport performance. Referring to Equation 1.1, the numerator of the thermoelectric figure of merit comprises the electrical contribution and the denominator comprises the thermal contribution. In the majority of the literature, researchers targeted one of these transport mechanisms and assumed the other mechanism is based on a known relation, such as Wiedmann-Franz. The Wiedmann-Franz law states that the electrical conductivity is proportional to the thermal conductivity. The use of Wiedmann-Franz law is questionable when applied to semiconductors and even more when applied nanostructured materials. Research by others (Bian et al., 2007) has determined that the Lorenz constant in Wiedmann-Franz can be up to fifty percent lower in some nanostructures. This corresponds to a fifty percent under estimation of ZT value. The modeling approach taken in this research is to calculate both the thermal and electrical contribution simultaneously to limit the need for assumed transport of the unknown quantity. Furthermore, the results developed in this research could be used as a means to predict the unknown values in experimental studies that currently rely on the Wiedmann-Franz approximations.

In the context of calculating the continuum electrical performance of bulk thermoelectric materials such as PbTe and SbTe alloys, a Boltzmann approach is commonly used to determine the electrical conductivity and Seebeck coefficient. Often when these models were used, scattering was incorporated to account for defect and electron-phonon interactions through an average scattering rate that is a free parameter for the researcher to select. Boltzmann type modeling approaches are based on particle-based theories and thus their limited applicability to bulk materials. For completeness, the device length where Boltzmann models are appropriate are at device scales three times the mean free path of electrons. Thus, a silicon device would need to be approximately 90 nm for a Boltzmann approach to be appropriate. This stems from the fact that particle based theory cannot capture quantum mechanical effects such as confinement and tunneling, which are an integral part of the physics in nanostructured thermoelectrics.

The Boltzmann particle based modeling approach can also be applied to the study of thermal transport where the phonons are treated as particles. Again, this

approach relies on knowing the scattering rate of phonons in response to defects and impurities. Often these scattering rates can be looked up in the literature. The Boltzmann thermal approach is limited to studying bulk materials in the absence of nanoscale features. The limits on this particle based modeling approach are confined to bulk device length above 90 nm similar to the treatment of electrons.

As mentioned in the previous section, the recent advances of nanostructured thermoelectric ushered in a new era of thermoelectrics material study. Along with these new materials came the need for new modeling techniques that could capture the transport trends. The use of quantum models was applicable because of their ability to calculate the ballistic nature of electrons and phonons. In addition to ballistic transport, confinement and electron-electron interaction are important and are able to be captured within the quantum framework. Researchers within the electrical engineering community and physics communities drove the advances in transistor technology and started developing modeling techniques to model sub-tens of nanometer transistor technology. Many of these models were based on solving Schrödinger's equation in a very similar fashion to that one would see in a entry level quantum mechanics course. Unfortunately, many of the models developed were very computationally intensive and extremely limited in the device sizes that could be studied. Additionally, it was difficult to deduce transport trends from these types of simulations because the contacts often govern the transport in these devices. Many of the recent advances in high performance computing have made larger simulations possible and through some clever mathematics and understanding quantized nanoscale transport of electron and phonons to determined the transport.

There have been recent advances in atomistic type modeling where a first principal ab-inito approach is taken to calculating the electronic transport (Derosa and Seminario, 2001). These modeling approaches are exponentially more computationally intensive then a discretized wave-equation finite-element approach. The current state of the modeling approach based on first principles is centered around a density functional theory (DFT) approach which relies on solving the exact wave-function for each orbital. This approach may be reasoned most comprehensive but it is often over kill when the researcher is strictly interested in the transport dynamics based on geometric changes. These atomistic approaches allow dispersions to be calculated that resemble experimental dispersion. Many of the dispersion that are calculated from DFT can be used by transport models to predict the transport. Approaches done by Brandbyge et al. (2002) use this very principle where the DFT solution is used to determined the dispersion and then the dispersion is implemented in the non-

equilibrium Green's function approach to determined the transport. Often times you will see this approach in the literature as a DFT-NEGF approach.

The approach taken in this research is similar in many respects to the DFT-NEGF approach except a composite effective mass approach is taken where the interest lies in determining the transport of the de-localized electrons within the solid. Special emphasis on constructing a composite system is critical to calculating the correct transport because the contacts often dominate the transport. In a brief overview, the approach taken solves a discretized Schrödinger equation using a Green's function formalism for the wave-function of the valence or de-localized electrons within the system. This approach has grown out of the electrical engineering community Guo et al. (2004) where they are interested in nanoscale field effect transistors. It should be pointed out that this approach has also been applied to understanding molecular junctions Ghosh et al. (2004); Taylor et al. (2001). This is a novel approach because the Green's function allows the PDE (Schrödinger equation) to be solved through integration of impulse responses that lie on a finite difference mesh which comprise the channel of the device. Complexity of the Green's functions solution comes from adding an external potential that arise from applied fields and particle interactions. Additionally, the Green's function allows complex self-energy contacts which represent a semi-infinite contact to be connected at the source and drain. Through the use of complex contacts and self-consistent approach many of the transport trends which incorporate dissipation can be captured. This approach can ultimately be framed to solve both the electron and phonon transport solution. Where the phonon solution relies on an atomistic approach, and the electron is a discretized domain approach.

History of Thermal-Field Emission Devices

Thermionic emission devices are very similar to thermoelectric devices in that the objective is to transport electronic charge but limit the amount of thermal energy transported. The real advantage of thermionic devices is that the contacts are separated by a vacuum region. This vacuum region does cause an obstacle for electron transport, but it creates an even greater obstacle for thermal transport. At the beginning of this chapter, Equation 1.1 was defined as the figure of merit for thermoelectric power generation. In order to modify this equation to capture the performance of thermionic power generation the lattice thermal conductivity (k_p) in the denominator of the figure of merit must be removed. The figure of merit becomes Equation 1.2 where k_r is added to capture the thermal conductivity due to radiation

heat transfer. Because the lattice thermal conductivity is removed, thermionics are often used in high temperature application where a large thermal gradient can be maintained. Along with maintaining a thermal gradient, thermionics often require a high temperature heat sink to thermally excite enough electrons to create a sufficient flux.

$$ZT = \frac{S^2 \sigma T}{k_e + k_r} \tag{1.2}$$

The devices of interest in this research are vacuum thermionic devices. It is assumed that the vacuum region is extremely high (less than $10^{-5} torr$) and thus there is no convective thermal transport from the anode to the cathode and the thermal losses are limited to radiative thermal transport across the vacuum. This is critical especially in nanoscale thermionic devices to maintain a thermal gradient.

The applied motive behind thermionic device is very similar to thermoelectrics except for two aspects. The first aspect as mentioned above is the absence of a lattice thermal conduction. The second aspect is the increased barrier height require to excite electrons over to transport across the structure. Again, because these thermionic devices are targeted to be direct energy conversion devices a thermal gradient is applied across the device and a electrical potential is collected from the conversion of thermal energy to electrical energy. More specifically, electrons are thermally excited on the cathode side in order to evaporate them off the surface and into the vacuum region. The electrons then transport to the cooler anode electrode, taking thermal energy along where they condense on the surface of the anode. The transport of electrons from the hot cathode to the cold anode results in an apparent cooling effect on the cathode.

Thermionic energy conversion has been limited to very select remote power generation applications. One of the more notable proof-of-concept devices is the SNAP-11 devices used in space power generation (Corliss and Harvey, 1964). Many of these devices used nuclear radioisotope power generation to produce a large temperature. By the 1960's much of the literature in thermionics moved away from vacuum devices and onto devices with interelectrode atmospheres such as cesium vapors. This proved to be a promising avenue because device efficiencies on the order 10 to 20% were possible. Many of the limitations were outlined by Langmuir (1932); Carabateas (1962) dealt with kinetics of the positive ions and space charge limitations. Because these cesium vapor thermionic devices had a atmosphere they formed a plasma at the surface which is often referenced as ignited thermionics. The use

of a cesium atmosphere was also questionable due to its carcinogenic nature. In the 1970's after the space race thermionic research transitioned to thermoelectrics and use of semiconductors which required a much lower temperature heat sink.

Historically, researchers have searched the periodic table to determine which intrinsic elements would be the best performing thermionic emitters. Referring to Figure 1.3 at the beginning of this chapter, in order to achieve an efficiency comparable to a fossil fuel power generation cycle, the material must have either a low work function or high melting temperature. The definition of the work function is defined as the distance from the vacuum level to the Fermi level. By selecting a material with a lower work function the population of electrons above the vacuum level at a given temperature will increase exponentially leading to increased emission.

A survey of the solid elements from the periodic table can generate a plot of the intrinsic work function as a function of atomic weight, see Figure 1.6. The trends follow the bonding orbital trends, especially in the d orbitals where the increase in bonding orbits follows increase in work function values. The lanthanides prove to have some of the lowest intrinsic work functions which can be attributed to the orbital hybridization between the 5d orbitals. It is important to point out that the work function of graphitic carbon has a value of 5 eV , while the work function of tungsten is around 4.5 eV .

Before the advent of semiconductors much of the focus was on materials with high melting temperatures. Referring to Figure 1.3 again, the efficiency can be increased by increasing the operating temperature that the material can withstand. Thus, one of the highest melting temperatures of any elements is tungsten, with a melting point around 3422°C. Figure 1.7 is a plot of the work function normalized by the thermal energy melting point ($k_B T_m$). A material with the lowest values in this plot are the most desirable. The materials with the lowest values correspond to low work functions and high melting points. The two elements that prove to be the lowest are carbon and tungsten. The focus of this thesis will look at applying diamond allotrope of carbon.

Thermionic and Thermal-Field Emitter Applications

Thermionic devices in the context of this research are centered around their application to direct energy conversion. However they have application to electronic cooling similar to the Peltier thermoelectric device. In the context of cool applications thermal-field emitters have a distinct advantage. The field of thermal-field emitters is

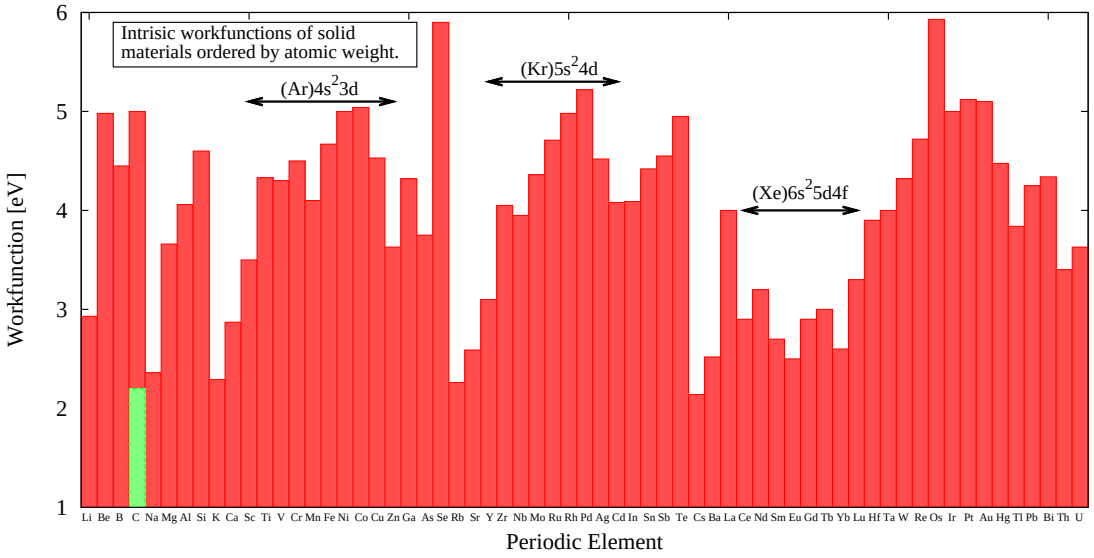

Figure 1.6 Plot of intrinsic work functions for a range of solid period elements. The elements are in order of atomic weight. The green bar within the carbon bar is associated with the effective work function when nitrogen is incorporated. Ramalingam (2000)

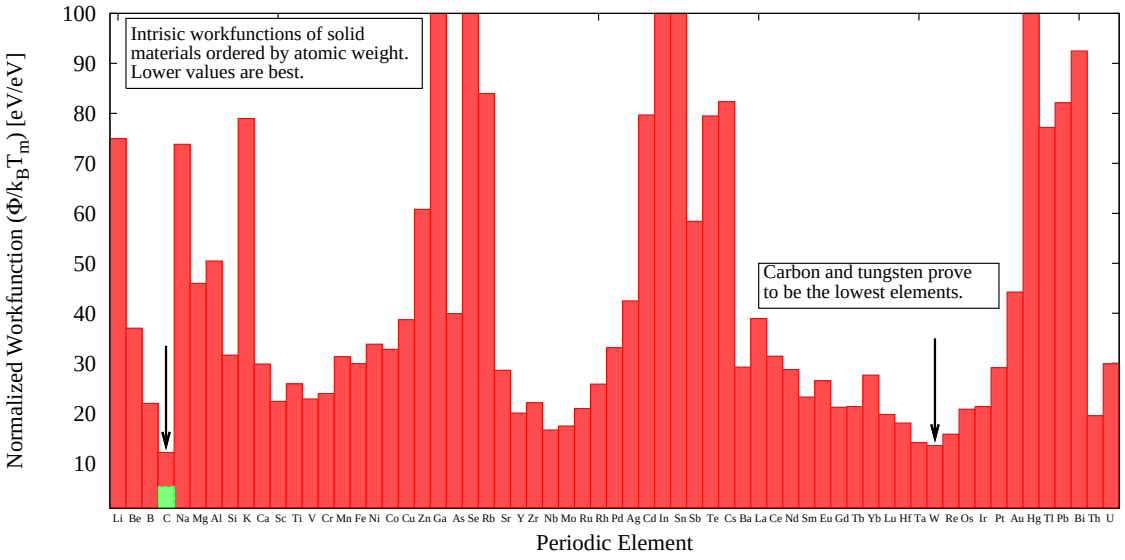

Figure 1.7 Plot of intrinsic work functions normalized by the thermal melting energy for a range of solid period elements. The lower the number the better the performance. The elements are in order of atomic weight. Carbon and tungsten are the two lowest elements with moderate work function and high melting temperatures.Ramalingam (2000)

a combination of thermionic emission and field emission. The addition of an electric field to a good thermionic device is the attenuation of the field in the vacuum region resulting in an increased emission. Conceptually, the addition of an applied field can be thought of as ripping the electrons off the surface. Because the electrons are being forced from the surface there is a high flux of electrons moving from the hot cathode to the cold anode. These thermal-field emitters have an application in cooling space vehicles and sensing. Also, the thrust of this research concentrates on its relevance in direct energy conversion. As mentioned in the previous sections, the efficiency is governed by the operating temperature and as the temperature increases the efficiency of these devices also increases. It has thus been the focus to apply such thermionic devices in operation, such as the top-cycle in large production fossil fuel plants. This device generates large amounts of high temperature waste heat and require only a small fraction of energy recovered to be deemed efficient. The objective of this research is to investigate materials with lower work function values which are more efficient at lower operating temperatures permitting a broader application and increased efficiency at the high operating temperatures.

The argument stands that thermal-field emitters have the potential to outperform thermoelectric power generators if the electrical conductivity could be increased in such a way to sustain a marginal current density and the anode could be designed to act as a constant temperature bath. Increasing the electrical conductivity provides a formula that is supported by the non-existent thermal conductivity (neglecting radiation), resulting in extremely high theoretical ZT values.

Diamond Films and Nanostructured Tips

One of the methods that material scientists have been trying to increase is the current producing capabilities of thermal-field emitter devices by implementing materials which can withstand high fields along with high temperatures. The underlying material parameter is ultimately the work function of the material that governs the flux of electrons escaping the surface. The work function is the potential energy required for an electron to go from the the Fermi level to the vacuum level of the device. By decreasing the work function of the material, the equilibrium population of electrons that can migrate over the barrier increases and the overall current density increases. As pointed out in Figure 1.7, carbon is a perfect candidate due to its high melting temperature and ability to be doped, which effectively lowers the work function value increasing emission characteristics.

Many researchers (Kock et al., 2002; Koeck et al., 2011) have looked at chemical vapor deposited (CVD) diamond because of the materials thermal properties and ability to withstand high electric fields. However, it was not until recently did researchers begin to add interstitial dopant atoms to the diamond materials with such elements as nitrogen and hydrogen. It was found that these dopants increase emission characteristics (Kock et al., 2002; Koeck et al., 2011). With the inherent thermal properties and ability to dope diamond semiconductor materials, the performance increase has brought this material to the forefront. In Figure 1.7, a green bar in the carbon column is associated with the state-of-the-art in nitrogen-incorporated diamond with an effective work function of 2.2 eV .

Researcher have also looked at incorporating nanocrystalline diamond materials with nitrogen (Koeck et al., 2011) and also sulfur (Koeck and Nemanich, 2005). Koeck determined for sulfur-doped diamond at room temperature that the emission does not change when compared to natural diamond. However at elevated temperatures he noted that there was a deviation from the Schottky formula suggesting that the sulfur was contributing to the increased emission. In Koeck's later publications of nitrogen doped diamond (Koeck et al., 2004) he demonstrates that a high temperature emission current is greater for nitrogen-doped diamond over sulfur-doped diamonds.

There have been very few conclusions in the literature about the exact mechanism for increased emission of these doped diamond materials. Recent work done by Paxton (2011) come to some hypothesis that the emission is along the grain boundaries of the nanocrystalline diamond. This is justified by the dangling sp^2 content along the grain boundaries.

The nature of the CVD diamond in much of the literature (Subramanian et al., 2007) is polycrystalline, resulting in a patchwork of different work functions and different properties. As was shown in Figure 1.6, the bonding state of the material is critical to the work function. This is especially apparent in the hybridization of orbitals seen in the f and d states. The allotrope of carbon in this research is assumed to be fully hybridized diamond structured carbon. However, the content of the CVD diamond is not only polycrystalline, but also includes graphitic content and non-hybridized carbon along the grains.

Thermal-Field Emitters Modeling Approaches

Previous researchers have focused on either modeling thermionic emission or field emission and have not extensively studied thermal-field emitters. The theory of thermionic emission was developed back in the early 1900's by Richardson (1916). Richardson described the emission from hot bodies using kinetic theory of electrons in a metal. At the time he was interested in understanding the emission of electrons from metallic surfaces.

The emission of electrons from a metallic surface under an applied field requires a more rigorous view of the electron dynamics. Around the same time Richardson was characterizing the emission electrons from a hot surface (Schottky, 1914) describing the interaction of a point charge with a plane surface. Schottky was responsible for defining the image potential responsible for the interactions of a charge close to a flat surface. Schottky is best known for the potential energy described by $U = -q^2/(16\pi\epsilon_0 x)$ (Schottky, 1914). This potential is very important in describing the emission of electrons from a surface as it defines the image barrier.

It was not until in the late 1920's that Schottky's theory was applied to describing the field emission of electrons. Fowler and Nordheim (1928) were responsible for applying a wave-mechanical theory or commonly known as a quantum theory to describe the emission process. The quantum theory that was developed by Fowler and Nordheim was based around modeling an one-dimensional barrier defined by the image potential and vacuum level. They determined that under an applied field the band would bend creating a thin barrier inside the vacuum region. This thin region which decreased in thickness with increased applied field had an associated finite probability for which electrons could tunnel. The associated probability could be determined from the quantum mechanic tunneling probability through this region.

Both Richardson theory and Fowler-Nordheim theory stand on their own to define the two regions. These models proved to be good at explaining emission from metal emitters, where the density of states could be approximated as single analytic expression. The theory of both of these has been restated in the literature with certain modification to capture the emission from non-metallic surfaces (Modinos, 1984).

Much of this theory developed the emission of electrons into a vacuum in response to a temperature and electrical bias was revisited when the development of semiconductor devices took place in the 1960's. Analogous to an electron emitting into a vacuum, the emission of an electron from into semiconductor is very similar. It turns out that Schottky's theory only need slight modification in terms of the addition of a dielectric constant. This theory proved to be very important in describing the

correct transport through diodes where the space-charge regions are critical to the transport.

Not until recently did researchers turn their interest to the emission of electrons from semiconductors in a vacuum for a possibility of direct energy conversion. The transition to vacuum-semiconductor devices as opposed to metal-semiconductor devices has brought to question applicability of many of theories. There is also the issue of nano-structured surfaces where the potential could vary drastically. Much of the theory originally developed for emission from metal surfaces has reached a length scale in which the continuum expressions based on kinetic theory of electrons are being questioned. This is especially true in the nano-tip emitter devices, where the confinement of states within the tip and the high localized fields around the tip are not captured in the standard Fowler-Nordheim theory.

In terms of modeling approaches, there is literature on ignited thermionics where the energy distribution within the cesium vapor is calculated from a Boltzmann approach (Shaw and Margolis, 1969). This approach requires that the electron-electron scattering rates are determined a priori. Shaw and Margolis (1969) suggest that high fields cause the distribution of electrons within the vacuum to deviate from an equilibrium Maxwellian distribution. Unfortunately, because the emission of electrons in a vacuum is dependent on quantum mechanics, particle-based theory such as Boltzmann is not well suited.

The majority of the work in the literature has looked at the emission from carbon nanotubes (Maiti et al., 2001) and graphitic ribbons (Tada and Watanabe, 2002). Additionally, the literature include DFT simulation of field emission and absorbates on the surface of materials Grujicic et al. (2003). In these DFT simulation the focus was on the spectral emission and not the transport. There is a critical aspect to the space charge effects especially in vacuum devices which is important to the transport. Many of these DFT spectral responses can be coupled with the approach taken in this research which focused on the transport. Because a discretized Schrödinger approach was taken in this work, a more general treatment of the quantum mechanics can look at more complex structure. The model can then be used to validate the application of Fowler-Nordheim to characterized the emission from nanostructured wide-band gap materials. Furthermore, the modeling approach developed in this research has the ability to explore the intermediate region defined by thermionic and field emission resulting. Often, in the literature this region is either characterized by field emission or thermionic emission theory and often difficult to define the intermediate. Because the model developed can capture this intermediate it can help understand the physics

that lies within this region all fun a fundamental quantum point of view.

CHAPTER II

THEORY

This chapter will focus on developing the background necessary to model nanoscale transport in thermoelectrics and thermionic devices. The theory will first introduce electron and phonon transport within semiconductors and the governing equations to calculate the transport properties based on a non-equilibrium Green's function (NEGF) method in which both the nanoscale electrical and thermal transport is calculated. An overview of thermal-field emitters, including thermionic and field emission and how their counterparts were modeled using a similar NEGF modeling approach will follow the theory. The majority of the NEGF formalism described in this thesis is built from the ballistic theory for both the electron and phonons which can be found in Datta (2005). The research builds on and adapts this ballistic theory to include dissipative effects, specifically the addition of multiple electron-phonon interaction and phonon-phonon interaction with rigorous treatment of the spatial location of phonon densities. Additionally, this research provides a unique approach to modeling the thermal-field emission from nano-tip vacuum devices.

The thermoelectric modeling approach taken in this research is an abstraction of the actual device configuration that one might find in a operational thermoelectric device. This research focuses on studying and increasing the efficiency of a single leg of the thermoelectric devices, which would ultimately increase the overall efficiency of the device. Figure 2.1 is an illustration of a complete thermoelectric device with a hot and cold side, along with both a n-type and p-type material to limit the amount of thermal leakage. In the same figure, a subset of the device outlines the region of a single leg of a n-type material that will be the modeling focus for this research. Assuming both the n-type and p-type leg have approximately the same performance trends in response to nano-features, when the material optimized in this research is implemented in a full thermoelectric device construction with both legs, the overall performance should increase proportionally to what was seen in a single leg. In context to nanostructured materials within a single leg, this research will specifically focus on the cross-plane superlattice transport.

Similar to the thermionic approach, in Figure 2.2, the modeling effort of thermionic and field emission devices will be limited to modeling a single emitter with periodic boundary conditions. Likewise, it is assumed that the performance of a

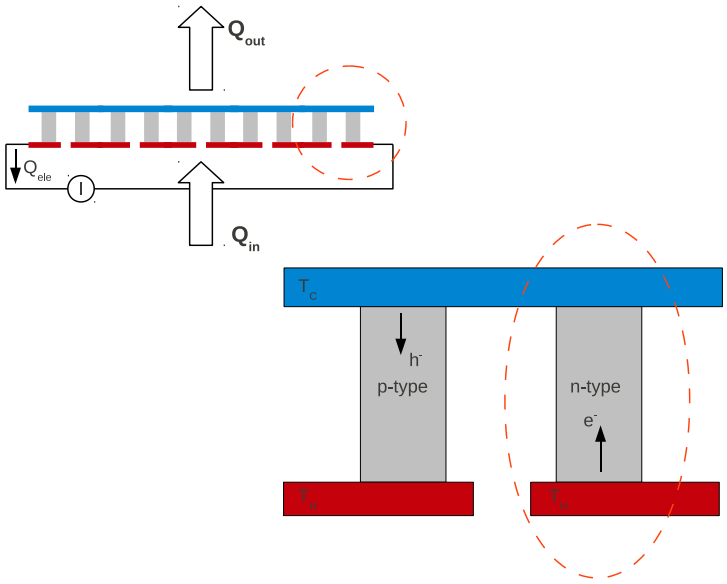

Figure 2.1 Illustration of the single leg approximation that is modeled as a simplified geometry from a fully functioning thermionic device. The models developed in this research focus on optimizing the performance of a single leg.

single emitter modeled will be realized in the overall performance of an actual device when hundreds of emitters are assembled in parallel. Additionally, the anode and cathode are assumed constant temperature baths where the temperatures at both the anode and cathode are specified and remain constant. In actuality, there is a transient effect and a non-ideal heating effects which results in anode heating due to both hot electrons transfered to the anode and radiative heat transfer from the cathode to the anode. Additionally, it will be assumed that the radiative effects are negligible and the anode and cathode remain at a constant temperature. The modeling approach developed in this research is strictly aimed at determining the electrical current originating from the emission tip with these assumptions. The reader should be aware that the open circuit voltage is critical in direct energy devices and should be considered when selecting anode and cathode materials.

Electron Transport in Semiconductors

Electron transport on the nanoscale is governed by the statistical mechanics of a fermion. In device transport, the system is constantly trying to reach an equilibrium state or minimize the free energy of the system. The constant pursuit for equilibrium

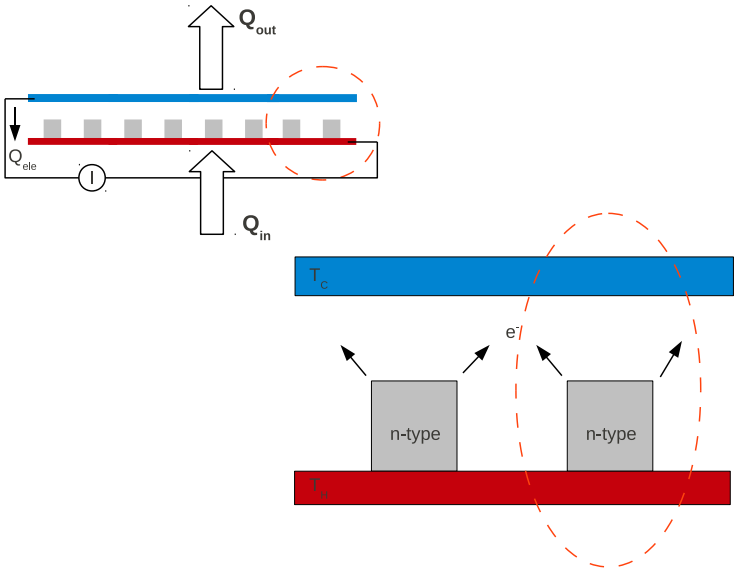

Figure 2.2 Illustration of the single emission tip approximation that is modeled as a simplified device. The anode and cathode are assumed constant temperature baths. The models developed in this research are design to optimize a single leg simulating the neighboring emitters through periodic boundary conditions.

between the contacts is what drives the transport of electrons giving rise to a current within the system. The expression that governs the equilibrium number of electrons at any given temperature is the Fermi-Dirac (FD) distribution, Equation 2.1. The FD distribution demonstrates that as the temperature of the system increases, the equilibrium number of fermions within the system increases exponentially. This idea of increasing the temperature to increase the electron population is a key aspect of thermoelectric transport. By specifying different temperatures at the contacts, the system is in non-equilibrium. Non-equilibrium in a system can be driven by having two dissimilar materials that have two different chemical potentials (μ) or by adjusting the temperature across materials. In a practical sense, this is why a thermocouple works. It also demonstrates how thermoelectric devices operate.

$$f_{FD} = \frac{1}{exp((\epsilon - \mu)/k_B T) + 1)} \tag{2.1}$$

In the quantum theory of a free electron gas, the Pauli principle must always be followed, which states that no two fermions can have the same quantum numbers. The quantum number is defined by the spin of the electron and the size of the orbital. The

states that the electrons can occupy are defined by the Schrödinger equation, equation 2.2, where ψ is the wave-function and ϵ_n are the eigenstate. These eigenstates are discrete in nature and are what gives rise to the energy levels that the electrons can occupy. In the context of nanoscale devices, this is critical because the length of the device can confine the wave-function, causing a divergence of eigenvalues or electron states.

$$H\psi = \frac{-\hbar^2}{2m}\left(\frac{\partial^2}{\partial x^2} + \frac{\partial^2}{\partial y^2} + \frac{\partial^2}{\partial z^2}\right)\psi = \epsilon_n \psi_n \tag{2.2}$$

Noted in Equation 2.2 of the free-particle Schrödinger equation, the only variable that defines the eigenvalues is the mass of the electron. When talking about electrons within a semiconductor, the same potential theory of electrons still applies, however, the mass of the electron, m_e, is replaced with an effective mass, $m_e^\star$. The effective mass is derived from the relationship between the energy and momentum of a electron moving through the solid. In most literature (Kittel, 1986), the effective mass will be described as the curvature of the dispersion and is dependent on the crystallographic direction in which the electron is moving. This is a mathematical approximation to allow the free electron model to still be used for electrons moving through a periodic solid and does not necessarily associate with the electron becoming more massive or less. The effective mass of silicon in the $\langle 001 \rangle$ direction is $0.91m_e$ and for germanium, the effective mass is approximately $0.95m_e$ in the same direction.

Because there are discrete states associated with Schrödinger solution, these states are associated with acting as current carrying channels to transport electron across a device. In essence, the electrons can be thought of as hopping from one state to the next until they reach equilibrium. In nanoscale transport, there is a finite current-carrying capacity for each energy level, even when the transport is assumed ballistic. The current-carrying capacity is defined by the quantum conductance, $2e^2/h$. In a two contact system, the current is dependent on the Fermi function at either contact, multiplied times the density of states within the device, and is a result of either excess carriers moving right or left. In Kittel (1986), the net current is simply defined as,

$$I = \frac{D_{1D}(\epsilon)qV}{L} qv = \frac{2q^2}{h} V, \tag{2.3}$$

where $D_{1D}(\epsilon)$ is the density of states of a 1D device and $\mu_1 - \mu_2 = qV$ is the applied potential difference. Because μ_1 and μ_2 are different, it gives rise to an electron population up to μ_1 on the left contact and up to μ_2 on the right contact,

providing a non-equilibrium distribution of charge across the system. Because of this disparity in charge between contacts, a left or right moving charge from the area of high potential to the low potential is taking place in order to drive the system back to equilibrium.

The expression in Equation 2.3 describes that the current is dependent on a known constant multiplied by the applied potential. The proportionality constant, $2e^2/h$, is defined as the quantum conductance, and has a fundamental effect to the conductivity of the system. The quantum conductance defines the finite conductance a single energy level can conduct. The quantum conductance is the absolute upper limit and the addition of scattering will scale down current carry capacity based on the quantum conductance.

In turn, when the device is not a perfect conductor (dissipative effects) at all energy levels, arriving from scattering or broadening at a given energy, the expression for the current becomes,

$$I_{tot} = \frac{D_{1D}(\epsilon)qV}{L} qv\Xi = \frac{2e^2}{h} V\Xi, \tag{2.4}$$

where the same quantum conductance term is multiplied by Ξ, the transmission probability. The essence of this expression is what drives the Green's function formalism and is often times referenced as the Landauer formula. The Landauer formula describes the summation over all the contribution energy levels to get the total current. Often times, the expression will be written in integral form, as follows in Equation 2.5, where the transmission for the one electron model is summed across a range of electron energies to arrive at the overall current. The applied voltage is within the FD terms f_1 and f_2.

$$I_{tot} = \int_0^\infty \frac{2e^2}{h} \Xi \left(f_2 - f_1\right) dE \tag{2.5}$$

The sole objective of the Green's function is to solve Schrödinger's equation such that a transmission probability can be determined. In nanostructured materials, the density of state's landscape (where states lie spatially) is a key element in the transmission and ultimately the transport of the material. The Green's function solution, which will be elaborated in the next section, provides a mathematical simplification to solving complex systems by allowing the superposition of impulse responses from contacts and scattering mechanism to be included easily.

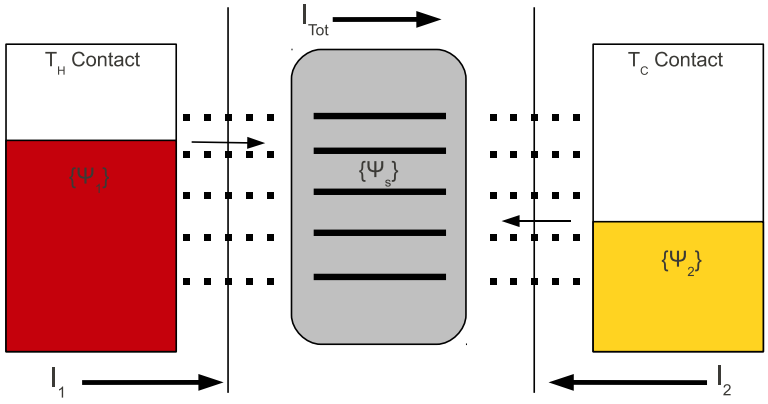

Figure 2.3 Composite non-equilibrium Green's function system for treatment of contacts. Contacts are treated as semi-infinite where the analytic wave functions ($\Psi_{1,2}$) are known. The region in the middle is defined as the channel where the Hamiltonian (Ψ_s) defines the discrete energy levels.

NEGF Electron Transport

The main objective of the non-equilibrium Green's function (NEGF) is to obtain the transmission probability between two contacts for a range of energy levels, in order to obtain the transmission. The NEGF solution provides a many-particle wave-based matrix treatment, incorporating boundary effects through a composite self-energy representation. It is the self-energy aspect that gives NEGF a real advantage, with two of the most important advantages being: 1) general expression can be applied to complicated structures and 2) the Green's function allows the electron density to be calculated easily. Refer to Datta's text (Datta, 2005) for a description from a single electron point of view to a many-electron point of view. Examples are outlined in the appendix of Datta's book and Mahan's book (Mahan, 2000).

One of the most complicated aspects of dealing with nanoscale devices and transport is in the treatment of contacts. The NEGF is unique in that it constructs a composite type system, illustrated in Figure 2.3. The contacts are treated as continuum contacts in which the wave-functions are known and derived from the analytic Schrödinger equation. In addition, the concentration of electrons at each contact is specified by the Fermi-Dirac distribution at a given temperature. The overall wave-

function of the composite Schrödinger equation will look like the following,

$$\begin{pmatrix} EI - H_1 + i\eta & -\tau_1^+ & 0 \\ -\tau_1 & EI - H & -\tau_2 \\ 0 & -\tau_2^+ & EI - H_2 + i\eta \end{pmatrix} \begin{pmatrix} \Psi_1 + \chi_1 \\ \Psi \\ \Psi_2 + \chi_2 \end{pmatrix} = \begin{pmatrix} S_1 \\ 0 \\ S_2 \end{pmatrix}, \tag{2.6}$$

where ψ and χ are a result of the wave-function Φ and the spilling over of states from the isolated contact. H is the Hermitian uncoupled Hamiltonian. The $i\chi$ is a small anti-Hermitian part, which results in the broadening of electron states. The Hamiltonian is described by $H = H_o + H_{ee}$ where H_o is the single particle effective mass Hamiltonian described by the Hubbard model. The H_{ee} term is derived from the many-electron coulombic interaction and will be touched on later when the self-consistent method is discussed.

When coupling the channel to the contacts, a spilling over of electrons near the contact gives rise to a Lorenzian type distribution of carriers within the channels. This broadening of electronic energy is important in capturing the transport on the nanoscale and real effect of contacts. The coupling of the contacts and the channel are governed by the off-diagonal terms τ; these can be thought of as scattering rate terms. The term that is of interest in this expression is χ, which are thought of as scattering waves in the source and drain region. Expanding the matrix expression above, the following expression drops out,

$$\{\chi\} = G_c \tau^+ \{\psi\}, \tag{2.7}$$

where,

$$G_c = [EI - H + i\eta]^{-1}. \tag{2.8}$$

.

This expression gives rise to the Green's function and the following expression can be taken a step further to derive the Green's function within the channel.

$$\psi = [G]S \tag{2.9}$$

$$G = [EI - H - \Sigma]^{-1} \tag{2.10}$$

Where Σ is defined as the self energy term and is what gives rise to the perturbing of the uncoupled Hamiltonian when it is connected to the contacts.

$$\Sigma = \tau G \tau^{+} = \Gamma f(E) \tag{2.11}$$

The superposition of additional Σ terms will later be shown to provide a means to couple phonon contacts in the same way a physical contact is connected. The superposition of impulse responses from contacts is a major advantage in the Green's function formalism.

The Green's function provides an elegant method for solving the non-homogeneous PDE arriving from Schrödinger's equation. Because the contacts are treated as infinite, they can be treated as impulses at the boundary points neighboring them. As expressed in Equation 2.10, the Green's function is constructed from the inversion of the eigenvalue problem, giving rise to an orthonormal set of plane-wave eigenfunctions (Arfken and Weber, 2005). Using Hilbert space transformations (Datta, 2005) a series of general expression can be derived.

$$A = i[G - G^{+}] \tag{2.12}$$

$$\Gamma = i[\Sigma - \Sigma^{+}] \tag{2.13}$$

The variable A is defined as the spectral density and Γ is defined as the broadening term. It will be shown later that these expressions are general and can be used in the multiple particle representation. Likewise, the electron density or number of filled states can be determined as follows,

$$G^{n} = G\Sigma^{in}G^{+}, \tag{2.14}$$

where G is the Green's function at a given energy level and G^{+} is the complex conjugate Green's function. Σ^{in} is the in-scattering term that can be defined by the Fermi function at the contact times the broadening term, Γ, at the contact. If there are multiple contacts, the in-scattering term is a summation of the terms derived from their individual Fermi and broadening terms. Note that the Fermi function is known in the ballistic case, but when scattering is added, additional exercises must be done to determined the Fermi function at the contacts, including scattering centers which act as contacts to the system.

The following expression can be used to calculate the number of unfilled states G^{p}, in the system.

$$A = G^{n} + G^{p} \tag{2.15}$$

Here, G^{n} is the density of filled states and G^{p} is the density of unfilled states. The

composite total density of local states for a Si/Ge superlattice is shown in Figure 2.4. Notice that the plot of the filled density of states (G^n) in Figure 2.4 is a gradient across the device demonstrating that the electrons are filling from the contact with the higher potential. In this case a 100 mV potential is applied to the left contact and the right contact is grounded.

The amount of in-scattering from the contacts is defined by the surface Green's function and the broadening of the contacts.

$$\Gamma_n = \tau a \tau^+ \tag{2.16}$$

$$\Sigma_1^{in} = \Gamma_1 f_1 ... \Sigma_2^{in} = \Gamma_2 f_2 \tag{2.17}$$

Where f_n is the Fermi function at each contact. For a two contact system the self energy terms are simply the addition of the two. Notice the broadening term, Γ_n is a function of the contact spectral function, a, and coupling energy τ. The coupling energy will arrive from the off diagonal terms of the Hamiltonian. This same expression will be used later when calculating the in-scattering from phonons derived from the phonon Green's functions.

Now that the mechanics are in place, it is necessary to construct a working description of a device using the Green's function formalism. This is done through an effective mass Hamiltonian, a depiction of the discretization scheme is shown in Figure 2.5. It should be noted, the electronic Green's function is not an atomistic calculation but rather the domain is discretized in spatial energy. This can be thought of as simply discretization of Schrödinger equation for the delocalized conduction electrons that lie above the conduction band edge. There is an underlying assumption that the electron lie near the bottom of the conduction band edge and therefore the effective mass near the bottom is used. As mentioned before, the states of these delocalized electrons are described by a parabolic effective mass relation. Additionally, the NEGF formalism here is spin independent and for all the analyses in this work the spins are assumed degenerate and the charge is simply multiple times two to compensate for this fact.

In constructing a well behaved effective mass Hamiltonian (the routine used to construct the Hamiltonian is provide in the Appendix), previous studies (Musho and Walker, 2011b) have shown the domain should be discretized such that a cell spacing of at least $1\mathring{A}$ for convergence. In addition to spatial discretization the discretization of the energy range is also critical to convergence. A rule of thumb stated by Datta (2005) is to makes sure the bonding term, τ (off diagonal Hamiltonian term), is always larger than the energy range you are interested in. In terms of elementary

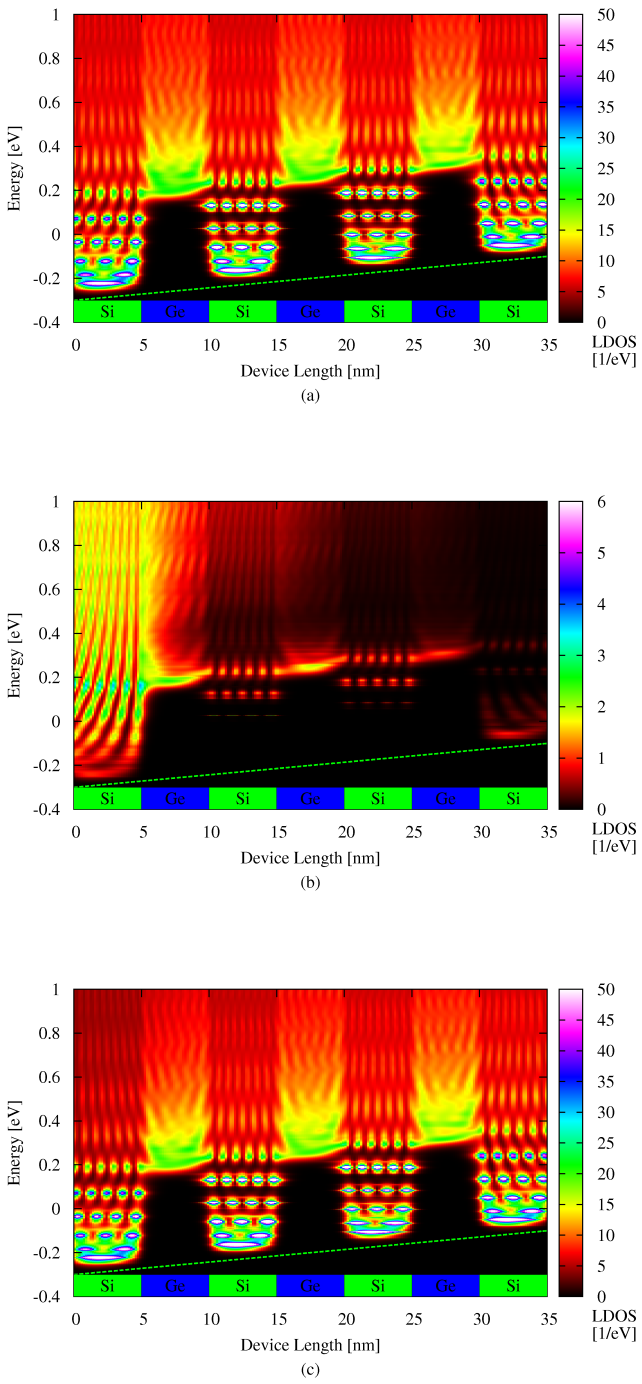

Figure 2.4 Plot of the local density of state (LDOS) for three difference states which satisfy the relation $A = G^n + G^p$. Above, (a) total local density of states (A), (b) filled density of states (G^n), and (c) unfilled density of states (G^p). These results were calculated from the fully coupled model which includes electron-phonon interactions.

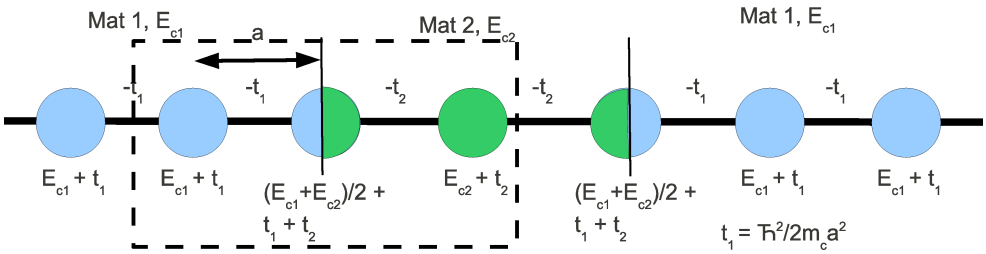

Figure 2.5 Sketch of two dissimilar material heterostructure described by a one-dimensional effective mass Hamiltonian. This structured is used to define a superlattice material where the Hamiltonian has units per area. The dotted box corresponds to the example Hamiltonian matrix provide in Equation 2.19.

wave mechanics, the domain size specified in the model only allow a finite number of modes in a range of energy, thus the value selected for the cell size must make sure the cuff-off frequency or allowed modes are greater than our range of interest.

When constructing the Hamiltonian matrix, it is necessary to make sure that the matrix is Hermitian in order to get real eigenvalues. The equation for formulating the Hamiltonian is as follows,

$$[E_c - \frac{\hbar^2}{2m_c^\star}\nabla^2 f(r) = Ef(r)]. \tag{2.18}$$

Applying this equation to the example of a 1D structure in Figure 2.5, a heterojunction is formed by sandwiching two dissimilar materials. The point of contact between the two materials is a cell that is composed of both, providing a transition. Note that the transpose complex conjugate of the Hamiltonian must be zero, and the resulting Hamiltonian for a three cell matrix with an interface atom at the center is,

$$\begin{pmatrix} E_c + 2t_1 & -t_1 & 0 \\ -t_1 & Ec + t_1 + t_2 & -t_2 \\ 0 & -t_2 & E_c + 2t_2 \end{pmatrix}, \tag{2.19}$$

The variable $t_n = \frac{\hbar^2}{2m^*}$ is the bonding energy defined by the effective mass and E_c is the conduction band edge determined from the equilibrium calculation reference from the specified Fermi level.

If a finite difference type expression is used to construct the matrix, the resulting matrix will not be Hermitian. This is because a standard finite difference scheme averages the off diagonal terms in the mixed cell.

The Hamiltonian is initially implemented to calculate the open channel eigenvalues of the system using the equilibrium equation,

$$(EI - H)\tilde{u} = 0, \tag{2.20}$$

where I is the identity matrix and E are the eigenvalues. The eigenvalues, referred to as the allowed energy levels or modes, provide the sub-band level which govern the barrier height. Drawing the analogy to an elementary 1D barrier problem in quantum mechanics, the formalism here in similar is theory, as the eigenvalues of the system define a pseudo barrier height and there is an associated transmission probability to tunnel through it. The transmission probability is based on a range of incoming energy levels that are calculated for each sub-band. It is from these 1D solutions that the transmission is integrated over all sub-band energies to determine the overall transmission through the channel; this was demonstrated earlier in the Landauer formula, see Equation 2.5. It should not be overlooked that the actual dispersion of the material is direction dependent in that along the $\langle 100 \rangle$ or $\langle 111 \rangle$ direction the energy levels are different. Because this research focuses on the transport of the conduction electrons, only the band minimums are of interest. It coincidently turns out that the band minimums of both Si and Ge are close to the $\langle 001 \rangle$ direction, near the X and Δ directions.

The only other consideration in solving the NEGF problem is to incorporate the interaction of many electrons or electron-electron interaction. This type of coulombic interaction is handled through a self-consistent field (SCF) method. Poisson's equation is solved on the same lattice as the Hamiltonian matrix was constructed. A spatially varying dielectric field is constructed based on the permittivity of each material within the channel.

$$- \bigtriangledown \bullet(\epsilon_r \bigtriangledown U) = \frac{q^2}{\epsilon_0} n(z) \tag{2.21}$$

The Poisson equation has a similar construction to the Schrödinger equation, where the Laplace operator, $\bigtriangledown$, relates the potential to the charge distribution. If it is assumed the potential varies slowly over the device, the potential can be calculated by only taking the diagonal terms of Poisson's equation, $U = \frac{q^2}{\epsilon a}(N_o a^2)$. N_o is the probability electron distribution calculated from the spectral density relation, G_n, calculated in Equation 2.14. The potential, U, is then passed to Schrödinger equation and looped until a converged potential is determined. A self-consistent potential is plotted in Figure 2.6 for a 6 bilayer Si/Ge superlattice structure. A large charge is

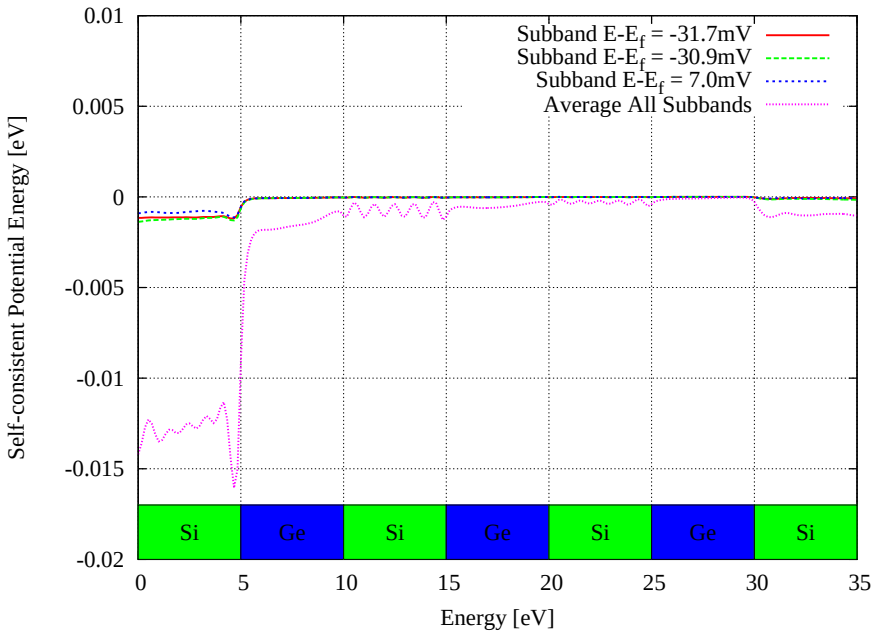

Figure 2.6 Plot of the self-consistent potential which accounts for the many-electron view point of the electronic NEGF model. There is a 100mV bias on the left boundary inducing a current from left to right. Thus, the charge density is higher near the left contact.

built up near left portion of the device due to a 100mV potential applied to the left contact. As apparent on in the figure is the wave nature of the charges within the silicon well regions.

The self-consistent method of solving Poisson's equation iteratively outside the Schrödinger solution gives a mean particle view point. In the context of this research, the potential is converged based on an Anderson mixing routine (Eyert, 1996), which the previous five values of the potential landscape are weighed to determine a new estimation at the potential. The convergence is increased considerable with this type of method compared to a simple mixing technique.

Strain Induced Band Shifting

Before continuing, it is important to discuss one aspect that is often overlooked in nanoscale structures: the straining and subsequent modification to the electronic structure. As was shown in Chapter I, previous research (Bulusu and Walker, 2007a) used deformation potentials (Van de Walle, 1989) to modify the conduction band edge. For a system with two layers, Van de Walle calculated an effective lattice

constant, $a_{||}$, in-plane and cross-plane, $a_{\perp}$.

$$a_{||} = \frac{a_1 G_1 h_1 + a_2 G_2 h_2}{G_1 h_1 + G_2 h_2} \tag{2.22}$$

$$a_{\perp} = a_1[1 - D_i(a_{||}/a_n - 1)] \tag{2.23}$$

In Equation 2.22, a_n is the lattice constant of the material, G_n is the shear modulus, and h_n is the thickness. The shear modulus, $G_n^{001} = 2(c_{11}+2c_{12})(1-c_{12}/c_{11})$, is a function of the elastic constants. The effective lattice constant, $a_{||}$ can now be used to determine the in-plane strain tensor based on the ratio of the effective lattice constant to the actual lattice constant.

$$\epsilon_{n||} = \frac{a_{||}}{a_n} - 1 \tag{2.24}$$

$$\epsilon_{n\perp} = \frac{a_{\perp}}{a_n} - 1 \tag{2.25}$$

The expression for the conduction band offset is as follows,

$$\Delta E_c^{001} = \frac{2}{3}\Xi(\epsilon_{\perp} - \epsilon_{||}) \tag{2.26}$$

where Ξ is the tabulated deformation potential in Table 2 of Van de Walle (1989). In Bulusu's research, (Bulusu and Walker, 2007b) she determined using Equation 2.26, that conduction bands of silicon and germanium invert when a superlattice device is formed. Van de Walle mentions this possibility and notes that information about the higher bands is necessary for good confidence. Further investigation into the inversion can show that this is true. There is some ambiguity in the transport model in this work because the model is only interested in the band minimums. Figure 2.7 is the full band diagram calculated by Krishnamurthy et al. (1986) with some additional labeling to point out the direction of interest for this research. Since the transport of the 1D structures in the this research are of interest are along the $\langle 001 \rangle$ direction, the focus will be on between the Δ and X direction of the band diagram. In applying the equation above for the Δ direction shift in conduction band edge, it is noted that the Si band edge shifts up and the Ge shifts down resulting in the inversion.

Phonon Transport in Semiconductors

The method for calculating the non-equilibrium transport of phonons using non-equilibrium Green's function is very similar to the electron model except for two

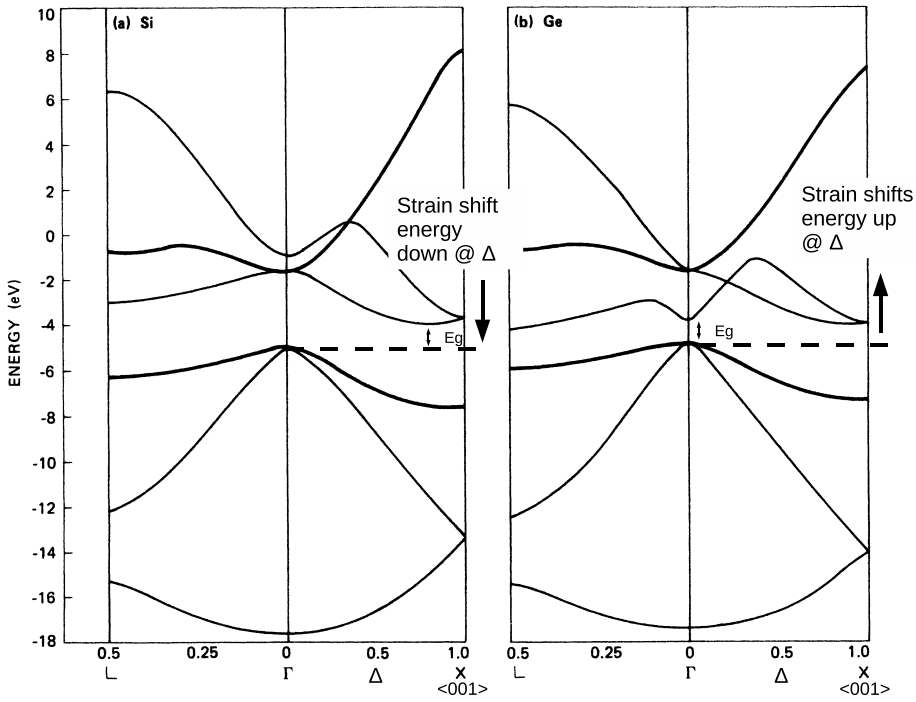

Figure 2.7 Full band diagram describing the band minimums along the ⟨001⟩ direction. Krishnamurthy et al. (1986)

aspects: 1) an atomistic harmonic potential is implemented instead of a effective mass Hamiltonian, and 2) Poisson's equation does not have to be solved because phonons do not have a forcing function.

To begin, it is necessary to understand that phonons are bosonic in nature. Bosons are particles with zero or integral spin (Kittel, 1986) and have a drastically different equilibrium distribution than fermions up to the classical limit. The distribution of phonons follow the Bose-Einstein (BE) distribution is shown in the following equation.

$$f_{BE} = \frac{1}{exp((\epsilon - \mu)/k_B T) - 1} \tag{2.27}$$

When compared to Equation 2.27, Fermi-Dirac distribution, the only difference is the minus in the denominator. The BE distribution will be implemented in the NEGF formalism in the same manner as the FD was implemented for electrons. Equation 2.5 has the same Landaur approach, except with a slightly modified quantum conductance for phonons.

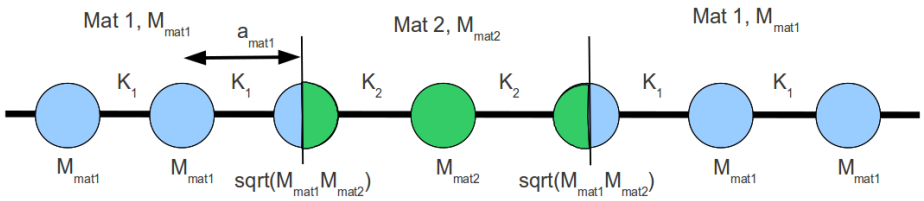

Figure 2.8 Sketch of two dissimilar material heterostructure described by a one-dimensional atomistic Hamiltonian. A harmonic pair potential is used to construct the Hamiltonian. The phonon model describes planes of atoms oscillating where the Hamiltonian has units of per area.

NEGF Phonon Transport

The model developed in this research is built on the foundation of the ballistic model outline in the literature (Zhang et al., 2007; Hopkins et al., 2009). The model developed in this research includes additional physics to allow larger devices to be studied. Once the device size reaches the size of the mean free path of phonons it is necessary to take into account the dissipative mechanisms such as phonon-phonon interactions. It will be shown in the results sections that this is critical for devices above 50 nm where the ballistic solution severely over predicts the transport.

The model begins with an atomistic non-equilibrium Green's function description used to calculate the thermal transport in nanoscale materials. Added complexity in the description of the Hamiltonian stems from a discretization scheme, where the cell center corresponds to equilibrium atom positions, hence the atomistic Green's function (AGF). Because of the one-dimensional planar geometry of the device, each cell center along the device is treated as a basis of two atoms. This is derived from the crystalline structure in the $\langle 001 \rangle$ directions of Si/Ge diamond cubic crystallographic structure. Furthermore, there is an underlying assumption that the model represents planes of atoms oscillating along the direction of transport generating the motion of plane waves. This forces the assumption that the waves travel in a straight line and for that reason, this steady state solution is thought of as an average path of motion described by the wave-function (Ziman, 1960).

Unlike the electron model, the phonon solution does not require self-consistency with an external field, decreasing the computational time required to reach a solution. The NEGF phonon treatment is a wave-based solution that treats the phonons as waves, not particles, accounting for the tunneling of phonons similar to that of electrons. Additionally, through an atomistic formalism, the system has discrete phonon

frequencies that are unique for each device configuration. The dispersion is derived from the unperturbed eigenvalue problem of the Hamiltonian. As the device length increases, the dispersion becomes more continuous. The discreteness gives rise to the quantum conductance of a single phonon frequency that governs the theoretical transport of a single discrete phonon frequency. The objective of the NEGF is to determine the transmission probability of each discrete phonon frequency, in order to use a similar expression to the Landauer formalism. The total thermal energy, q_{tot}, transported as a function of the integrated transmission probability, Ξ, and single phonon mode, $\hbar\omega$, takes the following form,

$$q_{tot} = \int_0^{\omega_{max}} \frac{\hbar\omega}{(2\pi)^3} \Xi \left(f_2 - f_1\right) d\omega, \tag{2.28}$$

where the thermal quantum conductance is $\frac{\hbar\omega}{(2\pi)^3}$. Applying Fourier's law and the known temperature gradient between contacts, the phonon thermal conductivity, k_p, can be calculated based on the calculated heat flux. The method of including thermal dissipation simply comes by adding an additional perturbing potential to the system that affects the transmission probability.

In order to calculate the transmission probability, the Hamiltonian must be constructed appropriately using an atomistic description. The atomistic harmonic potential is based on an inter-atomic pair potential, which is derived from the equilibrium position of atoms within the device. The harmonic matrix is constructed using the Harrison potential (Harrison, 1989), which defines the potential energy of the pair bond based on the lattice strain within the system (Equation 2.29). The Harrison potential is essentially the second term in the Taylor expansion of the total potential energy of the system and takes the following form,

$$U = \frac{1}{2} C_o \frac{(d_i - d_e)^2}{d_e^2}. \tag{2.29}$$

There are other pair potentials and three body potentials that are applicable, but the Harrison potential has proven to be adequate for one-dimension construction and reproduces the phonon dispersion derived from the analytic model.

The anharmonic lattice forces that are needed to facilitate inelastic scattering transition are not included in the unperturbed Hamiltonian description, but are accounted for in the perturbing potential, which is determined self-consistently. Often the higher order terms of the pair potential that comprise the anharmonic terms are difficult to determine and often over restrict the model or are simply used as fitting

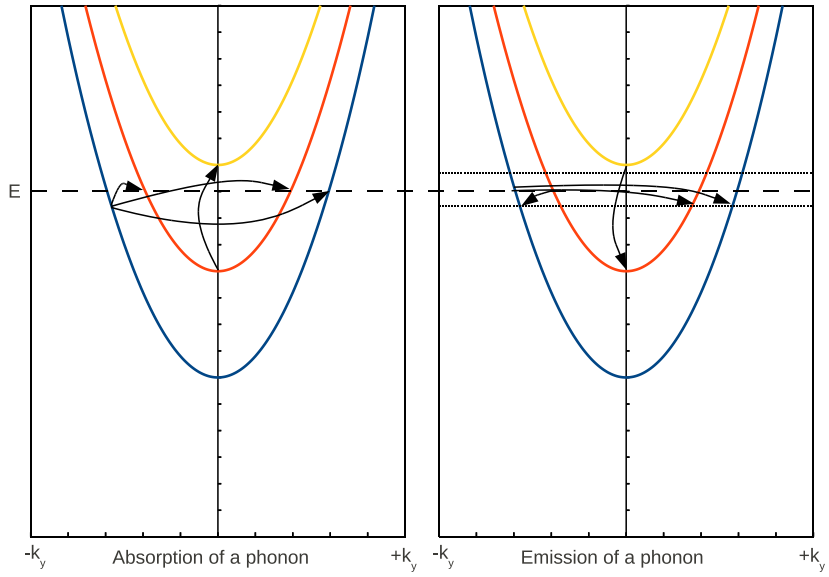

Figure 2.9 This figure illustrations the possible intrasubband and intersubband transitions with either the emission or absorption of a phonon frequency. The phonon model handles the intraband transition explicitly and the interband transportion implicitly.

parameters (Ziman, 1960). This is a unique approach taken for this research and will be elaborated on in the later sections.

The Hamiltonian is constructed by placing atoms at a position near the equilibrium lattice constant such that there is a divisible number of atoms within the layer. This inherently induces a strain in the system of atoms, inducing potential energy in the system. The Hamiltonian matrix is assembled in the same manner as the effective mass Hamiltonian, in that the matrix must remain Hermitian to obtain real eigenvalues. Knowing the potential energy at each lattice point and the mass of each atom, the following Hamiltonian matrix is assembled.

$$H_{ij} = \frac{1}{\sqrt{M_i M_j}} \frac{-\partial^2 U}{\partial u_i u_j} \tag{2.30}$$

Here M is the mass and U is the potential energy derived from Equation 2.29. The open channel equilibrium equation is similar to the electron equilibrium equation except in the phonon model, the terms are framed in units of angular frequency, see the following equilibrium equation,

$$(\omega^2 I - H)u = 0. \tag{2.31}$$

Here ω^2 is the angular frequency squared of the phonon eigenvalues, which can be related to the discrete energy level of a phonon through $E = \hbar\omega$. These eigenvalues describe the allowed modes within the channel region or the discrete phonon frequency that are responsible for the transport. The simple 1D barrier analogy can be applied to calculate the overall transmission of the structure from these eigenvalues. The superposition of the transmission probabilities for each phonon frequency give rise to the overall heat flux (see Equation 2.28).

The steps to calculate the phonon transport using NEGF are as follows, 1) the harmonic matrix is assembled, 2) the eigenvalues are determined, 3) the transmission probability for each phonon frequency that was defined by the eigenvalues is calculated, and 4) the thermal transport energy and thermal conductivity are calculated. In reference to Equation 2.28 and step 3, each phonon frequency has a finite thermal current governed by the phonon quantum conductance. The notion of a finite current at discrete energy levels is very similar to the case of a single electron level in the electron framework. The transmission times the thermal quantum conductance between either contacts is what limits the current carrying capacity of each phonon frequency. The culmination of the transmission probabilities at discrete phonon frequencies gives rise to the overall calculated thermal conductivity of the device.

Dissipative Modeling Approach

The dissipative effects which encompass the electron-phonon interaction in the electron NEGF model and the phonon-phonon model in the NEGF phonon model were handled through the addition of scattering contacts along the length of the device. This increases the complexity and computational effort required to reach a solution but it allows devices to be studied that have lengths that lie between the ballistic and non-ballistic regime. The electron-phonon dissipation technique can be found in the literature for a single phonon interaction but the added complexity of coupling the phonons and electron NEGF description is unique to this research. Likewise, the phonon-phonon interaction has never been handled so rigorously in the literature to capture the dissipative phonon scattering, which has previously only been investigated in the ballistic regime.

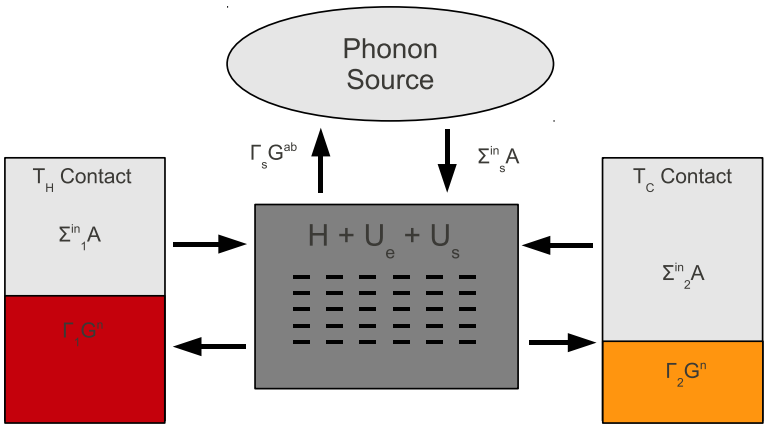

Figure 2.10 Sketch of the NEGF self-energy diagram where the in-scattering and out-scattering depend on the correlation (Σ) and spectral (Γ) functions. The correlation function for the phonon source are solved self-consistently along with an effective Fermi function for the phonon contact. Figure provided from Datta (2005).

Phonon-Phonon Scattering

The three phonon interaction is classified as either a normal process (N process) or and Umklapp process (U process). Only the three phonon scattering process influences the thermal conductivity directly. The normal process is synonymous with elastic scattering, where the Umklapp scattering is ultimately what is of interest in this research and is inelastic, forcing the phonons to lose coherency. In either process, the total energy of the phonons must be conserved $\omega_1 + \omega_2 = \omega_3$; however, the momentum is not conserved for a U process.

It should be emphasized that a phonon is classified into two energy ranges and two polarizations. For the studies, the model only captures the longitudinal optical (LO) and longitudinal acoustic (LA) branches. The transverse optical (TO) and transverse acoustic (TA) phonons are approximated by assuming the spring constant is about the square root of the longitudinal spring constant. When studying higher dimension structures, the addition of transverse optical (TO) and acoustic (TA) branch becomes necessary. The optical branch designation arrives from phonons with wave vectors near the edge of the Brillouin zone and is noted in the dispersion curve as leveling off at higher phonon energies. These optical modes can be thought of as standing waves within the structure. The acoustic branch is the remaining part of the dispersion for phonons, with wave-vectors near the center of the Brillouin zone. The model allows both the acoustic and optical phonons to interact.

To facilitate the phonon-phonon scattering, a self-consistent technique must be used to determine the scattering matrices which are used as a perturbing potential in the Green's function. The scattering matrices will depend on the spatial population of phonons across the device. This is similar to the electron-phonon interaction except there is no deformation potential but rather an anharmonic factor replaces this term. Additionally, the deformation potential is the electrical response to a certain phonon frequency where the anharmonic factor defined in the phonon model is a phonon response to a certain phonon frequency. This will be handled in the detailed explanation of the phonon model.

The phonon-phonon interaction is carried out by allowing each phonon frequency to scatter with each other. The superposition of all of the scattering matrices due to multiple phonon-phonon scattering events compose the overall scatter at each discrete phonon frequency. This is carried out for all phonon frequencies in the same manner. In the end, each phonon frequency has a single scattering rate and all these scattering rates are averaged for a single spatial location or scattering site.

The selection rules for the three-phonon interaction are handled by shifting the final density of states and the assumption is that all phonons scatter with each other. The objective is to calculate a scattering rate for each phonon frequency using a Fermi's golden rule approach. As stated in the literature, the probability of scattering is dependent on the allowed transition from initial to final state and the available density of states of the final state.

$$P(E) = \frac{2\pi}{\hbar} \mid \langle i \mid H' \mid f \rangle \mid^2 D_f(E) \tag{2.32}$$

In the framework of NEGF formalism, there are four transitions which are facilitated from the view point of a single scattering site. They include the inflow (in-scattering) and the outflow (out-scattering) of scattered phonons, which both include the absorption and emission of phonons. Figure 2.11 is an illustration of the four transitions relative to the current scattering state. The selection rules are governed in the model govern such that a scattered phonon energy must not be greater than highest phonon frequency and must not scatter below the lowest scattering frequency. This avoids the complication of having the phonon frequencies scattering into states which do not exist for the given system.

Fermi's golden rule is written as a self-energy contact term, so the scattering sites can be incorporated as an additional contact along the device at every cell center in the Green's function. The perturbing potential or self-energy term, which is calculated in Equation 2.33, includes a scattering factor (f_o) to govern the amplitude

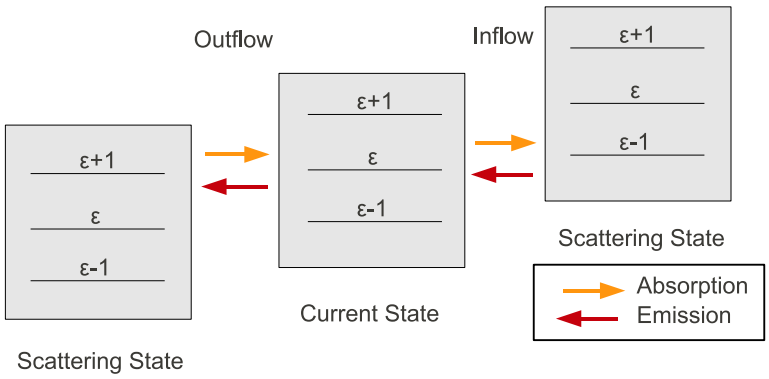

Figure 2.11 Illustration of the four transition channels which include inflow and outflow with absorption and emission of a phonon. These transitions apply to both the shifting of the electron and phonon density of states for both the electrical and thermal models.

of the scattered phonon. The scattering parameter governs the strength of the anharmonicity in the lattice and is a free parameter of the phonon scattering model. If the factor f_o increases, the scattering rate increases, resulting in decreased transport between the device contacts. The response will be shown in the results that this parameter was varied to determine an optimal value for the material. This term varies from zero (no scattering) and increases until the scattering saturates the transport and all phonons are scattered into the scattering contacts.

The model handles the calculation of the scattering term, Σ, by performing matrix manipulation to the filled (G^n) and unfilled (G^p) density of states to represent the final density of states (D_f). Remember, the final density of states can either be an absorption ($E + \hbar\omega$), the shifting of matrices down the energy axis, or an emission ($E - \hbar\omega$), the shifting of matrices values up in energy. These new matrices, ($G^n(E \pm \hbar\omega)$ and $G^p(E \pm \hbar\omega)$), define the final states. The shifting of matrices is carried out for all phonon frequencies to account for all the possible scattering interactions. Because phonons are bosonic, the term G^p, which defines the unfilled states where $A = G^p + G^n$, must be slightly modified from the electron formalism. In the previous equation, A is the local density of states (LDOS) which is readily determined from the difference between the retarding and advancing Green's function. The modification to the phonon formalism comes by making $G^p = A$, describing the situation that the phonons can scatter into any state. This comes from the fact that more than one boson can occupy a single state and the Pauli exclusion principle does

not hold for bosons.

The following equations are the in-scattering ($\Sigma^{in}_{s,ph}$) and the out-scattering ($\Sigma^{out}_{s,ph}$) terms for the phonon-phonon interactions. These are derived from the expression similar to the in-elastic electron scattering expressions where N_w is the Bose-Einstein number. It is reasoned that the rate of absorption is $1+N_w$ and the emission rate is N_w.

$$\begin{aligned}\Sigma^{in}_{s,ph} = &\int_{\hbar\omega_{min}}^{\hbar\omega_{max}} \frac{d(\hbar\omega)}{2\pi} f_o[(N_\omega + 1)G^n(E + \hbar\omega) \\ &+ N_\omega G^n(E - \hbar\omega)]\end{aligned} \tag{2.33}$$

$$\begin{aligned}\Sigma^{out}_{s,ph} = &\int_{\hbar\omega_{min}}^{\hbar\omega_{max}} \frac{d(\hbar\omega)}{2\pi} f_o[(N_\omega + 1)G^p(E - \hbar\omega) \\ &+ N_\omega G^p(E + \hbar\omega)]\end{aligned} \tag{2.34}$$

The model incorporates the new Σ scattering term as another contact along the device channel. This is often referred to as the Butticker approximation (Datta, 2005). In addition to adding a contact, the model needs to make sure that the thermal energy is conserved in the system. The energy entering and leaving the contacts and scattering sites must add up to zero. An unknown Fermi function that defines the rate of inflow and outflow through the scattering contacts is used to conserve energy. The unknown Fermi function (f_s) for the contacts is determined iteratively and used to govern energy conservation. The expression $\Gamma = \Sigma/f_s$ used to described the scattering terms in the Green's function. The final scattering term which includes the in-scattering and out-scattering follows the complex form,

$$\Gamma_s = (\Sigma^{in}_{s,ph} - i(\Sigma^{out}_{s,ph} - \Sigma^{in}_{s,ph}))/f_s. \tag{2.35}$$

The solution is iterated self-consistently until the scattering solution has converged. The overall Green's function takes the following form,

$$G = [\omega^2 I - H - \Sigma_1 - \Sigma_2 - \Sigma_s]^{-1}. \tag{2.36}$$

Once a solution is found, the overall scattering rates and the thermal conductivity can be calculated.

Electron-Phonon Scattering

Now that the foundation has been assembled in the previous sections on how to independently calculate the electron transport and phonon transport, it is necessary to understand how to resolve a fully coupled system that incorporates the electron-phonon interactions of multiple phonon frequencies. The major aspect that is unknown when doing electron-phonon interactions is the rate at which the electrons and phonons interact. Note, the following formalism assumes steady-state interactions of electrons and phonons. No attempt has been made to resolve the transient effects of electron-phonon scattering. In order to incorporate the phase-breaking operation in which the background (phonons) interact with the electrons, a slightly more complicated view point must be taken from the perspective of coherent (ballistic) electron transport. The phonons disrupt the coherency of the electron wave-functions

The theory of scattering in this model is based on a self-consistent Born approximation (SCBA) to determine the scattering matrices. It has been shown by (Datta, 1990; Lee and Venkatasubramanian, 2008) that the SCBA theory has a wide range of validity and can apply to weakly and strongly coupled electrons and phonons. The limitations of SCBA theory can only be determined by comparing to experimental results. From this understanding, it is assumed that SCBA is valid for the nanostructured thermoelectric materials of interest in this research.

The basic Hamiltonian that describes the electron-phonon interaction has the form, $H = H_p + H_e + H_{ei}$. Here H_p describes the oscillators (phonons) and H_e describes electrons using the Hubbard model and H_{ei} describes the electron phonon interaction. Writing the Hamiltonian in second quantization (Mahan, 2000), the following terms can be partitioned so that the electron NEGF model solves $H_e + H_{ei}$ and the phonon NEGF solves the remaining H_p. The electronic Green's function model which includes the electron-phonon interaction can be written as follows,

$$G = [EI - H - U_{ee} - \Sigma_1 - \Sigma_2 - \Sigma_s]^{-1}. \tag{2.37}$$

Here Σ_1 and Σ_2 are the in-scattering from the contacts, and Σ_s is the in-scattering from the phonons. The in-scattering due to phonons is handled as multiple contacts (Butticker probes) located along the length of the device.

The research is strictly interested in the intra-band transition of electrons as a result of phonon-carrier (electron) interactions, see Figure 2.9. The scattering of phonons from electron carriers or vice versa is influenced through the interaction of strain induced by a phonon mode distorting the lattice as it propagates. As the

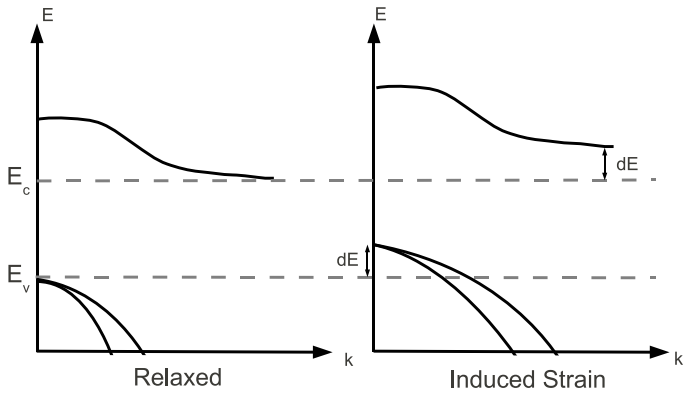

Figure 2.12 Induced straining from the occupation of a phonon mode in the lattice results in a shift in the energy relationship. This staining effect is described by potential response calculated from a deformation potential. There are two deformation potentials which describe the response of a acoustic and optical phonon mode. This figure is from Harrison (1989).

lattice spacing changes under a localized strain, the band structure of the material is modified, shifting the energy level as a results of orbitals overlapping, see Figure 2.12. This is very similar to the shift in conduction band edge due to hydro-static strain from the difference in neighboring lattice constants. The only difference is the parameters that govern the electron-phonon interaction are dependent on localized parameters such as number of phonon and electrons; therefore, a self-consistent method must be used to iteratively fit the scattering parameters.

Fermi's Golden Rule, which includes the deformation potential (Equation 2.38), demonstrates this fundamental straining.

$$S(k,k') = \frac{2\pi}{\hbar} \mid H^{ab}_{k',k} \mid^2 \delta(E(k') - E(k) - \hbar\omega) + \frac{2\pi}{\hbar} \mid H^{em}_{k',k} \mid^2 \delta(E(k') - E(k) - \hbar\omega) \tag{2.38}$$

Fermi's Golden Rule describes the transition rate at which the electrons can transition from an initial state, k, and to a final state, k'. The straining is incorporated through the scattering Hamiltonian, $H_{k',k}$, which is a function of the wavefunction

and scattering potential, $H_{k',k} = \langle \Psi \mid U^s \mid \Psi \rangle$.

The total scattering rate can be related to the Equation 2.38 through the following expression,

$$\frac{1}{\tau} = \sum_k S(k, k'), \tag{2.39}$$

where τ is the overall scattering time for all the scattering phonon frequencies.

The localized stain that is induced from a given phonon mode can be treated as a perturbing potential in the electronic framework. It is possible to derive the potential response when an acoustic phonon mode is locally present resulting in a strain displacement of neighboring atoms in the same direction. For a 1D chain of atoms, the acoustic potential would follow this relation

$$U^s_{AP} = D_{adp} \frac{\partial u}{\partial x} \tag{2.40}$$

where D_A is the acoustic deformation potential.

When an optical phonon mode is present, the expression for the perturbing potential looks similar, however, since an optical phonon is a standing wave, the neighboring atoms are displacing in the opposite direction thus,

$$U^s_{OP} = D_{odp} u, \tag{2.41}$$

where D_{odp} is the optical deformation potential. Both the acoustic and optical deformation potential values are tabulated in Lunstrom's text (Lundstrom, 2000) and can be related to the momentum relaxation times.

Buttiker Approximation

The previously derived spectral function for both the electrons and phonons will give rise to the rate at which the electrons and phonons scatter using the Fermi Golden Rule expression. Assuming that the phonons and electrons interact as if contacts were placed along the length of the device, one can make the analogy that there is a Buttiker probe attached at each discretized cell center. These probes provide a means of in-scattering and out-scattering along the length of the device. Each of these scattering contacts have an associated delta potential that allows the interband and intraband transition to be facilitated with the creation or annihilation of phonons.

In other's work(Bulusu and Walker, 2007a; Koswatta et al., 2007) and Datta's text (Datta, 2005), the Σ_s term is calculated using a single phonon frequency with

a deformation potential approach and the Bose-Einstein dispersion relation to determine the number of phonons, see Equation 2.42. The approach in this research is similar, except multiple phonons frequencies will be included.

$$\Sigma^{in}_{s,e} = \int_{E_{min}}^{E_{max}} \frac{d(\hbar\omega)}{2\pi} D_o(\hbar\omega)((N_\omega + 1)G^n(E + \hbar\omega) + N_\omega G^n(E - \hbar\omega)) \tag{2.42}$$

The factor D_o is comprised of the phonon density of states and a deformation constant. The deformation potential provides a potential response due to the presence of a particular phonon frequency. Thus, if multiple phonon frequencies are incorporated, multiple potential responses are possible. This research will assume that the superposition of multiple responses are related to the scattering of a single scattering site along the device.

There are two types of deformation potentials, acoustic and optical, which are selected based on the type of interaction. The deformation potential was selected based on an optical cut-off frequency. If the incoming scattering phonon is below the optical cut off frequency, it was assumed acoustic and the acoustic deformation potential was used. Likewise, if the incoming phonon frequency was greater than the cut-off, the optical deformation was used. The deformation potential is thought of as the potential response due to the presence of a phonon which is a localized lattice strain. Because the lattice strain is different for optical phonons, where the neighboring atoms oscillate opposite each other, and acoustic phonons, where neighboring atoms oscillate in the same directions, there are two different deformation potentials. The acoustic deformation potential takes the following form,

$$D_{adp} = \frac{D_a^2 \beta^2 q}{24\rho\nu_s}, \tag{2.43}$$

where D_a is the tabulated acoustic deformation potentials factor determined from experimental studies (Jacoboni and Reggiani, 1983; Jacoboni et al., 1977). The term β is the wave-vector, ρ is the density of the material, and ν_s is the sound speed of the material.

The optical deformation potential is similar except the deformation factor D_{odp} has different units. The optical deformation takes the following form,

$$D_{odp} = \frac{D_o^2 \beta^2 q}{16\rho\omega_o}, \tag{2.44}$$

where ω_o is the cut-off frequency for optical phonons. Both of these deformation potentials were calculated based on the scattering rate for both optical and acoustic phonons from a density of state description (Lundstrom, 2000).

Shifting the spectral function, $E + \hbar\omega$ and $E - \hbar\omega$, allows the calculation of probabilities from transition of an initial state to a final state. The rate of transition is determined by the number of phonons in each state, N_w.

The approach by Bulusu and Walker (2007a) and Koswatta et al. (2007) focused on using a single deformation potential as a means of fitting the experimental data because they only worked with a single phonon frequency to encompass all phonon frequencies in the actual structure. They also limited their scattering to the optical phonon scattering, which may be a valid assumption, but more modes can be captured in the foregoing method, resolving transitions absent in their calculation.

To increase the fidelity of Equation 2.42, the model devised in this research was to couple to the NEGF phonon solution to the NEGF electron model. The NEGF phonon method calculates the dominate phonon modes of the structure and the associated spatially varying correlation matrices allowing multiple phonon modes to be coupled. Because the correlation matrices essentially provide the density of filled phonon states (G^n) and empty phonon states (G^p), a greater fidelity in the model can be resolved because the phonon distribution no longer relies on the equilibrium Bose-Einstein equation. The following expression is what is required to couple the output from the phonon NEGF to the electron NEGF.

The steady state equation is as follows for the self-energy term of the scattering contacts placed along the device.

$$\begin{aligned}\Gamma_{s,e} = \int_{E_{min}}^{E_{max}} \frac{d(\hbar\omega)}{2\pi} D_{odp,adp}(\hbar\omega)(G_e^n(E-\hbar\omega)G_{ph}^{ab}(\hbar\omega) \\ + G_e^p(E-\hbar\omega)G_{ph}^{em}(\hbar\omega) + D_{odp,adp}(\hbar\omega)(G_e^n(E+\hbar\omega)G_{ph}^{em}(\hbar\omega) \\ + G_e^p(E+\hbar\omega)G_{ph}^{ab}(\hbar\omega))\end{aligned} \tag{2.45}$$

$$\begin{aligned}\Sigma_{s,e}^{in} = \int_{E_{min}}^{E_{max}} \frac{d(\hbar\omega)}{2\pi} D_{odp,adp}(\hbar\omega)(G_e^n(E-\hbar\omega)G_{ph}^{ab}(\hbar\omega) \\ + D_{odp,adp}(\hbar\omega)(G_e^n(E+\hbar\omega)G_{ph}^{em}(\hbar\omega))\end{aligned} \tag{2.46}$$

$$\Sigma^{out}_{s,e} = \int_{E_{min}}^{E_{max}} \frac{d(\hbar\omega)}{2\pi} D_{odp,adp}(\hbar\omega)(G^p_e(E-\hbar\omega)G^{em}_{ph}(\hbar\omega) + D_{odp,adp}(\hbar\omega)(G^p_e(E+\hbar\omega)G^{ab}_{ph}(\hbar\omega)) \tag{2.47}$$

The terms $G^{ab,em}_{ph}$ are collapsed down into a scalar representation of the density of states for each given frequency. The term can be though of as the following expression,

$$N_w \propto \int G^{ab,em}_{ph} dE/2\pi f_s. \tag{2.48}$$

Now the rate depends on the actual density of phonons and not the equilibrium number of phonons for a given phonon frequency.

$$\Gamma_s = (\Sigma^{in}_{s,e} - i(\Sigma^{out}_{s,e} - \Sigma^{in}_{s,e}))/f_s \tag{2.49}$$

The $G^n(E-\hbar\omega)$ terms are determined by shifting the correction matrix by the corresponding phonon energy, $\hbar\omega$, to take the view point of that final state. The translation is carried out for all the terms in Equation 2.46 and Equation 2.47.

The gamma term in Equation 2.45 can be related to the scattering rate by using Equation 2.49. Additionally, the σ term of Equation 2.50 can be related back to the Boltzmann description as the scattering term S^{in}.

$$\Gamma_{s,e} = S^{in}\hbar = \frac{\hbar}{\tau} \tag{2.50}$$

Now that the gamma term is known, the self-energy term can be added to Equation 2.37 as an additional contact. The gamma term is a matrix with scattering rates along the main diagonal, reflecting the scattering along the devices. The gamma term can be related to the self-energy term, sigma, by the following relation,

$$\Sigma_{s,e} = \Gamma_{s,e} f_s. \tag{2.51}$$

Here f_s is the unknown Fermi function of the scattering contact. This term was determined through an iterative method to conserve the energy of the system.

Coupled Model Implementation

By coupling both the electron and phonon models together a system which accounted for the dissipative effects of electron-phonon and phonon-phonon interactions was accounted for. This is a unique approach where the phonon model is solved which accounts for the phonon description and the dissipative phonon description. Because the full dispersion is known that information could be passed to the electron model to allow all the phonon frequencies to be scattered. By tracking all the scattered energy which was scattered with phonons. That energy could be passed back to the phonon model. This coupling and passing of the scattered energy was carried out until a convergence criterion was reached that depended on the temperature of system.

Figure 2.13 is a pseudo code diagram of the two models and the path of interaction between the phonon and electron codes. All of the messages between the two models were handled using a producer consumer message passing model. The passing involved a status file from both the phonon model and electron model that altered the status of available data or ready to receive data. If spatial grid data were being passed between codes, an additional step in formatting the data was required. This additional step was a result of the different grid discretization of the phonon (atomistic) and the electron models (finite volume). In addition to the spatial interpolation, the energy discretization of the two models also had to be interpolated because of the difference in energy ranges. All the interpolation was done by using a Hermite polynomial interpolation for each phonon frequency in the spatially direction, followed by an interpolation in the energy axis, resulting in an overall surface interpolation. It was found that interpolation of the phonon surface (atomistic distance versus energy) to the electron surface (finite volume distance versus energy) was less accurate than the independent interpolation of the spatial coordinates followed by the energy coordinates. The accuracy also went down for extremely small device sizes because the electron (finite volume) mesh only require a few cells which limited the resolution of the phonon description after interpolation. Particular emphasis was taken to conserve energy between the two meshes and to maintain the correct spatial resolution.

Both the electron and phonon NEGF model were written to take advantage of high performance computing techniques. Traditionally, the ballistic model of both the electron and phonon model scale linearly up to sixty processors depending on the size of the energy axis. This was done by allowing each parallel process to take a subsection of the energy range, which does not rely on intermediate messaging,

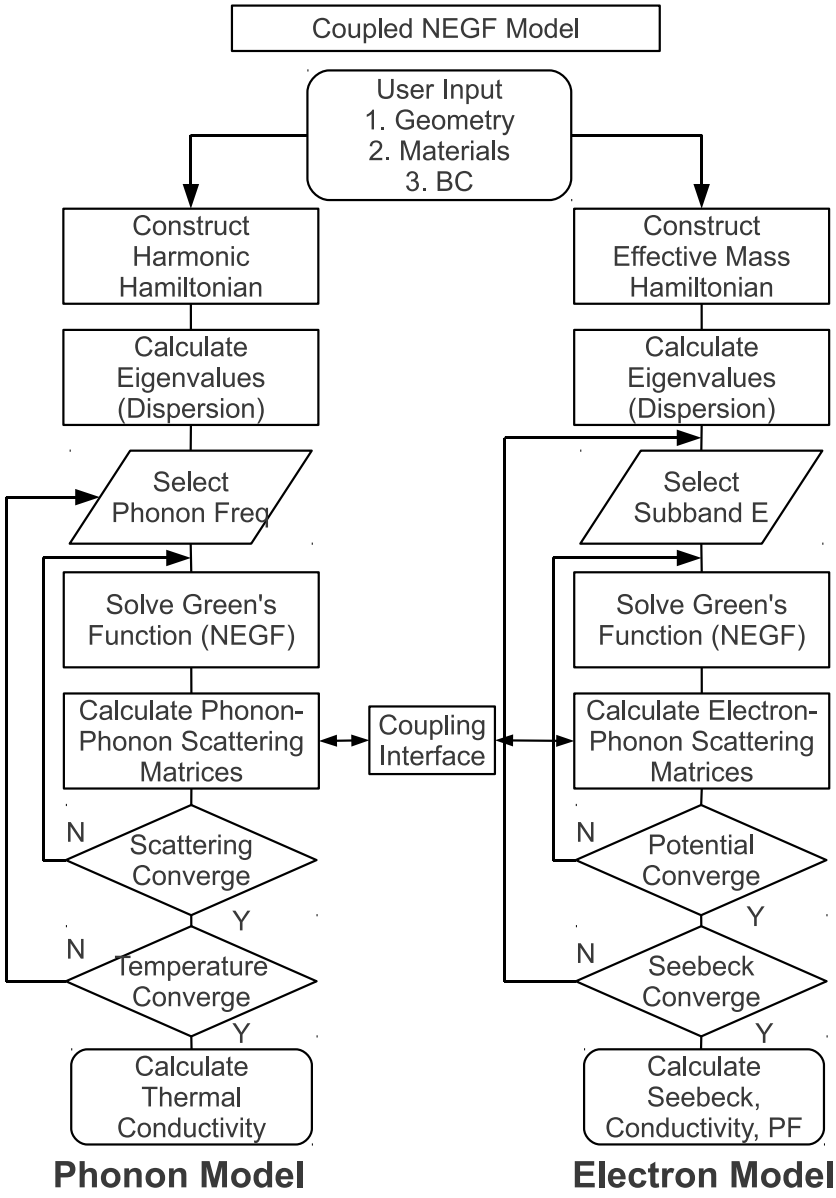

Figure 2.13 Electron and phonon coupled model pseudo code. Models are executed separately and communicate through a message passing coupling interface. The coupling interface is responsible for mesh interpolation between the atomistic phonon model and the effective mass electronic model.

Description	Parameter	Value
Grid spacing	a_n	1 A
Number of energy steps	NE	7201 *steps*
Fermi Energy	E_f	0.1 eV
Effective Density States, Si	Nc_{Si}	2.8e19 cm^{-3}
Effective Density States, Ge	Nc_{Ge}	1.04e19 cm^{-3}
Reference Temperature	T_p	300 K
Temperature Difference	dT	10 K

Table 2.1 NEGF general model parameters. Sources: † - Kittel (1986)

Part	Material	Effective Mass	Relative Permitivity
Mat 1	Silicon $\langle 001 \rangle$	$0.91\mathrm{m}_e$ ††	11.7 †
Mat 2	Germanium $\langle 001 \rangle$	$0.95\mathrm{m}_e$ ††	16.0 ††
Contacts	Silicon $\langle 001 \rangle$	$0.91\mathrm{m}_e$ ††	11.7 †

Table 2.2 Electronic NEGF material parameters. Sources: † - Kittel (1986),†† - Bulusu and Walker (2008a)

but simply the reduction of the current at the end of completion of each subsection. However, when scattering is included in the model, the construction of the scattering matrices after each energy integration proves to be a large bottleneck. The routine that mixes or shifts the states to facilitate the scattering requires more computational effort than a single matrix inversion. Significant time was spent to increase the performance of the scattering matrices shifting by implementing the task in parallel by passing a subsection of the total number of phonons that needs to be scattered to each concurrent process and allowing that processor to shift the matrices accordingly.

The modeling parameters that were used for both the electron and phonon formalism are tabulated in the following tables. Examples of the modeling results will be found in the validation section where all the scattering parameters were varied.

Part	Material	Mass (kg)	Atoms/basis	C_o (J)	d_i (nm)	d_e (nm)
Mat 1	Silicon $\langle 001 \rangle$	$1.69{\cdot}10^{-26}$	2	49.1†	0.543	0.235
Mat 2	Germanium $\langle 001 \rangle$	$4.37{\cdot}10^{-26}$	2	47.5†	0.565	0.244
Contacts	Silicon $\langle 001 \rangle$	$1.69{\cdot}10^{-26}$	2	49.1†	0.543	0.235

Table 2.3 Phonon NEGF material parameters. Sources: † - Harrison (1989)

Part	Material	Acoustic Def. Pot. (eV)	Optical Def. Pot. (eV/m)
Mat 1	Silicon $\langle 001 \rangle$	9.0 †	$0.5{\cdot}10^{10}$ †
Mat 2	Germanium $\langle 001 \rangle$	9.0 †	$0.79{\cdot}10^{10}$ †

Table 2.4 Electronic NEGF scattering material parameters. Sources: † - Jacoboni and Reggiani (1983); Jacoboni et al. (1977)

All the models progress by initially specifying the geometry of interest, and the material and boundary conditions. The geometry is passed to the phonon model through a message passing interface and the phonon execution begins. The message handling relies on the execution of both the electron and phonon model within the same directory, where each model generates message files that describe whether the models are ready to receive or transfer data. The electron model constructs the Hamiltonian and calculates the eigenvalues or subbands and waits for the phonon model to complete. Once the phonon model has calculated the solution, it passes the scattering parameters to the electron code. The coupling relies on the model's communication between files. The scattering calculation was determined to be the limiting process in the execution, preventing the scaling above eight processors.

Thermionic and Field Emission Model

The theory of thermal field emission can be broken up into two sub-categories. Those two categories include thermionic emission and field emission regimes which will be handled separately below. Thermionic emission is the response of electrons due to a thermal bias. Field emission is the response of electrons to a potential bias. Likewise, thermal-field emission is the response to both a thermal and electrical bias. Often in the literature, results of field emission are framed in terms of metal semiconductor interfaces in the context to modern transistor technology. The theory of transistors transport is built from these elementary equations which are related to the emission of electrons from a metal surface into a vacuum. The only added complexity with metal semiconductors interfaces is the addition of space charge effects. This creates a depletion layer that is related to a non-unity relative permittivity in the semiconductor along with a non-unity effective mass in the semiconductor, due to the electrons momentum dynamics changing within the solid.

The theories of both emission regimes, be it thermionic or field emission, are derived from non-equilibrium in the system. Again, similar to the thermoelectric argument framed at the beginning of this chapter, the charge disparity in either contact

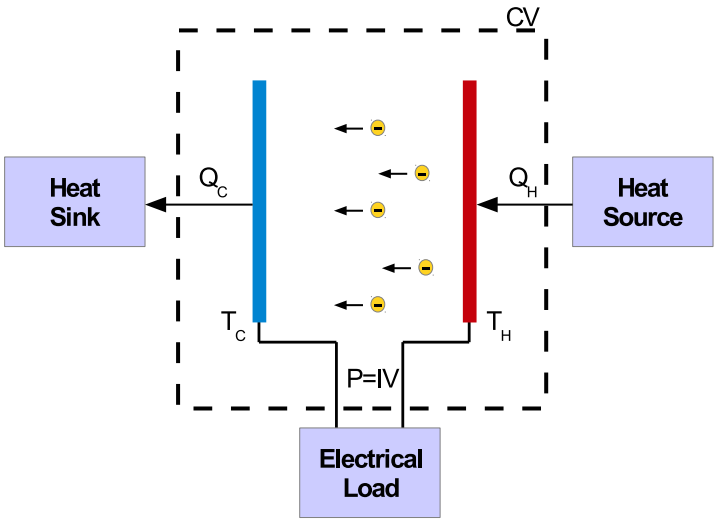

Figure 2.14 Illustration of a thermionic device emitting electrons from the hot cathode. This research assumes the cathode and anode are constant temperature sources. Electrons evaporate from the hot cathode and condense on the cold anode taking a quantized amount of energy proportional to the kinetic energy of the electron.

is a results of the specified temperature at the contacts. Additionally, charge disparity can arrive from the addition of an electrical potential which shifts the distribution of electrons accordingly. This is the notion around thermal-field emitters where the emission characteristic are a function of the non-equilibrium in the system, arriving from both the thermal and electrical boundary conditions. It is the non-equilibrium in the system that drives the transport for which equilibrium is desired.

Commonly, the current of any device will be written as

$$J = e \int_0^\infty N(E,T)D(E)dE, \tag{2.52}$$

where J is the current density, e is the charge of an electron, N is the number of electrons described by the Fermi-Dirac distributions and is a function of energy and temperature, and finally, D is the density of states that is a function of energy. The following expressions for thermionic and field emission are simply a closed formed analytic expression to Equation 2.52, in which assumptions were made in order to make the density of states (D) and number of electrons (N) more tractable. It will be demonstrated that the modeling approach taken in this thesis research relaxes these assumptions previously imposed on the closed formed analytic solutions, providing a

more general treatment of both thermionic and field emission which still follows the expression in Equation 2.52.

Thermionic Emission - Richardson-Dushman Theory

The theory of thermionic emission is based on thermally exciting electrons or commonly referred to as boiling electrons over the barrier (defined by the vacuum level) in order to drive transport imposed by the temperature non-equilibrium in a system. This transport of electrons is collected as a charge, at the anode which can be used to power an electronic device or stored as a potential. Thermionic emission as mention prior in the historical section (Section I), was focused around materials such as tungsten with extremely high melting temperatures. These metals could be operated at higher efficiencies because of their high operating temperatures although they had large work function values. Much of the research focused on characterizing the transmission from metal and is ultimately from where the Richard-Dushman theory is derived. Equation 2.53 is the Richardson-Dushman equation,

$$J = AT^2 \exp \frac{-\phi}{k_B T}, \tag{2.53}$$

where J is the current density, A is a fundamental pre-factor which has a value of $120\,\mathrm{Jcm^{-2}K^{-2}}$), T is the cathode emission temperature, and ϕ is the associated work function of the cathode. This equation is often referenced in the literature as Richardson's equation and will be commonly re-written in a linear fashion described by Equation 2.54.

$$ln(\frac{J}{T^2}) = ln(A) - \frac{-\phi}{k_B T} \tag{2.54}$$

It will be shown below that the use of Equation 2.54 to describe the emission from semiconductor materials such as diamond is still approximate, however, this equation should be used with caution at the onset of thermionic emission, where Richardson's equation overestimates the emission current.

The derivation of Richardson's equation is formulated in the literature (Richardson, 1916; Modinos, 1984), where the thermionic theory is founded on a quantum mechanical description of emission of electrons at high temperature from surface states. The use of Green's functions to solve for the transmission in the present work is very similar to the analytic approach taken by Murphy and Good (1956), except the treatment in this research is more general and more rigorous to allow complex structures and materials to be studied.

In thermionic devices the transport of electrons within the device is driven by the equilibrium distribution of charges across the system. In the case of thermionics, the non-equilibrium that drives the electrons between two similar materials separated by a interelectrode vacuum region is a temperature bias across the system. The constant pursuit of the system to reach equilibrium is facilitated by electrons emitting from the cathode region (heat source) to the anode region (heat sink). In a closed loop configuration, the collected charge on the anode can be used as potential energy to operate a load. This same principal of equilibrium is still applied when two dissimilar materials comprise the system. However, the difference in chemical potentials between the two materials provides additional non-equilibrium which can either aid or hinder the desired transport.

As illustrated in Figure 2.14, this analysis assumes the cathode is in contact with a constant temperature heat source and the anode is in contact with a constant temperature heat sink. Additionally, for this analysis the difference in Fermi levels is compensated such that there is no internal voltage drop which arises from using two dissimilar materials for the anode and cathode. The disparity in charge population that governs the non-equilibrium in the system increasing as a function of $k_B T$ when the cathode temperature increases. More specifically, the charge distribution in the anode and cathode regions can be described as a function of temperature by a Fermi-Dirac distribution. Thus, to increase the emission characteristics, the system must be driven further from equilibrium by increasing the temperature of the cathode region. The expression which demonstrates the dependence of current on temperature is as follows,

$$I(T, E) \propto \int f(T) D(E) dE. \tag{2.55}$$

This expression states that the total current is proportional the equilibrium distribution of charge described by the Fermi-Dirac term $f(T)$ times the density of states $D(E)$. This statement can be used to describe the electrical current in a metallic or semiconductor material and even insulator materials. However, care must be taken when describing the density of states especially in the case of a semiconductor and insulator material.

There are two aspects that must be accounted for in describing the density of states of a semiconductor. The first aspect is the effective mass description which relates the momentum of electrons to the kinetic energy within a solid based on free particle dynamics. The second aspect is the confinement of states which can alter

the low lying density of states due to symmetrical degeneracies. Focusing on the first aspect, depending on the crystallographic direction, the density of states along the transport direction can change considerably. The density of states of a Fermi gas can be equated to the change in energy over the change in momentum as described in the following expression,

$$g(E) = \frac{dE}{dk}. \tag{2.56}$$

The energy expression in the numerator of Equation 2.56 can be related to the electron mass through a particle in a box expression that assumes a parabolic description as shown in the following manner,

$$E = \frac{\hbar^2}{2m^*}(k_x^2 + k_y^2 + k_z^2) = \frac{\hbar^2|k|^2}{2m^*}, \tag{2.57}$$

where m^* is the effective mass. It should be noted that the effective mass description is simply a mathematical adaptation of free particle theory modified to predict the behavior of an electron in a solid. Because crystallographic solids have different lattice vectors and bonding states in different crystallographic directions, the effective mass is directionally dependent.

An expression for the density of states can be developed through manipulation of the previous two expression resulting in the following expression,

$$g(E) = \frac{1}{2\pi}\left(\frac{2m^*}{\hbar}\right)^{3/2}\sqrt{E}, \tag{2.58}$$

for a bulk solid.

Equation 2.58 demonstrates that given an effective mass of a material, the density of states will be influenced and ultimately the emission characteristics described by Equation 2.55 will be altered. Assuming that an non-localized electron inside a metallic material can be approximated by the free electron dynamics and a free-electron inside a semiconductor has an effective mass less than one, the density of states for the metal can be assumed to be greater resulting in a larger current than a semiconductor. This expression in Equation 2.58 is a classical distribution of a three dimensional solid.

The second aspect that effects the density of states is the confinement. The confinement of states forms degeneracies in the density of states resulting in increased low lying states. This is especially important in nanoscale device such as thin films and nanotips where electrons are confined in one or more directions. Due to this

confinement effect the density of states is modified from the expression derived above in Equation 2.58. More specifically, the confinement of states can aid in the number of low lying energy states resulting in increased emission characteristics not captured in the bulk density of states expressions.

The theory used to derive Richardson's equation is formulated from a statistical thermodynamics view point of electrons and is dependent on a similar expression outlined in Equation 2.55. Richardson related the emission current from a flux of particles through a differential area to the number of particles times the velocity normal to the surface. The velocity of these particles is related to the change in energy over the change in momentum. In describing the momentum he relied on a Maxwellian distribution of velocities. In making this assumption the density of states is forced to be continuous and originate at the equilibrium Fermi energy. Simplification of the physics by Richardson to describe the emission of electrons from a metallic surface resulted in a few underlying assumptions imposed on the formalism. The major underlying assumption is that the electron within the metallic emitter can be described as a bulk degenerate electron gas. In order to make this assumption a Boltzmann distribution replaced the Fermi-Dirac distribution to describe the equilibrium distribution of electrons within the solid. In association with the electron distribution, the density of states was restricted to a continuous distribution. Ultimately, as a result, Richardson's theory is restricted to high temperatures between 1000K and 2000K where the Boltzmann approximation is valid. A categorical list of assumption in Richardson's theory is presented by Seitz (1940) along with a detailed derivation which was beyond the scope of this work.

$$n_o = \frac{2(2\pi m k_B T)^{3/2}}{h^3} \exp\left(\frac{-E_f}{k_B T}\right) \tag{2.59}$$

Richardson theory can be derived from a more fundamental view point by starting with Equation 2.60. This equation is determined from a Maxwellian velocity distribution which describes required velocity normal to the surface an electron must have to escape from the surface. Here n_o is the number of electrons per unit volume. If this term is described with a classical distribution as in Equation 2.59 the overall equation that describes the emission current will simplify to the same expression Richardson determined, Equation 2.53.

$$J = q n_o \sqrt{\frac{k_B T}{2\pi m^*}} \exp\frac{-\phi}{k_B T} \tag{2.60}$$

The term n_o can be framed outside of the classical statistic regime by using the density of states expression from Equation 2.58 and the Fermi-Dirac distribution as seen in the following equation,

$$\begin{aligned} n_o = \frac{N}{V} &= \int g(E) f(T,E) dE \\ &= \int \frac{1}{2\pi} \left(\frac{2m^*}{\hbar} \right)^{3/2} \sqrt{E} \frac{1}{1 + \exp\left(\frac{-(E-E_f)}{k_B T} \right)} dE. \end{aligned} \tag{2.61}$$

Here $g(E)$ is the density of states and $f(E,T)$ is the Fermi-Dirac term which are both functions of energy. Unfortunately, it is difficult to analytically integrate this term and the density of states is often complex and geometric dependent as described above. It is important to point out that the pre-exponential terms of Equation 2.60 comprise the Richardson constant term. One would expect from the expression in Equation 2.61 that Richardson's constant is a function of the spectral landscape of the density of states but also temperature. Equation 2.62 demonstrates the dependence of Richardson's constant on temperature and energy. This expression will come in useful in the result section where the model developed in this research explicitly calculates the emission from a similar view point.

$$A_{Fermi}(T,E) \propto \sqrt{\frac{k_B}{2\pi m^*}} \int g(E) f(T,E) dE. \tag{2.62}$$

The simplification of Richardson's theory through classical derivations provides reason for a more rigorous treatment of the physics to correctly predict the emission trends from semiconductor materials. Especially, in the case of wide-band gap semiconductors which have a drastically different density of states from a metallic material. Additionally, because the density of states is shifted the low lying energy levels now lie at a energy which needs to be described more accurately through a Fermi-Dirac distribution. The model developed this work is based on Fermi-Dirac statistics and the calculation of the approximate density of states derived from a discretized effective mass domain.

Field Emission - Fowler-Nordheim Theory

Similar to the thermionic emission equation, the equation which describes the emission of electrons from metal surfaces in response to electric fields has also been examined extensively. The Fowler-Nordheim Theory (FN) is a quantum mechanical

description which relies on the tunneling of electrons through a potential barrier that is lowered by the applied electric field. The equation that describes the emission of electrons from a metal in response to an applied field is shown in Equation 2.63.

$$J = \frac{K_1 \beta^2 E^2}{\phi} \exp \frac{K_2 \phi^{3/2}}{\beta E} \tag{2.63}$$

Here, $K_1 = 1.541434 \times 10^{-6} AeVV^{-2}$ and $K_2 = 6.830888 \times 10^{-9} eV^{-3/2} Vm^{-1}$ are constants, ϕ is the work function, E is the electric field, A is the area, I is the current, and β is a geometric enhancement factor. The FN curve is a relationship that was derived to describe the emission performance of metal field emitters. The standard physical assumption to the Fowler-Nordhiem equation can be found in several cited references (Forbes, 2001). These assumptions, however, have not shown to capture the emission of nanoscale field emission, which is of interest in this research.

Similar to the Richardson equation, the Fowler-Nordheim expression can be linearized. Again, the slope depends on the work function values of the cathode. The beta term is responsible for the field enhancement increase of the field due to the geometry of the cathode. In the results section, the beta enhancement will account for nano-tip emitters, where the beta term can be on the order of several thousands.

$$ln(\frac{J}{E^2}) = ln(\frac{K_1 \beta^2}{\phi}) - \frac{K_2 \phi^{3/2}}{\beta E} \tag{2.64}$$

NEGF Thermal-Field Emission Model

The adaptation of NEGF used from previous microelectronic research (Bulusu and Walker, 2007a; Musho and Walker, 2011b) of nanoscale thermoelectric materials was readily straight forward. The NEGF method in the context of electronic transport is a self-consistent field (SCF) approach, in which Schrödinger's equation and Poisson's equation are solved self-consistently. Schrödinger's equation solves the electron spatial probabilities, while Poisson's equation maintains the many electron interaction. Care has been taken to use an Anderson mixing technique as opposed to a simple mixing technique to reach a less computational intensive convergence. The NEGF electric ballistic modeling developed the study of thermoelectrics, which was described extensively at the beginning of this chapter, is where the modeling approach here was derived.

Modifications have been made to the NEGF model to allow field emission devices to be studied. The first modification from microelectric bilayer device models

is the addition of a third material, which captures the effects of the vacuum region. Second, the conduction band of the diamond was determined based on the reference of the Fermi level ($0.1eV$) and the vacuum level with the associated work function for each material. Additionally, the copper conduction band was determined from the work function and vacuum level. The reverse bias which is apparent when the copper anode and diamond cathode are connected is assumed offset by an applied voltage so that the results can be compared to experimental values in which this same offset voltage was applied.

The transport in thermionic emitters is very similar in context to solid-state dynamics of electrons and can be described by non-equilibrium thermodynamics. The modeling approach developed in this research relies on the theory of non-equilibrium statistics in which a charge disparity between the cathode and anode regions drives the transport. The model developed predicts the emission characteristics due to the temperature response of a diamond thin film emitter. The model developed is a rigorous approach to calculating thermionic emission from semiconductor material by taking key material aspects into account such as the density of states of the wide-band gap material.

The motivation for using a NEGF method stems from the ability to calculate electronic transport from a quantum description through self-energy contacts. The model assumes the electron transport is ballistic in nature and accounts for the effects of the semi-infinite contacts through broadening terms at either contact.

The Green's function approach to solving Schrödinger's equation provide an elegant method of including potential responses along the device from electron-electron scattering and the addition of impulse responses from the contacts. The fully constructed Green's function provides a means of determining the transmission probability from a single electron view point. The culmination of many single electron solutions provides a general view of the transport. More precisely, once transmission is known for a discretized range of levels, the Landauer formula can be implemented to determine the overall current. The Landauer formula states that the transmission for the single electron model can be integrated over a range of electron energies to arrive at the overall current of a system. This approach assumes that each energy level has a finite current-carrying capacity, even when the transport is assumed ballistic. The current-carrying capacity is defined by the quantum conductance, $2e^2/h$. The quantum conductance is a fundamental constant commonly found in quantized nanoscale transport and has applicability for confined structures such as thin films. Additionally, the Landauer approach can be applied to bulk structures as long as the

number of discretized energy levels which is integrated over is substantial such that the energy levels become continuous in nature over the integration range.

The Landauer formula can be written in a general integral form of Equation 2.5 where Ξ is the transmission and the applied voltage and temperature difference at the anode and cathode are accounted for in the Fermi-Dirac terms f_1 and f_2. The total current is I_{tot} which is integrated for each energy level.

Before the Green's function can be solved the model first constructs an effective mass Hamiltonian describing the band structure and conduction band edges. When constructing the Hamiltonian matrix, it is necessary to make sure that the matrix is Hermitian in order to obtain real eigenvalues. The interface between materials is a mixed effective mass grid point and the hermicity is critical at this intersection. The equation for formulating the Hamiltonian is as follows,

$$[E_c - \frac{\hbar^2}{2m_c^\star}\nabla^2\Psi = E\Psi]. \tag{2.65}$$

The total Green's function is assembled through a composite manner where broadening effect from the device contacts and the device channel is coupled together. The boundary condition at either contact are specified with a Fermi function at a prescribed temperature, applied bias, and in-scattering or broadening term. The remaining two boundaries on the lateral sides of the two dimensional domain are assumed periodic and are handled through reflective boundary terms in the matrix. A full Poisson equation inversion was solved due to importance of resolving how the potential varied within the system.

The total Green's function takes the form of Equation 2.66 which accounts for the impulse response of the contacts and the response of the many-electron effect determined from the self-consistent calculation. The term E is the energy of the selected single electron energy level multiplied times the identity matrix I. The Hamiltonian described above is contained within the H term followed by the spatial impulse response of the electron-electron interaction which is described by the term U_e. The remaining Σ terms correspond to each of the two semi-infinite contacts of the cathode and anode region.

$$G = [EI - H - U_e - \Sigma_1 - \Sigma_2]^{-1} \tag{2.66}$$

The Green's function is solved for each discretized energy level by a matrix inversion operation. The current is integrated for each energy level using Landaur's formula. On top of solving the Green's function for each energy level, the total

energy integration is carried out for a threshold number of sub-bands. The sub-band energy is specified in the contact terms Σ and is governed by the eigenvalues of the unperturbed Hamiltonian prior to constructing the Green's function.

Along with integrating the current for each energy level the integrated spatial electron density was also calculated by the following expression,

$$\rho = \int G^n dE/2\pi, \tag{2.67}$$

where G^n is the spatial density of occupied states. The spatial density of charge is calculated from the overall density of states G^d, where $G^d = G^n + G^p$. The term G^p is the spatial density of unoccupied states. The spectral function G^d is the difference in advancing and retarding Green's functions, $G^d = i[G - G^+]$. In depth derivation of these spectral function can be found in the literature Datta (2005) and is beyond the scope of this article. Ultimately, the density of electrons ρ can then be used in Poisson's equation to determined the potential response U_e which accounts for the interaction of many electrons.

The band structure described by the Hamiltonian where a copper material comprises the anode and a diamond material comprises the cathode with the vacuum region in between. Particular emphasis is taken in describing the band structure of the emitter (crystalline diamond material). The internal voltage drop associated with two dissimilar materials as the anode and cathode ($\Phi_a - \Phi_c$) was assumed offset such that the difference is zero. This was imposed to compare the model results to experimental results.

The construction of the band structure began with the anode material by specifying a reference Fermi-level of 0.1 eV and assuming the conduction band lies at that same energy level. The anode material was assumed copper with a tabulated work function (Φ_a) of approximately 4.5 eV. The vacuum level, which is a static reference level across the entire material was defined by the following, $E_{vac} = E_{fa} + \Phi_a$. Within the vacuum region the conduction band was assumed to lie at the system vacuum level. The Fermi-level of the cathode is referenced from the static vacuum level using the specified work function of the cathode (Φ_c), $E_{fc} = E_{vac} - \Phi_c$. The work function of the cathode, Φ_c, was the primary independent variable of these studies. The conduction band edge of the cathode (E_c) was specified from the cathode Fermi-level using a difference in electron affinity and work function, $E_{ca} = \Phi_c - \chi$. The difference in electron affinity and work function inside the cathode was held at 0.65 eV. The open circuit voltage is offset such that in the closed circuit configuration

the bands are horizontal.

Because the cathode material of interest in this research is a semiconductor material, the electron dynamics within the cathode region required an effective mass description. An average effective mass was specified to be $0.54m_e$ which was assumed typical of diamond material Nava et al. (1980). Since the remaining regions were assumed to rely on free electron dynamics the effective mass was unity.

An important aspect of electron emission is the band bending at the semiconductor vacuum interface. To account for this in the model a relative permittivity was specified for the cathode region. The band bending due to space charge effects was calculated self-consistently with the calculation of Poisson's equation. The relative permittivity of the vacuum and anode regions were assumed unity to impose the space charge effects of free space.

In addition to assembling the Hamiltonian, a spatially varying dielectric field is constructed that is described by the permitivity of the emitter and collector. The Hamiltonian description is used in the Green's function to calculate the space charge effects, while the permitivity is used in Poisson's equation to calculate the potential. Lastly, the Green's function is assembled through a composite manner where broadening effect from the device contacts and the device channel are coupled together. The boundary condition at either contact are specified with a Fermi function at a prescribed temperature, applied bias, and in-scattering or broadening term. The remaining two boundaries on the lateral sides of the domain are assumed periodic and are handled through reflective boundary terms in the matrix. A full Poisson equation inversion was solved due to the importance of resolving the potential within the system and the fact that the potential does not vary smoothly over the length of the device. The material parameters specified can be found in the following table.

The current voltage characteristics were determined by specifying a voltage bias between the emitter and collector and calculating the corresponding current transmission. The code calculates the transmission for a range of electron energies at a given sub-band energy. One can think of this as solving an elementary quantum barrier structure for a range of electron energies and barrier heights, with the added complexities of a two dimensional wave equation and a more complicated geometry. The integral of these transmission probabilities multiplied by the difference in Fermi functions at either contact times the quantum conductance determines the current through the device. This approach of calculating the one electron ballistic current is often referred to as the Landauer formalism, see Equation 2.5.

To determine the current versus temperature characteristics, the exact same

procedure as outlined in the previous paragraph is used, except the Fermi function of either contact is held at a zero voltage bias and the temperature (k_BT) of the cathode is increased. The integrated current is calculated and the temperature is increased again by a specified amount which is governed by the user, as well as specified temperature range and number of temperature steps. Poisson's equation is still solved to account for the many-electron effect, and number of sub-bands integrated over is based on a current threshold. The current criterion is determined by calculating the contribution of current to the total current from additional sub-bands.

Thermal-Field Emission Model Implementation

The model which was developed to capture the emission is based on a two-dimensional wave equation. The implementation is very similar to the thermionic implementation. The work function of both the anode and cathode is required. Additionally, the effective mass is required. If the material is metallic it is assumed that the electrons will follow free electron dynamics so the effective mass is assumed unity. Additionally, the permitivity of the cathode and anode was required. Again, the permitivity in the metallic regions are assumed to have a permitivity of free space along as is similar in the vacuum region.

The code is implemented by the user providing the geometry and temperature and voltage boundary condition. The mesh is assembled within the code using a two dimensional structured mesh with variable size. The size depends on the Hamiltonian condition for the range of energy. Care was taken to write the Hamiltonian such that the minimum number of cells were required.

One of the limiting cases in the thermal-field model is the inversion of the matrix for each energy level. The routine for the inversion use a LU factorization. Initially, the code implemented a full matrix complex inversion using LAPACK routines but it was determined to be too slow. The two dimensional Hamiltonian is a banded matrix with a tri-diagonal and a single off-diagonal term. A sparse LU decomposition was used to speed up the inversion routine. There as about a three time speed up with the sparse solver. Furthermore, to increase the throughput of the model the LU factorization routines were implemented on GPU architecture using the MAGMA full matrix LU factorization routines. This proved to have a increase of three to four times over the standard full matrix LAPACK LU factorization. It was determined that the use of a sparse LU factorization on a GPU would be most advantageous once those routines become available.

Part	Material	Effective Mass	Relative Permitivity	Work function (eV)
Cathode	Diamond	$0.54m_e$	5.5 †	2.2-4.6 ††
-	Vacuum (UHV)	m_e	1	-
Anode	Copper	m_e	1	5.4 †††

Table 2.5 Thermal-field NEGF model parameters. Work function values are referenced from a Fermi level of 0.1eV. (Sources: † - Kittel (1986), †† - Robertson (1999), † † † - Lide (2007))

The table above outlines the material parameters used in the modeling of the thermal-field emitters. Note that the anode is assumed copper and there is no effort to discern to which crystallographic direction the anode or cathode is emitting.

CHAPTER III

VALIDATION

To determine whether the models were calculating reasonable results, both the electron NEGF and phonon NEGF models were independently validated and verified with empirical equations, ballistic results and available literature values. Therefore both the electron and phonon models were validated and verified to gain confidence that the models would correctly predict intermediate values when exploring the design space of thermoelectrics and vacuum devices.

The validation will begin with thermoelectrics, both the thermal and electrical models will be investigated independently and finally together. For this validation silicon and germanium are the two materials of interest due to their well characterized dynamics and availability of literature values. On top of the availability of data on silicon and germanium, they have been demonstrated as decent high temperature thermoelectric materials with an alloy ZT of 1.0 (see Introduction Section). There are additional advantages to selecting silicon and germanium as thermoelectric materials due to their similar crystallographic nature and their moderate Seebeck coefficient. Other materials are within the scope of this model; however, dominant scattering mechanisms must be understood and accounted for in order to gain confidence that the trends are correct. As a side note, materials which are binary and ternary type materials have significant polar optical scattering which is not accounted for in the model and would require additional modification to the scattering parameters.

Similar to the thermoelectric electronic and thermal models the thermionic model developed was validated and verified against Richardson's equation and experimental values provided from a collaborator. The material of interest was a diamond single crystal nitrogen incorporated material.

The last part of this section will explain how all the models were written to take advantage of high performance computing facilities. The objective was to write these models such that larger devices were feasible and the design space could be explored. The thermal model has the potential to model devices upwards of microns in size where the electron size can scale devices on the order of 200 microns.

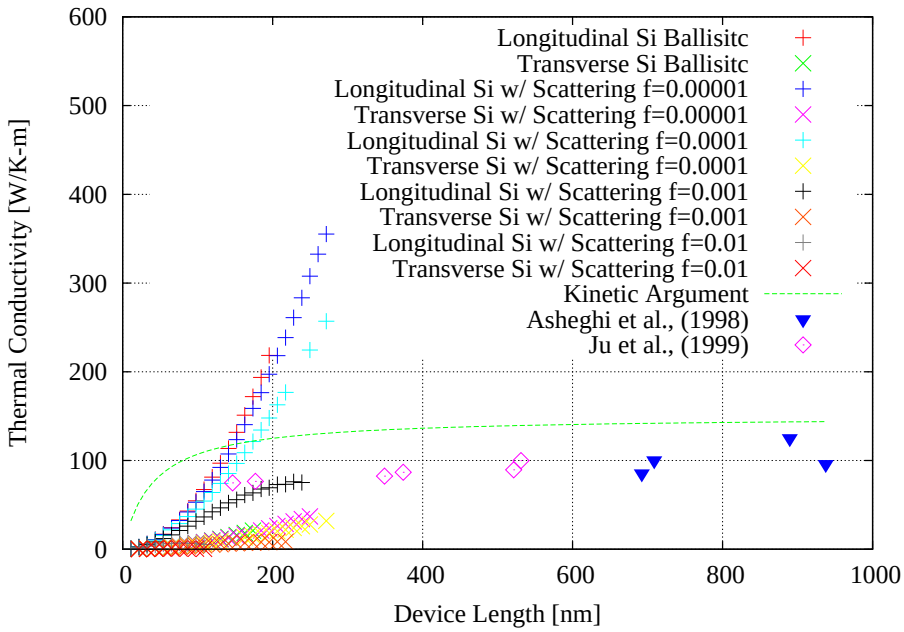

Figure 3.1 Plot of the thermal conductivity versus length for ballistic simulation, phonon-phonon scattering, and literature values. The temperature is maintained at 300K and the material is homogeneous silicon $\langle 001 \rangle$ doped at 10^{18}cm^{-3}.

Dissipative Thermal Quantum Model Validation

To determine if the phonon scattering was operating correctly, a study to calculate the thermal conductivity versus length was carried out for homogeneous silicon material. Both the longitudinal and transverse directions were taken into account. Figure 3.1 is a plot of the ballistic case, phonon-phonon scattering case with varying anharmonic parameter, and experimental values found in the literature.

Homogeneous Silicon - Thermal Conductivity

As mentioned in the discussion, the phonon model relies on selecting a correct anharmonic scattering parameter, (f_o), which relates the incoming amplitude to the scattered amplitude of a phonon. By increasing this factor, the strength of the scattering increases and the thermal conductivity decreases. From Figure 3.1 the anharmonic scattering parameter is determined to be of the order of 10^{-5} to obtain values approximately on the order of the experimental thermal conductivity values. As mentioned in the discussion section, a harmonic description is used to describe the oscillators in the unperturbed Hamiltonian and the anharmonicity which is required for the scattering is added to the system through the scattering parameter and the

self-consistent scattering contacts which lie along the device. In essence, by adjusting the scattering factor, the magnitude of the anharmonicity of the system is increased or decreased thus influencing the rate of scattering and ultimately driving the thermal conductivity up or down.

In reference to Figure 3.1, if the scattering parameter is selected to be $5 \cdot 10^{-5}$, then as the device increases in length, the trends begin to match the experimental values. At larger device sizes, above 400 nm, it is assumed that the trends would level off. The maximum device size which is calculated is limited by current computational resources. In comparison to the ballistic phonon model, as the device length surpasses 100 nm the ballistic and dissipative model diverge due to the increase influence of the phonon-phonon interaction.

When the device length is below 200 nm confinement in the transport direction becomes relevant and an analogy with low temperatures can be made as for the curvature of the thermal conductivity at small device lengths. Additionally, the kinetic argument (dotted line in Figure 3.1), which relies on a particle-based argument where the boundary scattering dominates the scattering rate at small device lengths, severely overestimates the thermal conductivity at device lengths below 200 nm. The particle-based theory is the essence for developing a model which can capture the transport at small device lengths.

Figure 3.1 demonstrates that the ballistic phonon model is only valid up to approximately 50 nm. Above 50 nm the ballistic model overestimates the thermal conductivity. At 200 nm the ballistic model is approximately 1.5 times greater than the bulk value. This provides an argument for developing a scattering model which can capture the intermediate ballistic bulk trends.

Si/Ge Superlattice Phonon Material - Thermal Conductivity

To illustrate the spatial scattering of the phonon model, a superlattice device was investigated. Figure 3.2 is a plot of the phonon scattering rate for a 30 nm four bilayer Si/Ge superlattice device. The right portion of the figure is the associated transmission for both the ballistic and scattering cases. The scattering rate changes as a function of the material composition within the device, noted by the change in scattering rate (color) in the left portion of Figure 3.2. The spatial variation of the scattering rate gives rise to non-equilibrium within the system. This non-equilibrium is traditionally not captured when one assumes a single scattering rate across the device. Passing the spatial scattering rate at each location along the device to the

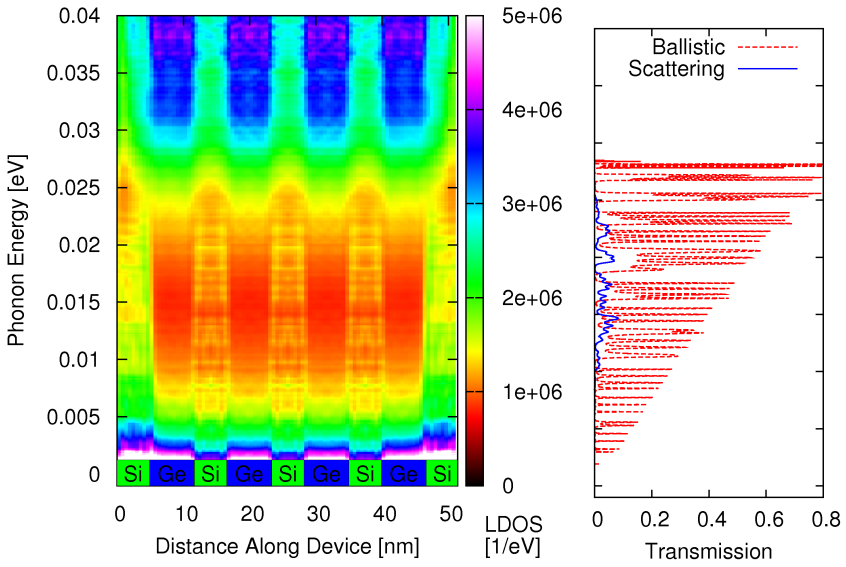

Figure 3.2 Contour plot of the phonon scattering rate as a function of spatial location along device. To the right is the associated transmission for the ballistic case and the scattering case. The device is a 30 nm superlattice device with four bilayers of Si/Ge and a silicon end cap.

electron model provides an argument for localized Seebeck voltage between layers which can influence the thermoelectric performance of the material.

The plot of the transmission in right part of Figure 3.2 demonstrates the difference in the ballistic and scattering model. The ballistic model has sharp peaks of transmission while the scattering model tends to dampen the response. The scattering model also decreases the transmission at low frequencies attributed to the acoustic modes. The acoustic modes are traveling waves which are the dominant carrier of thermal energy. As the device length increases the number of acoustic modes increases due to the addition of lower frequencies permitted between boundaries. In Figure 3.1 the ballistic model overestimated the thermal conductivity above 50 nm because of the large or non-zero transmission of acoustic thermal energy carrying phonons. While the scattering model diminishes the transmission of the acoustic phonons due to acoustic phonon-phonon interactions, this in turn limits the thermal conductivity and why in Figure 3.1 the thermal conductivity of the scattering model plateaus. As the anharmonic parameter is increase the transmission probability of Figure 3.2 would decrease for the scattering model and ultimately, as is shown in Figure 3.1, the thermal conductivity would decrease.

This model does well at calculating the room-temperature (300K) dynamics where the scattering is dominated by phonon-phonon interactions. However, the model lacks knowlege of impurity scattering which is the dominate mechanism at low temperatures.

Dissipative Electrical Quantum Model Validation

To validate and verify the operation of the ballistic, single and multiple electron-phonon NEGF model, the results from the independent electron NEGF model were studied in a similar fashion to the phonon study above. The electron model was validated by comparing current-voltage characteristics of homogeneous material to available literature along with the comparison of thermoelectric figures such as Seebeck coefficient and conductivity. Finally, a sample of superlattice devices found in the literature were modeled to validate thermoelectric quantities. These validation were strictly limited to n-type materials which were phosphor doped. This is not to say that p-type material cannot be modeled.

Homogeneous Silicon - Seebeck, Conductivity

A homogeneous silicon sample of 30 nm was modeled using just the electron NEGF model with three methods which include, ballistic, single phonon and, multiple phonon interaction. The doping density was varied from 10^{17} cm^{-3} to 10^{21} cm^{-3}. The crystallographic direction was $\langle 001 \rangle$ direction, temperature was held at 300 K and the remaining modeling parameters are outlined in Table **??**.

Figure 3.3 is a plot of the Seebeck coefficient and the electrical conductivity versus doping density. The lines in both figures outline the Boltzmann approximation which is a particle-based theory and depends on specifying a known scattering rate. The circles in Figure 3.3 are literature values (Geballe and Hull, 1955; Morin, 1954) of single crystal (bulk length) homogeneous thermoelectric properties. The plot of the Seebeck demonstrates that the NEGF model can capture the bulk trends especially at high doping density. The Boltzmann approximation is linear, described by Equation 3.1, and requires the user to know the scattering rate (τ_{RTA}) in order to match the experimental data. The Boltzmann approximation also is not able to handle the the high doping concentration. Ultimately, Figure 3.3 demonstrates that the NEGF model is an appropriate model to recover the trends and does not require the scattering rate to be known before the simulation as shown for the particle based Boltzmann approach.

$$S = k_B(5/2 + \nu_{RTA} - ln(N_d/N_c)) \tag{3.1}$$

The same comparison can be made for the second plot of Figure 3.3 which is a plot of the electrical conductivity versus doping concentration. The line represents in Figure 3.3 described the particle based theory described by the relation in Equation 3.2. Equation 3.2 requires that a scattering rate, τ_{RTA} is known prior to calculating the transport which is based on a relaxation time approximation. The figure demonstrates that the multiple phonon model does the best at predicting the electrical conductivity. The ballistic and single phonon models both over estimate the electrical conductivity which would ultimately exaggerate the ZT values. There is a key scattering mechanism which is not captured in the model which could explain the slight over estimation of all the NEGF models and that reason is the model does not capture the effects of impurity scattering. The substitution dopant atoms (phosphorous) are related to the impurity scattering which is lacking in the NEGF model and would be expected to lower the conductivity.

In Figure 3.3 the ballistic case is greatest as expected, followed by the single phonon frequency and then the multiple phonon frequency, which has the lowest conductivity. Noted from the figure, the single phonon frequency underestimates the actual scattering given by the experimental values. Researchers often use a single phonon frequency scattering model and increase the deformation potential until desired results are reached. In foresight, this may obtain correct magnitude of the scattering; it is suggested that the accuracy of the transport trends are lost as the scattering is artificially increased from the deformation potential. A more physical approach demonstrated in this figure is to take into account the phonon frequencies of the structure through a superposition of scattering rates. Because there are multiple phonon frequencies more electron transitions can be facilitated.

$$\sigma = \frac{q\tau_{RTA}N_d}{m^*} \tag{3.2}$$

Another study of homogeneous silicon was to investigate the thermoelectric properties as a function of length of the device, see Figure 3.4. The model parameters used, such as effective mass are the same as above and are outline in Table **??**. For this study the multiple phonon NEGF model was the only model investigated based on the justification of Figure 3.3. Figure 3.4 demonstrates that as the device length increases the Seebeck coefficient is decreased slightly with increasing length. Where the electrical increases significantly below 20 nm and then begins to plateau as

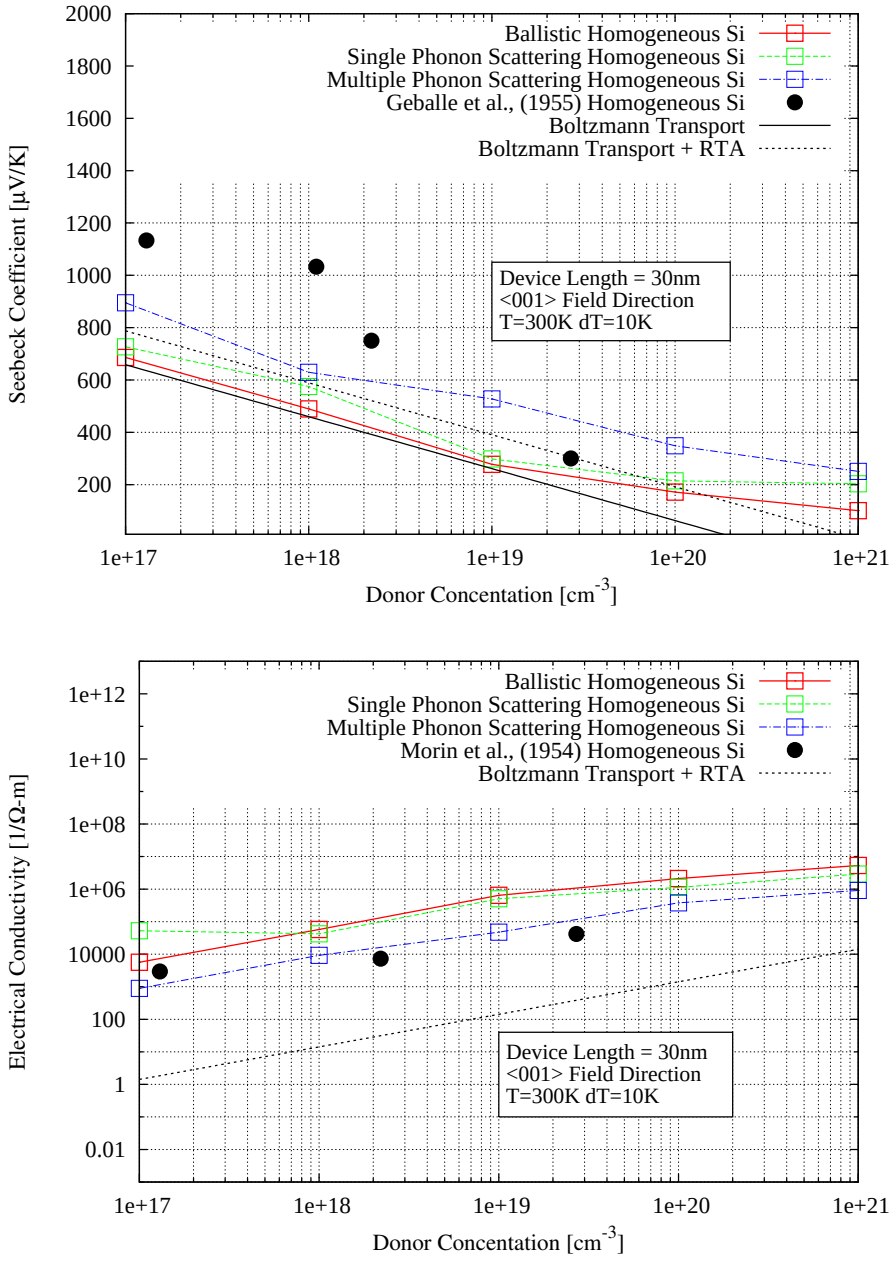

Figure 3.3 Homogeneous silicon Seebeck coefficient and conductivity versus doping density for ballistic, single phonon, and multiple phonon scattering NEGF model. The temperature is maintained at 300K. Line represent Boltzmann model with relaxation time approximation (RTA) and dots are associated experimental values.(Geballe and Hull, 1955; Morin, 1954)

the device length increases. This suggests that boundary scattering at the contacts dominates the transport to device lengths over 60 nm. Again the effects of impurity scattering are missing from the NEGF model which would become effective at higher dopant concentration and lengths above 30 nm. The increasing electrical conductivity can also be explained by the confinement of states and the introduction of additional states as the device length increases. Because the quantum simulation is based on discrete states and as the device increases all dimensions the states will become more continuous and the states as a whole will look continuous.

Taking the analysis a step further from Figure 3.4 and using the model to calculate the electrical contribution to the thermal conductivity (k_e). The model initially calculates k_e from determining the electron flux with a temperature specified at either contact. If there is a difference in temperature between the contacts then a current is generated and it is this current that is electrical contribution to the thermal conductivity. Recalling from the figure of merit equation, $ZT = S^2\sigma T/(k_e + k_p)$, the reason why homogeneous silicon does not make a good thermoelectric is because the denominator is rather large corresponding to low ZT values. Figure 3.5 demonstrates this argument by providing k_e values versus length. For reference the lattice thermal conductivity (k_p) for bulk homogeneous silicon is approximately $145\,\mathrm{W/m-K}$.

Homogeneous Silicon - Mobility, Drift

The electronic code was written so that the current voltage characteristic could be determined for a given thermoelectric material. The IV characteristics were carried out for a homogeneous silicon material in the $\langle 001 \rangle$ direction at a doping density of 10^{13} cm^{-3} and a temperature of 300 K. The applied field was varied from $1{\cdot}10^{-4}$ V/m to $1{\cdot}10^{7}$ V/m. The results are plotted in Figure 3.6 against an empirical mobility available in the literature (Jacoboni et al., 1977).

The empirical relation following the expression of Equation 3.5 with the associated values in Table III. The expression represents bulk silicon at an intrinsic doping density 10^{13} cm^{-3} at a temperature of 300 K.

The NEGF model is slightly less then the empirical relation for several reasons, those reasons include a lower effective mass than the bulk at 0.54 and the absence of impurity scattering which is important at low temperatures (which this is not) and low doping concentrations.

$$v = \mu E \tag{3.3}$$

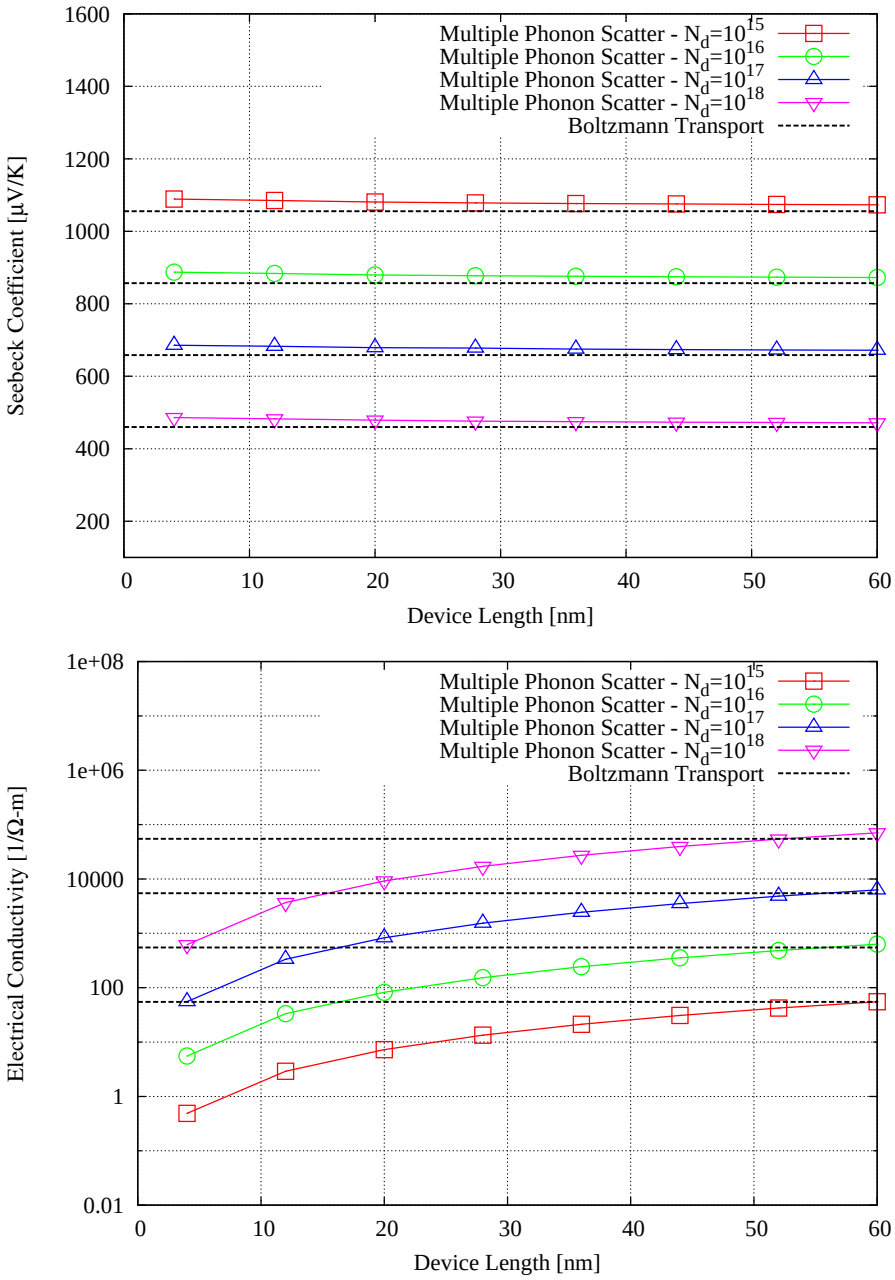

Figure 3.4 Homogeneous silicon Seebeck coefficient and conductivity versus device length for multiple phonon scattering NEGF model. The temperature is maintained at 300K. The electrical conductivity reaches bulk transport at device lengths greater than 60 nm.

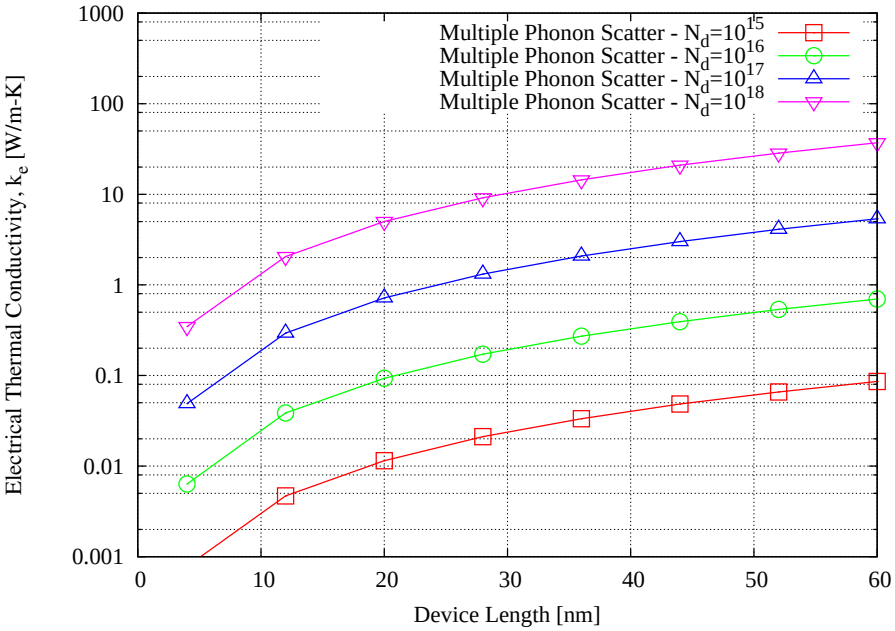

Figure 3.5 Homogeneous silicon electrical contribution to the thermal conductivity (k_e) versus device length for multiple phonon scattering NEGF model. The temperature is maintained at 300K. The large k_e value is why homogeneous silicon is a poor thermoelectric independent of nanostructures.

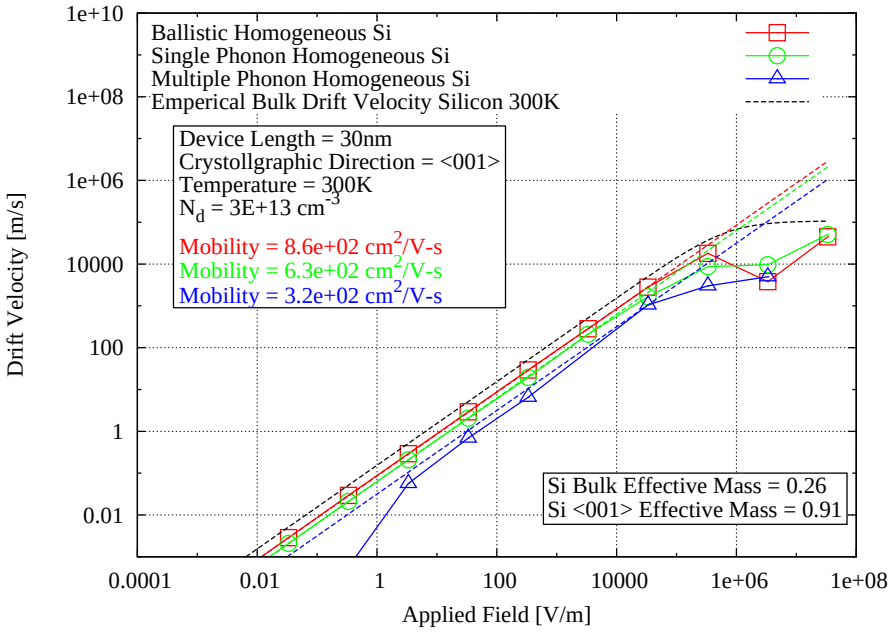

Figure 3.6 Drift velocity of electrons at 300K in a intrinsic single crystal silicon sample versus applied field calculated by all three electron NEGF models. The slope of the plot is proportional to the mobility of the materials. Notice the lowest mobility is the case with multiple phonon interactions.

Parameter	Expression	at 300K
$\nu_l[cm/s]$	$1.5{\cdot}10^9 \cdot \mathrm{T}^{(-0.87)}$	$1.07{\cdot}10^7$
$\epsilon_c[V/cm]$	$1.01{\cdot}\mathrm{T}^{1.55}$	$6.91{\cdot}10^3$
β	$2.57{\cdot}10^2 \cdot \mathrm{T}^{0.66}$	1.11

Table 3.1 Empirical parameters for bulk field and temperature dependent drift velocity in silicon. Parameters are associated with Equation 3.5. T is the average absolute temperature of the material.(Jacoboni et al., 1977)

Figure 3.6 also depicts the mobility of the NEGF model through the expression in Equation 3.3 and by the slope of the drift velocity versus applied field. Comparing the slope of the empirical equation plotted in Figure 3.6 to that of the model through visual inspection they look comparable. The fitted mobilities are listed in the figure which are slightly less the bulk mobility of $1400\,\mathrm{cm}^2/\mathrm{V}-\mathrm{s}$. This can be attributed to the bulk effective mass being larger than the $\langle 001 \rangle$ effective mass. As described in Equation 3.4 the mobility should decrease with a lower effective masses.

$$\mu = \frac{q\tau}{m^*} \tag{3.4}$$

$$v = v_l \frac{\epsilon}{\epsilon_c} \left[\frac{1}{1 + (\frac{\epsilon}{\epsilon_c})^\beta} \right]^{(1/\beta)} \tag{3.5}$$

Figure 3.8 is a plot of the current-voltage characteristics for a 30 nm homogeneous silicon device. Notice that the ballistic and single phonon curve are fairly similar with the single phonon model resulting in slightly lower current throughout the voltage range. The multiple phonon model shows some non-linearities at low bias energies which can be attributed to inelastic scattering of electrons. This non-linearity at low fields is the ability of the multiple phonon frequency scattering model to capture the interaction of the acoustic phonons. Often, in the literature, the IV characteristics of experimental devices show this very trend where the current is non-linear. Take for example the work done by Burr et al. (1997) on silicon materials where the IV characteristics are nearly zero until a turn-on voltage is reached. It is reasoned that the addition of a more descriptive phonon scattering process through multiple phonon frequencies allows a better estimate a the actual IV characteristics. This should not over shadow the consideration for other scattering mechanisms that may be present in experimental structures such as grain boundaries and dislocations. In reference to Burr's work, the nano-particles in his silicon matrix may have de-

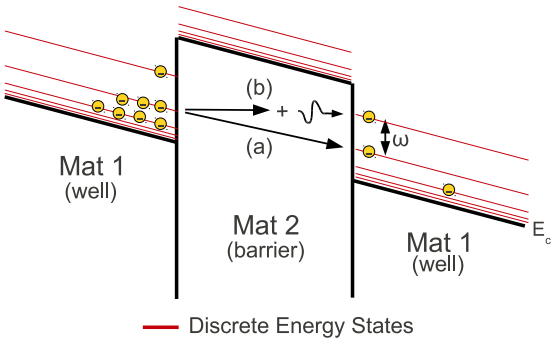

Figure 3.7 Illustration of the inelastic electron phonon tunneling. (a) is the elastic tunneling and (b) is the inelastic tunneling which requires a phonon ($\hbar\omega$).

creased the mobility or the slope but it is assumed the non-linearities would still be present in the absence of boundary scattering.

The non-linearities in the IV characteristics is even more substantial in thin film structures. This comes from the aid of phonon assisted tunneling. Again the trends of the multiple phonon scattering frequency model from Figure 3.8 is very similar to the trends one would find in an actual thin film structure. Researchers (Lambe and Jaklevic, 1968) have studied the tunneling of electron through thin film oxides and demonstrates this trend in current voltage characteristics as seen in Figure 3.8. The non-linearities at a flow field noted by Lambe are attributed to the phonon interaction influencing the electrons tunneling through inelastic electron tunneling. Figure 3.7 is an illustration of the tunneling dynamics and the interaction of phonons. As these phonons interact with the electrons, the electrons essentially gain or lose energy thermally in order to achieve as desired state on the other side of the barrier. In most cases it is more probable to lose energy to phonons. This loss of energy is demonstrated in the IV curve as a decrease in current for a given voltage. This argument of phonon assisted tunneling will be touched on later and will be illustrated in the plots of the local density of states, see Figure 3.12.

Additionally, as the number of electrons increase in the system due to increased field, the influence of the electron-phonon interactions is less significant and the slope of the single and ballistic models is recovered. This is seen in Figure 3.8 around 0.01-0.1μV.

Because the multiple phonon model takes into account the acoustic phonons, the non-linearities in the IV curve are a results of the lower energy electrons inter-

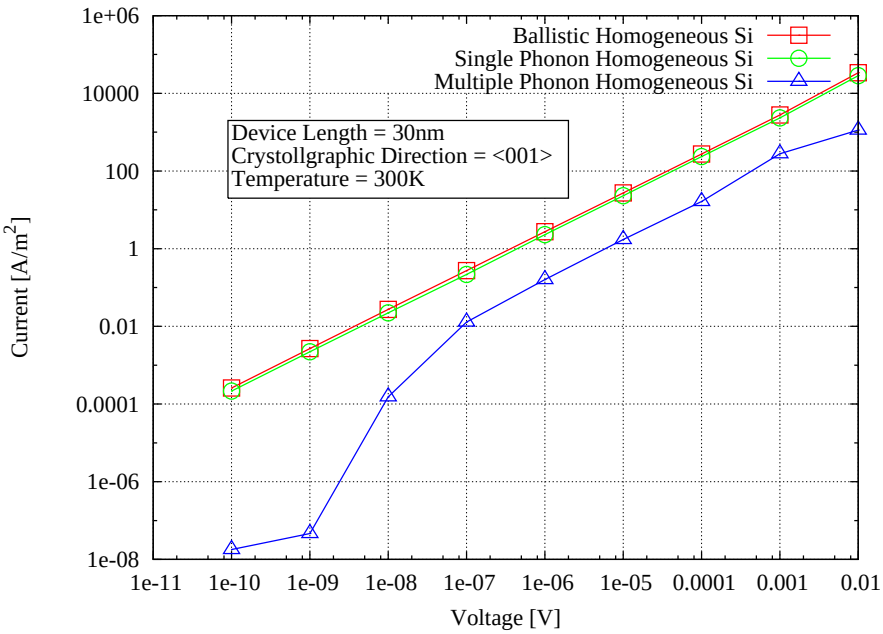

Figure 3.8 Current voltage characteristics at 300K versus applied voltage for electron NEGF at low dopant concentration. The multiple phonon scattering model has non-linearities associated at the low fields that is attributed to the significance of the electron-phonon interaction when the total number of charge carriers is low.

acting with the lower energy phonons which results in inelastic electron tunneling through the barrier material. The acoustic phonon description is not included in the single phonon model. Only the interaction of electrons with a single optical phonon frequency is considered.

An additional aspect of Figure 3.8 is the tailing off the current at higher fields. This is reasoned to be an artifact of the effective mass description. It is assumed for this research that the effective mass describes the curvature near the bottom of the conduction band edge. As the field is increased the electrons are dependent higher energies where non-parabolicity can become important. In an effort to describe high field dynamics either another effective mass that describes the top of the bands should be considered or a non-parabolic effective mass should be considered.

Si/Ge Superlattice Material - Thermoelectric Properties

The model demonstrated above for homogeneous silicon was applied to study Si/Ge superlattice thermoelectrics materials. The motivation behind developing this modeling approach was to capture the interactions of electrons and phonons at the

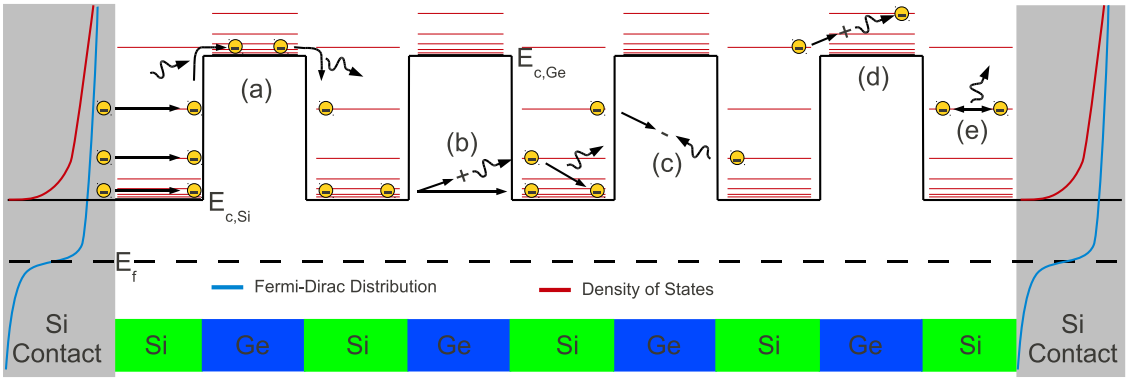

Figure 3.9 Plot of the possible transport mechanisms and transition for a electron in a superlattice structure. With the addition of electron-phonon interactions more states are available to the electron which are critical to capturing the transport. Transition (a) is electron surpassing the barrier with loss or contribution of phonon energy, (b) is phonon assisted tunneling, (c) is phonon assisted tunneling with a loss of energy to phonons, (d) is the phonon assisted transition above the conduction band, and (e) is electron-electron interactions with a loss of energy to a phonon.

nanoscale. Figure 3.9 is a sketch of the most common transition of a electron which involves a phonon. One of the most significant contributions of modeling the phonon interactions is the ability to capture phonon assisted tunneling as demonstrated by inset (b) of Figure 3.9. Figure 3.9 demonstrates other important transitions that are captured by the model such as (a) the phonon assisted transition over a barrier by the addition and loss of phonon energy. Likewise, (d) demonstrates a transition above the conduction band edge of both materials, which includes phonon assistance. The opposite of this, where a electron above the conduction band edge loses energy is the common electron-phonon interaction attributed to Joule heating. By capturing these interactions a more realistic electron environment is modeled resulting in greater confidence in the transport results.

The Seebeck coefficient and electrical conductivity were calculated for varying donor concentrations (n-type, phosphorous doped) for several superlattice configurations found in the literature. Results are shown in Figure 3.13 for three models and three superlattice configurations which are identical in construction to several experimental devices also included in the plot. The three models include the ballistic, single phonon and multiple phonon scattering models. The multiple phonon model proved

to be the most accurate at predicting the overall performance of these thermoelectric materials. Because the electrical conductivity can span a large range of values and can heavily influence the thermoelectric performance, the multiple phonon model as described above provides a more physical model of the transition leading to a more accurate conductivity calculation. The single phonon model tends to over-predict the electrical conductivity, while the multiple phonon model was within a order of magnitude of the experimental values.

In the superlattice material the interaction of several different phonon frequencies is critical to predicting the correct electrical transport. In the single phonon case, when an electron interacts with an electronic barrier, the electron either has to tunnel or scatter into an energy state above the barrier which is divisible by the electron energy plus the scattered phonon energy. However, in the multiple phonon scattering model the electron can be thermalized with a range of phonon energy and transported across the barrier and be re-emitted as an electron on the other side. Due to the increased number of allowed transitions from multiple phonon energies, not just a single phonon energy, the transport is more representative of the actual transport in the material.

Figure 3.10 is a plot of the scattering rate for multiple electron-phonon interactions and the total calculated scattering rate which is an average of all the individual scattering rates. The conduction band edge lies around 0.15 eV which is near the Fermi level (0.1 eV). The occupancy of electrons below the Fermi level is zero and this is why the associated scattering rate is zero. The phonon frequencies listed in Figure 3.10 corresponds to few of the lowest acoustic phonon frequencies. These lower frequencies have a lower scattering rate because the occupancy is low and the therfore the scattering rate is low compared to the high energy optical phonons which dominate the overall scattering rate. This is the basis in which many researchers only include optical phonon frequencies, however, when the devices gets larger the acoustic phonon become more critical to the transport dynamics.

The model also resolves the spatial scattering rate of electrons and phonons, similar to the phonon scattering above. Figure 3.11 is a plot of the spatial scattering for a two bilayer Si/Ge superlattice. The phonon model calculates the phonon content for each phonon frequency and the probability of finding it spatially which is passed to the electron code. The plot in Figure 3.10 is the spatial average of Figure 3.11. The scattering rate within the germanium layer is different than the silicon layers which is a concept that is absent when the scattering rate is assumed the same throughout the device, as seen in single phonon scattering models. The scattering rates here

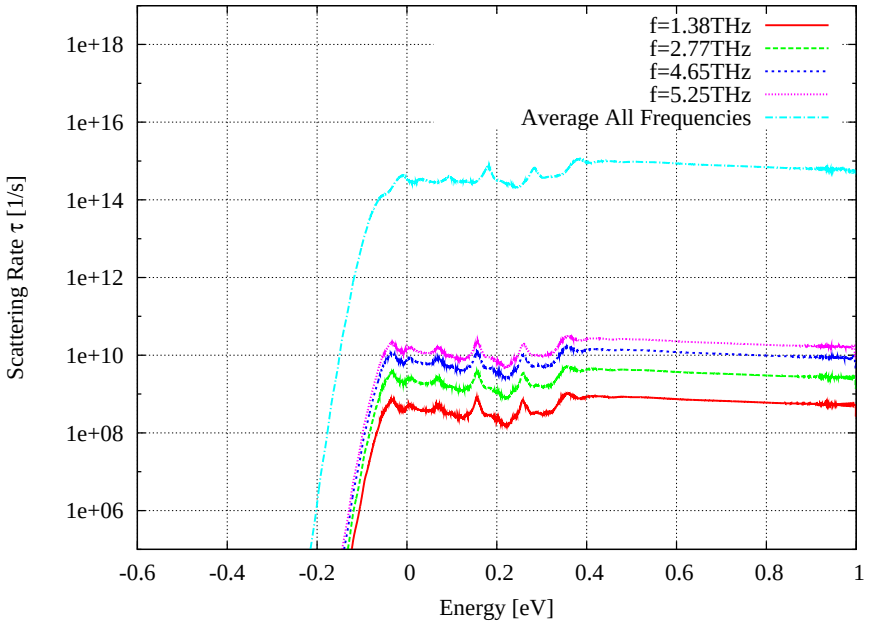

Figure 3.10 Plot of the calculated scattering rates for multiple electron phonon interactions in a Si(2 nm)/Ge(2 nm) two bilayer superlattice device at 300K. The total scattering rate is an average of all the scattering rates. Note the oscillation in the scattering rate which correspond to concentrations of high density of states that lie across the device channel.

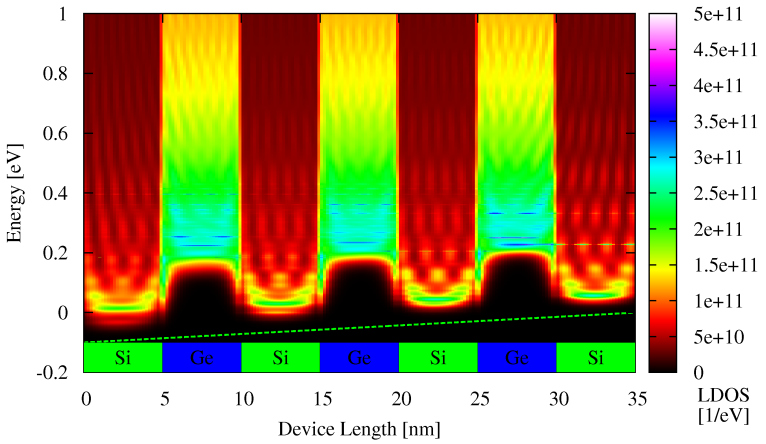

Figure 3.11 Plot of the total averaged spatial scattering rate for a Si(5 nm)/Ge(5 nm) six bilayer 35nm superlattice device at 300K. Notice that the scattering rate is different in the silicon (material closes to contacts) then the germanium due to the difference in scattering deformation potentials and phonon content. The phonon content in each superlattice layer is determined from the phonon model and passed to the electron model.

are on the order of typical rates that researchers Restrepo et al. (2009) report for single crystal silicon. Often, reported scattering rate in the literature are for a single dominant phonon frequency where the model developed in this research is able to discern the scattering rate for multiple phonon frequencies. The average scattering rate reported in Figure 3.10 is comparable to the single scattering rate reported in the literature. The average scattering was determined through a simple arithmic mean,

$$\frac{1}{\tau_{avg}} = \frac{1}{N}(\frac{1}{\tau_1} + \frac{1}{\tau_2}...\frac{1}{\tau_n}) \tag{3.6}$$

where τ_{avg} is the average scattering rate and N is the number of phonon frequencies. It was reasoned that a simple scalar addition of the scattering rate is inappropriate because the number of frequencies is over ten which could change the magnitude by one. In actuality, the number of unique phonon frequencies calculated by the phonon model is proportional to the length of the device and is approximately 70 unique phonon scattering rates for a 35 nm device.

To illustrate the importance of scattering with multiple phonon frequencies a plot of the local density of states was constructed for the three models. Figure 3.12 is

a plot of the local density of states for the multiple phonon frequency, single phonon frequency and ballistic case. It is important to point out that in the multiple phonon case the low lying states within in the well regions are accessible to the transport electrons. Where is the ballistic case the transport electrons are restricted to energies above the high conduction band edge. In the single phonon scattering case there is a intermediate condition where a few of the states in the well region are accessible but must be divisible by the single phonon scattering energy. This is a transition to a model which is clearly including more of the physics through multiple scattering pathways to capture a greater understanding of the electron transport.

It is important to point out that straining was left out of these superlattice calculations. Further investigation of how straining influences the model could shift both Seebeck coefficient and electrical conductivity values closer to experimental values; however, the amount of straining when comparing to literature requires an understanding of the interface conditions. How strain influences the thermoelectric performance will be investigated in the following section by varying the degree of strain. This is not an encompassing theory of straining and should distract from the objective of this research which is to understand the influences of the electron-phonon interaction in an ideal superlattice in the absence of straining.

Si/Ge Superlattice Material - Phonon Mode Selection

When the phonon mode passes the description of the phonon content to the electronic model, it is difficult to discern which of the content is optical and which is acoustic. This difficulty arises from the fact that there is not a clear defining point at which a phonon becomes an acoustic phonon or an optical phonon. This is important from a modeling point of view because the deformation potentials which describe the perturbation in terms of strain depends on whether the phonon mode is optical (neighboring atoms displaced opposite relative to each other) or if the phonon is acoustic (neighboring atoms displaced in the same direction). Figure 3.14 is a plot of the thermoelectric properties when the optical cut-off is 0.3 eV, label Multiple Phonon Scattering, when all the phonons are assumed optical (optical deformation potential only used) and when all the phonons as assumed acoustic phonons.

When all the phonon content passed from the phonon model to the electron model is assumed acoustic the scattering is overestimated due to the increased scattering rate. This is demonstrated in Figure 3.14 as a large increase in Seebeck coefficient and extremely low electrical conductivity which are direct results of a large scattering

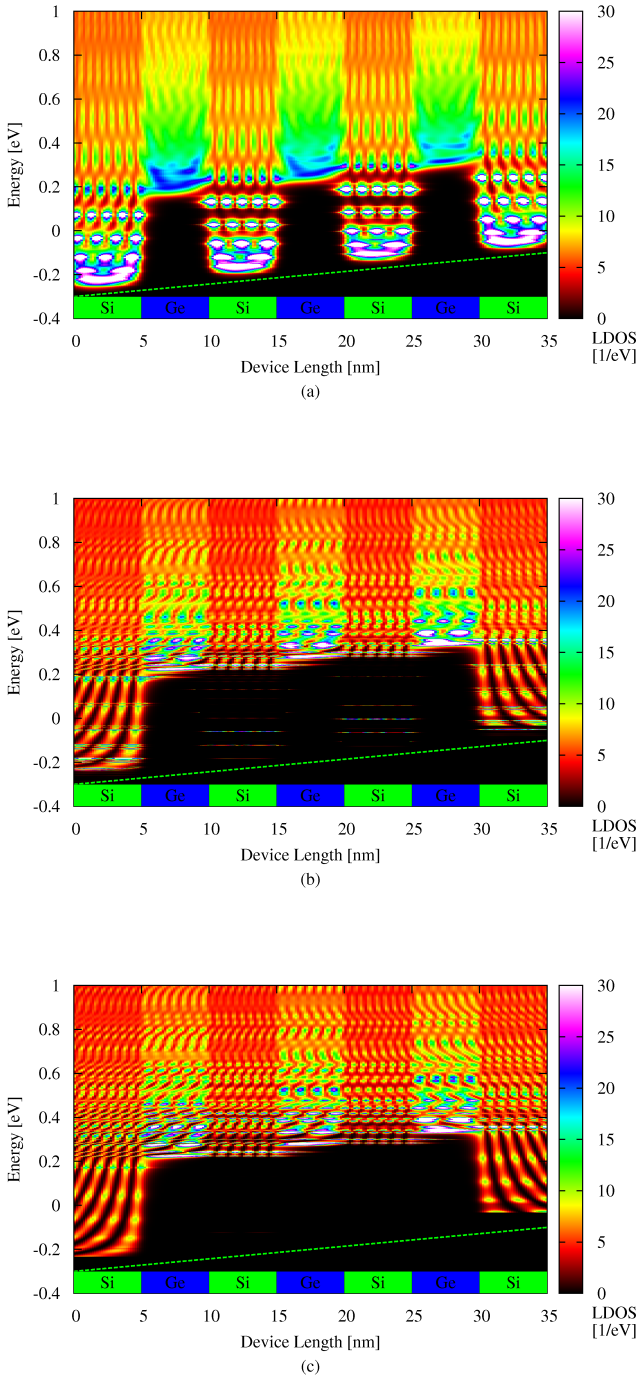

Figure 3.12 Plot of the local density of state (LDOS) for the three models, starting from the top figure: (a) multiple phonon frequency scattering, (b) single phonon frequency scattering, and (c) ballistic. Note that by allowing more transition from scattering with a range of phonon frequencies the density of states within the well region is accessible by electrons. The ballistic case limits the electron to take states above the high conduction band.

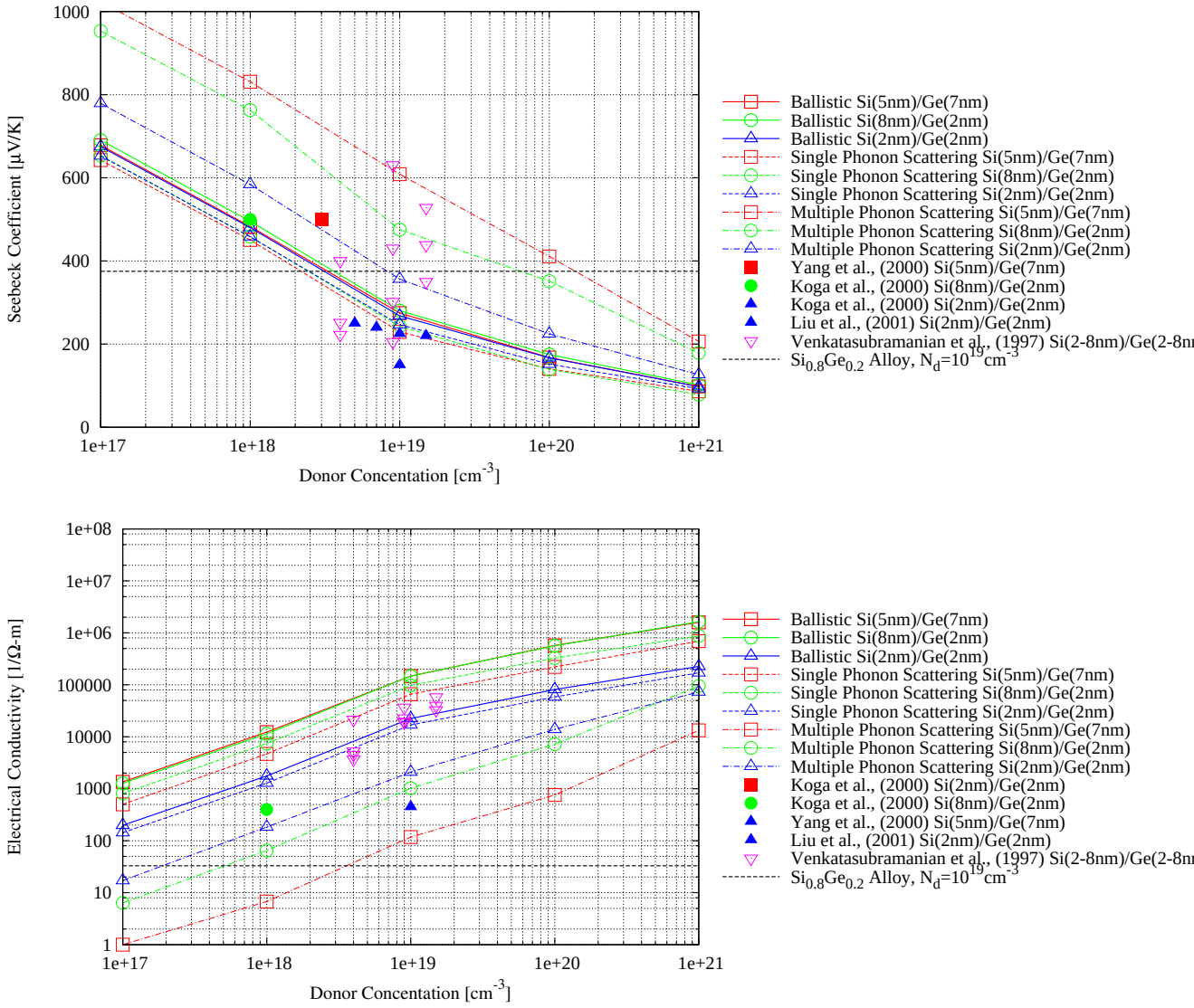

Figure 3.13 Plot of Seebeck coefficient and electrical conductivity as a function of donor concentration for several superlattice configurations. Ballistic, single and multiple phonon models are compared. Multiple phonon model has best accuracy at predicting experimental values.

rates. In the opposite case, where all the phonon content is assumed optical in nature, the influence is less noticeable and more comparable with experimental values. The literature and intuition suggests that the phonon content of these nanoscale monolayers are mainly comprised of optical phonon content due to the confined lattice dynamics preventing low frequency acoustic phonons.

The ZT values for difference phonon content, assuming the phonon content is all acoustic or all optical also demonstrates the dominance of the acoustic phonon scattering, see Figure 3.15. Again, the phonon content is assumed mostly optical type phonons based on the figure. The next section will study the influence of moving the optical cut-off frequency which defines which of the phonons passed from the phonon code are optical and which are acoustic.

Si/Ge Superlattice Material - Optical Cut-off Frequency

In the multiple phonon model the method of handling the passing both the acoustic phonon and optical phonon content is different depending on the mode of the phonon. The root of the difference lies in the how the deformation potential is formulated as that fact that acoustic phonons produce lattice strain by displacing neighboring atoms in the same direction and acoustic phonons displace the neighboring atoms in opposite directions. As discussed in the previous section there is not a clear distinction of where the cut-off is between optical and acoustic phonons. The model therefore requires the user to specify an energy cut-off for which all phonons with energy below this level are assumed to be acoustic in nature and all phonons above this cut-off are assumed to be optical in nature. Figure 3.16 is a plot of the Seebeck coefficient and electrical conductivity for increasing doping concentration and difference levels of optical cut-off frequency. As the cut-off frequency is increased, more phonon frequencies are assumed acoustic in nature and the Seebeck increases due to an increased gradient of charge across the device. The electrical conductivity decreases as the mobility increases due to the increased electron acoustic phonon scattering.

Taking the analysis a step further from Figure 3.16, the ZT value is estimated as seen in Figure 3.17. As the doping concentration increases the k_e contribution to the ZT figure increase, decreasing the overall ZT. However, the electrical conductivity also increases with doping which creates a maximum in ZT values. Often, this will be seen in the literature as a maximum in the ZT which is reproduced by the model. As the optical cut-off frequency increases, the curve shifts down and to the right due

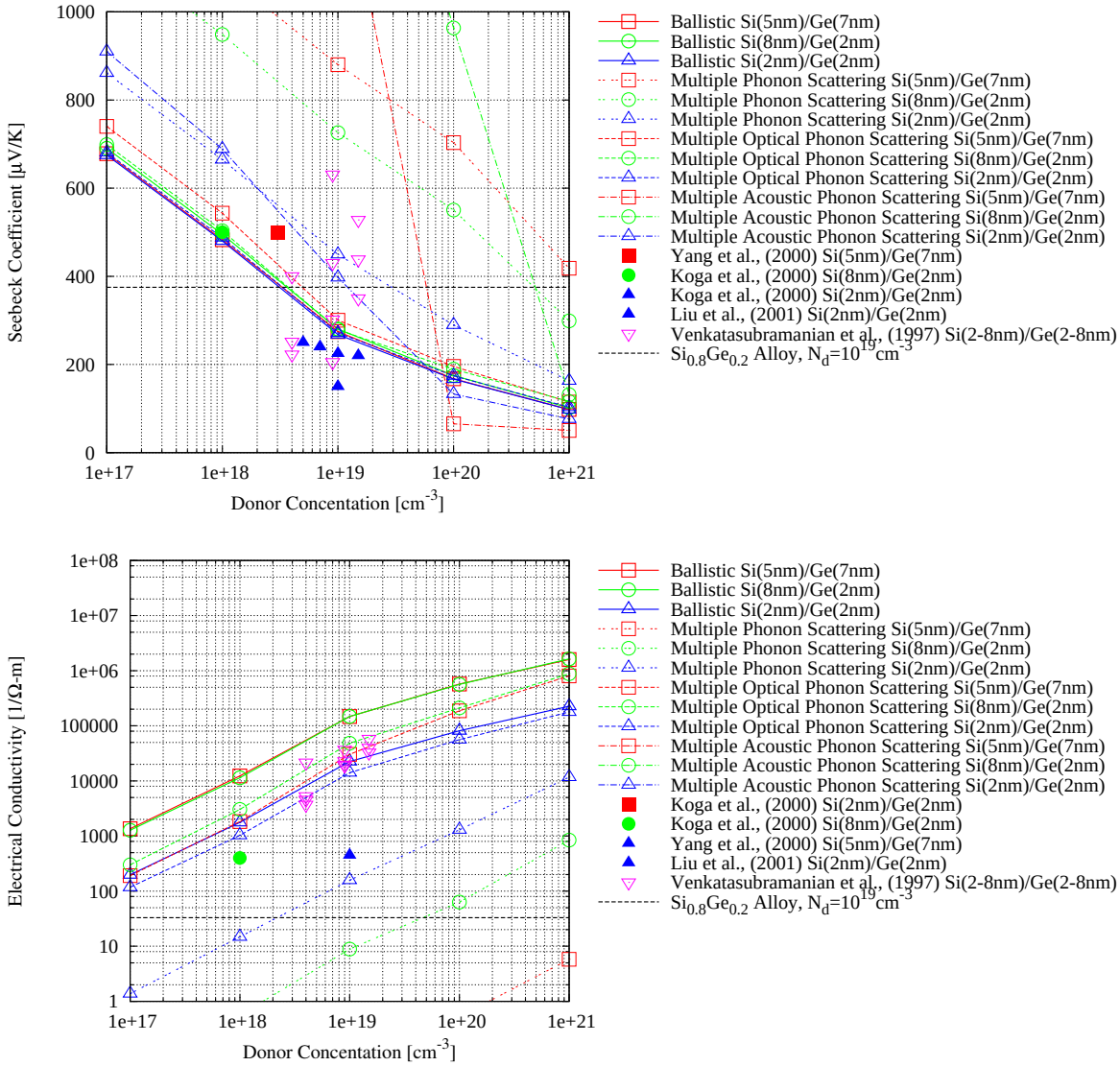

Figure 3.14 Plot of Seebeck coefficient and electrical conductivity as a function doping when the optical phonon cut off is 0.3 eV (Multiple Phonon Scattering), when all the phonons are assumed optical (Multiple Optical Phonon Scattering) and when all the phonons are assumed acoustic (Multiple Acoustic Phonon Scattering). The acoustic phonon scattering heavily influences scattering suggesting that majority of the phonon content should be handled as optical phonons.

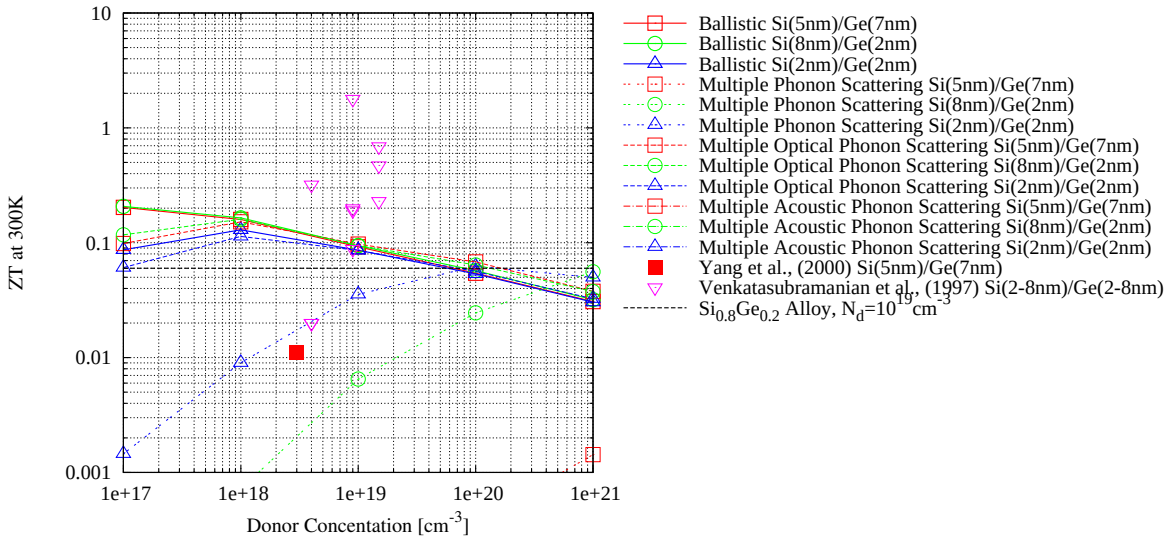

Figure 3.15 Plot of the ZT value as a function of doping concentration when the optical phonon cut off is 0.3 eV (Multiple Phonon Scattering), when all the phonons are assumed optical (Multiple Optical Phonon Scattering) and when all the phonons are assumed acoustic (Multiple Acoustic Phonon Scattering). When the total phonon content is assumed acoustic the scattering rate is over predicted providing evidence that the phonon content is mainly optical content.

to a decrease in electrical conductivity.

Si/Ge Superlattice Material - Acoustic Deformation Potential

Maintaining the optical cut-off frequency at 0.3 eV and varying the acoustic deformation potential from 0.0 eV to 9.0 eV provides a means of evaluating how the scattering rate is affecting the thermoelectric properties. Figure 3.18 is a plot of the Seebeck coefficient and electrical conductivity versus doping for varying acoustic deformation potentials. As the acoustic deformation potential is decreased, the scattering rate decreases. At an acoustic cut-off frequency of 0.0 eV the case of optical scattering only is recovered.

The ZT value can be determined by varying the acoustic deformation potential, see Figure 3.19. It is reasoned that the acoustic deformation should be fairly small because the majority of scattering in confined structures is a result of optical phonon scattering. The trends of increased scattering at low dopant concentration is noted in the literature (Burr et al., 1997) and is due to the low population of charge carriers being scattered, thus diminishing the overall conductivity. This is less an issue at

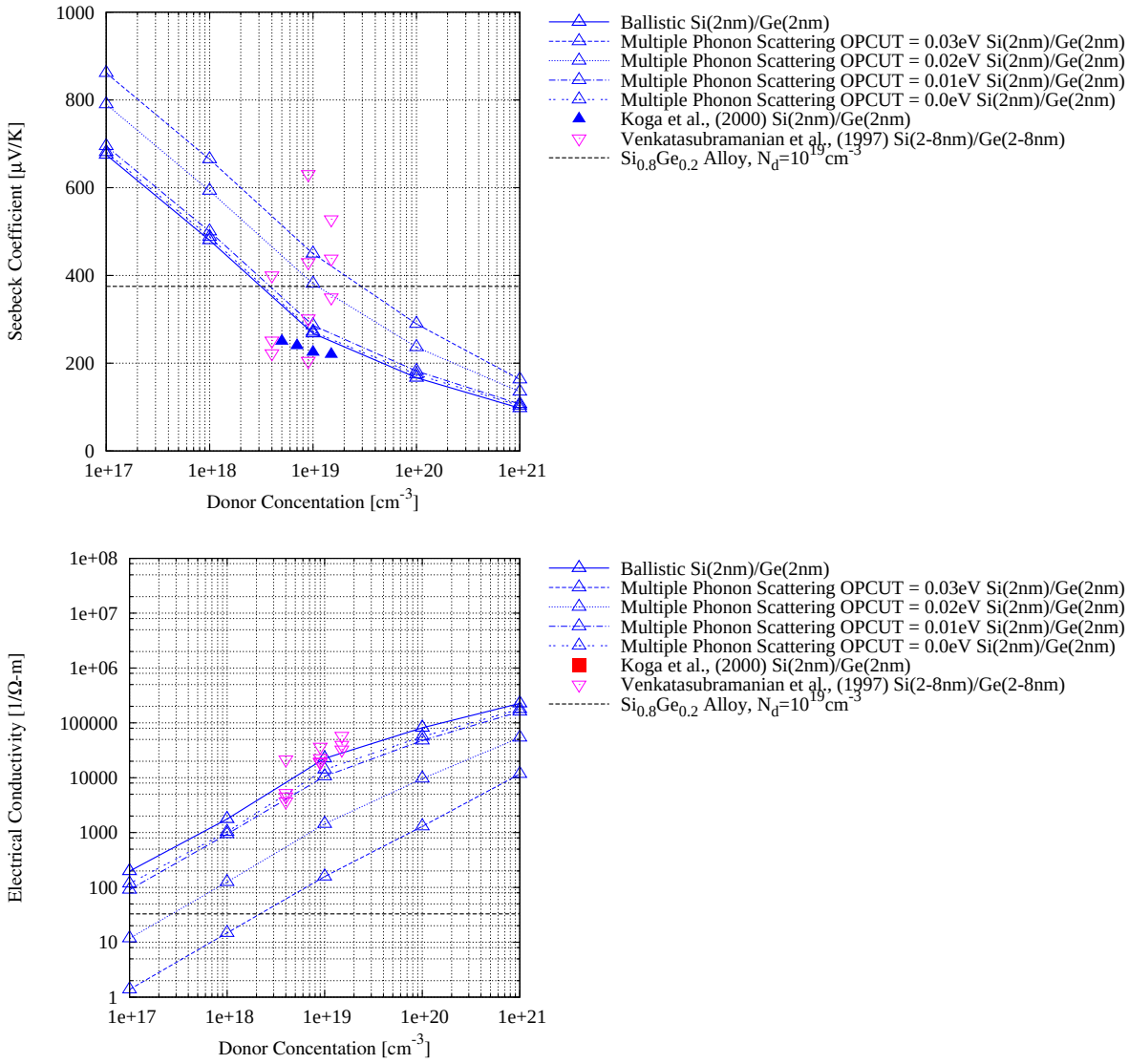

Figure 3.16 Plot of Seebeck coefficient and electrical conductivity as a function of optical phonon frequency cut-off. When OPCUT is 0 eV, all phonons are assumed optical. Notice the acoustic scattering dominates the scattering which suggests that the acoustic deformation potential could be too large.

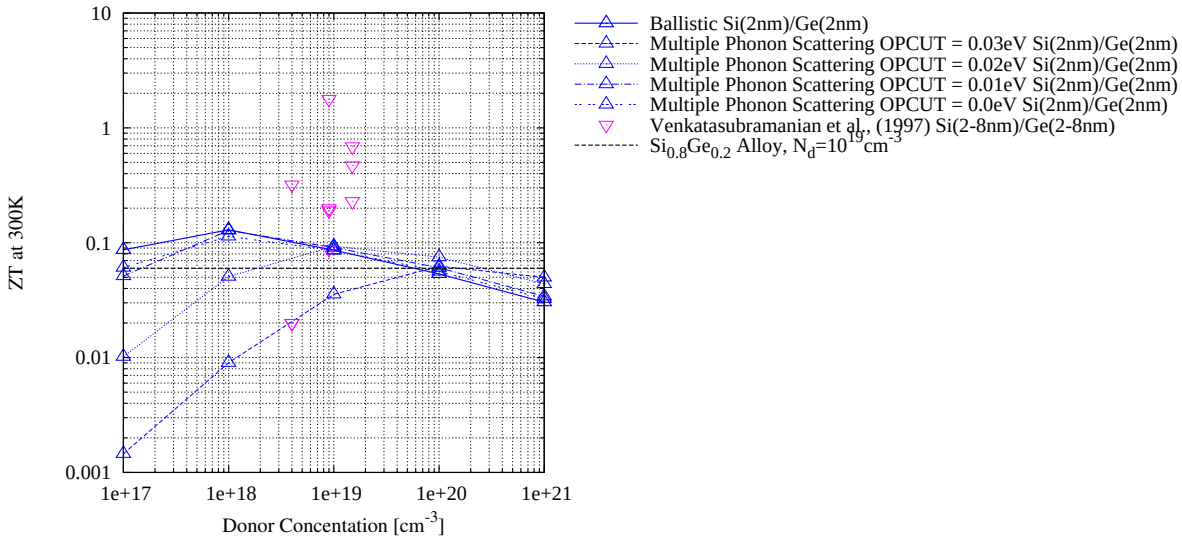

Figure 3.17 Plot of the ZT value as a function of doping concentration for several optical phonon frequency cut-offs. There is a maximum in the ZT values associated with the influence of k_e and σ with increasing doping concentration.

doping concentrations of $10^{19}\,\mathrm{cm}^{-3}$ but then the ZT value decreases as k_e increases resulting in a extrema in the ZT curve.

Si/Ge Superlattice Material - Strain Effects

An aspect that is often critical in modeling thin film bilayers structures is the effect of induced layer straining and its influence on the transport behavior. In order to incorporate these effects to the model it requires that the researcher have some knowledge of what the actual surface interface looks like. However, there are modeling approaches which can be used with caution assuming a perfectly strained interface between layers. Using the straining model explained in the theory chapter (Section II), which is based the neighboring lattice constant of individual layers their associated thickness, a shifting of band energy can be determined in response to this hydrostatic load. The nature of the strain results from the difference in lattice constant between neighboring layers, in this case silicon and germanium; silicon has a smaller lattice constant than germanium. The straining model is only interested in the uniaxial strain which is a result of Poisson effects. As the lattices at the interfaces try to reach an equilibrium position between the two lattice constant a biaxial strain in-plane is created which is associated with a uniaxial strain perpendicular to the

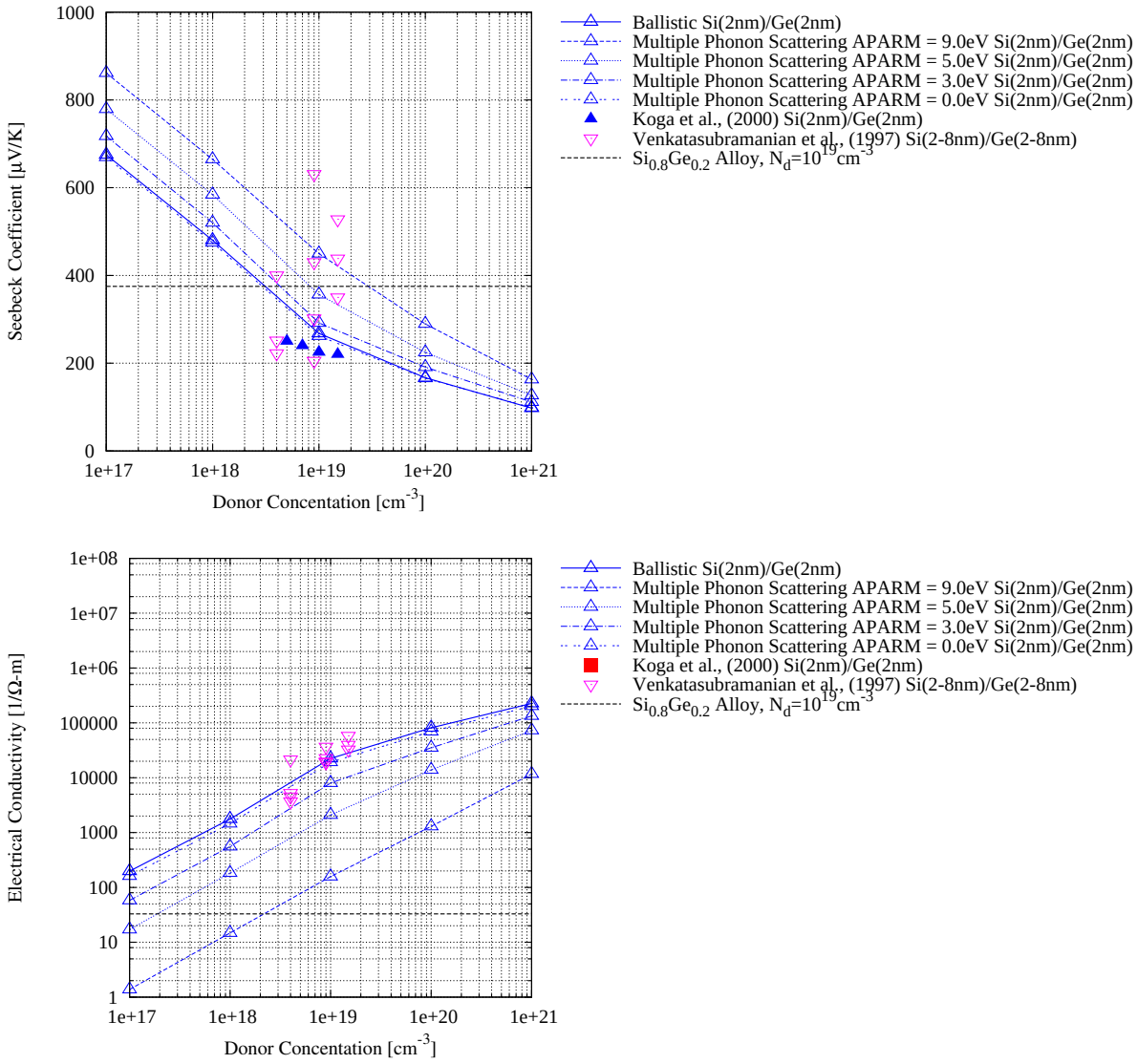

Figure 3.18 Plot of Seebeck coefficient and electrical conductivity as a function of acoustic phonon deformation potential. As the acoustic cut-off frequency increase the scattering rate increases and when the acoustic cut-off frequency is 0.0 eV where the case of only optical scattering is recovered.

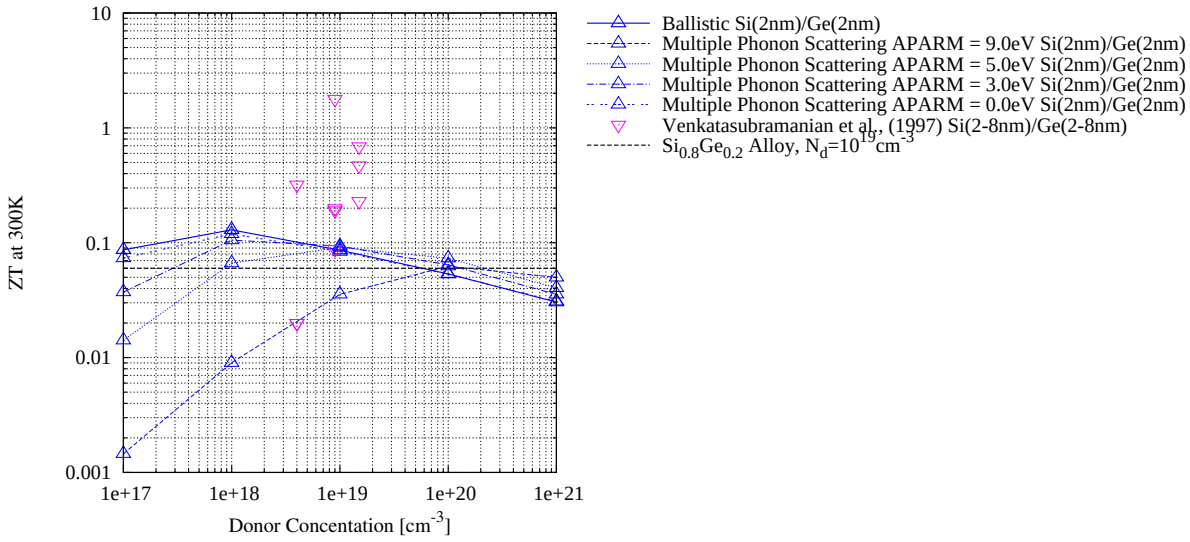

Figure 3.19 Plot of the ZT value as a function of acoustic phonon deformation potential. Note, a maximum in the ZT values which is influenced by the increase in acoustic deformation potential.

interface in the transport direction.

In Figure 3.21 a plot of a Si(8 nm)/Ge(2 nm) superlattice device with varying percentage of strain is plotted with associated Seebeck and electrical conductivity values. The dopant density was held at 10^{18} cm^{-3} for three difference temperatures. The inset figure below the Seebeck coefficient and electrical conductivity are the associated conduction band edge of the silicon and germanium superlattice material. When the percentage of the full strain is 100 that means the full conduction band offset calculated using the deformation strain theory is represented.

Figure 3.21 demonstrates how the amount of strain can significantly modify the the transport where the electrical conductivity can decrease four orders of magnitude and the Seebeck coefficient can increase by just less than two. Depending on the interface quality of the thermoelectric bilayer material, the actually strain could lie anywhere between 0 and 100 percent of the full strain. It is suggested by Van de Walle (1989) that the researcher must pay close attention when the conduction bands invert due to straining, as is seen around 5% strain in Figure 3.21.

The illustration in Figure 3.20 demonstrates the strain condition which would be seen in the actual superlattice structure. The illustration points out two effects which are absent from the straining model. The first effect, is dangling bonds shown

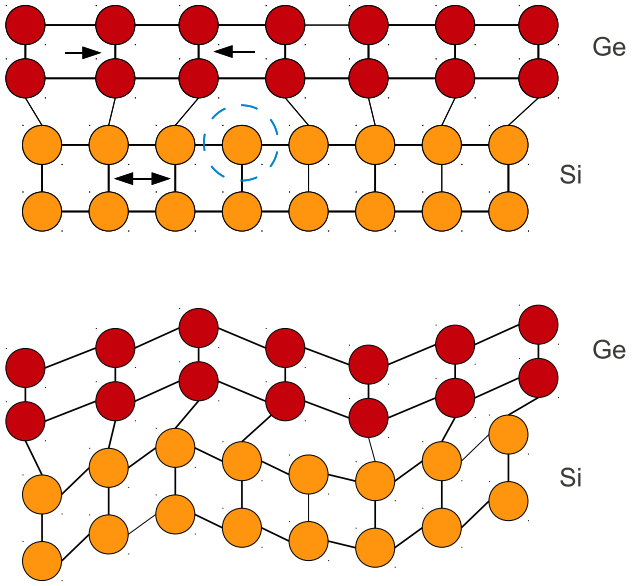

Figure 3.20 Illustration of the lattice strain induced from two dissimilar lattice constants in contact. The top figure demonstrates dangling bonds (blue circle) which are not capture in strain model. The bottom figure illustrates a wave effect in the thin films which decreases the induced straining effect which is also absent in strain model but possibly present in a real structure. The model assume perfect straining which all bonds are strained uniformly neglecting out-of-plane effects.

in the top illustration of Figure 3.20 outlined in a blue circle. The second effect is the wavy effect of the layers which is seen experimentally for very thin layers. The waviness is a mechanism of accounting for the strain. It results in decreasing the apparent strain in the layers. The modeled only accounts for perfect interfaces and does not account for slip or geometric changes. The model can, for that reason, be thought of in terms of the absolute maximum effect from stain. Therefore, it is useful to look at a percentage of that strain as shown in Figure 3.21.

Researchers Fischetti and Laux (1996) have investigated the straining of both silicon and germanium from a density function theory (DFT) calculated deformation potentials. Their results suggest that the germanium band structure is not heavily influenced by the strain along the $\langle 001 \rangle$ direction, but the effective mass increases as strain increases. The increase in effective mass would relate to a lower drift velocity and lower mobility, see Equation 3.4. In silicon, however, it is reported to have a moderate decrease in conduction band edge approximately 0.5 eV. The mobility in silicon is reported to only increase slightly; however, in compression the mobility increases

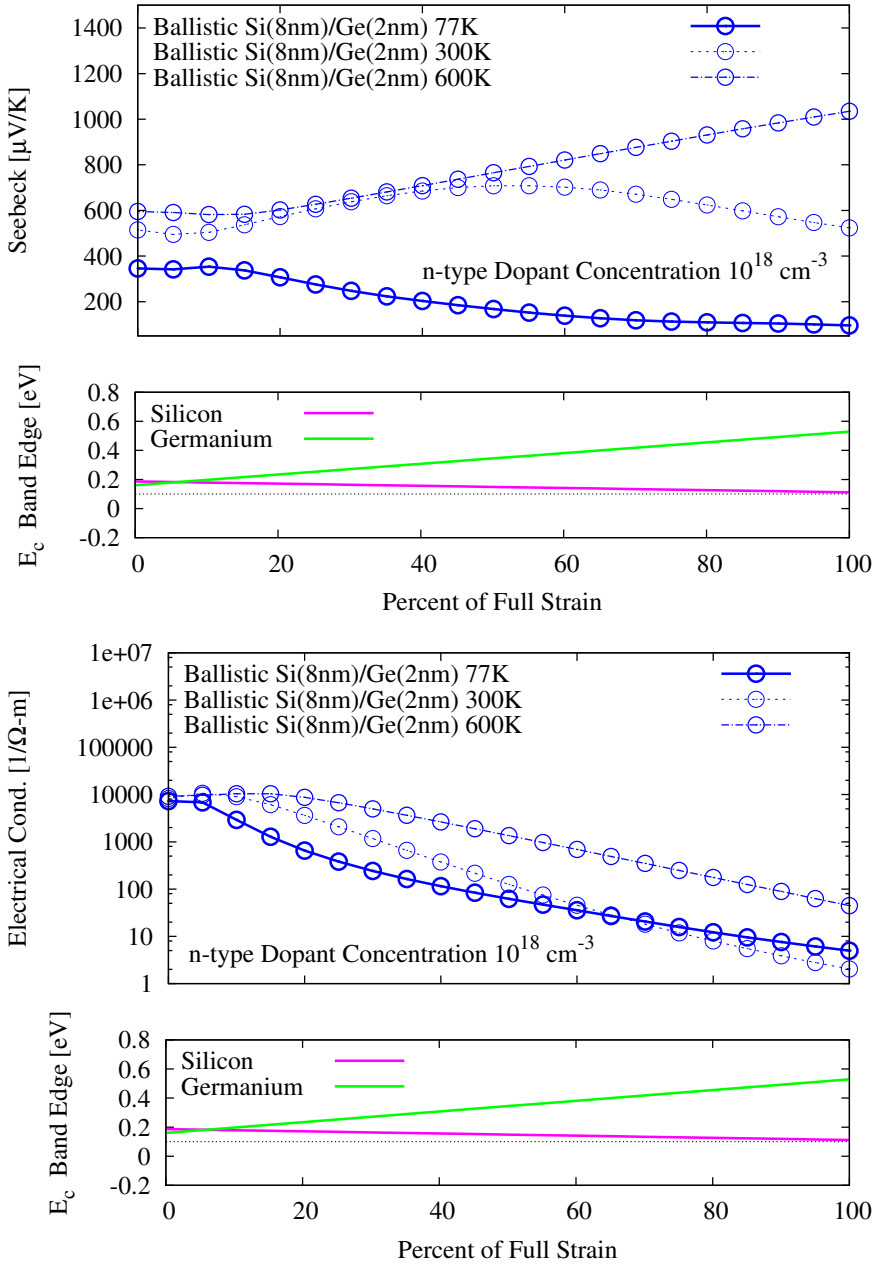

Figure 3.21 Plot of the (a) Seebeck coefficient, (b) electrical conductivity as a function of strain. Percent strain is a percentage of strain value derived from calculation of conduction band shift from deformation potential strain calculation.

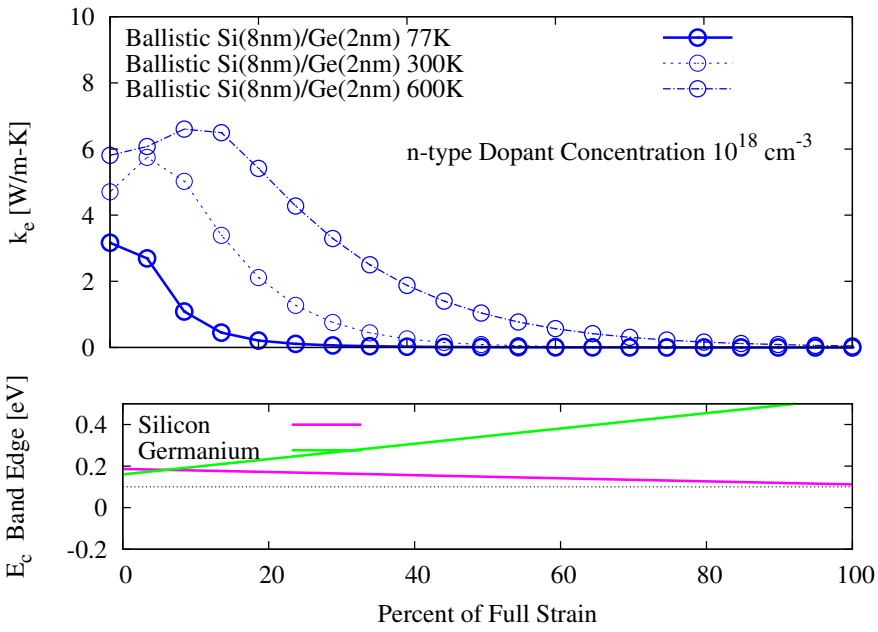

Figure 3.22 Plot of the electrical contribution to the thermal conductivity as a function of strain. Percent strain is a percentage of strain value derived from calculation of conduction band shift from deformation potential strain calculation.

tremendously. Because the silicon has a smaller lattice constant than germanium, the strain is assumed to be in tension in the silicon and compressive in the germanium. Based on these findings and the inability to characterize the interface surface of the experimental samples, the straining effects are neglected.

Si/Ge Superlattice Material - Effective Mass

The effective mass which governs the dynamics of electrons within the solid is a parameter that must be specified in the model for both the silicon and germanium superlattice material. Because the model is an effective mass formalism, the change in effective mass can be directly related (through Equation 3.4) to the mobility. Caution must be taken because this equation is for bulk electron dynamics, not discrete energy level dynamics of confined structures. Figure 3.23 is a plot of the Seebeck coefficient and electrical conductivity as a function of change in effective mass. The effective mass of the silicon layers was held at 0.91, while the effective mass of the germanium layers were varied from 0.1 to 1.1. Likewise, the germanium layer effective mass was held constant at 0.95 and the silicon layer effective mass was varied fro 0.1 to 1.1. The dependent effective mass values at which both layers were held constant

corresponds to the nominal effective mass values along the crystallographic $\langle 001 \rangle$ direction. The plot of Figure 3.23 demonstrates that the Seebeck coefficient is not heavily influenced by the selection of the effective mass with a less then 10% change in Seebeck coefficient. However the electrical conductivity as a function of effective mass varies up to one order of magnitude in conductivity at the maximum compared to the lowest conductivity value. Noted from the same conductivity figure, the change in germanium effective mass does not vary as large as the silicon material. The lack of response in germanium as the effective mass changes can be partially attributed to the fact that the superlattice layer thickness for germanium is quarter the size compared to silicon.

Based on the continuum argument of Equation 3.2 one would expect that the electrical conductivity should increase as the effective mass decreases. However, because this is a superlattice structure and the states within the layers are confined, as the effective mass increases, there are a greater number of states near the conduction band edge which increases transport, see Figure 3.24. Justification to this argument can be seen from Schrödinger's equation, $\hbar/2m^* \bigtriangledown^2 = E$, where the steady state eigenvalues, E, decrease when there is a larger effective mass (m^*). Therefore, in nanostructured materials it is not the drift velocity (governed by the effective mass) but rather the availability and location and number of transport states relative to the Fermi level and lowest conduction band edge. If the Si(8 nm)/Ge(2 nm) superlattice layers were increased in thickness, then the confinement effects would diminish as states fell down in energy and the conductivity would come to be governed by the drift velocity which would decrease as the effective mass increases.

Full ZT Model Validation

To determine the overall performance of the superlattice materials, the ZT values were calculated for the superlattice devices using $ZT = S^2\sigma T/k_e + k_p$. Both the electrical contribution and the lattice contribution were included in the thermal conductivity value. Figure 3.25 is a plot of ZT versus donor concentration for several superlattice devices. The multiple phonon model with the Si(2nm)/Ge(2nm) device depicts an inflection in the ZT values due to the increase in k_e. As the donor concentration increases, the increased number of conduction electrons drives the ZT value down. This resembles the correct trend which is absent in the ballistic and single phonon model.

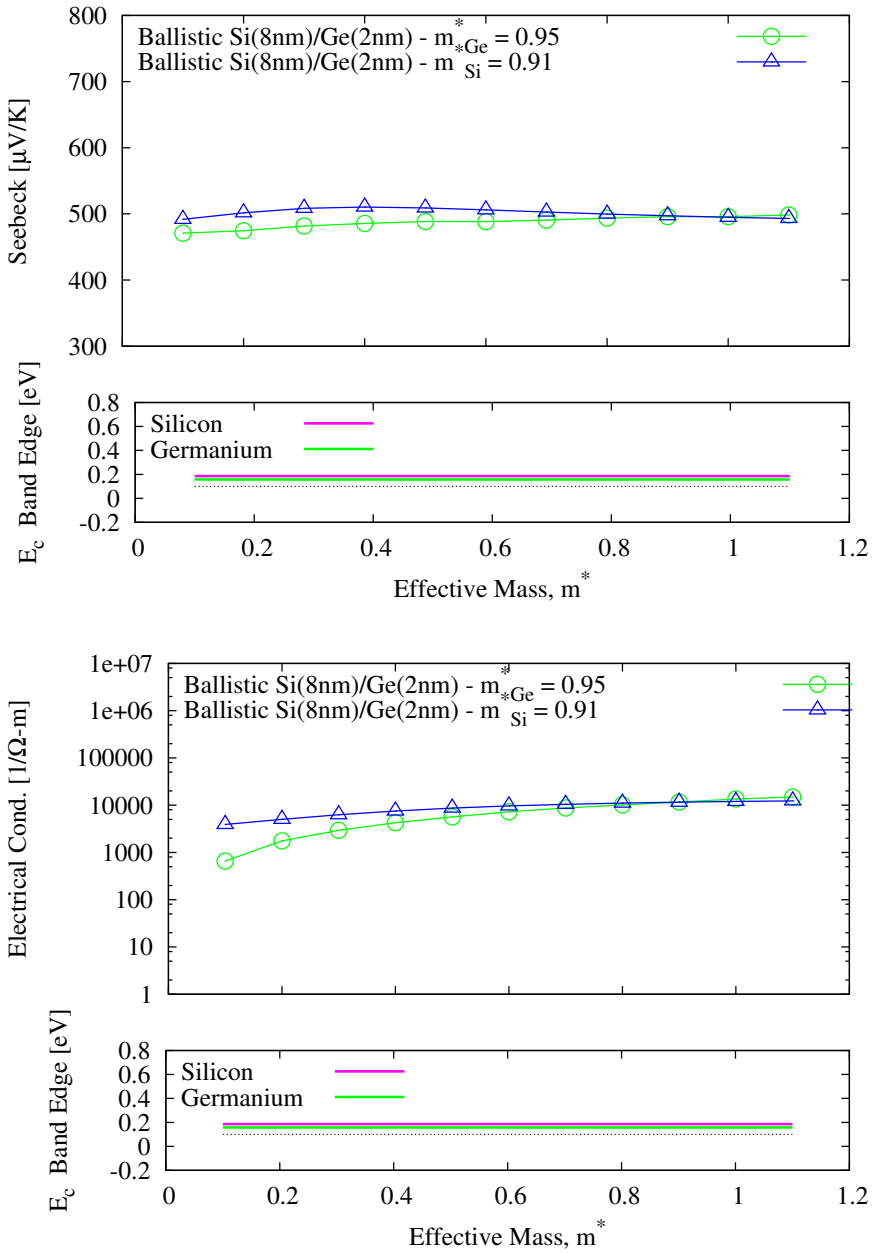

Figure 3.23 Plot of the (a) Seebeck, (b) electrical conductivity as a function of effective mass for a Si(8 nm)/Ge(2 nm) superlattice. The effective mass of was selectively held constant for the germanium (green circles) while the silicon effective mass was varied from 0.1 to 1.1. Similarly, silicon (blue triangles) effective mass was held constant while the germanium effective mass was varied from 0.1 to 1.1.

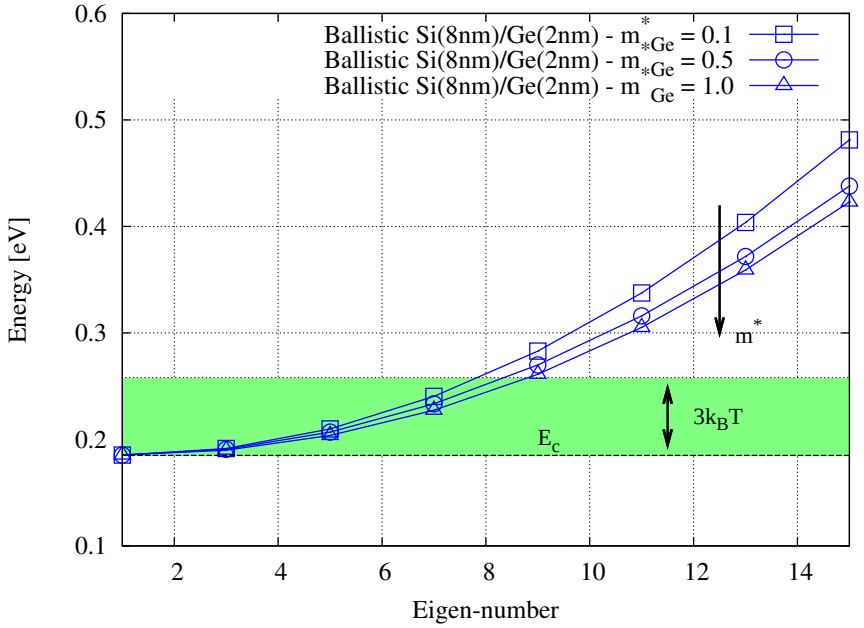

Figure 3.24 Plot of the steady state eigenvalues of a Si(8 nm)/Ge(2 nm) superlattice as a function of effective mass. The increase in electrical conductivity with increasing effective mass which is opposite continuum arguments is due to the low lying energy level when the effective mass is increased.

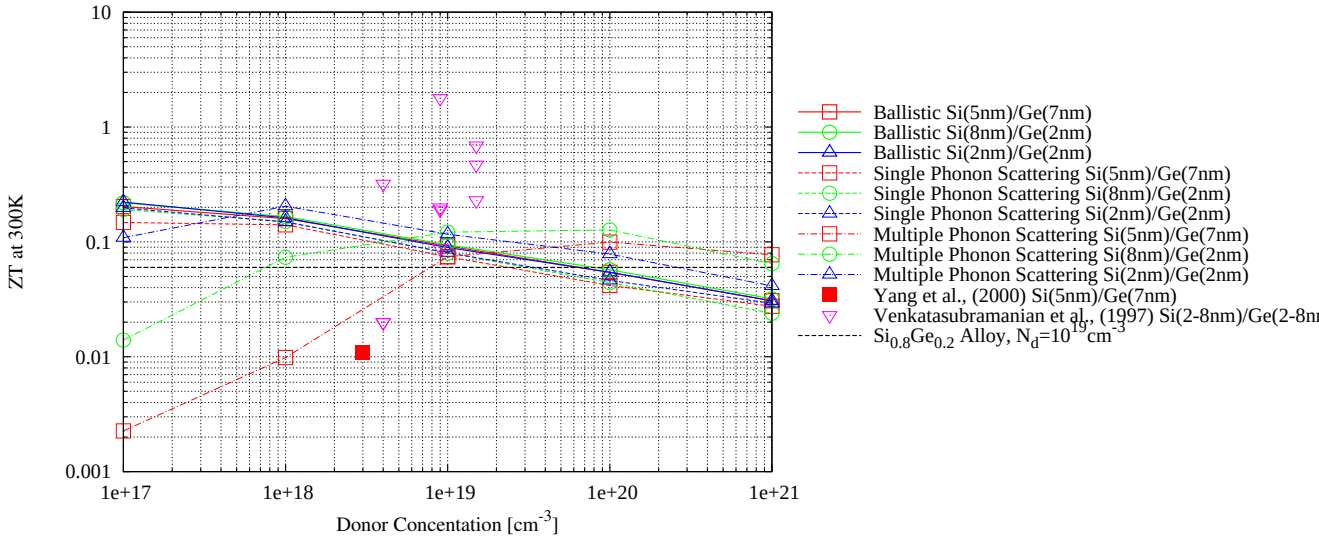

Figure 3.25 ZT predictions using ballistic, single phonon and, multiple phonon model for several superlattice materials ranging from 2 nm to 8 nm layer sizes. Temperature was held a 300K. The multiple phonon model has a higher ZT value than the ballistic model due to the decreased electrical contribution (k_e) to the thermal conductivity.

Temperature Distribution Validation

One of the appealing aspect of the coupled modeling approach is the ability to predict the temperature distribution across a device. The model is initially specified with an equilibrium temperature in the case of this study that temperature was 300K. Both the electron and thermal model are specified with the device geometry. A voltage bias is specified for the electrical model. The model of energy transfer between the electrical and thermal model is through electron-phonon interactions. The amount of energy for scattered from the electrons into phonon energy is tracked for each frequency. That energy is then put into the phonon model through the contacts along the device. This thermal energy disrupts the equilibrium of the thermal system. The coupling of the two thermal and electrical model is allowed to iterate until the change in the temperature distribution is less than a user specified 10%.

The temperature across the device was calculated in three difference methods. The first method was done by solving for the temperature by fitting the equilibrium distribution to the electron density of the sub bands. The following equation was used to determine the temperature,

$$T = \frac{-E(k)}{k_B ln(1 - exp(-f(k)/N_o)}, \tag{3.7}$$

where E(k) is the energy of each phonon frequency with wave vector k. The term f_k is the distribution of transport phonons which include the scattering phonons from the electron interactions. N_o is the equilibrium distribution of phonons at the equilibrium temperature of 300K. The maximum temperature is determined by solving for the maximum temperature at each energy level using Equation 3.7. The other methods were to collect the electron distribution across all subband and carry out Equation 3.7. The third method was to collect the overall energy of all the phonons knowing the phonon distribution and iteratively fit a equilibrium distribution to that energy.

The third method of fitting the equilibrium temperature using the total energy did not correctly estimate the temperature as the temperature was extremely small. It was reasoned that the discrete energy of the phonon distribution does not fit a continuous energy distribution as many of the energy is scattered into low lying phonon frequencies. Meaning the phonon distribution in a nanostructure is not continuous but rather irregular. Ultimately, the first method of using Equation 3.7 and calculating the temperature at each energy level was reasoned to be a better estimate of the actual temperature distribution across the structure. However, caution must

be taken when you use this conclusion. All of this analysis comes back to the fundamental definition of temperature. Commonly the definition of a temperature comes from how you are measuring the temperature. If passive measurement of temperature is used caution must be taken because the phonon content in the channel cannot be described as a Planck distribution for the same reason a Boltzmann distribution cannot be fit and temperature backed out.

Figure 3.26 is a plot of the temperature distribution of a six bilayer Si/Ge strained superlattice where Ge acts as the barrier. The bias applied to this sample was 300 mV at a total device length of 35 nm. The figure depicts a build up of temperature near the first barrier interfaces that are closest to the contacts. This is reasoned to be directly related to the charge build up at that interface and can be confirmed by investigating the charge density in the electronic model. Also, this figure suggests that the generation within each the different silicon and germanium layers is different. This provides reason of a local Seebeck effect which is absent when the generation from electron-phonons is not included in the model.

The temperature distribution of a superlattice channel in Figure 3.26 is an interesting finding as the temperature landscape within the channel is often difficult to experimentally determine. The reader should be aware that in many devices, especially in high frequency electronics majority of the thermal energy within the channel is a result of conduction from the contacts regions. In power devices, joule heating in the contacts diffuses into the channel and is more significant than the thermal energy generated in the channel due to electron-phonon generation. For this very reason it is often difficult to experimentally measure the channel generation and the corresponding temperature profile of channel.

In comparison to Figure 3.26 the same analysis was run for a 35nm homogeneous silicon device, see Figure 3.27. The generation is constant along the device as would be expected. The temperature near the contacts is lower due to the decreased electron population near the edge region. This comes from a wave nature of an electron and the probability of finding that electron within the channel region. A majority of the energy is in lower lying energy levels which occupy states that have a higher probability of being near the center of the channel. As the temperature increases high states are filled which has greater probability of being closer to the contacts. In an experiment either the diffusion of heat from the contacts or the diffusion of heat from the center of the channel would diminish this effect.

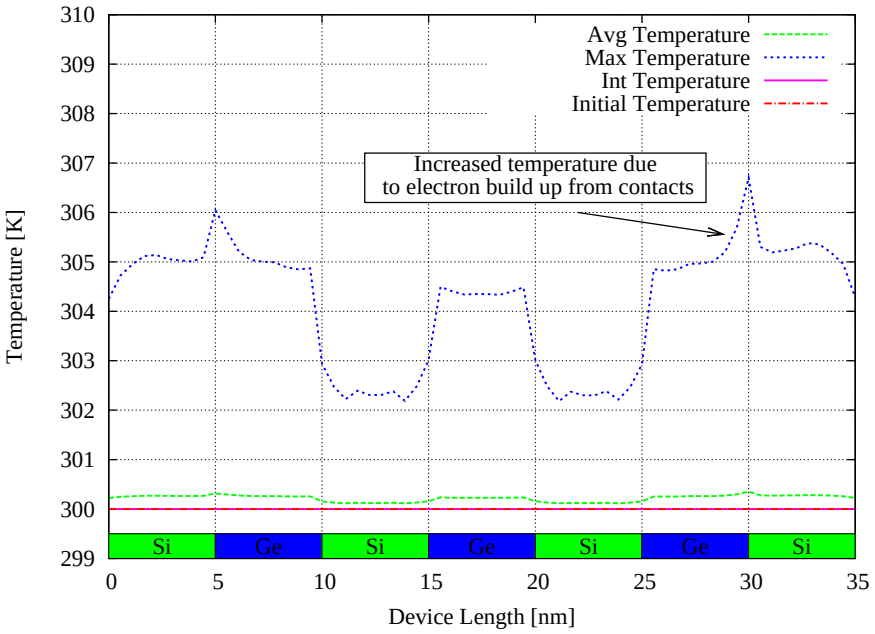

Figure 3.26 Plot of the temperature distribution along a 6 bilayer superlattice device with a 300mV bias and a equilibrium temperature of 300K. The temperature bias was determined from the fully coupled model which accounts for the phonon energy scattered from the electron-phonon interactions. The max temperature was determined by solving for the temperature distribution at each energy level and taking the corresponding max temperature. Note, the figure demonstrates a slight increase in temperature as a result of electron build up prior to the first Ge barrier.

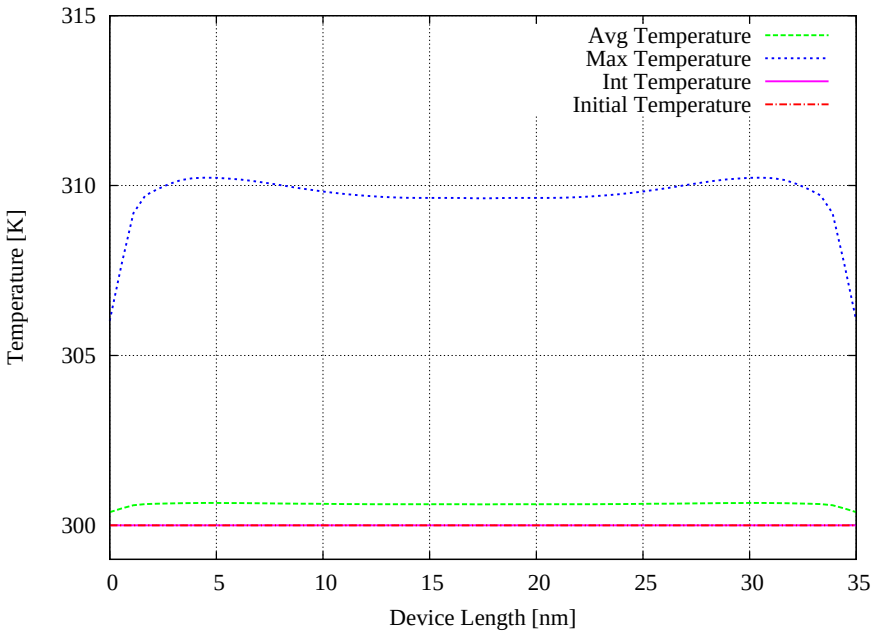

Figure 3.27 Plot of the temperature distribution along a 35nm homogeneous silicon device with a 300mV bias and a equilibrium temperature of 300K. The max temperature was determined by solving for the temperature distribution at each energy level and taking the corresponding max temperature.

Thermal-Field Emission Model Validation

The NEGF thermal-field model that was developed to study both thermionic and field emission was validated by investigating the models response to the two independent biases. First the model was validated for the response from a temperature bias in the thermionic regime. Then the model was studied from a field emission point of view calculating the response of a electrical bias. The performance of these two independent case gives the model confidence that it can handle any intermediate regime in which the response lies in between thermionic and field emission regimes. Figure 3.28 is an illustration of the band diagram for a thermionic devices labeled with the dominate modes of energy transmission between the anode and cathode. The NEGF model does not account for the anode heating due to the fact that a constant temperature bath is specified at either boundary.

Thermionic Model Validation

In the case of thermionic response when a specified temperature is applied to both the anode (collector) and cathode (emitter), it is assumed that both contacts are

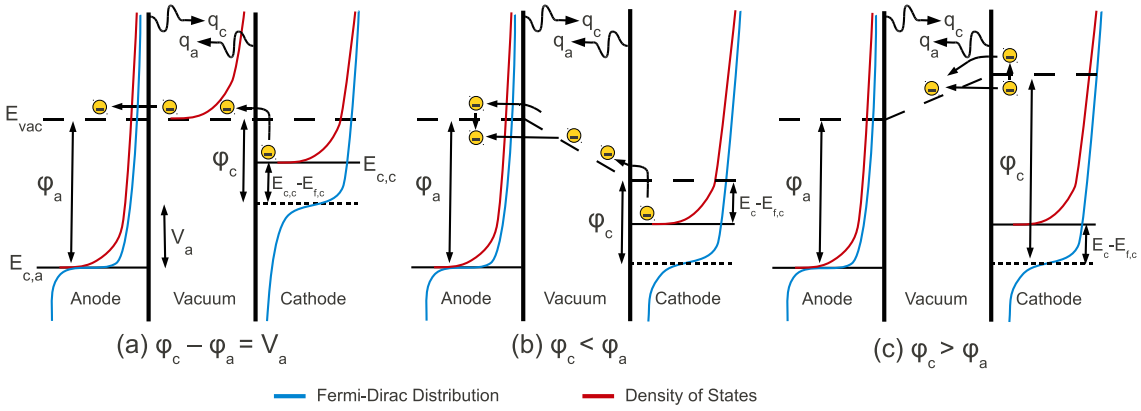

Figure 3.28 Illustration of the band diagram of a semiconductor thermionic emission device with indicated energy transport mechanisms labeled. Energy flux due to thermionic emission and the energy flux due to radiation ($q_{a,c}$) between the anode and cathode. The model neglects the effects of anode heating as a results of specifying a constant temperature bath at the anode and cathode region. There are three conditions, (a) applied voltage states, (b) cathode work function less than anode work function, and (c) cathode work function greater than anode work function.

constant temperature baths so radiation effects can be neglected. The argument of negligible radiative effects is demonstrated in Figure 3.29 which is a plot of the heat flux from two infinite parallel plates. The plots are derived from Equation 3.8 which states the heat flux (q) is proportional the Stefan-Boltzmann constant (σ) times the difference in temperature to the fourth of both the cathode (T_c) and the anode (T_a). The justification for this argument comes when the heat fluxes from the radiation are compared to the total emission current due to the electrons.

$$q_r = \epsilon\sigma(T_c^4 - T_a^4) \tag{3.8}$$

The model accounts for the thermionic emission from both the anode and the cathode by specifying the appropriate temperature at both boundaries. Figure 3.30 is a plot of the band structure derived from the effective mass Hamiltonian which is plotted on the left of the figure and the associated current density versus energy on the right of the figure. The current density in Figure 3.30 is monitored at either boundary and the energy into the system is positive and the energy out of the system is negative. It is critical that the integral of the anode and cathode current is equal

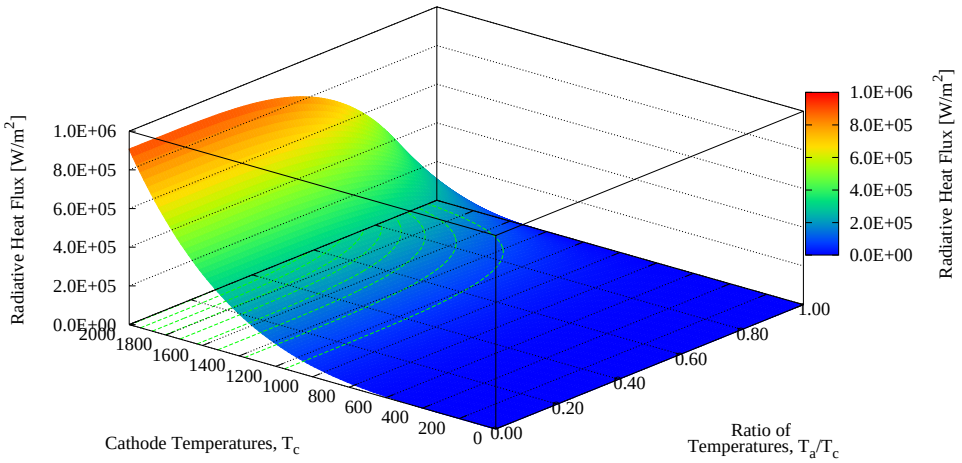

Figure 3.29 Plot of the radiative heat flux as a function of cathode temperature and ratio of cathode temperature (T_c) and anode temperature (T_a). This plot is calculated from Equation 3.8 for the heat flux between two infinite parallel plates in the far field with an assumed emissivity (ϵ) of unity.

in order to conserve charge. Figure 3.30 is classically what you would expect from a thermionic emitter, in that the emission current resides above the vacuum level. The figure also demonstrates an additional effect that is related to the quantum mechanical nature of the simulation such that the emission current is not continuous but rather has peaks of energy which correspond to the discrete states within the system. If the system were increased in all spatial dimensions, then the number of states would increase and the degree of confinement would decrease. States would fall and the emission current would become more continuous as would be expected in the continuum.

For ease of computational effort it was determined that the critical size at which continuum values could be reproduced of thermionic emission were when the vacuum was greater than 10 nm, as shown in the left plot in Figure 3.30. By easing the degree of confinement within the vacuum, states fell down in energy and emission current increases to a steady value in which the addition of more states did not heavily influence the emission current. Furthermore there is justification for making the vacuum level larger then 5 nm in order to avoid the possibility of electrons tunneling through the vacuum region at an energy lower than the vacuum energy.

As pointed out in the introduction of this thesis (Section I), traditionally before the advent of semiconductor technology, researchers had focused on using materials

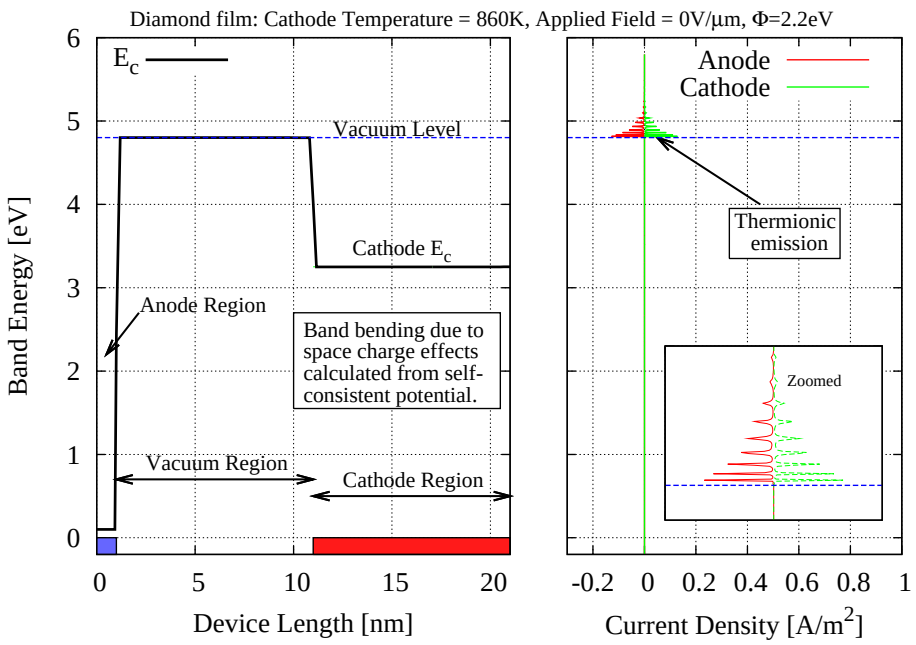

Figure 3.30 Plot of the conduction band edge derived from the effective mass Hamiltonian (left) and a plot of the current versus energy (right). Note the response of classic thermionic emission above the vacuum level.

with high melting points such as tungsten for thermionic emitters. To demonstrate the ability of the model developed in this research to not only capture the emission from semiconductors but also metal emitters, a metal Tungsten material was modeled. Tungsten with a work function of approximately 5.4 eV was simulated using the model and compared to Richardson's equation, Equation 2.53. To recall, Richardson's equation is based on analytic simplification of the density of states and Fermi function to be commensurate with the trends of thermionic emission from a metal surface. Figure 3.31 is a plot of the three materials including tungsten, amorphous carbon with a work function of 5 eV and the current state of the art doped diamond with a work function of 2.2 eV. The model which is depicted at points in Figure 3.31 demonstrates that the model can capture the trends of Richardson's equation (lines) along with the ability to predict the on set of thermionic emission which is outside the scope of the analytic expression.

The model provides a means of determining the charge density across the structure. This provided validation that the model was operating correctly. Figure 3.32 is a plot of a diamond film with the cathode at an elevated temperature. Notice that

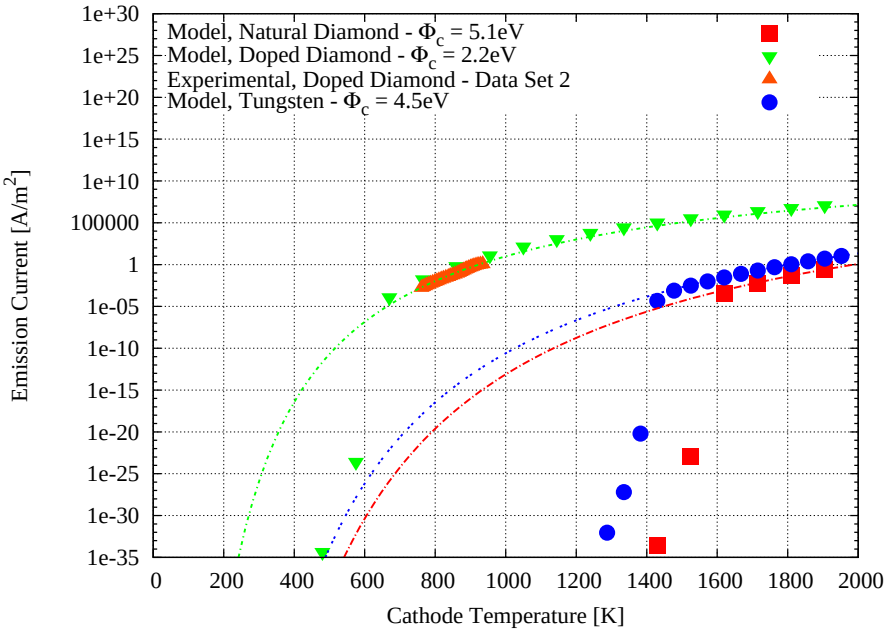

Figure 3.31 Comparison of NEGF thermionic model prediction of tungsten, intrinsic diamond and doped diamond. The model predicts the onset of thermionic emission which is absent from the Richardson relationship.

the contact region has an extremely high charge density which is spilling over into the cathode material. There is also a slight image potential near the edge of the cathode which is due to the gathering of charge near the vacuum barrier. Because of this larger charge density one would expect a image potential to be present also near the tip which is an additional barrier the thermally excited electrons must overcome to escape into the vacuum.

Thermionic Emission vs. Temperature

To validate and verify the response of the thermionic NEGF model the work function and temperature of the cathode were varied. Figure 3.33 is a plot of the emission current versus cathode temperature. Radiation effects are neglected. Both the anode and cathode are assumed to be constant temperature baths, neglecting the effects of anode heating from the electron collecting on the anode. In order to match to experimental data by Paxton (2011) the difference in work function of the anode and cathode ($qV_o = \Phi_c - \Phi_a$) were considered offset by an applied voltage, resulting in modeling pure thermionic in the absence of a field.

Figure 3.33 demonstrates the NEGF thermionic match Richardson's equation

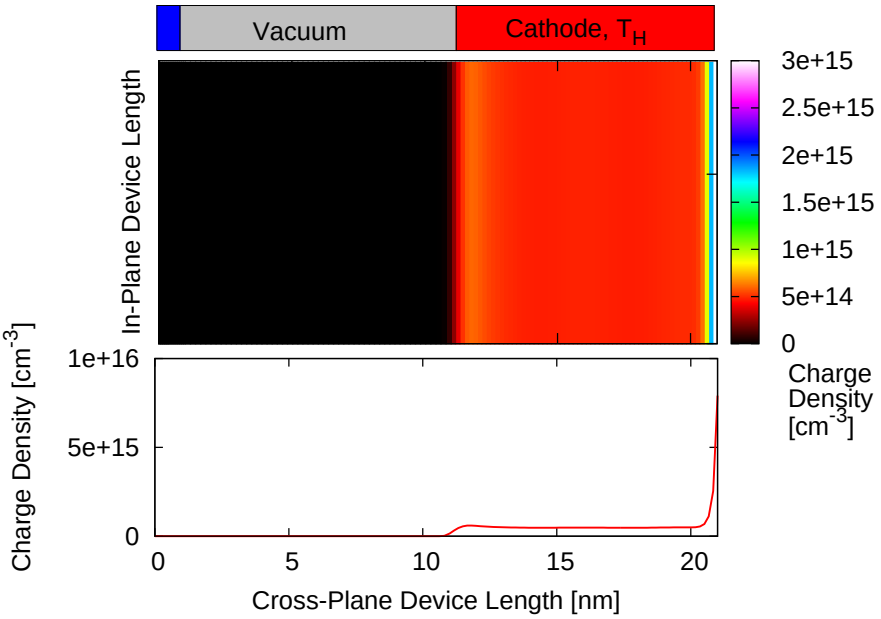

Figure 3.32 Plot of the charge distruption calculation for a thin film thermionic material with an elevated cathode temperature.

(Equation 2.63) and the experimental data (Paxton, 2011). One key element of the model is the ability to predict the onset of thermionic emission. Comparing the lines to the model's predicted values in Figure 3.33, Richardson's equation for a work function of 2.2 eV would predict thermionic emission beginning at approximately 200 K. However, the model predicts thermionic emission begins around 500 K. This can be supported by the experimental results in which emission was only able to be measured after about 600 K.

In addition to predicting emission characteristics, the goal of the model is to determine the cooling effect or heat flux at the cathode which is in response to electrons leaving the cathode region. Knowing the spectral emission shown in the right part of Figure 3.30 and the kinetic energy of the electron associated with the thermal energy ($1/2mv^2 = k_BT$) an estimate of the power or heat flux can be determined. Figure 3.34 is a plot of the heat flux for varying work functions and cathode temperatures. The lines are estimated heat fluxes from Richardson's equation and a Maxwell distribution of velocities. The fitted Richardson's equation is used to predict the cooling effect of the experimental device. However, the models value of a work function of 2 eV is a better predictive measure of heat flux. Further explanation of this will be provided in the results section.

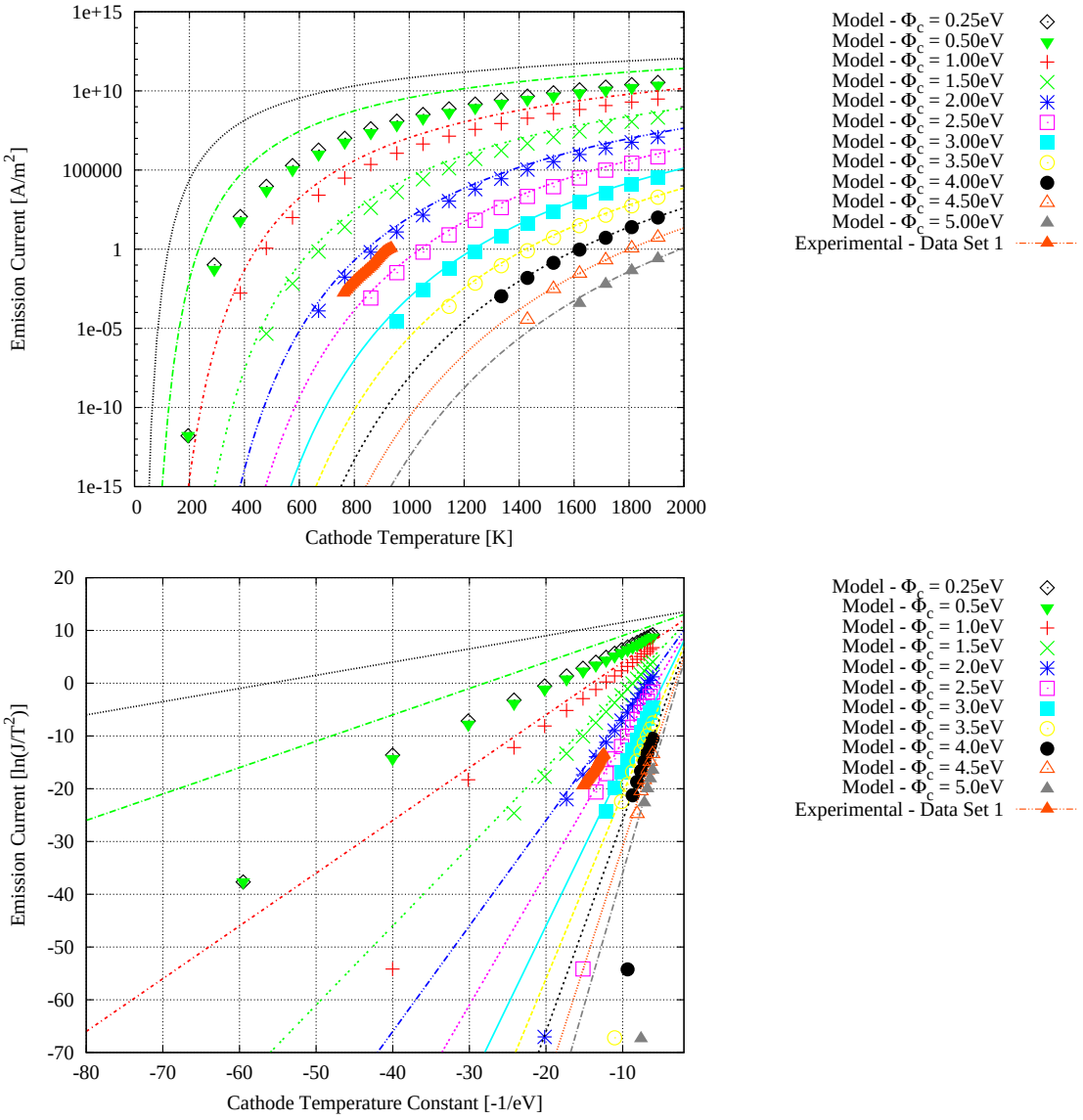

Figure 3.33 The NEGF thermionic model was compared to experimental doped diamond samples by varying the associated workfunction of the material. A work function of around 2.2 eV was required to reproduce the experimental trends. (a) Current versus applied cathode temperature. (b) Richardson plot of thermionic emission.

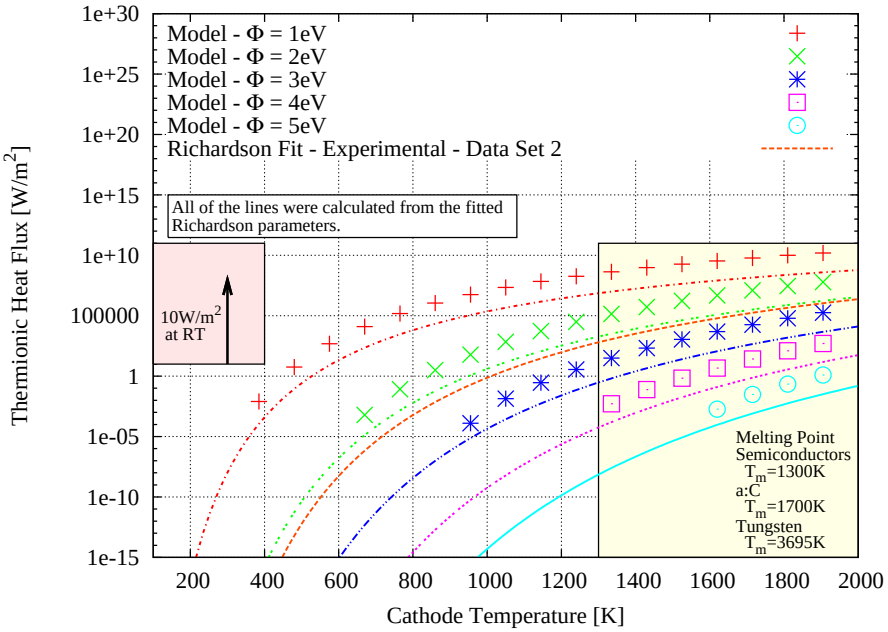

Figure 3.34 Calculation of the heat flux from the cathode based on the energy distribution of electrons and their thermal velocity.

Computational Scaling and Parallel Performance

All the models developed in this research were written using a native Fortran 95 language and implemented to take advantage of high performance computing (HPC) facilities. Effort was spent during the programming phase to optimize the code so that large device sizes could be studied. For the 1D structures which include the superlattice thermoelectric devices the electrical and thermal models were parallelized by dividing the energy range across multiple processors. MPI routines were used to pass the information back and forth. Because both the thermal and electrical model involve a matrix inversion for each energy level there is considerable speed up if these can be done in parallel on difference processors. When dissipation is added to the models the bottle neck of the program is no longer the inversion but rather the mixing done to calculate the scattering matrices. Effort was spend optimizing the shifting routines but the scaling was limited to 8 processors.

The inversion of the Green's function was handled by a LU decomposition routine. Standard direct solver LU decomposition (LAPACK) routines were used for the tri-diagonal 1D superlattice models. Before the models were written in Fortran and optimized the ballistic theory was test in a MATLAB code. The speedup by using a direct tri-diagonal solver and being smart about the sparse matrix multiplication

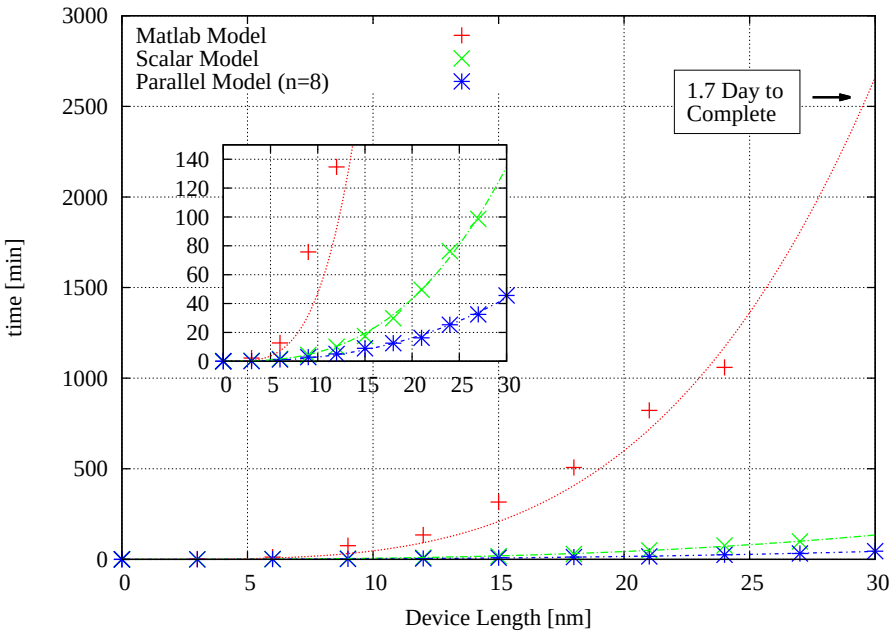

Figure 3.35 Plot of the MATLAB model and parallel Fortran model performance. About a 52 times speed up was achieved by solving the energy range in parallel and using direct solver techniques.

gain a tremendous speedup as demonstrated in Figure 3.35. In MATLAB you would expect a 30nm device to take about 1.7 days to complete where compared to the parallel (number of processors = 8) Fortran model, about 50min. That speed up equates to about a 52 times speed up.

The performance of the parallel Fortran model was evaluated by calculating the speedup as a function of the number of processors. Figure 3.36 is a plot of the speedup as a function of the number of processors. The solid line in the figure represents the idea speed or linear speedup which corresponds to the decrease in run by half for each additional processor that is added. If you draw a line through the points which are evenly divisible by 8 then a of about 20 is expected when ran across 32 processors. The reason why it is less than a theoretical linear speedup has to do with the reduction of spatial matrices and the calculation of Poisson's equation on a single processor.

To aid in the speed up of the inversion routine of the 2D Hamiltonian for the thermionic and nanocrystalline composite thermoelectric model the inversion was handled by two methods. The first method was a sparse LU factorization using SuperLU. The second method was a LU factorization on graphic processing units

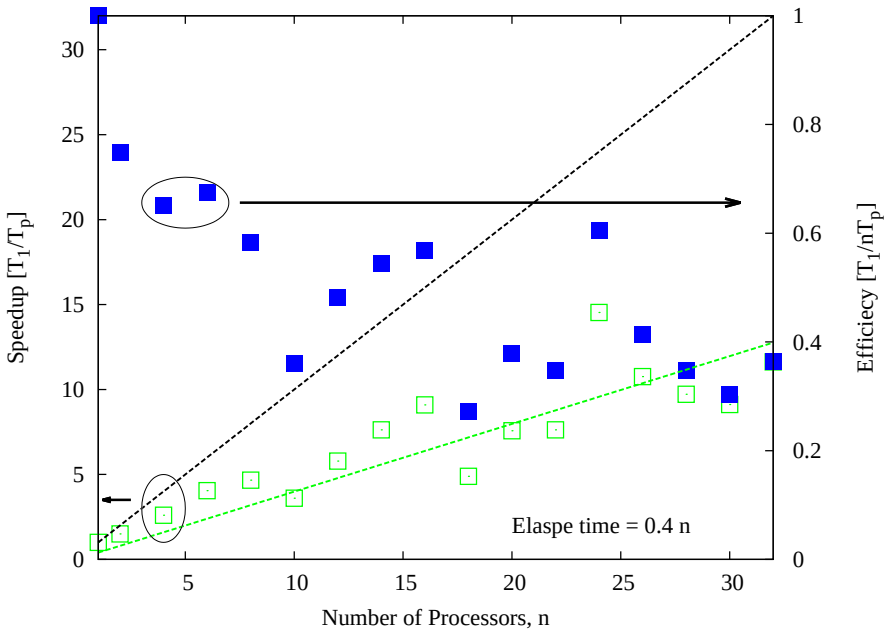

Figure 3.36 Plot of the parallel performance speedup of the model using HPC resources. Runs were made on a 8core/node Xeon E5520 cluster. The true scaling is more representative when the nodes are divisible by 8.

(GPUs) using MAGMA routines. Both the SuperLU and GPU LU factorization saw approximately a 3 times increase over full matrix LAPACK LU decomposition routines. As the matrix increases with device sizes the speed up over the LAPACK LU routine is even more evident. Once a sparse LU factorization routine is developed for GPU execution it is suspected that the speedup could be substantial.

CHAPTER IV

RESULTS

The previous chapters have familiarized the reader with the theory of thermoelectric and thermionic conversion. The validation chapter provided some confidence to the modeling trends. This chapter takes these developed models and uses them to optimize thermoelectric and thermionic nanostructured devices. One of the main uses of these models is to understand how the geometry affects the transport characteristics. Because these models were written to take advantage of high performance computing facilities they not only allow geometry to be studied but materials with lengths that you would find in operational devices. The first optimized thermoelectric device will be a variably spaced superlattice (VSSL) followed by a study of a two dimensional planar nanocrystalline composite thermoelectric device. Last will be the investigation of nano-tip thermionic devices.

Variably Spaced Superlattice (VSSL)

Through band engineering of superlattice materials it is hypothesized that a increased performance can be obtained from variably spaced superlattice (VSSL) structures, leading to further enhancement of thermoelectric properties. This presumption are based on electrical studies by other researchers(O'Dwyer et al., 2005; Summers and Brennan, 1986) and our own investigation into regular superlattice structures. This research study demonstrates how variably spaced semiconductor superlattice materials can not only out perform equally spaced superlattices but also exhibit anisotropic filtering behavior resulting in directionality of thermoelectric properties. This study is unique because 1) a directional Seebeck coefficient along a single crystalline axis has never been investigated or even suggested, and 2) variably spaced superlattices have not been investigated extensively for thermoelectric applications.

There are two distinct advantages to the electrical and thermal transport properties that arise from controlling the film thickness within the superlattice structure. The first advantage of increased electrical conductivity is illustrated in Figure 4.1 and is a result of electronic confinement of the low lying energy levels of the conduction band within the well region. The second advantage is the reduced thermal conductivity as a results of the increased thermal boundary scattering that arises from the

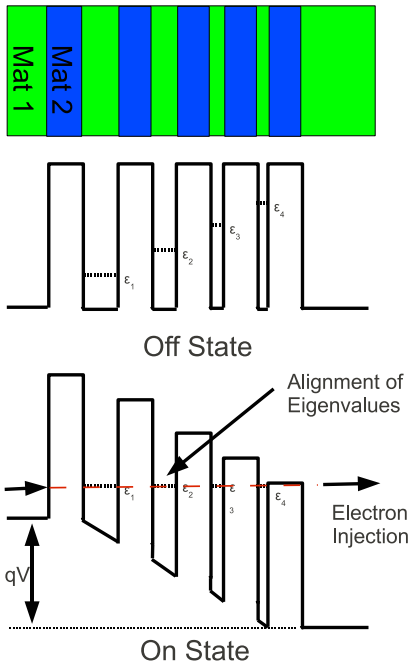

Figure 4.1 Illustration of the variable spaced superlattice device with in the off-state and on-state where there is band alignment and injection of electrons across structure.

varying layer thickness of the well regions and the increased number of interfaces. The design criteria are set by designing around a favorable electrical structure and assuming the thermal properties will follow.

The band structure of the VSSL material can be described by a rectangular periodic potential where the two different alternating film materials define well and barrier regions with the added complexity of decreasing the layer thickness over consecutive well regions. By adjusting the film thickness of the well region, the degree of confinement of the low lying energy states within this region can be shifted. If the consecutive layer thicknesses are selected appropriately such that they are proportional to the voltage drop, an injection of electrons can be achieved as a result of the apparent alignment of energy levels, see Figure 4.1. The directionality of the material arises from the alignment of states when the voltage drop is in the favorable direction, as opposed to a divergence of energy states in the opposing biased direction.

The decreased thermal conductivity of VSSL arrives from the phonon spectral response of the structure. Treating each layer of the superlattice structure independently and calculating the frequency content associated with each independent layer

an argument arises for the decreased thermal conductivity. From the wave equation, the frequency content will be a function of the thickness of each individual layer. Constructing a composite of the frequency content of the individual layers and analyzing the phonon spectra as a whole reveals phononic band gaps or frequencies where phonons are not allowed. In treating a phonon as a particle, as the phonon moves across a single layer of the structure it interacts with interface of a neighboring layer and the phonon must either scatter into an allowed energy level of the next layer or tunnel through the layer. The act of the phonon changing energy at these interfaces results in increased thermal boundary scattering.

The argument of phononic band gaps can also be framed in terms of a basis set. Treating the cumulative mass within each independent layer as two different nearest neighbor masses, we can make the analogy that a single bilayer forms a basis set as would be seen in a diatomic crystal. The acoustical branch of the dispersion will depend on the number of atoms within the larger of the two layers. The optical branch will be offset by some energy associated with smaller of the two masses and form a phononic band gap relative to the top of the previous branch. The number of branches will depend on the total number of bilayers within the structure. The dispersion relation can be conceptualized from the notion of the masses oscillating independently within their associated layer and together across multiple layers. It is the essence of two differing masses periodically arranged within a system that will provide the phononic band gap.

VSSL Material Configuration

The selection of the material configuration was based on demonstrating the trends associated with a VSSL and a non-VSSL material. There was no attempt to optimize the VSSL structure in this research but rather to show a performance difference. Due to the distribution of electrons entering the system, the strict energy level alignment of consecutive layers is relaxed. However perfect alignment of the energy levels is optimal, but using an approximate structure is reasonable for proof of concept. To design a general VSSL structure, thickness of consecutive layers can be estimated under simple assumptions. Because the Seebeck voltage is dependent on the device geometry this estimated design is only an approximation. To calculate and approximate structure, first focus on only two neighboring well regions, assuming the voltage drop is linear across the whole device region and the confined energy levels of the well follow the relation $\frac{\hbar}{2m^*}\frac{1}{a^2}$, where a is the layer thickness. The neighboring

layer has energy levels that follow $\frac{\hbar}{2m^*}\frac{1}{(a+L_g)^2}$, where L_g is an incremental increase or decrease of the neighboring layer thickness. Equating the voltage drop across the entire device region to the voltage drop between the neighboring layers a relation can be written as follows,

$$\frac{-\hbar^2}{2m^*}\left(\frac{1}{(L_w+L_g)^2}-\frac{1}{(L_w)^2}\right)=\frac{ST}{L_t}, \tag{4.1}$$

where L_w is the well width, L_b is the barrier width, L_g is the increment of consecutive layers and L_t is the total length. Specifying a device length of 55 nm and assuming the approximate Seebeck to be 500 μV/K. For a 55 nm device with a 10 K temperature bias the L_g parameters is 0.508 nm which is the basis for selecting 0.5 nm as the increment for the remaining studies in this research.

VSSL Performance

The first material of interest is a +0.5 nm VSSL (+VSSL); the thickness of the well region is increased consecutively by 0.5 nm over seven well regions and the barrier region is maintained at 5 nm. The first well region has a thickness of 0.5 nm and the last well region in the series has a thickness of 4 nm. The volume fraction of silicon within this material is approximately 51.4% Si. The second material is a -0.5 nm VSSL (-VSSL), the construction is the same as the first material except the bias is applied in the opposite direction. The third material, a non-VSSL structure, has a total length of 60 nm with seven heterojunctions and the individual layers all have a thickness of 4 nm for both the well and barrier regions.

The three structures are simulated at various temperatures to facilitate a relative comparison of performance. Figure 4.2 includes plots of the power factor (PF), thermal conductivity and figure of merit (ZT) for the three structures as a function of temperature. The first plot demonstrates the power factor ($S^2\sigma$) as a function of temperature labeled with closed symbols associated with left axis. On the same plot, the Seebeck coefficient (S) is plotted with open symbols associated with the right axis. The trends of the PF are typical for common TE materials for increasing temperature. The PF increased for all structures as the temperature increases and the relative difference in PF between the VSSL and non-VSSL structure decreases with increasing temperature. These trends are a result of the increased electron population as the temperature increases and corresponding to the increased number of tunneling electrons between contacts. Referring back to equation 2.9, as the Fermi function of

either contact increase with temperature the current will also increase proportionally, resulting in greater conductivity ultimately influencing the PF.

Focusing on the PF at 300 K for the +VSSL (closed circles), a value of approximately 3000 μWm^{-1}K^{-2} compared to 175 μWm^{-1}K^{-2} for a non-VSSL material is apparent. The PF is greater for the +VSSL material because the electrical conductivity increases considerably due to the alignment of energy levels resulting in the injection of the electrons across the structure. Investigating the PF of the -VSSL and non-VSSL suggest that the PF values are relatively close to each other as a result of the non-alignment of energy levels. In essence, the non-aligned level cause the transport in the -VSSL structure to be governed by tunneling through barriers and wells as seen in a traditional (uniform) superlattice (non-VSSL) structure.

In the same plot, focusing on the Seebeck voltage (open symbols), as the temperature increases the Seebeck decrease contrary to what was depicted for the PF values (closed symbols). Comparing the Seebeck values for the +VSSL structure at 300 K to that of the non-VSSL suggests that the Seebeck coefficient decreases at the expense a large electrical conductivity. This is a common trend in most materials where the Seebeck coefficient and electrical conductivity are inversely related. The Seebeck increases as a result of the material's ability to maintain a greater charge distribution as seen in the non-VSSL and -VSSL structures.

Comparing both the +VSSL and -VSSL Seebeck coefficient from the first plot of Figure 4.2 an apparent directionality is present. At 300 K the Seebeck voltage is nearly double for the -VSSL compared to the +VSSL. This directionality trend is reversed for the PF values due to the electrical conductivity having the opposite direction trend compared to Seebeck. The directionally is depicted in both the Seebeck and electrical conductivity but the PF trends are mostly influenced by the conductivity trends.

The second plot in Figure 4.2 is the thermal conductivity as a function of temperature. The electronic contribution (k_e) of the thermal conductivity (open symbols) and the thermal contribution (k_p) of the thermal conductivity (closed symbols) are both plotted. The summation of the electron and phonon contributions are composed into a single thermal conductivity ($k_e + k_p$) value depicted by the dashed lines. The total conductivity of the +VSSL material is the red line, the green line is the -VSSL, and the blue line is the non-VSSL.

The electrical contribution of the thermal conductivity (k_e) for the +VSSL (solid circles) has the largest overall conductivity of all the structures. This is a result of the electrons that carry thermal energy experiencing the same increase in

conductivity due to alignment of energy levels as the transport electrons. For a majority of the temperature range the +VSSL, thermal conductivity is almost entirely influenced by k_e from 200 K and greater. For the -VSSL and the non-VSSL material there is a transition at approximately 600 K in the dominate mechanism of thermal conductivity. Prior to this transition temperature the phonon thermal conductivity (k_p) is dominant; however, past 600 K the total thermal conductivity is dominated by the electrical contribution (k_e). This transition is situated close to the Debye temperature of silicon (645 K) where the phonon conductivity (k_p) plateaus. The Debye temperature of germanium is approximately (374 K) and the Debye temperature of the superlattice structure is that of the material with the greater Debye temperature. As the temperature increased above the superlattice Debye temperature the +VSSL and -VSSL/non-VSSL structure are dominated by both the k_e contribution and follow a similar trend.

Using Equation 1.1, the overall figure of merit, ZT, can be calculated from the composite of the two previous plots of PF and thermal conductivity. Multiplying the power factor (PF) times the temperature (T) and dividing by the total thermal conductivity ($k_e + k_p$) we arrive at the overall ZT value. The calculated ZT as a function of temperature, the third plot in Figure 4.2, demonstrates that the +VSSL materials (closed circles) outperforms the other two materials up to the thermal conductivity transition temperature of approximately 600 K. This transition temperature, as mentioned before, is a result of the electrical contribution (k_e) of the thermal conductivity dominating the total thermal conductivity. In addition, due to the increasingly large thermal conductivity value, as temperature increases the denominator of the figure of merit is overwhelmed by the trends of the thermal conductivity.

At a temperature of 400 K, a $ZT = 0.20$ for the +VSSL and a $ZT = 0.04$ for the non-VSSL material was calculated, resulting in five times increase in the ZT for a +VSSL material. These results suggest that +VSSL structures can achieve a greater ZT at room temperature over a non-VSSL due to a 17 times increase in PF and only a 4 times increase in thermal conductivity. The transition region where the non-VSSL begins to outperform the +VSSL material is associated with the electrical contribution (k_e) of the total thermal conductivity dominating the figure of merit. Again, comparing the +VSSL and -VSSL structure a directional dependence arises in the ZT plot and is heavily apparent at temperatures below 600 K. Additionally, the -VSSL structure follows the trend of the non-VSSL structure as expected due to the lack of alignment resulting in mainly tunneling electrical transport similar to the non-VSSL structure.

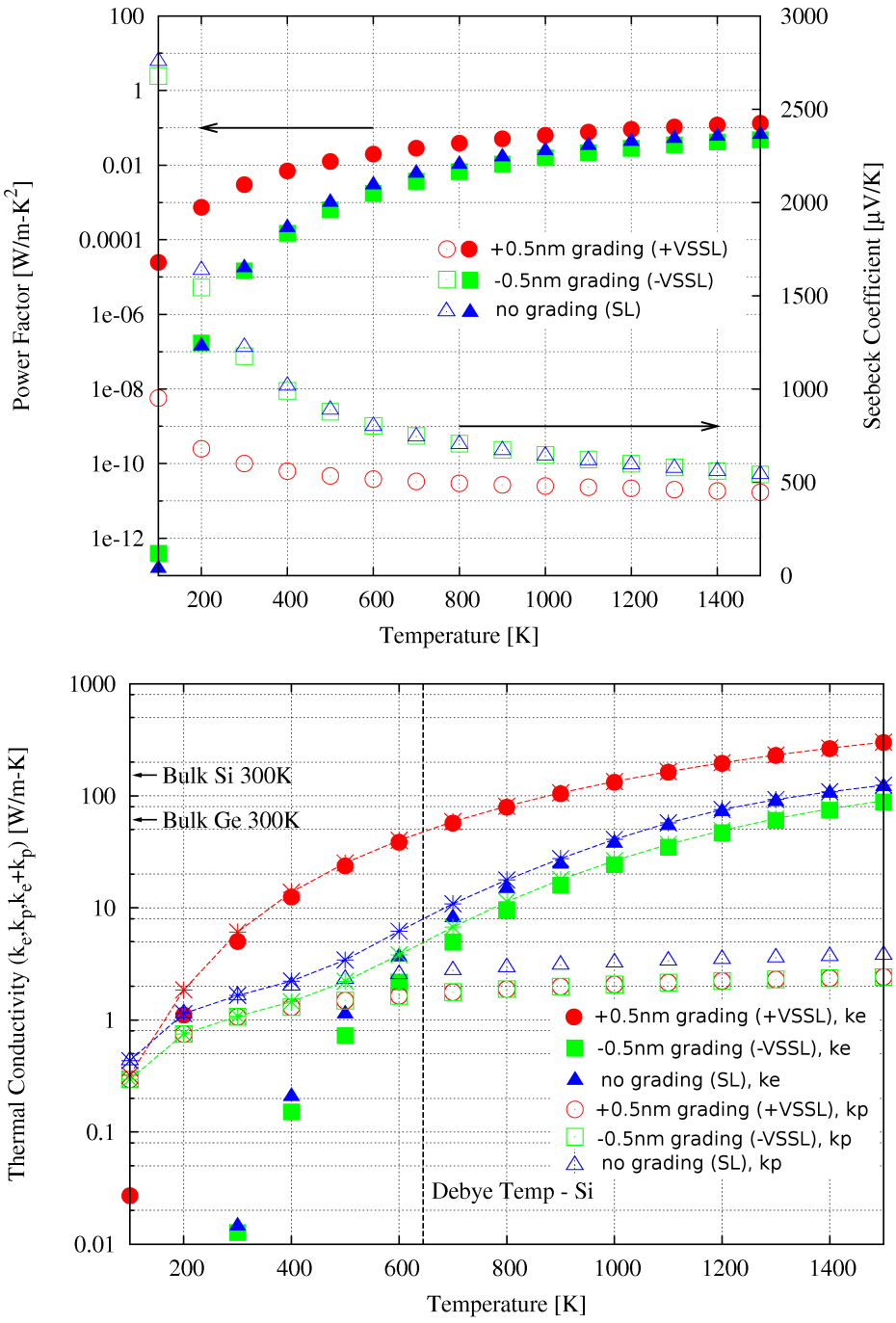

Figure 4.2 Ballistic electrical and thermal properties calculated for two oppositely graded VSSL and non-VSSL materials as a function of temperature. Circles: +0.5 nm grading (+VSSL), squares: −0.5 nm grading (-VSSL), triangles: no grading (non-VSSL). +VSSL material has a $ZT = 0.20$ compared to a $ZT = 0.04$ for non-VSSL at 400 K. Lines were added to guide the eye.

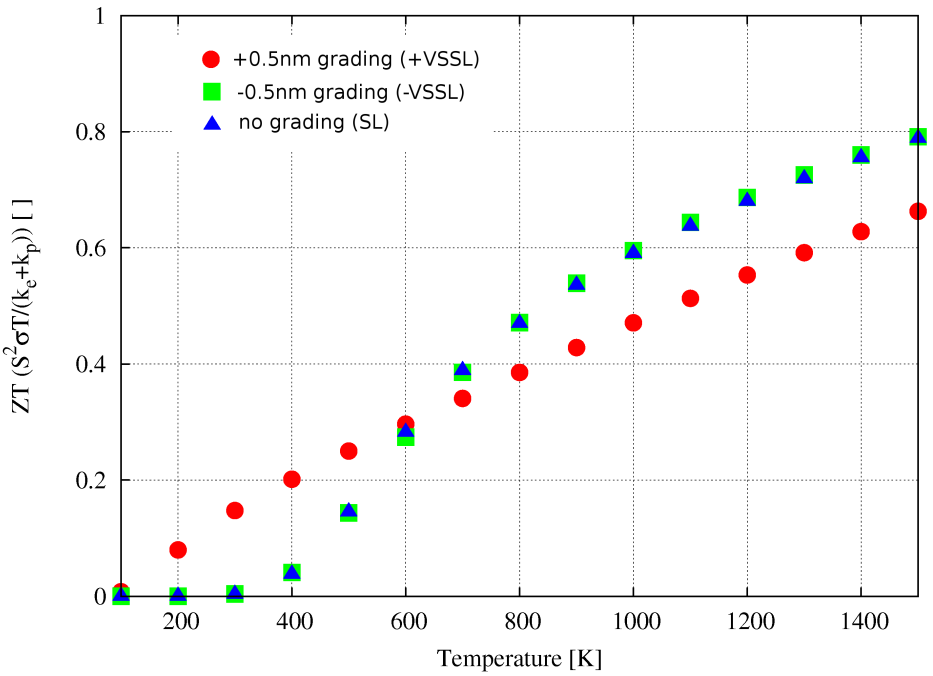

Figure 4.3 Ballistic ZT values calculated for two oppositely graded VSSL and non-VSSL materials as a function of temperature. Circles: +0.5 nm grading (+VSSL), squares: −0.5 nm grading (-VSSL), triangles: no grading (non-VSSL). +VSSL material has a $ZT = 0.20$ compared to a $ZT = 0.04$ for non-VSSL at 400 K. Lines were added to guide the eye.

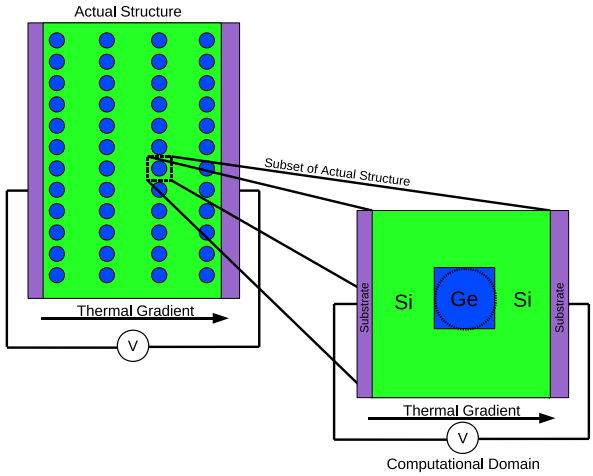

Figure 4.4 Illustration of the nanocrystalline composite (NCC) superlattice structure. Note that the model domain is an abstraction of a single crystalline modeled with periodic boundary conditions.

Nanocrystalline Composite (NCC) Superlattice

Nanocrystalline composite (NCC) device were analyzed by simulating a range of lengths by incrementally increasing the crystal spacing and crystal diameter respectively. Figure 4.6 depicts the Seebeck coefficient and electrical conductivity of homogeneous silicon (Si-Si), homogeneous germanium (Ge-Ge), silicon matrix germanium crystal (Si-Ge), and germanium matrix silicon crystal (Ge-Si) devices as a function of total device length. In this set of simulations the thickness of the matrix material (L_m) and diameter of crystal material (D) are increased by 0.2nm for each data point. The Seebeck coefficient is greatest for a silicon matrix, germanium crystal (Si-Ge) device as a result of the electronic band structure. The Si-Ge device can be thought as forming a classic quantum well-barrier structure, in which the conduction band offset between the germanium conduction band edge and the silicon conduction band edge is finite. The Seebeck performance is dependent on the equilibrium position (I=0) which is largely influenced by the low lying electron states in the electronic well (silicon layer for this configuration). A large build up of charge forms on either side of the barrier leading to non-uniform distribution of charge. This charge build up as a result of the barrier is beneficial from the point of view of increasing the Seebeck coefficient but is an obstacle for the electrical conductivity. The electrons either have to gain energy to go over the barrier or tunnel through the barrier, which

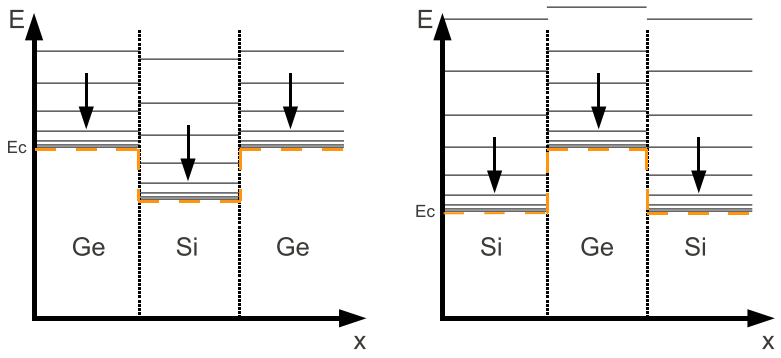

Figure 4.5 Illustration of the degree of energy confinement decreasing and energy levels collapsing causing alignment for select device lengths. Increase in conductivity is only apparent for the Ge/Si device due to presence of a barrier in the Si/Ge device.

is a function of the barrier length. In turn, the electrical conductivity is greatest for the homogeneous germanium device due to the absence of a barrier and the low conduction band edge (0.160eV). The crystal (barrier) is essential for increased Seebeck coefficient but can also be tuned through mindful selection of crystal size for good electrical conductivity performance.

The large increase in conductivity in Figure 4.6 for the Ge/Si devices is reasoned to be a result of the alignment of energy levels as the device length increases. As eluded to in Equation 2.2, the energy levels follow the relation, $\frac{\hbar^2}{2m^*a^2}$, where a has units of length related to the thickness of either the barrier or well region. Assuming the lowest lying conduction band edge of the barrier and well are located at a different energy, as the length of the barrier and well increases the energy levels will collapse as a result of decreased confinement. Illustration of the energy levels collapsing is shown in Figure 4.5. The increased transport is only apparent in the well case (Ge/Si device) due to the alignment of energy levels at conduction band minimum of the matrix material. In Figure 4.6, the conduction increases dramatically at L=2.5 nm as levels align then decrease and increase again at L=4.5 nm as additional levels align as they collapse and the device length increases. In the case of the Si/Ge device, where there is an electronic barrier is formed by the crystal material, the transport of the electrons in the low lying conduction band of the matrix material is always influenced by the barrier of the crystal and prevents the alignment of energy levels across the device at conduction band minima of the matrix material.

For the remainder of this article, we assume that the device is constructed from a silicon matrix with a germanium crystal based on the aforementioned Seebeck

performance.

Crystal Spacing

Constraining the crystal diameter (D) and increasing the crystal spacing, Figure 4.8 shows the corresponding Seebeck and electrical conductivity trends. Extrema in the Seebeck coefficient exist for devices with crystal diameter between 1.5nm and 2nm. For the 1.5nm crystal diameter, the maximum Seebeck coefficient lies where the gap between crystals is equal to 1nm. These extrema in the Seebeck can be attributed to a critical distance from the neighboring crystals in which discrete energy levels (eigenvalues) of the system diverge. As the spacing between crystals increases the energy levels collapse, forming a large localization of energy levels which are occupied by conduction electrons. If the device spacing decreases, the energy levels separate relative to each other forming widely spaced discrete energy levels. The shifting of energy levels limits the density of states below the conduction band edge of the barrier (0.602eV), inducing a filtering effect from the barrier Zide et al. (2006). This filtering effect limits the conductivity and alters the local density of filled electrons, ultimately influencing the Seebeck coefficient. The low lying energy states are visualized in Figure 4.7 in the plot of the local density of available states (LDOS) as pockets of states to the right and left of the barrier. Notice in Figure 4.7 that there are no states within the crystal (barrier) region which ultimately induces the filtering effect. Also, the low lying states next to the barrier are the states that contribute majority to the tunneling current because they lie within k_BT of conduction band edge of the matrix material.

Crystal Size

To study the relationship of crystal size on the electrical transport, the total device length (L) was held constant and the crystal diameter (D) was increased (Figure 4.9). The Seebeck coefficient increases as the crystal size increases; however, the electrical conductivity decreases at a much greater rate. Again, as the crystal increases in size it acts as a filtering mechanism and forces electrons to either transport around or tunnel through the crystal (barrier). The increased Seebeck is a result of the electron distribution below the crystal conduction band edge and is a function of energy levels within the electronic well region. The electrical conductivity decreases as the crystal size increases due to the decreased tunneling probability and the limited transport by low lying energy levels around the crystal. As the crystal diameter

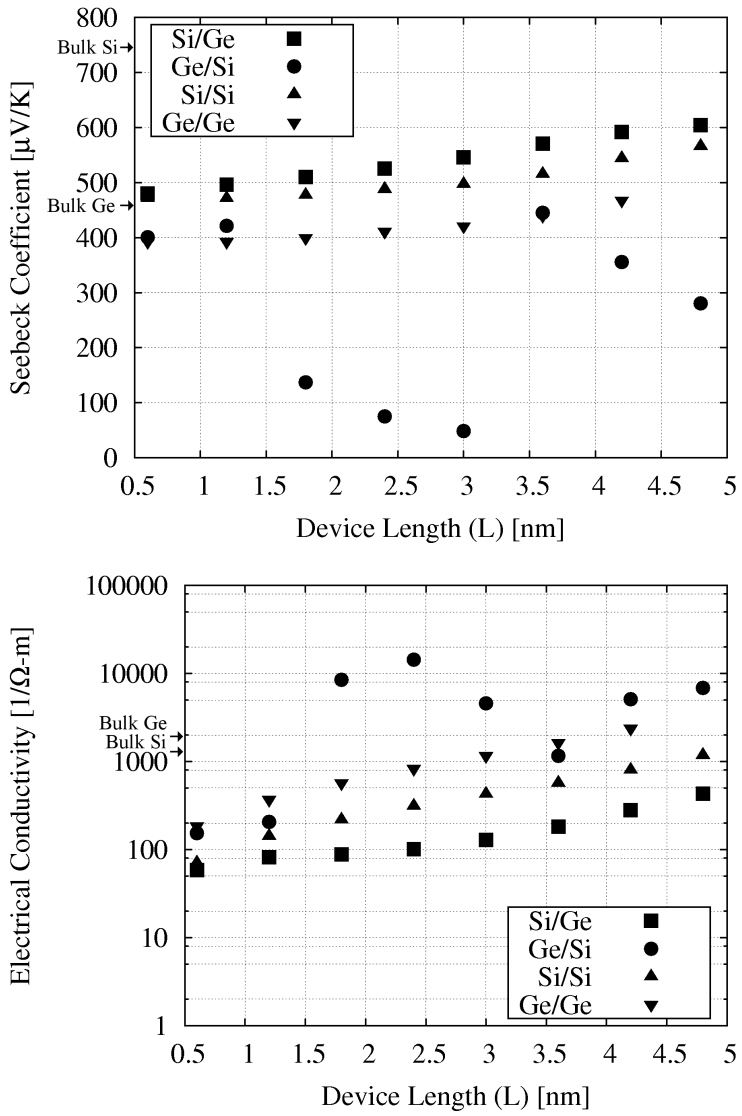

Figure 4.6 In-plane Seebeck and electrical conductivity for increasing device length. The matrix thickness (Lm) and crystal diameter are increased by 0.2nm and the device length (L) across the midspan is equal to two times the matrix thickness times the crystal diameter ($2L_m$+D).

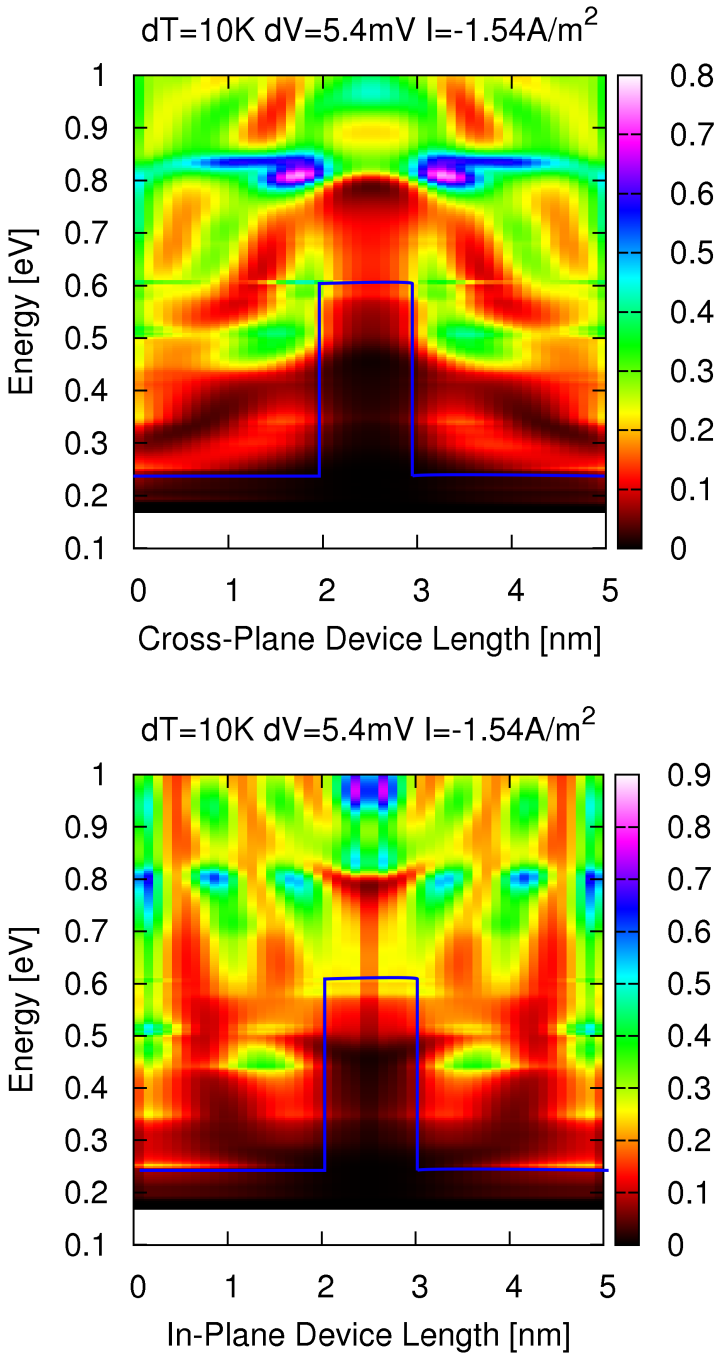

Figure 4.7 Local density of available states (LDOS) along the centerline in the cross-plane (transport) and in-plane (perpedicular transport) directions. Note the low lying states in the matrix (well) material. The device is a 2nm silicon matrix with a 1nm germanium crystal.

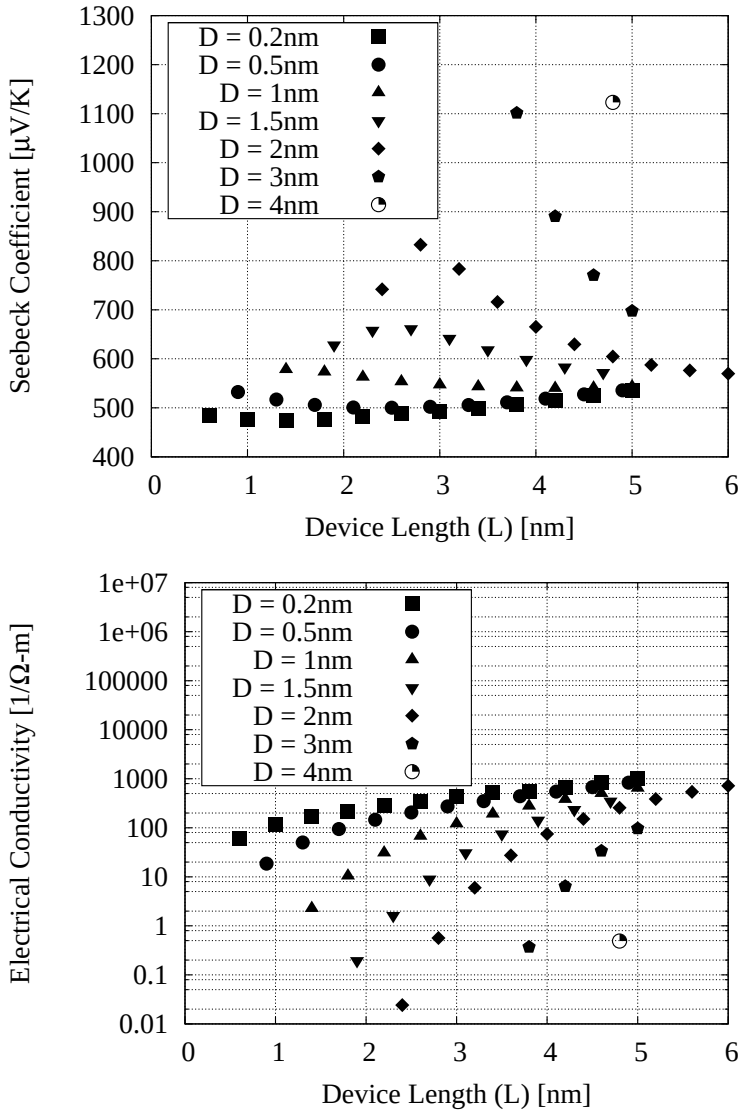

Figure 4.8 Seebeck and electrical conductivity for increasing crystal spacing (Lm) and constant crystal diameter (D). Silicon matrix germanium crystal(Si-Ge) device. Locus exists in the Seebeck coefficient for devices with crystal diameters between 1-3nm.

increases, the low lying energy levels in the matrix diverge limiting the number of states forcing electron to higher energy states decreasing conductivity. Because the conductivity decreases at a much greater rate than the Seebeck increases, the optimal power factor is obtained with a small crystal size.

Superlattice Comparison

A comparison of the power factor (PF) of nanocrystalline composite (NCC) devices to that of a superlattice (SL) device was carried out for a range of geometries (see Figure 4.10). The barrier material in both the SL and NCC device was chosen as the independent variable while maintaining an equivalent characteristic length. The characteristic length of both devices is defined as the distance between contacts in the transport direction. The superlattice results were calculated using a similar computational method described by Bulusu Bulusu and Walker (2008b,c).

In Figure 4.10, as the barrier thickness increases, the superlattice power factor drops at a much faster rate than for the nanocrystalline device. As discussed in previous sections of this article, the rate at which the NCC device decreases is governed not only by the probability of tunneling through the barrier, but also by transport around the barrier. Where the SL device is governed only by the probability to tunnel through the barrier due to the lack of dimensionality. Because the power factor is greater for the NCC device, there is confidence that the NCC device can out perform a SL device with equivalent characteristic lengths.

Thermionic Emission from Wide-Band Gap Materials

Much of the theory that revolves around the emission of electrons from a hot body is based on theories developed by Wilson (Wilson, 1908) and Richardson (Richardson, 1916) and Langmuir (Langmuir, 1923). It was not until recently did the application of wide-band gap semiconductor in thermionic device become advantageous. It was noted by researchers (Koeck and Nemanich, 2005; Maiti et al., 2001) that the addition of dopants and absorbates can significantly change the emission characteristics. This significant change in emission brought to question the applicability of Richardson's equation. Recall that Richardson's equation takes the form of Equation 2.53. Where J is the emission current, A is a fundamental pre-factor known as the Richardson constant, T is the temperature of the emitter, ϕ is the work function, and $k_B T$ is the thermal energy of the emitter. The Richardson equation can be linearized in the form of Equation 2.54 where the y-intercept is Richardson's

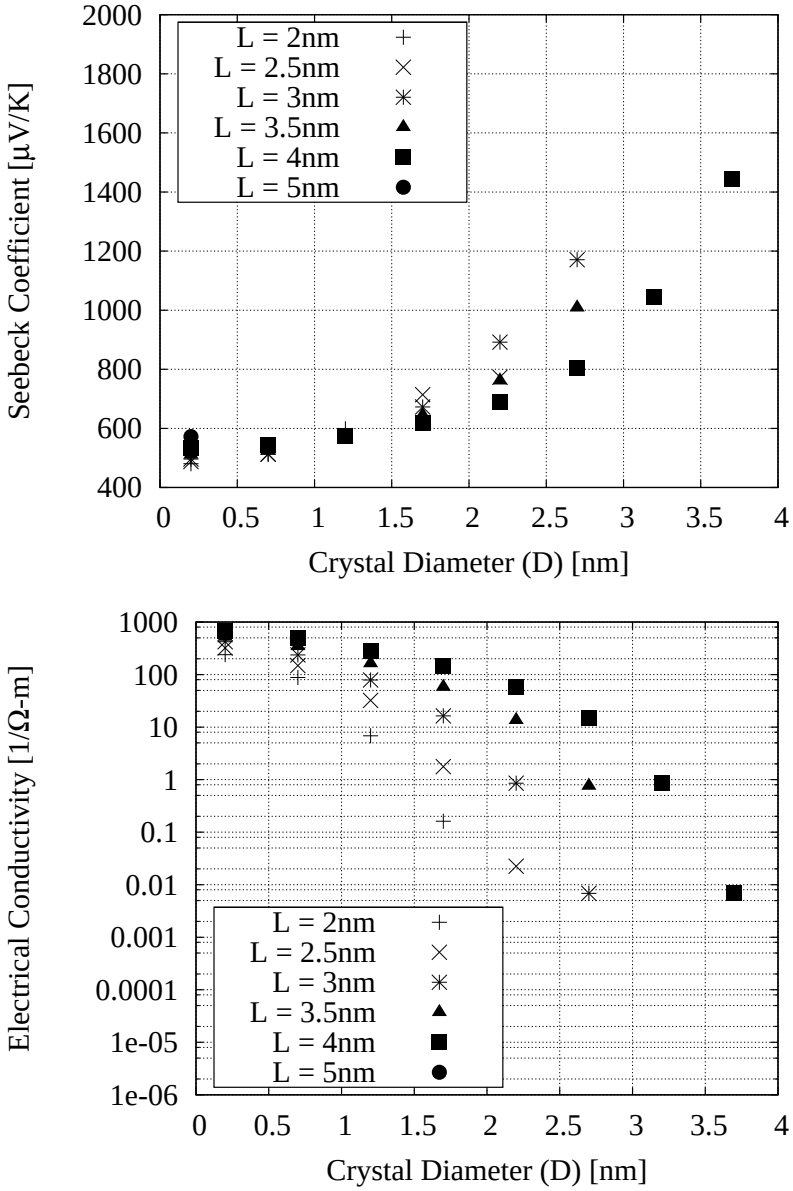

Figure 4.9 Seebeck and electrical conductivity for increasing crystal size, crystal spacing held constant. Silicon matrix germanium crystal(Si-Ge) device. Minimization of crystal size desired for optimal power factor.

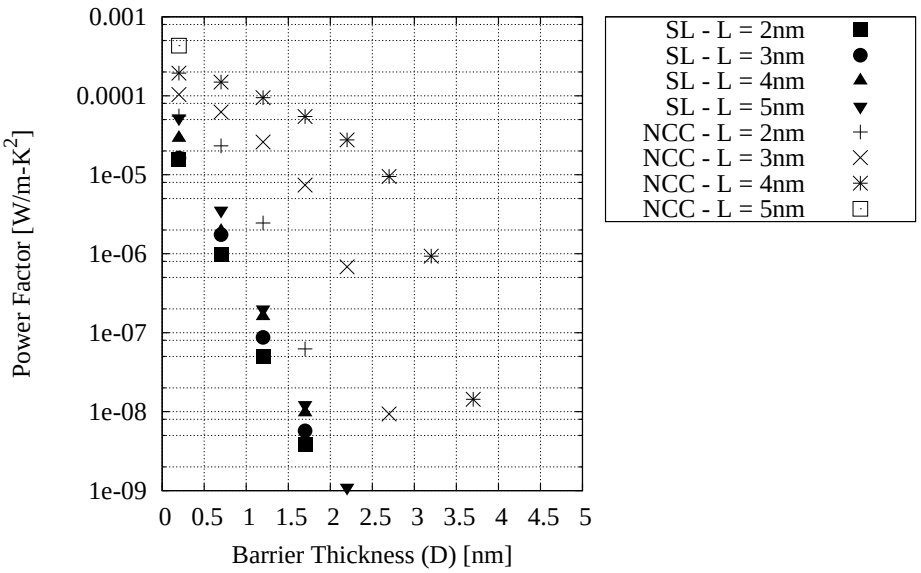

Figure 4.10 Power factor plot comparing superlattice device to a nanocrystalline composite device for increasing germanium barrier thickness. Greater efficiency can be achieved with NCC at equivalent SL device sizes.

constant A. This is very useful in helping explain the deviation in the models values from Richardson's theory.

Thermionic Emission - Richardson's Constant

Referring back to the validation section a plot of the current versus cathode temperature, Figure 3.33, demonstrated that the model (points) had the same trend of Richardson's theory (lines). However, there is a slight offset in the y direction which is evident in the linearized Figure 3.33b by a change in y-intercept. In the theory section the A term of Richardson's equation was determined to encompass the density of states description of a metallic emitter. In the case of the modeling approach developed in this research, an effective mass description was used which included an approximate effective mass term for the wide-band gap material. Because the effective mass term was less than unity for a diamond materials and there is a band gap associated with these material the density of states within the cathode is modified from a metallic description.

To further investigate the difference in Richardson's constant, a series of three cases were modeled with difference band offsets which is characterized by the distance between the Fermi level and the bottom of the conduction band edge. By varying

(eV)	$E_c - E_f$, ($Acm^{-2}K^{-2}$)		
Work function	0.0 eV	0.65 eV	1.0 eV
0.25	32.68	-	-
0.50	43.44	12.93	-
1.00	60.35	38.76	21.79
1.50	74.73	56.03	44.24
2.00	87.60	70.72	60.39
2.50	97.97	84.81	74.73
3.00	110.48	95.85	87.60
3.50	117.73	105.88	97.97
4.00	122.52	115.52	110.48
4.50	128.53	122.88	117.69
5.00	134.91	132.33	123.33
Richardson Theory	120.	-	-

Table 4.1 Table of the Richardson constant ($Acm^{-2}K^{-2}$) which is back calculated from the NEGF thermionic model by fitting Richardson's equation to the model's results for three materials with a band offset, $E_c - E_f$, from 0 to 1 eV . The effective mass was assumed unity.

the amount of energy between the equilibrium Fermi level in the cathode and the conduction band edge, $\phi - E_c$, Richardson's constant was back calculated by fitting Richardson's equation, Equation 2.54, to the model's predicted values. To limit the number of independent variables, the effective mass of these series of materials were assumed unity. Table 4.1 is the associated Richardson constant for a metal ($m^* = 1$) with a conduction band offset $E_c - E_f$ from 0 to 1 eV . The data from this table is plotted in Figure 4.11 with an associated fit. The fit of Richardson's constant versus work function is described with the following empirical equation,

$$A = A_o + \sqrt{\phi}\exp(A_m). \tag{4.2}$$

Here, A_o is the y-intercept, A_m is the slope of the line and ϕ is the work function of the material. A least squares method was used to fit all three sets of band offsets ($E_c - E_f$) with a unique slope (A_m) and a unique y-intercept (A_o). The relation of Equation 4.2 was reason from the derivative of the expression in Equation 2.62.

For the material which describes a metallic emitter with a band offset of $E_c - E_f$=0.0 eV the traditional Richardson constant of 120 $Acm^{-2}K^{-2}$ is recovered when the material has a work function of approximately 5 eV . Often in the literature, values of Richardson's constant for experimental metallic emitters varies around this

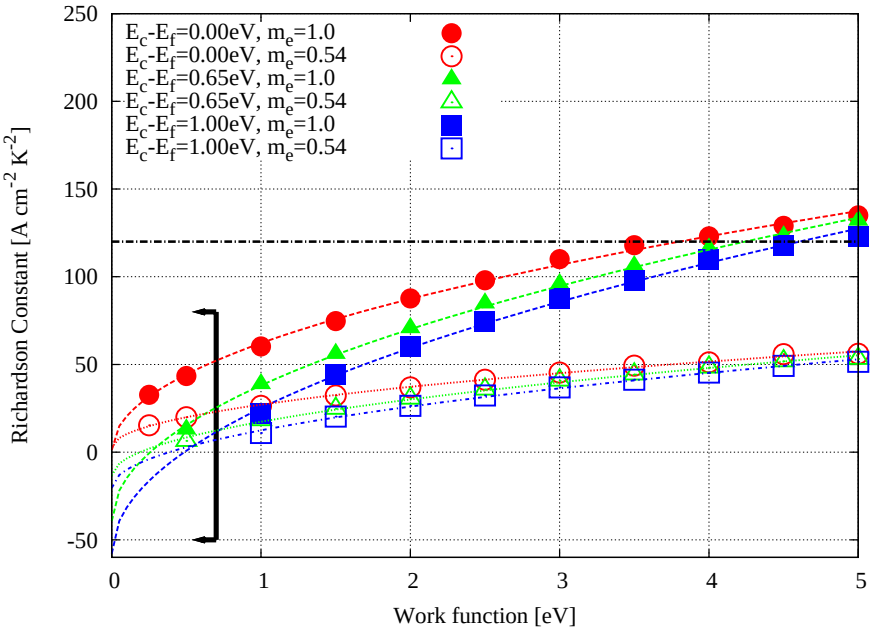

Figure 4.11 Plot of the Richardson constant as a function of work function and $E_c - E_f$. There is a linear relation between the Richardson constant and work function and a exponential dependence on $E_c - E_f$. The arrow denotes a region where Richardson's theory is not valid due to low or negative electron affinities.

nominal value. For example from Reimann's book (Reimann, 1934) Barium has a value of 60 $Acm^{-2}K^{-2}$ with a work function of 2.11 eV and Rhenium has a value of 200 $Acm^{-2}K^{-2}$ with a work function of 5.1 eV .

Figure 4.11 demonstrates the dependence of Richardson's constant versus work function as a near linear dependence. This dependence is a result of Richardson's constant being related to the density of states and the Fermi-Dirac term given in the expression of Equation 2.55. There is an added complexity that the Richardson's constant is the integral of the density of states and the Fermi distribution which is determined from the model. When the band offset ($E_c - E_f$) is increased the number of states per energy level increases by the square root of energy assuming for simplicity a bulk relation between density of states and energy as shown in Equation 2.58. As the work function (ϕ) of the material increases, moving along the x-dir in Figure 4.11, the Fermi-Dirac distribution, which is responsible for describing the filled states increases exponentially, while at the same time the density of states is increasing by the square root because the band offset ($E_c - E_f$) is fixed and moves the conduction band up. Therefore, from the expression in Equation 2.62, Richardson's constant is the

$E_c - E_f$	A_o	A_m
(eV)	($Acm^{-2}K^{-2}$)	($Acm^{-2}K^{-2}eV^{-1/2}$)
0.0	1.21	4.11
0.65	-39.3	4.35
1.0	-57.8.	4.42

Table 4.2 Table of the terms from Equation 2.64 where a least squares method was used to determine a common y-intercept (A_o) and the slope (A_m) by fitting the models results for three band energies $E_c - E_f$. The effective mass was assumed unity.

product of the density of states times the Fermi term resulting is a relation that is approximately square root. This is demonstrated in Figure 4.11 as a exponential relation times a square root dependence on the work function. However, when the work function is held constant and the band offset is changed the density of states increased by a square root of energy but the Fermi term remains constant therefore there is a squared relation between Richardson constant and band offset (conduction band edge).

It is often difficult to see the relation of band offset and Richardson constant in experimental devices because, the overall emission current (J) is dominated by the work function values in the exponential term of Equation 2.53. Meaning, if the material is a wide-band gap materials with a $E_c - E_f$=1.0 eV and a work function of 4 eV there is slight decrease in Richardson constant but the overall emission current is dominated by the term $\exp(-\phi/k_BT)$ which is more significant.

When the band offset ($E_c - E_f$) is greater in energy than the vacuum level then the emission changes regimes and the emission current begins to saturate with increasing electron affinity ($\chi = \phi - (E_c - E_f)$). This case is evident in Figure 4.11 where the material with a band offset of 1.0 eV has a work function that is less than 1.0 eV. The state where the conduction band edge of the wide-band gap cathode lies above the conduction band edge is illustrated in part (a) of Figure 4.12 and the case where the conduction band edge is below the vacuum level is in part (b). To aid in discerning where Richardson's theory applies for low and negative electron affinity materials black arrows where included in Figure 4.11. The black arrow defines the region where Richardson's equation is no longer valid due to low or negative electron affinities where the conduction band edge exceeding the vacuum level.

The emission current at low and negative electron affinity materials were able to calculated using the model. A plot that illustrates the saturation of the current as the conduction band reaching this low electron affinity regime is shown in Figure 4.13

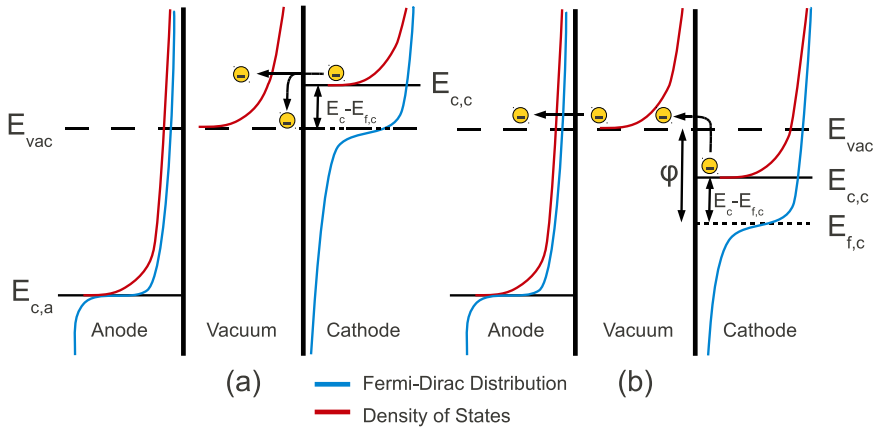

Figure 4.12 Band diagram of a diamond material with an associated band offset ($E_c - E_f$) in two states. State (a) is a wide-band gap cathode with a negative electron affinity such that the conduction band edge (E_c) lies above the vacuum level. To the right, state (b) is where the conduction band edge is below the vacuum level with a positive electron affinity.

for a material with a band offset of 1.0 eV. The points of interest in this figure are at the lower work function values which are less than or equal to 1.0 eV. For example, a 0.5 eV work function material has an emission current approximately equivalent to the emission current for a 1.0 eV work function material. As the electron affinity becomes negative (see Figure 4.12(a)) and when an electron is excited to the conduction band in the cathode the electron is quickly emitted into the vacuum. When the electron affinity is more negative, the electron maybe accelerated by an induced field as the electron drops down to the lower lying vacuum level. Studies (Pickett, 1994) have shown that materials which have negative electron affinities are possible when other materials are introduced to diamond cathodes. In the case of surface treatments on the cathode, the induced field as a result of the negative electron affinity could be rewarding in over coming surface effects. The notion of surface effects are left out of this analysis and the cathodes are assumed clean. Thus the addition of an induced field does not increase the emission current significantly.

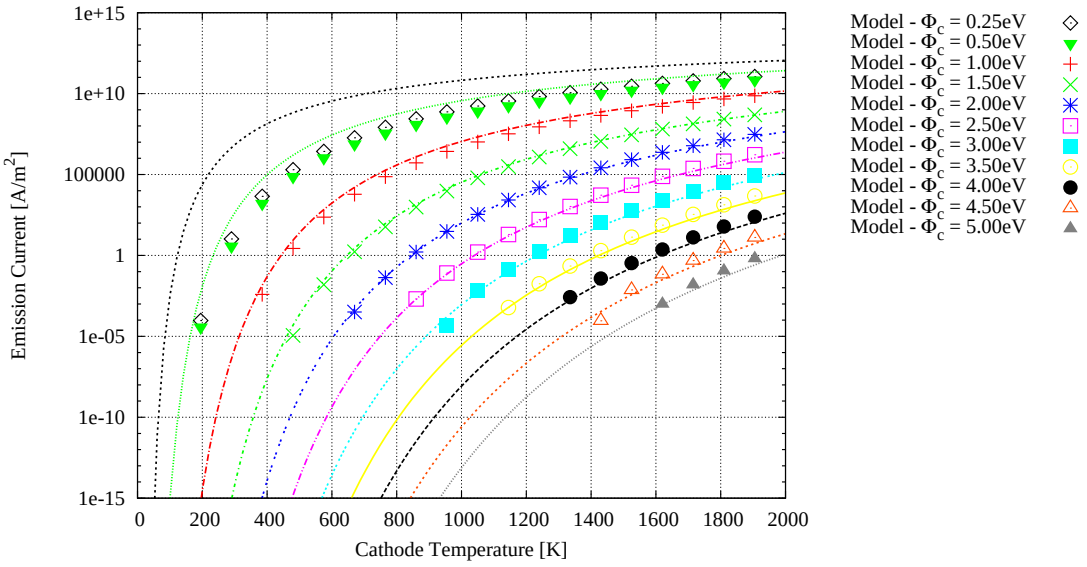

Figure 4.13 Plot of the emission current versus cathode temperature for a cathode with a band offset ($E_c - E_f$) of 1 eV. As the work function is decreased below 1 eV the conduction band resides above the vacuum and the emission current saturates. Richardson theory does not capture the emission when the conduction band is near of above the vacuum level.

Thermionic Emission - Applied Field Regime

In the validation chapter of this thesis (Chapter III) the thermionic emission was compared to Richardson's equation and experimental data with good agreement. The following analysis takes the modeling a step further and applies an electric field to the thin film devices in order to increase the emission. Figure 4.14 is a plot of the thermal-field emission for a 2.2 eV work function diamond-like cathode with a copper anode calibrated for zero band offset. The selection of a work function was based on the objective of predicting the experimental trends by Paxton (2011)

The model operates in the same manner as previously described, except now an applied field boundary condition is imparted on the device. Figure 4.14 is a plot of the resulting band diagram when an 30 V/μm field is applied to the device. Notice the vacuum region has a band offset which causes the slope of the conduction band within the vacuum region to slope downward towards the anode. Because of the slope, there is now a finite probability that electrons will tunnel through the narrow barrier which is created at the vacuum-cathode interface. Following this progression, as the field is increased, the slope of the conduction level within the vacuum region increases and the probability to tunnel also is increased. The increased probability of tunneling is

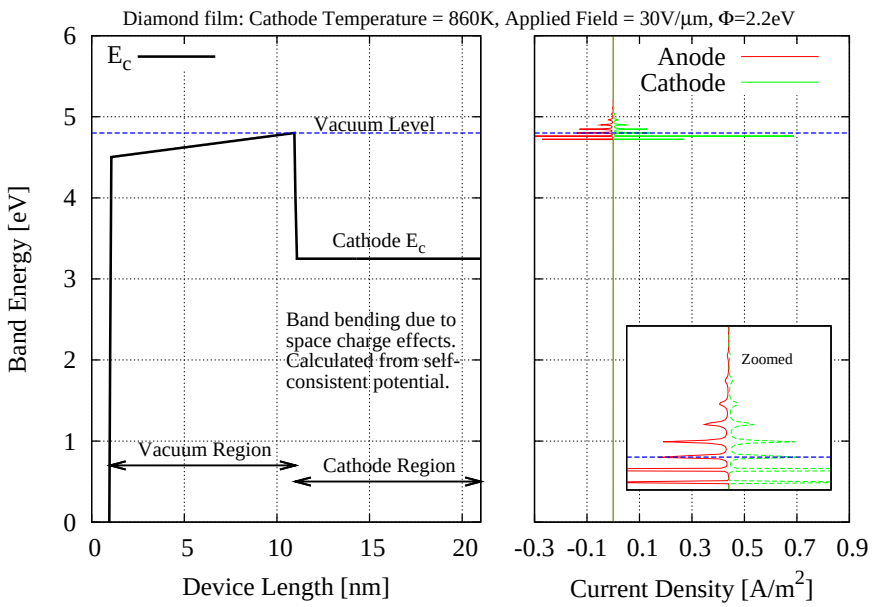

Figure 4.14 Plot of the band diagram of the thin film thermal-field emitter with an applied field of $30\,\mathrm{V}/\mu\mathrm{m}$.

demonstrated in the right portion of Figure 4.14 where there is emission current below the vacuum level which can only be a results of the tunneling electrons in response the narrowing of the vacuum-cathode interface barrier. This is classic thermionic emission and the following emission figures will corroborate this explanation.

In Figure 4.15, the emission current is plotted versus the cathode temperature with the same thermionic emission trend as seen previously. Again the emission is compared against Richardson's equation which is for pure thermionic emission from a metal surface. The data points in the figure represent the NEGF model's predicted values for each cathode temperature where the anode temperature is held at 300K. Each simulation was run by specifying the applied field through a voltage boundary condition and varying the cathode temperature. The cathode was held at ground and the anode was pulled down by an applied voltage.

As the applied field increases, the emission current increases, noted by the arrow in Figure 4.15. The on set values of thermionic emission are also influenced by the increased field. At higher temperatures the applied field is less noticeable, but is still discernible.

In re-plotting Figure 4.15 such that the trends are linear using Equation 2.54, an obvious trend is associated with change in applied field, see Figure 4.16. That

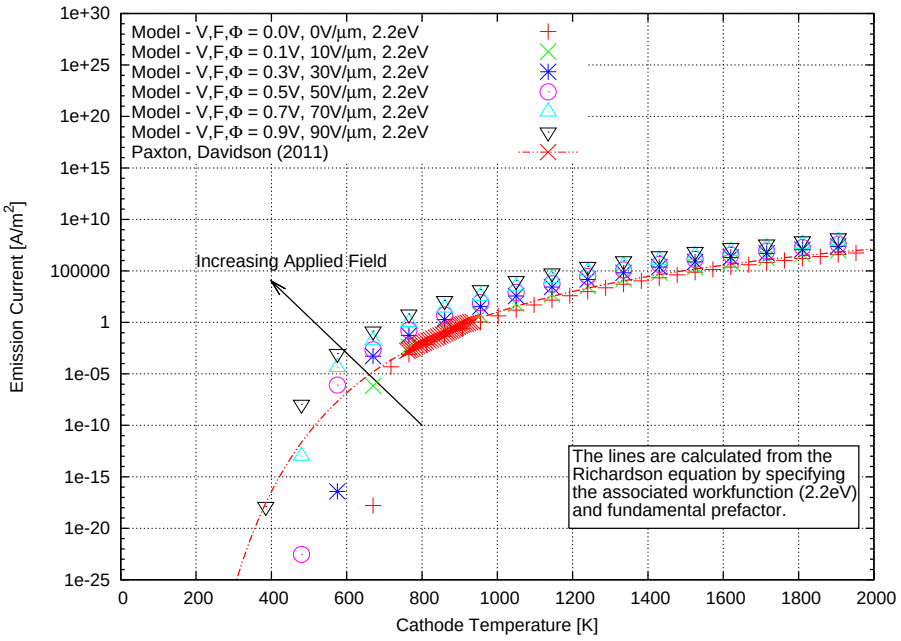

Figure 4.15 Plot of the emission current versus cathode temperature for a range of applied field from $0\,\mathrm{V}/\mu\mathrm{m}$ to $90\,\mathrm{V}/\mu\mathrm{m}$.

trend is a change in slope with applied field. The lines in Figure 4.16 are associated with fitting Equation 2.54 to the NEGF model and using the work function as the fitting parameter. As would be expected, the work function is lowered with increasing applied field.

The trend of decreased work function follows the general trend of Schottky theory (Schottky, 1914), which derived the following expression similar to the Richardson's equation,

$$J = AT^2 \exp \frac{-\phi - (q^3 F)^{1/2}}{k_B T}, \tag{4.3}$$

where q is a charge of an electron and F is the applied field. Often plots such as Figure 4.16 will be refereed to as Schottky plots. The Schottky equation is, however, only valid for applied fields to metal vacuum interfaces or metal semiconductor interfaces. To simplify Equation 4.3 the work function can be combined into a single term, $\phi^* = \phi - (e^3 F)^{1/2}$. This allows the fitted parameters in Figure 4.16 to be compared to the predicted value from Equation 4.3. Table IV is a comparison of the fitted effective work function ϕ^* values and Schottky values.

Gathered from Table IV, the model has a considerably lower predicted value of effective work function compared to the Schottky prediction. This can be attributed

Applied Field ($V/\mu m$)	Fitted Work Function (eV)	Schottky Work Function (eV)
0	2.28	2.28
10	2.19	2.28
30	1.99	2.27
50	1.92	2.26
70	1.80	2.25
90	1.68	2.24

Table 4.3 Comparison of thermal-field emission work function values from an 2.2 eV work function diamond cathode with an applied field from 0 V/μm to 90 V/μm. The models effective work function values are compared to Schottky work function values.

to be due to the nature that the Schottky equation is a generalization for low fields and metallic emitters. Recall, in the model the cathode material is described by an effective mass Hamiltonian representing a diamond cathode. Additionally, deviations from the Schottky prediction also stem from the discrete nature of states in the model. Because the model is a quantum description, states are not continuous, but have discrete probabilities of being at a certain energy and spatial location. In Figure 4.14 on the right figure, the current is noted as having peaks of high current density that are associated with increased current density. These peaks are a function of how well the states align across the device. As the device length increases in the transport direction, more states would converge as the confinement of the wave function is relaxed. The convergence of state results in the states as a whole becoming more continuous. Because the model has these discrete states there are confinement effects within the cathode film which are responsible for increased emission and deviation from the Schottky theory. This notion of confinement is a key aspect of increased transmission in thermoelectric superlattice devices.

Thermionic Emission - Heat Flux

The emission current calculated from the NEGF model can now be used to determine the cooling rate from the cathode due to the emission of electrons. The heat flux is determined from the current density and the energy of the electrons responsible for that current. The approximation that the kinetic energy from the electrons leaving the surface at a given energy is completely normal to the direction of cathode, $qV = KE = 1/2mv_x^2$. Figure 4.17 demonstrates the heat flux from the cathode as a function of cathode temperature and applied field. Again, as the applied

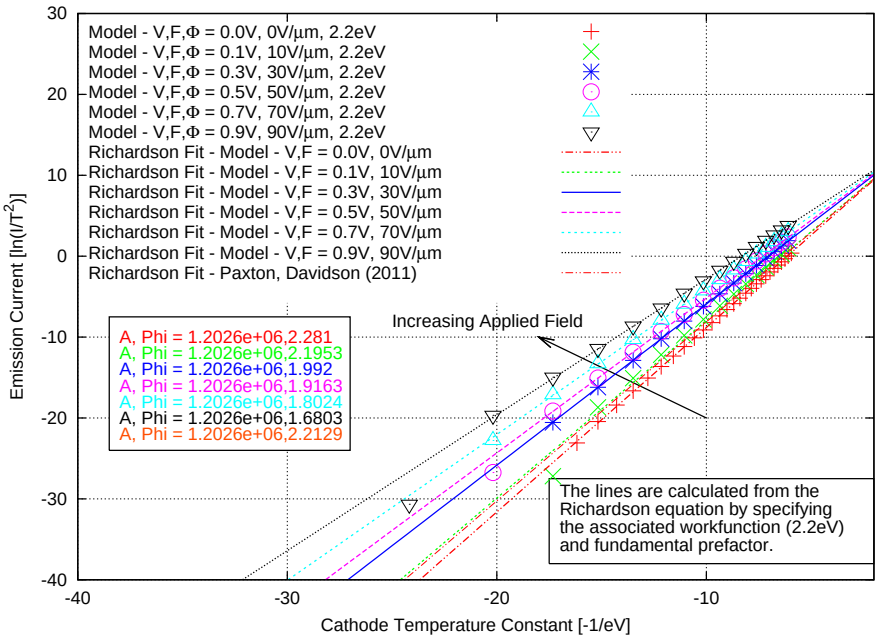

Figure 4.16 Plot of the thermal-field emission in Richardson form for a range of applied field from $0\,\mathrm{V}/\mu\mathrm{m}$ to $90\,\mathrm{V}/\mu\mathrm{m}$. The applied field effectively lowers the work function of the material.

field is increased the cooling potential of the cathode increases due to the effective lowering of the work function values.

By applying an increasing field to the material, the emission characteristics of these film increase significantly. There was no mention of efficiency associated with energy required to generate the applied field. This would be an inefficiency in the overall objective of a direct energy device. However, it is reasoned that a small field could exponentially increase the current characteristics. Furthermore, through geometric enhancement in non-planar geometries such as nano-tips, the field could enhance tremendously with lower applied fields, considerably increasing the emission current.

Thermionic Emission - Nano-tips Enhancement

The evolution from a thin film thermal-field emitter to a tip was carried out using the same modeling method. The only aspect that changed was the addition of a square tip emitter. It is approximated from SEM images and discussion with Wade (2011) that the actual nano-tip have a spherical cross-section with a diameter that range from 2 nm up to 10 nm but is on average 5 nm. The other approximation is

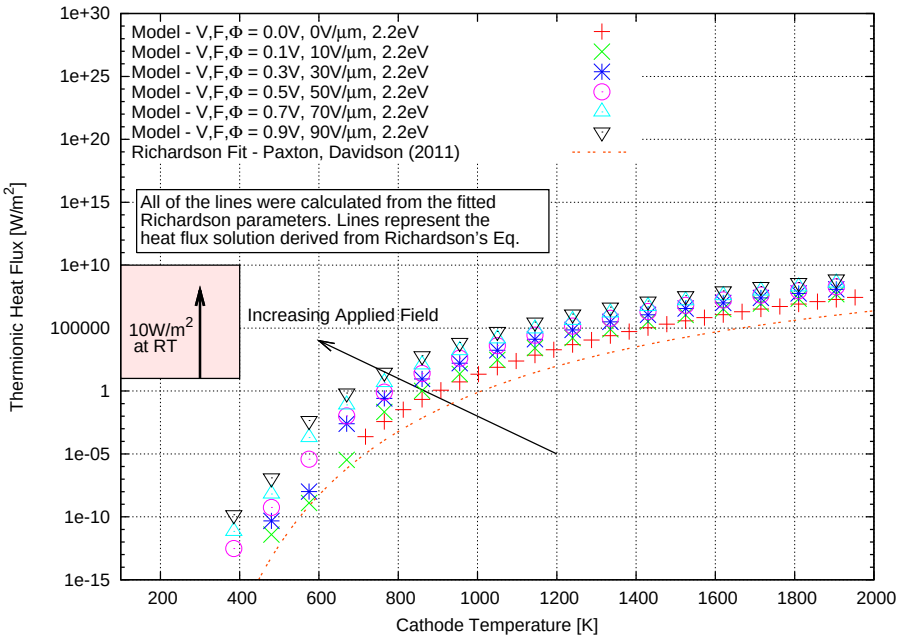

Figure 4.17 Plot of the heat flux at the cathode for a range of cathode temperatures and applied field from $0\,\mathrm{V}/\mu\mathrm{m}$ to $90\,\mathrm{V}/\mu\mathrm{m}$. An applied field increased the cooling potential of the cathode.

the tip length which is on the order of microns. Using this size feature was not possible due to computational resource limitations but the closest to this geometry was calculated. Figure 4.18 is an illustration of the nano-tip thermal-field emitter geometry which is modeled.

The same modeling parametric studies which were carried out for the thin film thermal-field emitters were also carried out for the nano-tips. The first plot, Figure 4.19, is a plot of the emission current as a function of cathode temperature for a range of applied field from $0\,\mathrm{V}/\mu\mathrm{m}$ to $90\,\mathrm{V}/\mu\mathrm{m}$. The plot is distinctly different from the film, Figure 4.15, in that there is an increased low temperature emission which is attributed to the field emission current. Additionally, the overall shift of the emission curve is attributed to the additional enhancement of field emission. The field emission is however, over-shadowed by the thermionic emission at higher temperature as seen by the emission following the thermionic trends.

The emission current in Figure 4.19 can be replotted such that the Richardson equation is linearized. The following figure allows the change in slope attributed to a change in work function and non linearities associated with field emission to be discerned. The slight slope in the emission current and, especially, the low temperature

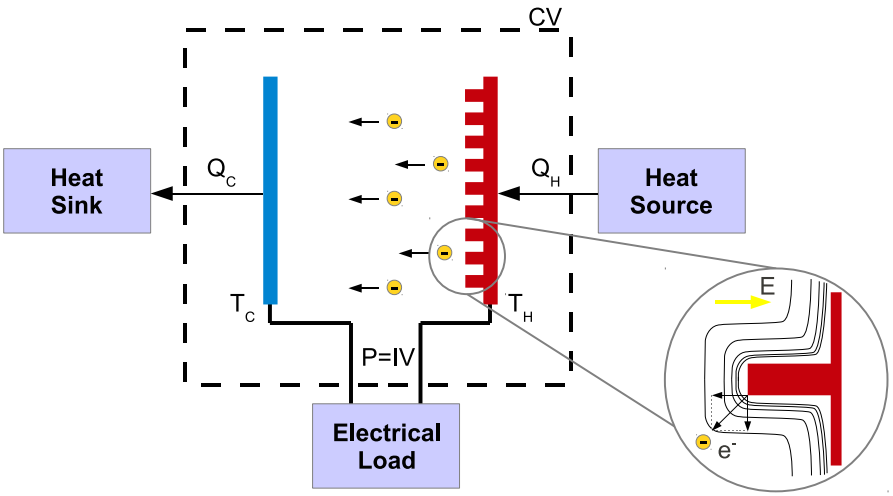

Figure 4.18 Illustration of a single square tip geometry thermal-field emitter which is modeled using a 2D NEGF model. As the iso-field lines contour the nano-tip cathode the electrons are enhanced by a x-component and y-component of the local field. The greater the curvature of the field lines the greater the enhancement.

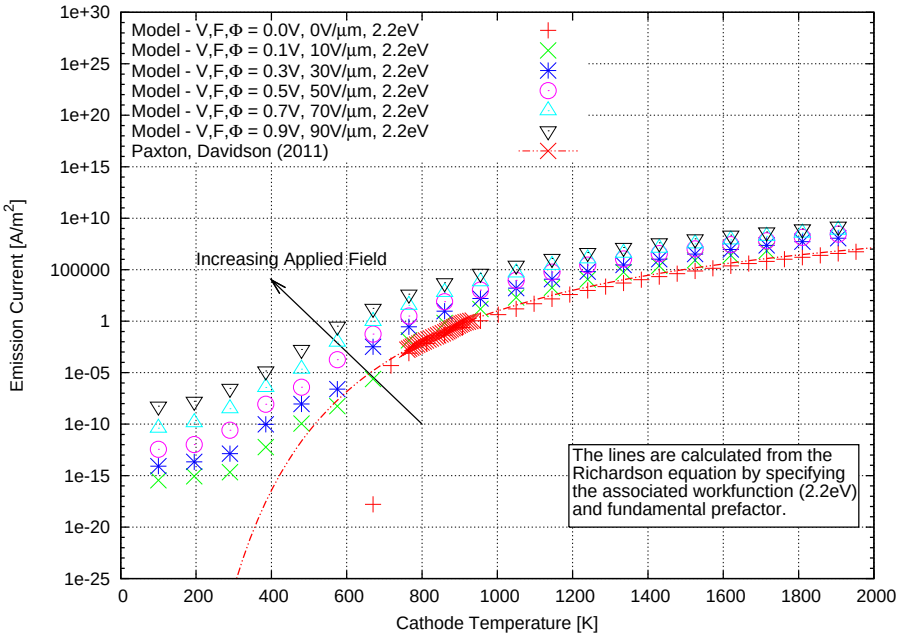

Figure 4.19 Plot of the emission current versus cathode temperature for a 2.2 eV work function nano-tip thermal-field emitter for a range of applied field from 0 V/μm to 90 V/μm. Note, the low temperature field enhancement is absent in the film analysis when compared to the nano-tips.

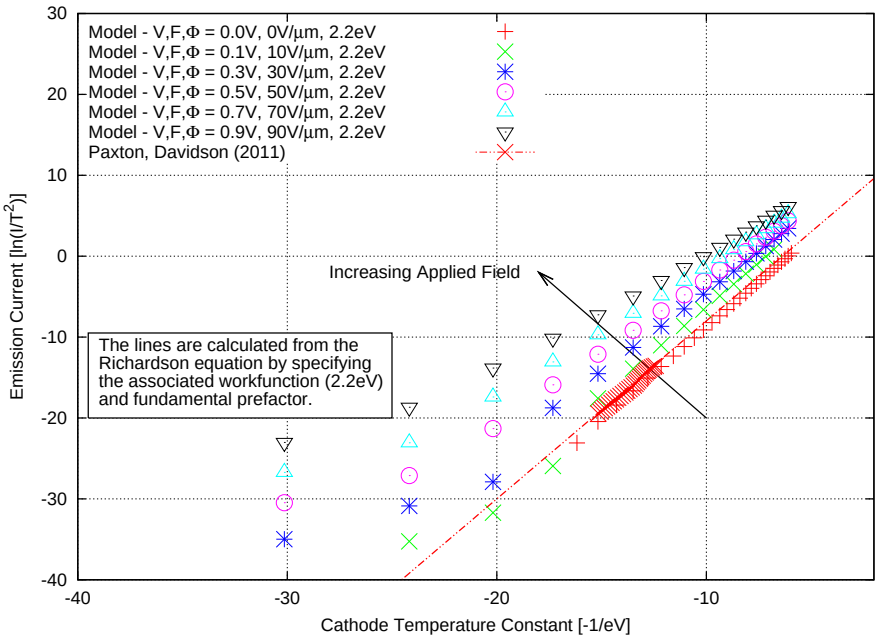

Figure 4.20 Plot of the linearized emission current versus cathode temperature for a 2.2 eV work function nano-tip thermal-field emitter for a range of applied fields from 0 V/μm to 90 V/μm. Non-linearities at low temperatures are attributed to the field emission regime.

values are attributed to the field emission and the field enhancement associated with the effects of geometry on the field lines. Because the field lines bend around the tip geometry, the local field at the edges of the square tips sees an enhanced field due to a field in both the x and y directions. Often, the geometric enhancement will be captured in the Fowler-Nordheim equation by a β pre-factor in front of the electric field term. This pre-factor is strictly a function of the geometry. But the β pre-factor can be attributed to the non-linearities in Figure 4.20.

The analysis of the heat flux from the cathode of the nano-tip thermal-field emitters is shown in Figure 4.21. The increase in heat flux at low temperatures is attributed to the geometric enhancement of field emission. Again the field emission at higher temperatures is overshadowed by the thermionic emission current. It is interesting to point out that the heat flux for the 90 V/μm is nearly constant up to the onset of the thermionic emission around 650 K. The other interesting finding is the ability to obtain 10 W/m^2 at room temperature. This analysis is, however, neglecting the effects of joule heating in the cathode and anode. Additionally, in terms of direct energy conversion, the heat fluxes obtain in this analysis required a potential to be

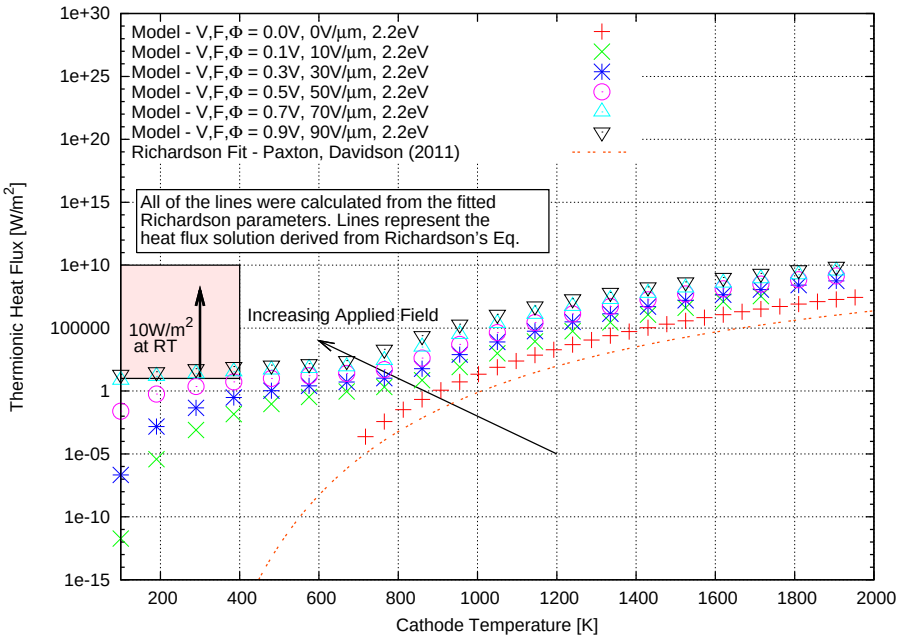

Figure 4.21 Plot of the heat flux of the constant temperature cathode versus cathode temperature for a nano-tip thermal-field emitter for a range of applied fields from $0\,\mathrm{V}/\mu\mathrm{m}$ to $90\,\mathrm{V}/\mu\mathrm{m}$. Enhanced low temperature emission is attributed to the geometric enhancement of field-field emission. The goal of $10\,\mathrm{W/m^2}$ is achieved for a 3nm nano-tip diamond cathode with a work function of 2.2 eV and an applied field of $70\,\mathrm{V}/\mu\mathrm{m}$.

applied as a field which is considered a loss due to energy being applied to the system in the form of output energy. This does not overshadow the ability to predict the cooling potential from a nano-tip thermal field emitter. Through the development of lower work function materials and nano-scale geometrical enhancements, these thermal-field emitters become excellent candidates for direct energy conversion and possibly the transcending of thermoelectric direct energy conversion materials.

CHAPTER V

CONCLUSION

The current states of the energy crisis has brought to the forefront the need for sustainable energy. A solution involves not only developing new energy systems but systems that can recover waste heat from existing infrastructures. In contributing to a solution, this research was focused on developing two solution approaches. Those approaches include development of quantum models along with the development of novel nanostructured materials. The computational models developed in this research are an essential tool for innovating these new, more efficient direct energy conversion materials. This work had a particular goal in understanding the transport on the nanoscale. Because the nano-features of interest are on the order of the mean free path, continuum type relations are no longer valid and new modeling approaches framed from a more fundamental view point were required. The modeling approach developed in this research was based on a non-equilibrium Green's function quantum approach. This work emphasized the incorporation of additional physics into the models such as electron-phonon and phonon-phonon interactions while implementing the use of high-performance computational techniques. By including additional physics and using HPC resources, device sizes of up to 200 nm were able to be studied, which resemble device length scales one might find in an working direct energy conversion device. Ultimately, the models developed in this research allowed the large design space of nanoscale thermoelectric and thermionic devices to be explored which provide a necessary tool to aid in innovating new more efficient direct energy conversion devices which could potentially lead to a real solution.

The simulation tools developed in this research to model the transport of nanoscale thermoelectrics and thermionic devices a non-equilibrium Green's function quantum model. The model predicted both the electron and thermal transport from a quantum point of view. The thermoelectric model developed for this research took a novel approach of coupling the electron and phonon descriptions to capture spatially varying multiple phonon frequency electron-phonon interactions along with the phonon-phonon interactions. This model approach is unique because rigorous coupling of the phonon and electron description has not been demonstrated in the literature. The model developed is not only able to calculate the scattering of electrons with multiple phonon frequencies, but also track the spatial scattering of varying

phonon content along the length of the device which is important in highly confined structures such as nanostructured superlattice devices. The ability to resolve the change in spatial scattering is a critical aspect in studying many nanoscale transport phenomena and provides an argument for determining the temperature distribution in the channel region.

The thermoelectric model developed in this research was ultimately used to explore the design space of Si/Ge superlattice materials for enhanced thermoelectric performance which has been explored experimentally, but has not extensively been studied theoretically. Validation and verification of the model was carried out by comparing to available literature values for both the electron and phonon NEGF model. Results demonstrated that multiple phonon scattering was a critical aspect for calculating the electric transport properties of nanoscale superlattice materials. By adding multiple phonon frequency scattering additional states within the well regions were accessible to transport electron due to the assistance of phonons. Due to phonon assistance, it was determined that the use of a single dominant phonon frequency scattering model under estimate the Seebeck coefficient and overestimate the electrical conductivity when compared to literature values. Because this coupled technique solved the full phonon description it was not necessary for the user to specify a single dominant phonon frequency. Instead the phonon frequencies were calculated explicitly by the phonon model and then passed to the electron model. This method proved to be more rigorous and computationally intensive but was reasoned to provided a more physical description of the electron-phonon interactions.

Within the thermal model, the phonon-phonon interaction were accounted for in a similar manner to the electron phonon interactions except an unknown anaharmic parameter was defined that accounted for the anharmicity in the system and the scattering was determined self-consistently based on the spatial phonon density. The model determined a deviate from the ballistic solution at device lengths greater than 50 nm where the ballistic solution is no longer valid and over estimates the thermal conductivity. The model proved to accurately account for the boundary scattering which is often the limiting scattering mechanism in nanostructured thermoelectrics. Ultimately, by solving both the electrical and thermal transport from a quantum point of view a prediction of the full ZT performance, which included scattering in both the electron and phonon transport was possible.

The coupled thermoelectric model developed in the research was implemented to study a new innovation in superlattice thermoelectric technology which is dependent on a band-engineered superlattice structure. This device was shown not only

to have a lower thermal conductivity but a greater electrical conductivity as hypothesized. More specifically, VSSL structures were seen to increase the ZT values up to seven times at room-temperature when compared to traditional regular-spaced superlattice structures. The regular superlattice did, however, prove to perform better at higher temperatures due to the increase electron contribution to the thermal conductivity of the VSSL device. This research suggests that VSSL structures are indeed candidates for increased thermoelectric performance, especially for near room temperature applications. Investigation of other materials in a VSSL configuration is a pressing research topic.

The modeling approach applied to superlattices was also applied to the study of a slightly more complex structure, nano-crystalline composite (NCC) material. To investigate NCC structures the one dimensional electronic NEGF model was evolved to look at planar structures that have two dimensions. This was necessary to resolve the 2D transport around nano-features. The model compared the performance of these NCC devices to equivalent superlattice (SL) devices suggesting that the NCC devices could outperform SL devices by up to 5 times. The NCC devices were reasoned to increase the electrical conductivity of the material compared to SL materials by providing moderate filter effect. This allowed charge to travel around the barrier unlike the SL material where charge was required to travel through the barrier. The NCC also had a larger Seebeck coefficient and lower thermal conductivity which increased the overall ZT values of the NCC material.

The last direct energy conversion devices that was investigated in this research was the evolution of the non-equilibrium Green's function modeling approach developed for thermoelectric studies to investigate the field and thermionic emission from wide-band gap diamond cathodes and nano-tips. The model was validated against Richardson's theory and experimental values. The model was proven to reproduce emission characteristics and also predict the onset of thermionic emission, which was over predicted in Richardson's theory. By modeling the thermionic emission from a fundamental view point results were able to determine the applicability of well accepted Richardson's theory and where it could be used with confidence. The model predicted the emission from wide-band gap cathodes and back calculated the associated Richardson constant, which was determined to be both a function of the electron affinity and the work function. The model was ultimately able to determine the cooling rate or heat flux from the thermionic emitter which could then be used to assess the cathode for direct energy conversion and refrigeration applications.

The thermionic model was also evolved to study thermal-field emission which

includes the response of an applied field resulting in the simultaneous thermionic emission and field emission. The thermal-field emission results demonstrated lowering of the effective work function values with increasing applied field at a rate which was greater than then the predicted emission from Schottky theory. The deviation from Schottky theory was based the approximation of Schottky theory and the confinement of discrete states within the thin film cathodes. The analysis of nano-tip thermal-field emission demonstrated increased enhancement with a 3 nm tip which provides cooling potential up to $10\,\mathrm{W/m^2}$ at 300K (neglecting anode heating) with 2.2 eV work function and $0.7\,\mathrm{V}/\mu\mathrm{m}$ applied field. An flat metallic cathode would require a work function around 0.7 eV. The model allows more advanced structures to be analyzed providing an essential tool to innovated new vacuum devices for direct energy conversion applications.

Significant effort was taken to write the model in parallel using high-performance computational techniques and state-of-the-art graphics processing unit (GPU) computational resources. The models developed in this research proved a valid means of modeling nanoscale devices from thermoelectrics to thermal field emitters and can be adapted to look at a broad array of nanoscale material configurations and an array of different materials. Many of the tools and finding from this research can be applied to engineering, physics and biology field that research innovative nanoscale materials for energy, devices, and sensing.

All the models and the associated source code will be available through an online nanoscale community, http://www.nanohub.org. Future research towards studying more complex materials such as doped oxides which have an inherently lower thermal conductivity values due to polar effects is of future aspirations. The thermal-field emission models are currently being evolved to study the emission characteristic from nitrogen incorporated diamond nano-tip emitters, which have geometric enhancement effects ideal for cooling applications. In all, the models developed in this research have the ultimate mission of evolving science in finding new, more efficient materials for a more sustainable future.

APPENDIX

1D Superlattice - Electron NEGF

This routine constructs the Hamiltonian for the 1D superlattice electronic portion. It is necessary that the Hamiltonian be Hermitian so care must be taken at mixed cell interfaces.

```
!!!!!!!!!!!!!!!!!!!!!!!!!!!!!!!!!!!!!!!!!!!!!!!!!!!!!!!!!!!!!!!!!!!!!!!!!!!!!!!!
!
! Hamil_Create - Create 1D Hamiltonian Matrix - 1D Electron NEGF
!
!!!!!!!!!!!!!!!!!!!!!!!!!!!!!!!!!!!!!!!!!!!!!!!!!!!!!!!!!!!!!!!!!!!!!!!!!!!!!!!!
subroutine Hamil_Create

    integer(kind=4) :: r, n, k

    !!! diagonal Hamiltonian terms
    k=0
    do r = 1, Nl
       if(r .eq. 1) then
         H(1,1) = Ecx(1) + 2*tsx(1)*(1/Gdx(1)**2)
         k = 0
         if(Nec .ne. 0) then
           do n = 2, Nec
             H(n,n) =  Ecx(n) + (tsx(n)/Gdx(n)**2+tsx(n-1)/Gdx(n-1)**2)
             k=n
           end do
           H(k+1,k+1) = (Ecx(k+1)+Ecx(k))/2 + (tsx(k+1)/Gdx(k+1)**2+tsx(k)/Gdx(k)**2)
         end if
       end if

       do n = k+2, k+Neb_l(r)
          H(n,n) = Ecx(n) + (tsx(n)/Gdx(n)**2+tsx(n-1)/Gdx(n-1)**2)
          k=n
       end do
       H(k+1,k+1) = (Ecx(k+1)+Ecx(k))/2 + (tsx(k+1)/Gdx(k+1)**2+tsx(k)/Gdx(k)**2)

       do n = k+2, k+New_l(r)
          H(n,n) = Ecx(n) + (tsx(n)/Gdx(n)**2+tsx(n-1)/Gdx(n-1)**2)
          k=n
       end do
       H(k+1,k+1) = (Ecx(k+1)+Ecx(k))/2 + (tsx(k+1)/Gdx(k+1)**2+tsx(k)/Gdx(k)**2)

       if(r .eq. Nl) then
          do n = k+2, k+Neb_l(r+1)
             H(n,n) = Ecx(n) + (tsx(n)/Gdx(n)**2+tsx(n-1)/Gdx(n-1)**2)
             k=n
          end do
          H(Np,Np) = Ecx(Np) + 2*tsx(Np)*(1/Gdx(Np)**2)
       end if
    end do

    !!! off-diagonal Hamiltonian terms
```

```
    k=0
    do r = 1, Nl
       do n = k+1, k+Neb_l(r)
         H(n,n+1) = -tsx(n)*(1/Gdx(n)**2)
         if(n .eq. 1) then
           H(n+1,n) = -tsx(n)*(1/Gdx(n)**2)
         else
           H(n+1,n) = -tsx(n)*(1/Gdx(n)**2)
         end if
         k=n
       end do

       do n = k+1, k+New_l(r)
         H(n,n+1) = -tsx(n)*(1/Gdx(n)**2)
         H(n+1,n) = -tsx(n)*(1/Gdx(n)**2)
         k=n
       end do

       if(r .eq. Nl) then
          do n = k+1, k+Neb_l(r+1)
             H(n,n+1) = -tsx(n)*(1/Gdx(n)**2)
             H(n+1,n) = -tsx(n)*(1/Gdx(n)**2)
             k=n
          end do
          if(Nec .ne. 0) then
            H(k+1,k+2) = -tsx(k+1)*(1/Gdx(k+1)**2)
            H(k+2,k+1) = -tsx(k+1)*(1/Gdx(k+1)**2)
            do n = k+2, k+Nec+1
              H(n,n+1) = -tsx(n)*(1/Gdx(n)**2)
              H(n+1,n) = -tsx(n)*(1/Gdx(n)**2)
              k=n
            end do
          end if
       end if
    end do

    if(Nec .ne. 0) then
       H(1,1) = Ecs_e + 2*tsc*(1/Gdx(1)**2)
       H(Np,Np) = Ecs_e + 2*tsc*(1/Gdx(Np)**2)
       H(2,1) = -tsc*(1/Gdx(1)**2)
       H(Np-1,Np) = -tsc*(1/Gdx(Np)**2)
       do n = 1, Nec
          H(n,n) = Ecs_e + tsc*(1/Gdx(n)**2+1/Gdx(n-1)**2)
          H(Np-n,Np-n) = Ecs_e + (tsc)*(1/Gdx(n)**2+1/Gdx(n-1)**2)
          H(n,n+1) = -tsc*(1/Gdx(n)**2)
          H(n+1,n) = -tsc*(1/Gdx(n)**2)
       end do
    end if

end subroutine Hamil_Create
```

This routine applies the electronic boundary conditions to the Hamiltonian and constructs the Green's function.

```
!!!!!!!!!!!!!!!!!!!!!!!!!!!!!!!!!!!!!!!!!!!!!!!!!!!!!!!!!!!!!!!!!!!!!!!!!!!!!!!!!!!!!!!!!!!!!!!!
```

```
!
! Negf_Bound - Boundary conditions - 1D Electron NEGF
!
!!!!!!!!!!!!!!!!!!!!!!!!!!!!!!!!!!!!!!!!!!!!!!!!!!!!!!!!!!!!!!!!!!!!!!!!!!!!!!
subroutine Negf_Bound

   integer(kind=4) :: n
   real(kind=8) :: tm_ss, tm_se

   tm_ss = tsc*(1/Gdx(1)**2)
   tm_se = tsc*(1/Gdx(Np)**2)

   !! Calculating Fermi functions of electrons entering through Silicon Source and Drain !!
   f1 = No1*dlog(1+dexp((-(E(k)-mu + Ua(1)))/kT1)) ! 2D Source fermi function. [1/m^2]
   f2 = No2*dlog(1+dexp((-(E(k)-mu + Ua(Np)))/kT2)) ! 2D drain fermi function. [1/m^2]
   f3 = No1*(1-dlog(1+dexp((-(E(k)-mu + Ua(1)))/kT1))) ! 2D Source fermi function. [1/m^2]
   f4 = No2*(1-dlog(1+dexp((-(E(k)-mu + Ua(Np)))/kT2))) ! 2D drain fermi function. [1/m^2]
   !f1 = 1/(1+dexp(((E(k)-mu - V/2))/kT1))
   !f2 = 1/(1+dexp(((E(k)-mu + V/2))/kT2))

   f5 = f_e(k)

   ka1 =  i*(1-(1 - ((dcmplx(E(k)) + zplus - dcmplx(Ds) - dcmplx(Ua(1)))/&
          &(2.0*dcmplx(tm_ss))))**2)**0.5
   ka1 = -i*cdlog((1 - ((dcmplx(E(k)) + zplus - dcmplx(Ds) - dcmplx(Ua(1)))/&
          &(2.0*dcmplx(tm_ss)))) + ka1)
   ! Real Wave vector of broadened waves at drain
   !(ACOS can be written in LOG Format See Matlab Manual)
   Sig1(1,1) = dcmplx(-tm_ss)*zexp(i*ka1) ! Self energy of source (eV)
   Gam1(1,1) = i*(Sig1(1,1) - conjg(Sig1(1,1))) ! Source broadening matrix (eV)
   SigIn1(1,1) = Gam1(1,1)*dcmplx(f1) ! Inscattering term for source (eV/m^2)
   SigOut1(1,1) = Gam1(1,1)*dcmplx(f3)

   ka2 =  i*(1-(1 - ((dcmplx(E(k)) + zplus - dcmplx(Ds) - dcmplx(Ua(Np)))/&
          &(2.0*dcmplx(tm_se))))**2)**0.5
   ka2 = -i*cdlog((1 - ((dcmplx(E(k)) + zplus - dcmplx(Ds) - dcmplx(Ua(Np)))/&
          &(2.0*dcmplx(tm_se)))) + ka2)
   ! Real Wave vector of broadened waves at drain
   !(ACOS can be written in LOG Format See Matlab Manual)
   Sig2(Np,Np) = dcmplx(-tm_se)*zexp(i*ka2) ! Self energy of drain (eV)
   Gam2(Np,Np) = i*(Sig2(Np,Np) - conjg(Sig2(Np,Np))) ! Drain broadening matrix (eV)
   SigIn2(Np,Np) = Gam2(Np,Np)*dcmplx(f2) ! Inscattering term for drain (eV/m^2)
   SigOut2(Np,Np) = Gam2(Np,Np)*dcmplx(f4)

   Gamp(:) = 0.0
   !Inscatter and Outscattering
   !To just include Inscattering only SigInp
   !Hilbert transformation to get real part
   if(f5 .gt. 0.0 .and. tst .lt. 8) Gamp = -SigInp(:,k)/f5-0.5*i*(SigOutp(:,k)+&
                                          &SigInp(:,k))/f5 !eV
   G(:,:) = (0,0);
   do n = 1, Np
     G1(n,n) = (0,0); G2(n,n) = (0,0)
   end do
```

```
   G1(1,1) = Sig1(1,1); G1(Np,Np) = Sig2(Np,Np) !(eV)

   do n = 1, Np
     G2(n,n) = ((dcmplx(E(k)) + zplus)*eye(n,n) - dcmplx(Ua(n)) - dcmplx(U(n,n)))
    !(eV) Simplify Addition Because Only Diagonal Terms
   end do

   call Matxopt_ztcpy(dcmplx(H),G,Np)
   call Matxopt_sub_zdtf(G2,G,Np)
   call Matxopt_sub_zdtf2(G1,G,Np)
   call Matxopt_sub_zvtf2(Gamp,G,Np)
   !G = (G2 - dcmplx(H) - G1) ! Green's function (1/eV)

end subroutine Negf_Bound
```

1D Superlattice - Phonon NEGF

This routine constructs the Hamiltonian for the 1D superlattice thermal portion. It is necessary that the Hamiltonian be Hermitian so care must be taken at mixed cell interfaces. A periodic potential is used to determine the spring constants.

```
!!!!!!!!!!!!!!!!!!!!!!!!!!!!!!!!!!!!!!!!!!!!!!!!!!!!!!!!!!!!!!!!!!!!!!!!!!!!!!!!!!!
!
! Hamil_Create - Create Hamiltonian Matrix - 1D Phonon NEGF
!
!!!!!!!!!!!!!!!!!!!!!!!!!!!!!!!!!!!!!!!!!!!!!!!!!!!!!!!!!!!!!!!!!!!!!!!!!!!!!!!!!!!
subroutine Hamil_Create

    integer(kind=4) :: r, n, k
    real(kind=8) :: t1, t2

    Le(:) = 0.0;
    !!! diagonal Hamiltonian terms
    k=0; n=0
    do r = 1, Nl
       if(r .eq. 1) then
         call Hamil_Couple(ms,Gdx(1),t1)
         if(Neb_l(1) .ne. 1) then
           H(1,1) = 2*t1*(1/Gdx(1)**2)
           k = 0
         else
           Neb_l(1) = 2; Neb_flag = 1
           k = -1
         end if
         if(Nec .ne. 0) then
           do n = 2, Nec
             call Hamil_Couple(ms,Gdx(n),t1)
             call Hamil_Couple(ms,Gdx(n-1),t2)
             H(n,n) = (t1/Gdx(n)**2+t2/Gdx(n-1)**2)
             k=n
           end do
           call Hamil_Couple(ms,Gdx(k+1),t1)
           call Hamil_Couple(ms,Gdx(k),t2)
           H(k+1,k+1) = (t1/Gdx(k+1)**2+t2/Gdx(k)**2)
```

```
      end if
    end if

    do n = k+2, k+Neb_l(r)
       if(n .gt. 1) then
         call Hamil_Couple(ms,Gdx(n),t1)
         call Hamil_Couple(ms,Gdx(n-1),t2)
         H(n,n) = (t1/Gdx(n)**2+t2/Gdx(n-1)**2)
       else
         call Hamil_Couple(ms,Gdx(n),t1)
         H(n,n) = 2*(t1/Gdx(n)**2)
       end if
       k=n
    end do
    call Hamil_Couple(mg,Gdx(k+1),t1)
    call Hamil_Couple(ms,Gdx(k),t2)
    H(k+1,k+1) = (t1*ms*ab_s/Gdx(k+1)**2+t2*mg*ab_g/Gdx(k)**2)

    do n = k+2, k+New_l(r)
       call Hamil_Couple(mg,Gdx(n),t1)
       call Hamil_Couple(mg,Gdx(n-1),t2)
       H(n,n) = (t1/Gdx(n)**2+t2/Gdx(n-1)**2)
       k=n
    end do
    call Hamil_Couple(ms,Gdx(k+1),t1)
    call Hamil_Couple(mg,Gdx(k),t2)
    H(k+1,k+1) = (t1*mg*ab_g/Gdx(k+1)**2+t2*ms*ab_s/Gdx(k)**2)
    if(New .eq. 0) H(k+1,k+1) = (t1/Gdx(k+1)**2+t2/Gdx(k)**2)

    if(r .eq. Nl) then
       do n = k+2, k+Neb_l(r+1)
          call Hamil_Couple(ms,Gdx(n),t1)
          call Hamil_Couple(ms,Gdx(n-1),t2)
          H(n,n) = (t1/Gdx(n)**2+t2/Gdx(n-1)**2)
          k=n
       end do
       if(Nec .ne. 0) then
         call Hamil_Couple(ms,Gdx(k+1),t1)
         call Hamil_Couple(ms,Gdx(k),t2)
         H(k+1,k+1) = (t1/Gdx(k+1)**2+t2/Gdx(k)**2)
         do n = k+2, k+Nec
           call Hamil_Couple(ms,Gdx(n),t1)
           call Hamil_Couple(ms,Gdx(n-1),t2)
           H(n,n) = (t1/Gdx(n)**2+t2/Gdx(n-1)**2)
           k=n
         end do
       end if
       call Hamil_Couple(ms,Gdx(Np),t1)
       H(Np,Np) = 2*t1*(1/Gdx(Np)**2)
    end if
  end do

  if(rank .eq. 0) then
    write(*,'(A,ES15.6,A)') '  ** Total Lattice Energy = ',Le(1),' J'
```

```
  write(*,'(A,ES15.6,A)') '  ** Mean Lattice Energy Per Atom = ',Le(1)/Np,' J/Atom'
  write(*,'(A,ES15.6,A)') '  ** RMS Lattice Energy Per Atom = ',Le(2)*2,' J/Atom'
end if

!!! off-diagonal Hamiltonian terms
k=0
do r = 1, Nl
   if(r .eq. 1) then
     call Hamil_Couple(ms,Gdx(n),t1)
     if(Neb_flag .ne. 1) then
       H(2,1) = -t1*(1/Gdx(n)**2)
       H(1,2) = -t1*(1/Gdx(n)**2)
       k = 0
     else
       Neb_l(1) = 1;
       k = 0
     end if
     if(Nec .ne. 0) then
       do n = 2, Nec-1
         call Hamil_Couple(ms,Gdx(n),t1)
         H(n,n+1) = -t1*(1/Gdx(n)**2)
         H(n+1,n) = -t1*(1/Gdx(n)**2)
         k=n
       end do
         call Hamil_Couple(ms,Gdx(k+1),t1)
         H(k+1,k+2) = -t1*(1/Gdx(k+1)**2)
         H(k+2,k+1) = -t1*(1/Gdx(k+1)**2)
     end if
    end if

   do n = k+1, k+Neb_l(r)
     call Hamil_Couple(ms,Gdx(n),t1)
     H(n,n+1) = -t1*(1/Gdx(n)**2)
     H(n+1,n) = -t1*(1/Gdx(n)**2)
     k=n
   end do

   do n = k+1, k+New_l(r)
     call Hamil_Couple(mg,Gdx(n),t1)
     H(n,n+1) = -t1*(1/Gdx(n)**2)
     H(n+1,n) = -t1*(1/Gdx(n)**2)
     k=n
   end do

   if(r .eq. Nl) then
      do n = k+1, k+Neb_l(r+1)
         call Hamil_Couple(ms,Gdx(n),t1)
         H(n,n+1) = -t1*(1/Gdx(n)**2)
         H(n+1,n) = -t1*(1/Gdx(n)**2)
         k=n
      end do
      if(Nec .ne. 0) then
        call Hamil_Couple(ms,Gdx(k+1),t1)
        H(k+1,k+2) = -t1*(1/Gdx(k+1)**2)
```

```
            H(k+2,k+1) = -t1*(1/Gdx(k+1)**2)
            do n = k+2, k+Nec+1
              call Hamil_Couple(ms,Gdx(n),t1)
              H(n,n+1) = -t1*(1/Gdx(n)**2)
              H(n+1,n) = -t1*(1/Gdx(n)**2)
              k=n
            end do
          end if
       end if
    end do

end subroutine Hamil_Create

!!!!!!!!!!!!!!!!!!!!!!!!!!!!!!!!!!!!!!!!!!!!!!!!!!!!!!!!!!!!!!!!!!!!!!!!!!!!!!!
!
! Hamil_Mass_Matrix - Create Hamiltonian Mass Matrix
!
!!!!!!!!!!!!!!!!!!!!!!!!!!!!!!!!!!!!!!!!!!!!!!!!!!!!!!!!!!!!!!!!!!!!!!!!!!!!!!!
subroutine Hamil_Mass_Matrix

    integer(kind=4) :: r, n, k

    !!! diagonal Hamiltonian terms
    !! ab_s number of atoms per basis
    k=0; n=0
    do r = 1, Nl
       if(r .eq. 1) then
         if(Neb_flag .ne. 1) then
           M(1,1) = ms*ab_s
           k = 0
         else
           Neb_l(1) = 2;
           k = -1
         end if
         if(Nec .ne. 0) then
           do n = 2, Nec
             M(n,n) = ms*ab_s
             k=n
           end do
           M(k+1,k+1) = ms*ab_s
         end if
       end if

       do n = k+2, k+Neb_l(r)
          M(n,n) = ms*ab_s
          k=n
       end do
       M(k+1,k+1) = ms*ab_s*mg*ab_g
       !M(k+1,k+1) = sqrt(ms*ab_s*mg*ab_g)
       !M(k+1,k+1) = sqrt((ms*ab_s)**2 + (mg*ab_g)**2)
       !M(k+1,k+1) = (ms*ab_s+mg*ab_g)/2
       do n = k+2, k+New_l(r)
          M(n,n) = mg*ab_g
          k=n
```

```
   end do
   M(k+1,k+1) = ms*ab_s*mg*ab_g
   if(New .eq. 0) M(k+1,k+1) = ms*ab_s
   if(r .eq. Nl) then
      do n = k+2, k+Neb_l(r+1)
         M(n,n) = ms*ab_s
         k=n
      end do
      if(Nec .ne. 0) then
        M(k+1,k+1) = ms
        do n = k+2, k+Nec
          M(n,n) = ms*ab_s
          k=n
        end do
      end if
      M(Np,Np) = ms*ab_s
   end if
end do
!!! off-diagonal Hamiltonian terms
k=0
do r = 1, Nl
   if(r .eq. 1) then
     if(Neb_flag .ne. 1) then
       M(2,1) = ms*ab_s
       M(1,2) = ms*ab_s
     else
       Neb_l(1) = 1;
       k = 0
     end if
     if(Nec .ne. 0) then
       do n = 2, Nec-1
         M(n,n+1) = ms*ab_s
         M(n+1,n) = ms*ab_s
         k=n
       end do
         M(k+1,k+2) = ms*ab_s
         M(k+2,k+1) = ms*ab_s
     end if
    end if

   do n = k+1, k+Neb_l(r)
     M(n,n+1) = ms*ab_s
     M(n+1,n) = ms*ab_s
     k=n
   end do

   do n = k+1, k+New_l(r)
     M(n,n+1) = mg*ab_g
     M(n+1,n) = mg*ab_g
     k=n
   end do

   if(r .eq. Nl) then
      do n = k+1, k+Neb_l(r+1)
```

```
             M(n,n+1) = ms*ab_s
             M(n+1,n) = ms*ab_s
             k=n
          end do
          if(Nec .ne. 0) then
            M(k+1,k+2) = ms*ab_s
            M(k+2,k+1) = ms*ab_s
            do n = k+2, k+Nec+1
              M(n,n+1) = ms*ab_s
              M(n+1,n) = ms*ab_s
              k=n
            end do
          end if
       end if
    end do
end subroutine Hamil_Mass_Matrix

subroutine Hamil_Couple(m,a,t)

    integer(kind=8) :: tt
    real(kind=8) :: U
    real(kind=8), intent(in) :: m, a
    real(kind=8), intent(out) :: t

    if(m .eq. ms_o) then
      tt = 1
       !call Atompot_LJ(a,U,tt) !Call interatomic potential
       call Atompot_Harrison(a,U,tt)
       !call Atompot_Harrison_Spring(a,U,tt)
       !call Atompot_Hooke(a,U,tt)
       !call Atompot_Stillinger_Weber(a,U,tt)
    else
      tt = 2
       !call Atompot_LJ(a,U,tt) !Call interatomic potential
       call Atompot_Harrison(a,U,tt)
       !call Atompot_Harrison_Spring(a,U,tt)
       !call Atompot_Hooke(a,U,tt)
       !call Atompot_Stillinger_Weber(a,U,tt)

    end if
    t = 2*U ! Inter-unit cell coupling energy for silicon
    Le(1) = Le(1) + U
    Le(2) = sqrt(Le(2)**2 + U**2/Np)


end subroutine Hamil_Couple

!!!!!!!!!!!!!!!!!!!!!!!!!!!!!!!!!!!!!!!!!!!!!!!!!!!!!!!!!!!!!!!!!!!!!!!!!!!!!!!!
!
! Atompot_LJ - Lennard Jones potential. Values from Kittel
!
!!!!!!!!!!!!!!!!!!!!!!!!!!!!!!!!!!!!!!!!!!!!!!!!!!!!!!!!!!!!!!!!!!!!!!!!!!!!!!!!
subroutine Atompot_LJ(r,U,t)
```

```
    real(kind=8), dimension(2) :: e,sig
    integer(kind=8), intent(in) :: t
    real(kind=8), intent(in) :: r
    real(kind=8), intent(out) :: U

    !e = 14e-16 * 6.24150974e11 ! [eV] LJ Parameters
    e(1) = 49.1e-16 * 1e+7 ! [J] LJ Parameters Silicon
    e(2) = 47.2e-16 * 1e+7 ! [J] LJ Parameters Germanium
    sig(1) = 4.753e-10 ! [m] Silicon
    sig(2) = 5.109e-10 ! [m] Germanium

    U = (4*e(t)*((sig(t)/r)**12-(sig(t)/r)**6)) ! [J] Lennar-Jones potential

end subroutine Atompot_LJ

!!!!!!!!!!!!!!!!!!!!!!!!!!!!!!!!!!!!!!!!!!!!!!!!!!!!!!!!!!!!!!!!!!!!!!!!!!!
!
! Atompot_Hooke - Hooke's law potential. Values from Kittel
!
!!!!!!!!!!!!!!!!!!!!!!!!!!!!!!!!!!!!!!!!!!!!!!!!!!!!!!!!!!!!!!!!!!!!!!!!!!!
subroutine Atompot_Hooke(r,U,t)

    real(kind=8), dimension(2) :: e,sig,c
    integer(kind=8), intent(in) :: t
    real(kind=8), intent(in) :: r
    real(kind=8), intent(out) :: U

    !e = 14e-16 * 6.24150974e11 ! [eV] LJ Parameters
    e(1) = 1.66e11 ! [N/m^2] Parameters Silicon
    e(2) = 1.29e11 ! [N/m^2] Parameters Germanium
    sig(1) = 3.835e-10 ! [m] Silicon
    sig(2) = 3.995e-10 ! [m] Germanium
    !rho(1) = ms/e(1)/vsi**2
    !rho(2) = mg/e(2)/vge**2
    c = 3*sig**3/16*e

    U = 0.5*c(t)*(r-sig(t))**2/sig(t)**2 ! [J] Lennar-Jones potential

end subroutine Atompot_Hooke

!!!!!!!!!!!!!!!!!!!!!!!!!!!!!!!!!!!!!!!!!!!!!!!!!!!!!!!!!!!!!!!!!!!!!!!!!!!
!
! Atompot_Stillinger_Weber - Stillinger Weber potential with just pair part
!                            This potential is for the a/4(x + y + z) direction of
!                            the diamond structure. Not correct for 1d chain
!
!!!!!!!!!!!!!!!!!!!!!!!!!!!!!!!!!!!!!!!!!!!!!!!!!!!!!!!!!!!!!!!!!!!!!!!!!!!
subroutine Atompot_Stillinger_Weber(r,U,t)

    real(kind=8) :: f,rr
    real(kind=8), dimension(2) :: e, A,B,p,q,aa,sig
    integer(kind=8), intent(in) :: t
    real(kind=8), intent(in) :: r
    real(kind=8), intent(out) :: U
```

```
    e(1) = 3.4723e-19 ! [J] Silicon
    e(2) = 3.4723e-19 ! [J] Germanium
    A(1) = 1.66e11
    A(2) = 1.29e11
    B(1) = 0.6022245584
    B(2) = 0.6022245584
    p(1) = 4
    p(2) = 4
    q(1) = 0
    q(2) = 0
    aa(1) = 1.8
    aa(2) = 1.8
    sig(1) = 2.0951e-10 ![m]
    sig(2) = 2.0951e-10 ![m]

    rr = r/sig(t)
    f = A(t)*(B(t)*rr**(-p(t))-rr**(-q(t)))*exp(1/(rr-aa(t)))
    write(*,*) 'rr, f =',rr,f

     U = -e(t)*f ! [J] Lennar-Jones potential

end subroutine Atompot_Stillinger_Weber

!!!!!!!!!!!!!!!!!!!!!!!!!!!!!!!!!!!!!!!!!!!!!!!!!!!!!!!!!!!!!!!!!!!!!!!!!!!!!!!!
!
! Atompot_Harrison - Harrison potential. Values from Mingo phonon papers
!
!!!!!!!!!!!!!!!!!!!!!!!!!!!!!!!!!!!!!!!!!!!!!!!!!!!!!!!!!!!!!!!!!!!!!!!!!!!!!!!!
subroutine Atompot_Harrison(r,U,t)

    real(kind=8), dimension(2) :: e,sig
    integer(kind=8), intent(in) :: t
    real(kind=8), intent(in) :: r
    real(kind=8), intent(out) :: U

    !e = 14e-16 * 6.24150974e11 ! [eV] LJ Parameters
    e(1) = (49.1)*q ! [J] LJ Parameters Silicon
    e(2) = (47.2)*q ! [J] LJ Parameters Germanium
    sig(1) = 2.35e-10 ! [m] Silicon
    sig(2) = 2.44e-10 ! [m] Germanium

    U = (0.5*e(t)*((r-sig(t))/sig(t))**2) ! [J] Lennar-Jones potential

end subroutine Atompot_Harrison

!!!!!!!!!!!!!!!!!!!!!!!!!!!!!!!!!!!!!!!!!!!!!!!!!!!!!!!!!!!!!!!!!!!!!!!!!!!!!!!!
!
! Atompot_Harrison_Spring - Harrison potential. Backout spring constant
!
!!!!!!!!!!!!!!!!!!!!!!!!!!!!!!!!!!!!!!!!!!!!!!!!!!!!!!!!!!!!!!!!!!!!!!!!!!!!!!!!
subroutine Atompot_Harrison_Spring(r,U,t)

    real(kind=8), dimension(2) :: e,e1,sig
```

```
    integer(kind=8), intent(in) :: t
    real(kind=8), intent(in) :: r
    real(kind=8), intent(out) :: U

    !e = 14e-16 * 6.24150974e11 ! [eV] LJ Parameters
    e(1) = 49.1*q ! [J] LJ Parameters Silicon
    e(2) = 47.2*q ! [J] LJ Parameters Germanium
    e1(1) = 1.07*q ! [J] LJ Parameters Silicon
    e1(2) = 0.845*q ! [J] LJ Parameters Germanium
    sig(1) = 2.35e-10 ! [m] Silicon
    sig(2) = 2.44e-10 ! [m] Germanium

    U = 0.5*4/3*(e(t))*r**2 ! [J] Lennar-Jones potential

end subroutine Atompot_Harrison_Spring

!!!!!!!!!!!!!!!!!!!!!!!!!!!!!!!!!!!!!!!!!!!!!!!!!!!!!!!!!!!!!!!!!!!!!!!!!!!!
!
! Atompot_Tersoff - Tersoff potential. Doesn't work in 1D
!
!!!!!!!!!!!!!!!!!!!!!!!!!!!!!!!!!!!!!!!!!!!!!!!!!!!!!!!!!!!!!!!!!!!!!!!!!!!!
subroutine Atompot_Tersoff(r,U,t)

    real(kind=8) :: fc
    real(kind=8), dimension(2) :: e,sig
    integer(kind=8), intent(in) :: t
    real(kind=8), intent(in) :: r
    real(kind=8), intent(out) :: U

    !e = 14e-16 * 6.24150974e11 ! [eV] LJ Parameters
    e(1) = 3.4*q !16.9e-16 * 1e+7 ! [J] LJ Parameters Silicon
    e(2) = 13.7e-16 * 1e+7 ! [J] LJ Parameters Germanium
    sig(1) = 2.74e-10 ! [m]
    sig(2) = 2.74e-10 ! [m]

    fc = 0.5-0.5*sin(pi/2*(r-sig(t)/r))
    U = 0.5*fc

end subroutine Atompot_Tersoff
```

This routine defines the boundary conditions and constructs the Green's function for the phonon NEGF model.

```
!!!!!!!!!!!!!!!!!!!!!!!!!!!!!!!!!!!!!!!!!!!!!!!!!!!!!!!!!!!!!!!!!!!!!!!!!!!!
!
! Negf_Bound - Boundary conditions - 1D Phonon NEGF
!
!!!!!!!!!!!!!!!!!!!!!!!!!!!!!!!!!!!!!!!!!!!!!!!!!!!!!!!!!!!!!!!!!!!!!!!!!!!!
subroutine Negf_Bound

   integer(kind=4) :: n
   real(kind=8) :: tm_ss, tm_se, wcut, Np1, Np2, dN

   tm_ss = abs(H(1,1))
```

```
tm_se = abs(H(Np,Np))
wcut = 2*sqrt(abs(tm_ss))

!write(*,*) 'wcut, ecut = ',wcut,hbar*wcut
!if(hbar*wcut .lt. E(k)) then
  !E(k) = 0
!  write(*,*) 'Warning: Above cut off frequency',E(k),hbar*wcut
!end if

!! Calculating Fermi functions of electrons entering through Silicon Source and Drain !!
call Startup_DOS(vsi,E(k),kT1,No1)
call Startup_DOS(vsi,E(k),kT2,No2)
!Derived the fermi function for Bose-Einstein particles, not the same as electronic NEGF
f1 = -No1*dlog(1-dexp((-E(k))/kT1)) ! 2D Source fermi function. Units of 1/m^2
f2 = -No2*dlog(1-dexp((-E(k))/kT2)) ! 2D drain fermi function. Units of 1/m^2
f3 = No1*(1-dlog(1-dexp((-(E(k)))/kT1))) ! 2D Source fermi function. Units of 1/m^2
f4 = No2*(1-dlog(1-dexp((-(E(k)))/kT2))) ! 2D drain fermi function. Units of 1/m^2

f5 = f_e(k,3) !fermi function of scatters -
! iteratively determine such that the current is conserved

!f1 = 1/(dexp(E(k)/kT1)-1)
!f2 = 1/(dexp(E(k)/kT2)-1)
!write(*,*) 'f1, f2 = ',f1,f2
!dN = E(k)/kT1*exp(E(k)/kT1)/(exp(E(k)/kT1)-1)**2*dT
!write(*,*) 'df, dN = ',f2-f1,dN

Sig1(:,:) = 0.0; Gam1(:,:) = 0.0; SigIn1(:,:) = 0.0; SigOut1(:,:) = 0.0
ka1 =  i*(1-(1 - ((dcmplx((E(k)/hbar)**2) + zplus - dcmplx(Ds))/&
       &(2.0*dcmplx(tm_ss))))**2)**0.5
ka1 = -i*cdlog((1 - ((dcmplx((E(k)/hbar)**2) + zplus - dcmplx(Ds))/&
       &(2.0*dcmplx(tm_ss)))) + ka1)
! Real Wave vector of broadened wave at drain
! (ACOS can be written in LOG Format See Matlab Manual)
!ka1 = acos(1-real(((E(k)/hbar)**2 + zplus - Ds)/(2.0*dcmplx(tm_ss))))
Sig1(1,1) = dcmplx(-tm_ss)*zexp(i*ka1) ! (omega^2) Self energy of source
Gam1(1,1) = i*(Sig1(1,1) - conjg(Sig1(1,1))) ! (omega^2) Source broadening matrix
SigIn1(1,1) = Gam1(1,1)*dcmplx(f1) ! (omega^2/m^2) Inscattering term for source
SigOut1(1,1) = Gam1(1,1)*dcmplx(f3)

Sig2(:,:) = 0.0; Gam2(:,:) = 0.0; SigIn2(:,:) = 0.0; SigOut2(:,:) = 0.0
ka2 =  i*(1-(1 - ((dcmplx((E(k)/hbar)**2) + zplus - dcmplx(Ds))/&
       &(2.0*dcmplx(tm_se))))**2)**0.5
ka2 = -i*cdlog((1 - ((dcmplx((E(k)/hbar)**2) + zplus - dcmplx(Ds))/&
       &(2.0*dcmplx(tm_se)))) + ka2)
! Real Wave vector of broadened wavGp at drain
! (ACOS can be written in LOG Format See Matlab Manual)
!ka2 = acos(1-real(((E(k)/hbar)**2 + zplus - Ds)/(2.0*dcmplx(tm_se))))
Sig2(Np,Np) = dcmplx(-tm_se)*zexp(i*ka2) ! (omega^2) Self energy of drain
Gam2(Np,Np) = i*(Sig2(Np,Np) - conjg(Sig2(Np,Np))) ! (omega^2) Drain broadening matrix
SigIn2(Np,Np) = Gam2(Np,Np)*dcmplx(f2) ! (omega^2/m^2) Inscattering term for drain
SigOut2(Np,Np) = Gam2(Np,Np)*dcmplx(f4)

Gamp(:) = 0.0
```

```
   if(f5 .ne. 0.0 .and. tst .lt. 5) Gamp = -SigInp(:,k)/f5-0.5*i*(SigOutp(:,k)+&
                                           &SigInp(:,k))/f5 !omega^2
   G(:,:) = (0,0);
   do n = 1, Np
     G1(n,n) = (0,0); G2(n,n) = (0,0)
   end do

   G1(1,1) = Sig1(1,1); G1(Np,Np) = Sig2(Np,Np) !(omega^2)

   do n = 1, Np
     G2(n,n) = ((dcmplx((E(k)/hbar)**2) + zplus)*eye(n,n))
     !(omega^2) Simplify Addition Because Only Diagonal Terms
   end do

   call Matxopt_ztcpy(dcmplx(H),G,Np)
   call Matxopt_sub_zdtf(G2,G,Np)
   call Matxopt_sub_zdtf2(G1,G,Np)
   call Matxopt_sub_zvtf2(Gamp,G,Np)
   !G = (G2 - dcmplx(H) - G1) ! Green's function (omega^2)

end subroutine Negf_Bound
```

This routine calculate the scattering matrices for the phonon NEGF model. The scattering is handled by shifting the density of states.

```
!!!!!!!!!!!!!!!!!!!!!!!!!!!!!!!!!!!!!!!!!!!!!!!!!!!!!!!!!!!!!!!!!!!!!!!!!!!!!!!!!!!
!
! Negf_Scatter - Calculate scattering matricies - Inelastic Scattering
!
!!!!!!!!!!!!!!!!!!!!!!!!!!!!!!!!!!!!!!!!!!!!!!!!!!!!!!!!!!!!!!!!!!!!!!!!!!!!!!!!!!!
subroutine Negf_Scatter

    double precision dlange
    external dlange

    integer(4) :: off, n, j, fp, fe
    real(8) :: NW, NE_off, w_ph

    SigInpNew(:,:) = 0.0; SigOutpNew(:,:) = 0.0

    fp = floor(sqrt(DH(1))/dw)-Ns !starting eigenvalue
    ! note first bin not at zero so subtract Ns
    fe = ceiling(sqrt(DH(Np))/dw)-Ns

    do n=1, Np
      w_ph = DH(n) !omega^2
      if(mwa .eq. 1) then !use Maxwellian Approx for Dist
        Nw = exp(-sqrt(DH(n))*hbar/kT) ! Simplified Bose-Einstein distribution
      else
        Nw = 1/(exp(sqrt(DH(n))*hbar/kT)-1) !true BE dist
      end if
      off = ceiling(sqrt(DH(n))/dw)-Ns

      !! Reassigning density of states to accomodate scattering
```

```
  !! Need to take the view point of the final electron state
  !nse = eoshift(Gnt, shift = -off, dim = 2) !E+hw emit phonon,  !1/omega^2-m^2
  !nsa = eoshift(Gnt, shift = off, dim = 2) !E-hw absorb phonon, !1/omega^2-m^2
  !pse = eoshift(Gpt, shift = -off, dim = 2) !E+hw emit phonon,  !1/omega^2-m^2
  !psa = eoshift(Gpt, shift = off, dim = 2) !E-hw absorb phonon, !1/omega^2-m^2
  call Matxopt_eoshift(Gnt,NE,off,nse) !E-hw final state is after emission
  call Matxopt_eoshift(Gnt,NE,-off,nsa)  !E+hw final state is after absorption
  call Matxopt_eoshift(Gpt,NE,off,pse) !E-hw
  call Matxopt_eoshift(Gpt,NE,-off,psa)  !E+hw

  ! need to zero matrix below lowest eigenvalue because +hw can't result
  ! in phonon scattered below allowed modes or above
  call Matxopt_eozero(nsa,NE,fe)
  call Matxopt_eozero(psa,NE,fe)
  call Matxopt_eozero(nse,NE,fe)
  call Matxopt_eozero(pse,NE,fe)

  call Matxopt_eozero(nsa,NE,-fp)
  call Matxopt_eozero(psa,NE,-fp)
  call Matxopt_eozero(nse,NE,-fp)
  call Matxopt_eozero(pse,NE,-fp)

  !unroll multiplications
  !use modified mattherson rule to add scattering rates, simple average
  !1/omega^2-m^2*omega^4 = omega^2/m^2
  !SigInpNewt and SigOutpNewt Calculated at beginning at top
  SigInpNew  = SigInpNew + So/(2*pi)*w_ph*SigInpNewt*((1+Nw)*nse + Nw*nsa)/Np
  SigOutpNew =  SigOutpNew + So/(2*pi)*w_ph*SigInpNewt* &
                &((1+Nw)*(nse+psa) + Nw*(nsa+pse))/Np

  if(debug_l >5) Si(:,:,n) = sqrt(So/(2*pi)*w_ph*SigInpNewt* &
                 &((1+Nw)*(psa+nse) + Nw*(nsa+pse))/Np) !scattering rate 1/s-m^2

end do

! Poisson convergence method
select case (coc_s)
  case (1) ! Simple mixing
    call Scatter_lin_smix(SigInpNew, SigInp)
    call Scatter_lin_smix(SigOutpNew, SigOutp)
  case (2) ! Anderson mixing
    call Scatter_anderson(SigInpNew,SigOutpNew,SigInp,SigOutp)
end select

norm(1) = dlange('i',Np,NE,(SigInpNew-SigInp),LDA,WORK)
norm(2) = dlange('i',Np,NE,SigInp,LDA,WORK)
norm(3) = dlange('i',Np,NE,(SigOutpNew-SigOutp),LDA,WORK)
norm(4) = dlange('i',Np,NE,SigOutp,LDA,WORK)

if(norm(2) .ne. 0.0 .and. norm(4) .ne. 0.0) then
  chng = norm(1)/norm(2) + norm(3)/norm(4)
else
  if(norm(1) .ne. 0.0 .and. norm(3) .ne. 0.0) then
    chng = 1;
```

```
      else
        chng = 0;
      end if
    end if

    ! Write change of charge to screen
    if(debug_l>2) write(6,'(/,A,ES11.4)') 'Scatter chg = ',chng

end subroutine Negf_Scatter
```

2D Thermionic - Electron NEGF

This routine constructs the Hamiltonian for the 2D thermionic device. It is necessary that the Hamiltonian be Hermitian so care must be taken at mixed cell interfaces. Templates are used to define the regions of material.

```
!!!!!!!!!!!!!!!!!!!!!!!!!!!!!!!!!!!!!!!!!!!!!!!!!!!!!!!!!!!!!!!!!!!!!!!!!!!!!!!
!
! Hamil_Create_5pt_std - Create Hamiltonian Matrix - 2D Electronic NEGF
!
!!!!!!!!!!!!!!!!!!!!!!!!!!!!!!!!!!!!!!!!!!!!!!!!!!!!!!!!!!!!!!!!!!!!!!!!!!!!!!!
subroutine Hamil_Create_5pt_std

   integer(kind=4) :: m, j, n
   real(kind=8) :: Hv1, Hv2, h1, h2, h3, h4
   real(kind=8) :: tsy1, tsy2, tgy1, tgy2, tsx1, tsx2
   real(kind=8) :: tgx1, tgx2, tpy1, tpy2, tpx1, tpx2

   do m = 1,Ndy
          do j = 1,Ndx
             n = (m-1)*Ndx + j

             !! Effective Mass Hamiltonian - H(1,1) Upper Left Corner
             h1 = 0; h2 = 0; h3 = 0; h4 = 0 ! Non-uniform Grid Parameters
             if(m .eq. 1) then
                h1 = Gdy(m)
                h2 = Gdy(m)
             else
                h1 = Gdy(m)
                h2 = Gdy(m-1)
             end if

             if(j .eq. 1) then
                h3 = Gdx(j)
                h4 = Gdx(j)
             else
                h3 = Gdx(j)
                h4 = Gdx(j-1)
             end if
             !Calculate Inter-unit cell coupling energy
             call Hamil_Couple(me_m,Ecm,h1,tsy1,m,n) ! Vacuum
             call Hamil_Couple(me_m,Ecm,h2,tsy2,m,n)
             call Hamil_Couple(me_e,Ece,h1,tgy1,m,n) ! Cathode
             call Hamil_Couple(me_e,Ece,h2,tgy2,m,n)
```

```
            call Hamil_Couple(me_m,Ecm,h3,tsx1,m,n)
            call Hamil_Couple(me_m,Ecm,h4,tsx2,m,n)
            call Hamil_Couple(me_e,Ece,h3,tgx1,m,n)
            call Hamil_Couple(me_e,Ece,h4,tgx2,m,n)
            call Hamil_Couple(me_p,Ecp,h1,tpy1,m,n) ! Anode
            call Hamil_Couple(me_p,Ecp,h2,tpy2,m,n)
            call Hamil_Couple(me_p,Ecp,h3,tpx1,m,n)
            call Hamil_Couple(me_p,Ecp,h4,tpx2,m,n)

            !! Warning - It is important that the Hamiltonian is Hermitian

            ! The conduction band edge is added here so it is Hermitian. Note
            ! we will only be iterating poissons eq for the electrostatic potential
            ! Conduction Band Edge For POTENTIAL!
            H(n,n) = (Ecm*Td(m,j) + Ece*(1-Tde(m,j)) + Ecp*Tdp(m,j))

            if (m .lt. Ndy .and. m .gt. 1) then
               Hv1 = tsy1*Tdc(m,j) + tgy1*(1-Tdc(m,j)) + tpy1*(Tdp_c(m,j))
               Hv2 = tsy2*Tdc(m-1,j) + tgy2*(1-Tdc(m-1,j)) + tpy2*(Tdp_c(m-1,j))
               H(n,n) = H(n,n) + Hv1 + Hv2
               H(n,n+Ndx) = H(n,n+Ndx) - Hv1 !Down
               H(n,n-Ndx) = H(n,n-Ndx) - Hv2 !Up
            else if (m .eq. Ndy) then
               Hv2 = tsy2*Tdc(m-1,j) + tgy2*(1-Tdc(m-1,j)) + tpy2*(Tdp_c(m-1,j))
               H(n,n) = H(n,n) + 2*Hv2
               H(n,n-Ndx) = H(n,n-Ndx) - Hv2 !Down, Reflective
               H(n,n-Ndx*(Ndy-1)) = H(n,n-Ndx*(Ndy-1)) - Hv2 !Down, Reflective
            else if (m .eq. 1) then
               Hv1 = tsy1*Tdc(m,j) + tgy1*(1-Tdc(m,j)) + tpy1*(Tdp_c(m,j))
               H(n,n) = H(n,n) + 2*Hv1
               H(n,n+Ndx) = H(n,n+Ndx) - Hv1 !Up, Reflective
               H(n,n+Ndx*(Ndy-1)) = H(n,n+Ndx*(Ndy-1)) - Hv1 !Up, Reflective
            end if

            if (j .gt. 1 .and. j .lt. Ndx) then
               Hv1 = tsx1*Tdb(m,j) + tgx1*(1-Tdb(m,j)) + tpx1*(Tdp_c(m,j))
               Hv2 = tsx2*Tdb(m,j-1) + tgx2*(1-Tdb(m,j-1)) + tpx2*(Tdp_c(m,j-1))
               H(n,n) = H(n,n) + Hv1 + Hv2
               H(n,n-1) = H(n,n-1) - Hv2 ! Left
               H(n,n+1) = H(n,n+1) - Hv1 ! Right
            else if (j .eq. 1) then
               Hv1 = tsx1*Tdb(m,j) + tgx1*(1-Tdb(m,j)) + tpx1*(Tdp_c(m,j))
               H(n,n) = H(n,n) + 2*Hv1
               H(n,n+1) = H(n,n+1) - Hv1 ! Right
            else if (j .eq. Ndx) then
               Hv2 = tsx2*Tdb(m,j-1) + tgx2*(1-Tdb(m,j-1)) + tpx2*(Tdp_c(m,j-1))
               H(n,n) = H(n,n) + 2*Hv2
               H(n,n-1) = H(n,n-1) - Hv2 ! Left
            end if

         end do
      end do

end subroutine Hamil_Create_5pt_std
```

```
!!!!!!!!!!!!!!!!!!!!!!!!!!!!!!!!!!!!!!!!!!!!!!!!!!!!!!!!!!!!!!!!!!!!!!!!!!!
!
! Hamil_Couple - Calculate Coupling Energy
!
!!!!!!!!!!!!!!!!!!!!!!!!!!!!!!!!!!!!!!!!!!!!!!!!!!!!!!!!!!!!!!!!!!!!!!!!!!!
subroutine Hamil_Couple(m,Ec,a,t,mn,nn)

    integer(kind=4), intent(in) :: mn, nn
    real(kind=8), intent(in) :: m, a, Ec
    real(kind=8), intent(out) :: t

    t = (hbar**2.0)/(2.0*m*(a**2.0)*q) ! Inter-unit cell coupling energy for silicon
    if(rank .eq. 0) call Errors_HamilE(t,Ec,Ef,a,mn,nn)

end subroutine Hamil_Couple
```

This routine defines the boundary condition for a 2D electron Hamiltonian and constructs the Green's function.

```
!!!!!!!!!!!!!!!!!!!!!!!!!!!!!!!!!!!!!!!!!!!!!!!!!!!!!!!!!!!!!!!!!!!!!!!!!!!
!
! Negf_Bound - Boundary conditions
!
!!!!!!!!!!!!!!!!!!!!!!!!!!!!!!!!!!!!!!!!!!!!!!!!!!!!!!!!!!!!!!!!!!!!!!!!!!!
subroutine Negf_Bound

   integer(kind=4) :: n
   real(kind=8) :: tm_p, tm_e, tm_m

   call Hamil_Couple(me_p,Ecp,Gdx(1),tm_p,1,1)
   call Hamil_Couple(me_e,Ece,Gdx(Ndx),tm_e,1,1)
   call Hamil_Couple(me_m,Ecm,Gdx(Ndx),tm_m,1,1)
   call Startup_Fermi(me_p,kT2,No1) ! Constant used in Fermi function (drain) (1/m2)
   call Startup_Fermi(me_e,kT1,No2) ! Constant used in Fermi function (emitter) (1/m2)

   !! Calculating Fermi functions of electrons entering through Silicon Source and Drain !!
   if((E(k)- mu + V)/kT2 .gt. 800 .and. (E(k)- mu2)/kT1 .gt. 800) then
   !left boundary
     f1 = No1*dlog(1+dexp((-(E(k)- mu + V/2))/kT2)) ! 2D Collector fermi function [1/m^2]
   !right boundary
     f2 = No2*dlog(1+dexp((-(E(k)- mu2 - V/2))/kT1)) ! 2D Emitter fermi function [1/m^2]
   else
     f1 = No1*dlog(1+1/(1+dexp((E(k)- mu + V/2)/kT2))) ! 2D Collector fermi function [1/m^2]
     f2 = No2*dlog(1+1/(1+dexp((E(k)- mu2 - V/2)/kT1))) ! 2D Emitter fermi function [1/m^2]
   end if

   ka1 =  i*(1-(1 - ((dcmplx(E(k)) + zplus - dcmplx(Ds) - V/2)/(2.0*dcmplx(tm_p))))**2)**0.5
   ka1 = -i*cdlog((1 - ((dcmplx(E(k)) + zplus - dcmplx(Ds) - V/2)/(2.0*dcmplx(tm_p)))) + ka1)
   ! Real Wave vector of broadened waves at drain
   ! (ACOS can be written in LOG Format See Matlab Manual)
   do n = 1, Np, Ndx
      Sig1(n) = dcmplx(-tm_p)*zexp(i*ka1) ! Self energy of source [eV]
      Gam1(n) = i*(Sig1(n) - conjg(Sig1(n))) ! Source broadening matrix [eV]
```

```
      SigIn1(n) = Gam1(n)*dcmplx(f1) ! Inscattering term for source [eV/m^2]
   end do

   ka2 =  i*(1-(1 - ((dcmplx(E(k)) + zplus - dcmplx(Ds) + V/2)/(2.0*dcmplx(tm_e))))**2)**0.5
   ka2 = -i*cdlog((1 - ((dcmplx(E(k)) + zplus - dcmplx(Ds) + V/2)/(2.0*dcmplx(tm_e)))) + ka2)

   !be careful, whole bottom or just emitter?
   do n = Ndx, Np+1, Ndx
      Sig2(n) = (0.0,0.0) !dcmplx(-tm_m)*zexp(i*ka2) ! Self energy of drain [eV]
      Gam2(n) = i*(Sig2(n) - conjg(Sig2(n))) ! Drain broadening matrix [eV]
      SigIn2(n) = Gam2(n)*dcmplx(f2) ! Inscattering term for drain [eV/m^2]
   end do
   !do n = Ndx, Np+1, Ndx
   do n = Ndx*(Neby+1), Ndx*(Neby+Nwey+1), Ndx
      Sig2(n) = dcmplx(-tm_e)*zexp(i*ka2) ! Self energy of drain [eV]
      Gam2(n) = i*(Sig2(n) - conjg(Sig2(n))) ! Drain broadening matrix [eV]
      SigIn2(n) = Gam2(n)*dcmplx(f2) ! Inscattering term for drain [eV/m^2]
   end do

   G1(:,:) = (0,0);G2(:,:) = (0,0)

   do n = 1, Np, Ndx
      G1(n,n) = Sig1(n) ![eV] Simplify Addition Because Only Periodic Diagonal Terms
   end do

   do n = Ndx, Np+1, Ndx
   !do n = Ndx*(Neby+1), Ndx*(Neby+Nwey+1), Ndx
      G1(n,n) = Sig2(n) ![eV]
   end do

   do n = 1, Np
      G2(n,n) = ((dcmplx(E(k)) + zplus)*eye(n,n) - dcmplx(Ua(n)) + dcmplx(U(n,n)))
      ![eV] Simplify Addition Because Only Diagonal Terms
   end do

   G = (G2 - dcmplx(H) - G1) ! Green's function [eV]

end subroutine Negf_Bound
```

This routine outputs a 3d plot of the local density of states in a VTK format to be opened in Paraview visualization software.

```
!!!!!!!!!!!!!!!!!!!!!!!!!!!!!!!!!!!!!!!!!!!!!!!!!!!!!!!!!!!!!!!!!!!!!!!!!!!!!!!!
!
! Output_vtk_ldos - Plot Density of State (3d plot)
!
!!!!!!!!!!!!!!!!!!!!!!!!!!!!!!!!!!!!!!!!!!!!!!!!!!!!!!!!!!!!!!!!!!!!!!!!!!!!!!!!
subroutine Output_vtk_ldos(A,c)

    integer(kind=4) :: r, n, j, k, err
    real(kind=8) :: w, l, Em
    character*100 :: var
    character*80 :: Fname
```

```
    integer(kind=4), intent(in) :: c
    real(kind=8), dimension(:,:), intent(in) :: A

    103 format (A)
    104 format (ES12.5)
    105 format (A,1X,I5,I5,I5)
    106 format (A,I5,A)
    107 format (A,I7)

    Fname = Utility_MakeFileName('ldos',c,'vtk')

    open (unit=19, file=Fname, status='NEW', action='write', iostat=err)
    write(var,*) Fname
    call Errors_Fileopen(err,var)

    write(19,103) '# vtk DataFile Version 2.0'
    write(19,103) 'Field Emission Device - LDOS'
    write(19,103) 'ASCII'
    write(19,103) 'DATASET RECTILINEAR_GRID'
    write(19,105) 'DIMENSIONS',Ndx,Ndy,NE

    l = 0; w = 0
    write(19,106) 'X_COORDINATES ',Ndx,' float'
    do n=1,Ndx
      write(19,104) l !Points
      l = l + Gdx(n)
    end do

    write(19,106) 'Y_COORDINATES ',Ndy,' float'
    do j=1,Ndy
      write(19,104) w !Points
      w = w + Gdy(j)
    end do

    Em = maxval(E)
    write(19,106) 'Z_COORDINATES ',NE,' float'
    do r=1,NE
      write(19,104) E(r)/Em*l !Points
    end do

    write(19,107) 'POINT_DATA', NE*Np
    write(19,103) 'SCALARS LDOS float 1'
    write(19,103) 'LOOKUP_TABLE default'
    do r=1, NE
       do k=1,Ndy
         do n=1,Ndx
         j = (k-1)*Ndx + n
           write(19,104) A(r,j)/(2.0*pi) !LDOS Contour Plot
         end do
       end do
    end do
   close(unit=19)

end subroutine Output_vtk_ldos
```

BIBLIOGRAPHY

Arfken, G. B. and Weber, H. J. (2005). *Mathematical Methods for Physicists*. Elsevier.

Bian, Z., Zebarjadi, M., Singh, R., Ezzahri, Y., Shakouri, A., Zeng, G., Bahk, J.-H., Bowers, J. E., Zide, J. M. O., and Gossard, A. C. (2007). Cross-plane seebeck coefficient and lorenz number in superlattices. *Phys. Rev. B*, 76(20):205311.

Brandbyge, M., Mozos, J.-L., Ordejón, P., Taylor, J., and Stokbro, K. (2002). Density-functional method for nonequilibrium electron transport. *Phys. Rev. B*, 65:165401.

Bulusu, A. and Walker, D. G. (2007a). Modeling of thermoelectric properties of semiconductor thin films with quantum and scattering effects. *Journal of Heat Transfer*, 129(4):492–499.

Bulusu, A. and Walker, D. G. (2007b). Quantum modeling of thermoelectric performance of strained Si/Ge/Si superlattices using the nonequilibrium green's function method. *Journal of Applied Physics*, 102(7):073713.

Bulusu, A. and Walker, D. G. (2008a). One-dimensional thin-film phonon transport with generation. *Microelectronics Journal*, 39(7):950–956.

Bulusu, A. and Walker, D. G. (2008b). Review of transport modeling for thermoelectric materials. *Superlattices and Microstructures*, 44(1–36).

Bulusu, A. and Walker, D. G. (2008c). State of the art technologies used to improve performance of thermoelectric devices. In *proceedings of the Joint ASME-ISHMT Heat Transfer Conference*, Hyderabad, India.

Burr, T. A., Seraphin, A. A., Werwa, E., and Kolenbrander, K. D. (1997). Carrier transport in thin films of silicon nanoparticles. *Phys. Rev. B*, 56:4818–4824.

Carabateas, E. N. (1962). Electron space-charge-limited operation of cesium thermionic converters. *Journal of Applied Physics*, 33(4):1445–1449.

Chung, D.-Y., Hogan, T., Brazis, P., Rocci-Lane, M., Kannewurf, C., Bastea, M., Uher, C., and Kanatzidis, M. G. (2000). CsBi4Te6: A High-Performance Thermoelectric Material for Low-Temperature Applications. *Science*, 287(5455):1024–1027.

Corliss, W. R. and Harvey, D. (1964). *Radioisotpic Power Generation*. Prentice-Hall, Inc., Englewood Cliffs, N.J.

Datta, S. (1990). A simple kinetic equation for steady-state quantum transport. *Journal of Physics: Condensed Matter*, 2(40):8023–8052.

Datta, S. (2005). *Quantum Transport: Atom to Transistor*. Cambridge University Press, New York.

Derosa, P. A. and Seminario, J. M. (2001). Electron transport through single molecules: scattering treatment using density functional and green function theories. *The Journal of Physical Chemistry B*, 105(2):471–481.

Eyert, V. (1996). A comparative study on methods for convergence acceleration of iterative vector sequences. *Journal of Computational Physics*, 124(2):271 – 285.

Fischetti, M. V. and Laux, S. E. (1996). Band structure, deformation potentials, and carrier mobility in strained si, ge, and sige alloys. 80(4):2234–2252.

Forbes, R. G. (2001). Low-macroscopic-field electron emission from carbon films and other electrically nanostructred heterogeneous materials: Hypothesis about emission mechanism. *Solid-State Electronics*, 45:779–808.

Fowler, R. H. and Nordheim, L. W. (1928). Field emission from metallic surfaces. *Proceedings of the Royal Society A*, 119:173–181.

Geballe, T. H. and Hull, G. W. (1955). Seebeck effect in silicon. *Physical Review*, 98(4):940–948.

Ghosh, A. W., Rakshit, T., and Datta, S. (2004). Gating of a molecular transistor: electrostatic and conformational. *Nano Letters*, 4(4):565–568.

Glatz, A. and Beloborodov, I. S. (2009). Thermoelectric and seebeck coefficients of granular metals. *Physical Review B (Condensed Matter and Materials Physics)*, 79(23):235403.

Goldsmid, H. J. (1964). *Thermoelectric Refrigeration*. Plenum Press, New York.

Goldsmid, H. J. and Douglas, R. W. (1954). The use of semiconductors in thermoelectric refrigeration. *British Journal of Applied Physics*, 5(11):386.

Grujicic, M., Cao, G., and Gersten, B. (2003). Enhancement of field emission in carbon nanotubes through adsorption of polar molecules. *Applied Surface Science*, 206(14):167 – 177.

Guo, J., Datta, S., and Lundstrom, M. (2004). A numerical study of scaling issues for schottky-barrier carbon nanotube transistors. *Electron Devices, IEEE Transactions on*, 51(2):172 – 177.

Harman, T., Walsh, M., laforge, B., and Turner, G. (2005). Nanostructured thermoelectric materials. *Journal of Electronic Materials*, 34:L19–L22. 10.1007/s11664-005-0083-8.

Harrison, W. (1989). *Electronic Structure and the Properties of Solids*. W.H. Freeman and Company.

Hicks, L. D. and Dresselhaus, M. S. (1993). Effect of quantum-well structures on the thermoelectric figure of merit. *Phys. Rev. B*, 47(19):12727–12731.

Hopkins, P. E., Norris, P. M., Tsegaye, M. S., and Ghosh, A. W. (2009). Extracting phonon thermal conductance across atomic junctions: Nonequilibrium green's function approach compared to semiclassical methods. *Journal of Applied Physics*, 106(6):063503.

Hostler, S. R., Qu, Y. Q., Demko, M. T., Abramson, A. R., Qiu, X., and Burda, C. (2008). Thermoelectric properties of pressed bismuth nanoparticles. *Superlattices and Microstructures*, 43(3):195 – 207.

Ingold, J. H. (1961). Calculation of the maximum efficiency of the thermionic converter. *Journal of Applied Physics*, 32(5):769–772.

Jacoboni, C., Cananli, C., Ottaviani, G., and Quaranta, A. A. (1977). A review of some charge transport properties. *Solid State Electronics*, 20(2):77–89.

Jacoboni, C. and Reggiani, L. (1983). The monte carlo method for the solution of charge transport in semiconductors with applications to covalent materials. *Reviews in Modern Physics*, 55(5):645–705.

Kim, W., Singer, S. L., Majumdar, A., Vashaee, D., Bian, Z., Shakouri, A., Zeng, G., Bowers, J. E., Zide, J. M. O., and Gossard, A. C. (2006a). Cross-plane lattice and electronic thermal conductivities of ErAs : InGaAs/InGaAlAs superlattices. *Applied Physics Letters*, 88(242107).

Kim, W., Zide, J., Gossard, A., Klenov, D., Stemmer, S., Shakouri, A., and Majumdar, A. (2006b). Thermal conductivity reduction and thermoelectric figure of merit increase by embedding nanoparticles in crystalline semiconductors. *Physical Review Letters*, 96(045901).

Kittel, C. (1986). *Introduction to Solid State Physics*. Wiley, New York, 6$^{\text{th}}$ edition.

Kock, F., Garguilo, J., Brown, B., and Nemanich, R. (2002). Enhanced low-temperature thermionic field emission from surface-treated n-doped diamond films. *Diamond and Related Materials*, 11(3-6):774 – 779.

Koeck, F., Garguilo, J., and Nemanich, R. (2004). On the thermionic emission from nitrogen-doped diamond films with respect to energy conversion. *Diamond and Related Materials*, 13(1112):2052 – 2055. Proceedings of the 9th International Conference on New Diamond Science and Technology (ICNDST-9).

Koeck, F. and Nemanich, R. (2005). Sulfur doped nanocrystalline diamond films as field enhancement based thermionic emitters and their role in energy conversion. *Diamond and Related Materials*, 14(1112):2051 – 2054. Proceedings of the 10th International Conference on New Diamond Science and Technology (ICNDST-10).

Koeck, F. A., Nemanich, R. J., Balasubramaniam, Y., Haenen, K., and Sharp, J. (2011). Enhanced thermionic energy conversion and thermionic emission from doped diamond films through methane exposure. *Diamond and Related Materials*, 20(8):1229 – 1233.

Koswatta, S., Hasan, S., Lundstrom, M., Anantram, M., and Nikonov, D. (2007). Nonequilibrium green's function treatment of phonon scattering in carbon-nanotube transistors. *Electron Devices, IEEE Transactions on*, 54(9):2339 –2351.

Krishnamurthy, S., Sher, A., and Chen, A.-B. (1986). Band structures of $si_x\ ge_{1-x}$ alloys. *Phys. Rev. B*, 33(2):1026–1035.

Lambe, J. and Jaklevic, R. C. (1968). Molecular vibration spectra by inelastic electron tunneling. *Phys. Rev.*, 165:821–832.

Langmuir, I. (1923). The effect of space charge and initial velocities on the potential distribution and thermionic current between parallel plane electrodes. *Phys. Rev.*, 21:419–435.

Langmuir, I. (1932). Vapor pressures, evaporation, condensation and adsorption. *Journal of the American Chemical Society*, 54(7):2798–2832.

Lee, M. L. and Venkatasubramanian, R. (2008). Effect of nanodot areal density and period on thermal conductivity in sige/si nanodot superlattices. *Applied Physics Letters*, 92(5):053112.

Lee, S. M., Cahill, D. G., and Venkatasubramanian, R. (1997). Thermal conductivity of Si-Ge superlattices. *Applied Physics Letters*.

Lide, D. R. (2007). *CRC Handbook of Chemistry and Physics, 88th Edition*. CRC.

Lundstrom, M. (2000). *Fundamentals of Carrier Transport*. Cambridge University Press.

Mahan, G. (2000). *Many-Particle Physics*. Kluwer Academic/Plenum Publisher.

Mahan, G. D. and Woods, L. M. (1998). Mulitlayer thermionic refrigeration. *Physical Review Letters*, 80(18):4016–4019.

Maiti, A., Andzelm, J., Tanpipat, N., and von Allmen, P. (2001). Effect of adsorbates on field emission from carbon nanotubes. *Phys. Rev. Lett.*, 87:155502.

Modinos, A. (1984). *Field, thermionic, and secondary electron emission spectroscopy*. Plenum Press.

Morin, F. J. (1954). Lattice-scattering mobility in germanium. *Phys. Rev.*, 93:62–63.

Murphy, E. L. and Good, R. H. (1956). Thermionic emission, field emission, and the transition region. *Phys. Rev.*, 102:1464–1473.

Murphy-Armando, F. and Fahy, S. (2008). First-principles calculation of carrier-phonon scattering in n -type $si_{1-x}ge_x$ alloys. *Phys. Rev. B*, 78(3):035202.

Musho, T. and Walker, D. (2011a). Quantum simulation of nanocrystalline composite thermoelectric properties [in-review]. *Solid State Electronics*.

Musho, T. and Walker, D. (2011b). Scalability of quantum simulations of thermoelectric superlattice devices. *Computational Materials Science*, 50(11):3265 – 3269.

Nava, F., Canali, C., Jacoboni, C., Reggiani, L., and Kozlov, S. (1980). Electron effective masses and lattice scattering in natural diamond. *Solid State Communications*, 33(4):475 – 477.

O'Dwyer, M. F., Lewis, R. A., Zhang, C., and Humphrey, T. E. (2005). Electronic efficiency in nanostructured thermionic and thermoelectric devices. *Phys. Rev. B*, 72(20):205330.

Orihashi, M., Noda, Y., Chen, L. D., Goto, T., and Hirai, T. (2000). Effect of tin content on thermoelectric properties of p-type lead tin telluride. *Journal of Physics and Chemistry of Solids*, 61(6):919 – 923.

Paxton, H., D. J. (2011). Nitrogen doped diamond films. Personal Communication.

Pickett, W. E. (1994). Negative electron affinity and low work function surface: Cesium on oxygenated diamond (100). *Phys. Rev. Lett.*, 73:1664–1667.

Ramalingam, M. (2000). *The Electrical Engineering Handbook*, chapter Direct Energy Conversion. CRC Press LLC.

Reimann, A. (1934). *Thermionic Emission*. John Wiley & Sons.

Restrepo, O. D., Varga, K., and Pantelides, S. T. (2009). First-principles calculations of electron mobilities in silicon: Phonon and coulomb scattering. *Applied Physics Letters*, 94(21):212103.

Richardson, O. (1916). *The Emission Of Electricity From Hot Bodies*. Longmans Green And Company.

Robertson, J. (1999). Mechanics of electron field emission from diamond, diamond-like carbon and nanostructured carbon. *Journal of Vacuum Science and Technology B*, 17(2):659–665.

Sales, B. C., Mandrus, D., Chakoumakos, B. C., Keppens, V., and Thompson, J. R. (1997). Filled skutterudite antimonides: Electron crystals and phonon glasses. *Phys. Rev. B*, 56(23):15081–15089.

Schottky, W. (1914). *Zeits. f. Physik*, 15:872.

Seebeck, T. J. (1823). Magnetische polarisation der metalle und erze durck temperatur-differenz. *Abhandlungen der Deutschen Akademie der Wissenschafren zu Berlin*.

Seitz, F. (1940). *The Modern Theory of Solids*. McGraw-Hill Book Company.

Shakouri, A., Lee, E. Y., Smith, D. L., Narayanamurti, V., and Bowers, J. E. (1998). Thermoelectric effects in submicron heterostructure barriers. *Microscale Thermophysical Engneering*, 2(1):37–47.

Shaw, D. T. and Margolis, S. G. (1969). Effect of large electric fields on the electron energy distribution and ionization rate in a cesium discharge. *Journal of Applied Physics*, 40(11):4377–4383.

Subramanian, K., Wong, Y., Kang, W., Davidson, J., Choi, B., and Howell, M. (2007). Field emission devices for advanced electronics comprised of lateral nanodiamond or carbon nanotube emitters. *Diamond and Related Materials*, 16(12):1997 – 2002. Proceedings of the Joint International Conference: Nanocarbon and Nanodiamond 2006.

Summers, C. J. and Brennan, K. F. (1986). Variably spaced superlattice energy filter, a new device design concept for high-energy electron injection. *Applied Physics Letters*, 48(12):806–808.

Tada, K. and Watanabe, K. (2002). *Ab Initio* study of field emission from graphitic ribbons. *Phys. Rev. Lett.*, 88:127601.

Taylor, J., Kippeny, T., and Rosenthal, S. J. (2001). Surface stoichiometry of CdSe nanocrystals determined by rutherford backscattering spectroscopy. *Journal of Cluster Science*, 12(4):571–582.

Van de Walle, C. G. (1989). Band lineups and deformation potentials in the model-solid theory. *Physical Review B*, 39(3):1871–1883.

Venkatasubramanian, R., Siivola, E., Colpitts, T., and O'Quinn, B. (2001). Thin-film thermoelectric devices with high room-temperature figures of merit. *Nature*, 413(11):597–602.

Vineis, C. J., Shakouri, A., Majumdar, A., and Kanatzidis, M. G. (2010). Nanostructured thermoelectrics: Big efficiency gains from small features. *Advanced Materials*, 22(36):3970–3980.

Vining, C. B., Laskow, W., Hanson, J. O., Van der Beck, R. R., and Gorsuch, P. D. (1991). Thermoelectric properties of pressure sintered si0.8ge0.2 thermoelectric alloys. *Journal of Applied Physics*, 69(8):4333 –4340.

Wade, T., D. J. (2011). Nitrogen/hydrogen doped diamond nano-tips. Personal Communication.

Wang, R. Y., Feser, J. P., Lee, J.-S., Talapin, D. V., Segalman, R., and Majumdar, A. (2008). Enhanced thermopower in pbse nanocrystal quantum dot superlattices. *Nano Letters*, 8(8):2283 – 2288.

Wilson, H. (1908). The effect of hydrogen on the discharge of negative electricity from hot platinum. *Phil. Trans. R. Soc. Lond. A*, 208:247–273.

Zeng, G., Joshua M. O. Zide, W. K., Bowers, J. E., Gossard, A. C., Bian, Z., Zhang, Y., Shakouri, A., Singer, S. L., and Majumdar, A. (2007). Cross-plane seebeck coefficient of eras:ingaas/ingaalas superlattices. *Journal of Applied Physics*, 101(3):034502.

Zhang, W., Fisher, T. S., and Mingo, N. (2007). The atomistic green's function method: An efficient simulation approach for nanoscale phonon transport. *Numerical Heat Transfer Part B-Fundamentals*, 51(4):333–349.

Zide, J. M. O., Vashaee, D., Bian, Z. X., Zeng, G., Bowers, J. E., Shakouri, A., and Gossard, A. C. (2006). Demonstration of electron filtering to increase the seebeck coefficient in $in_0.53$ $ga_0.47as/in_0.53$ $ga_0.28al_0.19as$ superlattices. *Physical Review B (Condensed Matter and Materials Physics)*, 74(20):205335.

Ziman, J. M. (1960). *Electrons and Phonons*. Oxford University Press, London.